Atom interferometry in an optical cavity

by

Matthew Jaffe

A dissertation submitted in partial satisfaction of the

requirements for the degree of

Doctor of Philosophy

in

Physics

in the

Graduate Division

of the

University of California, Berkeley

Committee in charge:

Associate Professor Holger Müller, Chair
Associate Professor Norman Yao
Professor Karl van Bibber

Fall 2018

Atom interferometry in an optical cavity

Abstract

Atom interferometry in an optical cavity

by

Matthew Jaffe

Doctor of Philosophy in Physics

University of California, Berkeley

Associate Professor Holger Müller, Chair

Matter wave interferometry with laser pulses has become a powerful tool for precision measurement. Optical resonators, meanwhile, are an indispensable tool for control of laser beams. We have combined these two components, and built the first atom interferometer inside of an optical cavity. This apparatus was then used to examine interactions between atoms and a small, in-vacuum source mass. We measured the gravitational attraction to the source mass, making it the smallest source body ever probed gravitationally with an atom interferometer. Searching for additional forces due to screened fields, we tightened constraints on certain dark energy models by several orders of magnitude. Finally, we measured a novel force mediated by blackbody radiation for the first time.

Utilizing technical benefits of the cavity, we performed interferometry with adiabatic passage. This enabled new interferometer geometries, large momentum transfer, and interferometers with up to one hundred pulses. Performing a trapped interferometer to take advantage of the clean wavefronts within the optical cavity, we performed the longest duration spatially-separated atom interferometer to date: over ten seconds, after which the atomic wavefunction was coherently recombined and read out as interference to measure gravity. This work demonstrates the feasibility and utility of bringing a cavity to atom interferometry.

Contents

List of Figures

List of Tables

Acknowledgments

There are many people behind the work presented in this thesis. Most notably, none of it would exist without my advisor, Holger Müller. When I joined Holger's group for the summer as a wildly uninformed late-first-year grad student, I had no idea how fantastic a decision I had stumbled sideways into. Spending the past six years in Holger's group has been truly formative. Holger and his expertise, drive, and raw enthusiasm for scientific research are inspiring. He has vision to recognize important research opportunities, technical prowess to overcome obstacles along the way, and a friendly, supportive and encouraging persona that makes you feel like you can do it too. For these things and many many more, I want to thank Holger.

The research group that Holger has assembled is likewise a joy to work with. When I was first starting in the group, Paul Hamilton was a postdoc. I knew nothing about atomic physics, and Paul taught me everything I could hang onto, with an endless supply of patience. Paul's vision charted the course for many of the scientific goals for the cavity interferometer, and I'm extremely thankful for the opportunity to have worked with and learned from him.

Before I stepped foot in Berkeley, the machinations and groundwork for a cavity interferometer were already underway. Brian Estey, Justin Brown, and Lothar Maisenbacher laid the foundation in designing and building the vacuum chamber, laser systems, and more. The excellent, forward-thinking and robust work they did allowed future cavity interferometeers like me to hit the ground running. Of these, I had by far the longest overlap in the group with Brian. Despite an affected aura of gruffness, Brian constantly lent his time, clear-headed technical powers, and sanity to the younger grad students around him.

On the cavity interferometer, I was lucky to work alongside Vicky Xu and Philipp Haslinger for several years. Both Vicky and Philipp have characteristic strengths and scientific styles that kept our experiment steadily moving in a variety of interesting directions. Philipp's "act first"-style helped us move quickly and uncover hidden details. Vicky is able to keep a resolute eye on big-picture importance while also handling critical day-to-day details of the experiment. It was also a pleasure to work with Sofus Kristensen over the past year, while he worked on the experiment as a visiting student from Denmark. Moving forward, the cavity interferometer will be in excellent, capable and creative hands with Vicky. I'm excited to see the next steps the experiment will take.

The rest of the Müller group are also inspiring and helpful colleagues. Chenghui Yu, Kayleigh Casella, Eric Copenhaver, Osip Schwartz, Weicheng Zhong, Xuejian Wu, Richard Parker, Sara Campbell, Jeremy Axelrod, Zack Pagel, Bola Malek: all of you have helped me solve multiple problems, and have been a pleasure to work with and grab coffee, food, and beer with. So much coffee....

I also need to thank our theory collaborators. Justin Khoury, Ben Elder, and Amol Upadhye tried to tell us all about how chameleons and symmetrons work, which was an exciting chance for an AMO experimentalist to dip a toe into cosmology. Helmut Ritsch, Matthias Sonnleitner and Monika Ritsche-Marte were instrumental in predicting the blackbody radiation force, and helping us to observe it.

I was lucky to spend a couple months in the group of Ernst Rasel at the Institut für Quantenoptik at the Leibniz Universität, Hannover. Dennis Schlippert deflected my noncommittal, American “Oh, that’d be great!” into a German “I have acquired funding, when will you arrive?” reality. I’m extremely grateful to Dennis both for being the driving force behind making it happen, and for showing incredible hospitality while I was there. I got to work with and learn from Étienne Wodey, who really does seem to know everything, despite downplaying it. Many other members of the Hannover group were wonderful hosts and friends, including Logan Richardson, Sven Abend, Dennis Becker, Maike Lachmann, Waldemar Herr, Christian Schubert, Henning Albers, Matthias Gersemann, Naceur Gaaloul, Torben Schulze, Til Rehmert and Christian Meiners.

Anne Takizawa, thank you for being the caring, endlessly helpful, first face of the Physics department seen by incoming grad students for 33 years (happy retirement!). Carlos Bustamante and Stephen Pride Raffel have also been amazingly helpful, friendly, and ready for a quick smile, chat or wave whenever you see them. I also want to thank Joseph Kant (happy retirement too!) for being a steadfast and caring presence in the student machine shop.

Sometimes things aren’t going so great in lab, and even if they are, maybe you’ve been spending too much time there. In times like those, the crew kept me going. Thanks to Brian, Mike, Eric, Elaine, Erik, Andy, Greg, and Seth for being you. Y’all are my friends more than you could ever know. I don’t know how I could have made it through grad school without any of you. I’m so thankful we ended up in the same place so we could meet.

I also want to thank the Bay Area frisbee community for the fun times, great competition, tough workouts and camaraderie. In particular, shoutout to San Francisco Mischief, Oakland Guerrilla, Cal Ugmo and the San Jose Spiders. It’s been a joy to play several years with each of these teams. The opportunities here have been incredibly fun, made me a much better player, and been my sanity-maintaining physical release. To all of my teammates and training partners: it has been so much fun sharing the field and training with you. It’s impossible to list everyone here, but I appreciate so much what you each bring to the community and have added to my life.

Thank you to Vinay, Colin, Jonathan, Carolyn, Chuck, Tommy, Xander, Kohji, Sean Ham, Lassie, Chris Akers, Chris Benson, and many more for your friendship.

Thank you to my family for your love and caring since before I can remember. Mom and Dad, I appreciate all of the thankless sacrifices you’ve made for me, Tim, and Sam (I’m sure I don’t even know the half of it).

Finally, I want to thank Kwai for everything. Thank you for smoothing out the valleys and elevating the peaks in my life. You are the most supportive person I know, and you are always there for me.

Chapter 1

Introduction

1.1 Interferometry and matter waves

Measuring is mostly about counting. Whether counting ticks on a ruler to measure distance, or counting swings of a clock pendulum to keep time, integers are doing the heavy lifting. Inferring spacing between the ticks is more difficult than the counting. In the ruler example, even with a great microscope, you'd be hard pressed to determine if a piece of paper was 0.1 or 0.15 mm thick, if the ruler ticks are spaced by 1 mm. If you stack 1000 papers on top of each other, these 1 mm rulings might now be of more use.

The paper example demonstrates the utility of finely spaced, countable rulings to making a precise measurement. This observation motivates the idea of a light interferometer, which splits, redirects and recombines an incident light ray along two paths. Depending on the path length difference, the two waves will be in or out of phase to some degree, giving bright or dark spots at the output ports. If a mirror on one of the paths moves, counting the dark/bright oscillations pass by gives a measure of the distance moved in units of the wavelength of light ($\sim$1 μm). This is much finer spacing than a ruler! Additionally, the wavelength of the light can be controlled to both high precision and high accuracy, giving the distance measurement a stable and known scale factor. A famous early scientific application of a light interferometer was the Michelson-Morley experiment [1] in 1887, disproving the existence of the *luminiferous ether*, through which electromagnetic waves were theorized to propagate. Recently, the first detections of gravitational waves were made using light interferometers designed, built and optimized over decades by the LIGO and VIRGO collaborations [2,3].

The advent of quantum mechanics beginning in the 1920s revealed that matter too has wave-like properties. Quantum particles are described by a wave equation (the Schrödinger equation) and exhibit familiar wave phenomena such as diffraction and interference. A matter wave interferometer, in analogy with a light interferometer, can thus be realized by reversing the roles of light and matter: rather than using matter (mirrors and beamsplitters) to manipulate a light wave, light waves (laser pulses) are used to manipulate matter waves. The resulting matter wave interference can then be used as a measurement device.

This laser manipulation of matter waves for interferometric metrology has been called *light pulse atom interferometry*, and has its origins in the early 1990s [4]. Since then, the technique has been used for a wide variety of purposes. Examples include measuring fundamental constants [5–8], tests of the equivalence principle [9, 10], gravimeters [11–13], gradiometers [14–16], and inertial sensors [17–19]. The strengths of atom interferometers are similar to those of light interferometers: fundamental stability, and large phase accumulation.

The parameters determining the phase of such devices can be well-controlled, making atom interferometry amenable to absolute measurements. Absolute stability is key in measuring the fine structure constant α [5, 6], the gravitational constant G [7, 8], and inertial metrology (accelerations, rotations, gravity gradients). Additionally, a huge amount of phase can be accumulated so that for parameters determining the phase, even small changes have a large lever arm to produce a sizable phase shift. This gives finely-spaced "rulings" to the measurement.

The sensitivity of atom interferometry has been pushed forward by increasing the momentum separation between the interferometer arms [20–24], and extending the interrogation time by building large atomic fountains [12, 25, 26]. In this thesis, we aim to further extend the scope of atom interferometer technologies by performing the laser pulses inside an optical cavity. We also investigate several types of interactions using the atoms to probe a small, in-vacuum source mass.

Motivation for a cavity

A cavity provides improvements to a free space laser beam by both (i) resonant enhancement of the optical intensity and (ii) smooth wavefronts via mode-filtering.

The higher intensity is useful in performing matter wave manipulations. The smooth wavefronts provided by the mode filtering allow for uniform addressing of the atoms by the laser beam. The intra-cavity phase fronts can have substantially reduced small-scale irregularities (wavefront distortions, or speckle) compared to the free-space input beam.

The utility of the cavity for interferometry is demonstrated and more thoroughly discussed in Chapters 4, 7 and 8.

Interactions with a source mass

We investigate three types of interactions between an in-vacuum source mass and an atom interferometer:

(i) Gravity (Chapter 5)

(ii) "Screened" interactions proposed to explain dark energy (Chapter 5)

(iii) A force mediated by blackbody radiation (Chapter 6)

1.2 Outline of thesis

The rest of this thesis is organized as follows. Chapter 2 lays out a theoretical framework for atom interferometry, and briefly describes optical resonators. The experimental apparatus is described in Chapter 3. Chapter 4 discusses our development of the first atom interferometer in an optical cavity. Using this interferometer, we measured the gravitational attraction between atoms and a small source mass to place strong constraints on dark energy candidates, outlined in Chapter 5. Chapter 6 presents the first measurement of a force mediated by blackbody radiation. Next, interferometer geometries that capitalize on advantages of the cavity are described. A new technique using spin-dependent kicks with adiabatic passage is presented in Chapter 7. A trapped interferometer is presented in Chapter 8 that allows for interrogation times of over 10 seconds, the longest-duration spatially separated atom interferometer to date. Finally, future prospects for cavity interferometers are discussed in Chapter 9.

Chapter 2

Atom interferometry: background and theory

A light pulse atom interferometer uses laser pulses to coherently manipulate matter waves. The wave function of an atom is split, re-directed and recombined by these laser pulses to produce interference. The phase of this interference pattern constitutes the measurement being performed. In this chapter, the formalism underlying these matter wave manipulations is developed, and the phase of an atom interferometer is derived. This presentation of atom interferometry follows closely the derivations of Ref. [27]. Finally, the basics of optical resonators are presented.

2.1 Overview of an atom interferometer

A toy model interferometer could split a wave into two components (arms), separately evolve those two arms, and then recombine the arms. For a quantum particle like an atom, we identify these two components as states in a two-dimensional Hilbert space, $|1\rangle$ and $|2\rangle$. The state of the particle is then a two-component spinor $|\psi\rangle = \begin{pmatrix} a \\ b \end{pmatrix} = a|1\rangle + b|2\rangle$. A beamsplitter is a rotation:

$$\hat{S} = \frac{1}{\sqrt{2}} \begin{pmatrix} 1 & i \\ i & 1 \end{pmatrix} \tag{2.1}$$

which maps either basis ket into an equal superposition of $|1\rangle$ and $|2\rangle$. This is a specific case of the general rotation operator in this 2-component space, given by

$$\hat{R}(\theta, \hat{\boldsymbol{n}}) = e^{i\boldsymbol{\sigma}\cdot\hat{\boldsymbol{n}}\frac{\theta}{2}} = \begin{pmatrix} \cos\frac{\theta}{2} - in_z \sin\frac{\theta}{2} & (-in_x - n_y)\sin\frac{\theta}{2} \\ (-in_x + n_y)\sin\frac{\theta}{2} & \cos\frac{\theta}{2} + in_z \sin\frac{\theta}{2} \end{pmatrix} \tag{2.2}$$

where $\boldsymbol{\sigma}$ is the Pauli matrix vector, and $\hat{\boldsymbol{n}}$ is the unit vector around which the rotation takes place. This beamsplitter $\hat{S}$ rotates the spinor about the $-\hat{x}$-axis by angle $\theta = \frac{\pi}{2}$, that is, $\hat{S} = \hat{R}(\frac{\pi}{2}, -\hat{x})$. A beamsplitter is thus also commonly referred to as a $\frac{\pi}{2}$ pulse.

Evolving the state during the second step of the interferometer, each spinor component acquires a phase ϕ_i. This is represented by an evolution operator:

$$\hat{U}(\phi_1, \phi_2) = \begin{pmatrix} e^{i\phi_1} & 0 \\ 0 & e^{i\phi_2} \end{pmatrix} \tag{2.3}$$

To recombine the two components, the state is rotated back by applying $\hat{S}^\dagger$ (we could equally validly apply the rotation $\hat{S}$ again instead of un-rotating). The output $|\Psi_\mathrm{F}\rangle$ of this interferometer acting on an input state $|\Psi_\mathrm{I}\rangle$ is then

$$|\Psi_\mathrm{F}\rangle = \hat{S}^\dagger \hat{U} \hat{S} |\Psi_\mathrm{I}\rangle \tag{2.4}$$

For initial state $|\Psi_\mathrm{I}\rangle = \begin{pmatrix} 1 \\ 0 \end{pmatrix} = |1\rangle$, the output state $|\Psi_\mathrm{F}\rangle$ is:

$$|\Psi_\mathrm{F}\rangle = \frac{1}{2} \begin{pmatrix} e^{i\phi_2} + e^{i\phi_1} \\ i\left(e^{i\phi_2} - e^{i\phi_1}\right) \end{pmatrix} \tag{2.5}$$

The probabilities to end up in either state, given by the square of the amplitudes, is

$$\begin{pmatrix} P_1 \\ P_2 \end{pmatrix} = \begin{pmatrix} \cos^2\left(\frac{\phi_2 - \phi_1}{2}\right) \\ \sin^2\left(\frac{\phi_2 - \phi_1}{2}\right) \end{pmatrix} \tag{2.6}$$

So the output of this interferometer oscillates between $|1\rangle$ and $|2\rangle$, with phase set by the phase difference along the interferometer arms $\phi_2 - \phi_1$. This procedure has succeeded in mapping a typically unobserved phase difference into a measurable population difference! We will find this mapping to be metrologically valuable, as many effects induce phase shifts, which can then be made measurable as demonstrated above.

2.2 Free evolution and the path integral formulation

How does the matter wave accumulate phase between the laser pulses? That is, how are the phases ϕ_1 and ϕ_2 in eq. 2.3 determined? This section addresses that question. We start by presenting quantum mechanics in the path integral formalism. The Schrödinger equation describing the time evolution of a quantum particle is

$$i\hbar \frac{\partial}{\partial t} |\Psi(t)\rangle = \hat{H} |\Psi(t)\rangle$$

where $\hat{H}$ is the Hamiltonian. We can declare a solution that satisfies the Schrödinger equation:

$$|\Psi(t)\rangle = e^{-i\hat{H}(t-t_0)/\hbar}|\Psi(t_0)\rangle \equiv \hat{U}(t-t_0)|\Psi(t_0)\rangle$$

where we have defined the time-evolution operator $\hat{U}(\tau) = e^{-i\hat{H}\tau/\hbar}$.

Consider a quantum particle in 1 dimension, initially located at position x_I at time t_I. That is, $|\Psi(t_I)\rangle = |x_I\rangle$. What is the amplitude for this particle to be found at position x_F at a later time t_F? Without gaining much insight, we can write the answer down as

$$\langle x_F, t_F|\Psi(t_F)\rangle = \langle x_F, t_F|U(t_F - t_I)|\Psi(t_I)\rangle \tag{2.7}$$

Now consider a path of $N+1$ points evenly spaced in time defining a path Γ from x_I to x_F: $\{x_I, x_1, x_2, \ldots, x_{N-1}, x_F\}$, where we will also identify $x_0 \equiv x_I$ and $x_N \equiv x_F$. We can write the amplitude to follow this path by stringing together N copies of eq. 2.7:

$$\langle x_F|U(\delta t)|x_{N-1}\rangle \, \langle x_{N-1}|U(\delta t)|x_{N-2}\rangle \cdots \langle x_1|U(\delta t)|x_I\rangle \tag{2.8}$$

The idea of the path integral formulation is that the amplitude we're looking to calculate in eq. 2.7 is obtained by integrating over all possible paths. Eq. 2.8 gives us a framework perform this integration: we integrate over all the x_j between x_I and x_F:

$$\langle x_F, t_F|e^{-i\hat{H}(t_F-t_I)/\hbar}|x_I, t_I\rangle = \prod_{j=1}^{N} \int dx_j \, \langle x_F|U(\delta t)|x_{N-1}\rangle \, \langle x_{N-1}|U(\delta t)|x_{N-2}\rangle \cdots \langle x_1|U(\delta t)|x_I\rangle \tag{2.9}$$

The quantity $\langle x_F, t_F|e^{-i\hat{H}(t_F-t_I)/\hbar}|x_I, t_I\rangle$ is known as the propagator between $\{x_I, t_I\}$ and $\{x_F, t_F\}$ and will be important to us for evaluating quantities of interest. With this in mind, let's look at an individual component of this integral, $\langle x_{j+1}|U(\delta t)|x_j\rangle$. We'll now specify the Hamiltonian as that of a massive particle in a potential V:

$$\hat{H} = \frac{\hat{\boldsymbol{p}}^2}{2m} + V(\hat{x})$$

Making use of the identity

$$\mathbb{1} = \int \frac{dp}{2\pi} |p\rangle\langle p|, \tag{2.10}$$

the momentum and position operators in the Hamilton can be manipulated to act on their respective eigenstates:

$$\begin{aligned} \langle x_{j+1}|e^{-i\hat{H}\delta t/\hbar}|x_j\rangle &= \int \frac{dp}{2\pi} \, \langle x_{j+1}|p\rangle \, \langle p|e^{-i\left(\frac{\hat{p}^2}{2m}+V(\hat{x})\right)\delta t/\hbar}|x_j\rangle \\ &= \int \frac{dp}{2\pi} \left(e^{ipx_{j+1}}\right) \left(e^{-i\left(px_j+\left(\frac{p^2}{2m}+V(x_j)\right)\delta t/\hbar\right)}\right) \end{aligned}$$

$$= e^{-iV(x_j)\delta t/\hbar} \int \frac{dp}{2\pi} e^{\left(-\frac{i\delta t}{2m\hbar}p^2 + i(x_{j+1}-x_j)p\right)} \tag{2.11}$$

Terms of order δt^2 have been neglected (since we will take $N \to \infty$ and thus $\delta t \to 0$) by taking taking $e^{(\ldots)\delta t} = 1+(\ldots)\delta t+\mathcal{O}(\delta t^2)$, calculating, and then later re-taking $1+(\cdots)\delta t+\mathcal{O}(\delta t^2) \to e^{(\cdots)\delta t}$. We have also used the relation $\langle x|p\rangle = e^{ipx}$. Evaluating the gaussian integral [1] in eq. 2.11 gives us

$$\langle x_{j+1}|e^{-i\hat{H}\delta t/\hbar}|x_j\rangle = \left(\frac{-im\hbar}{2\pi\delta t}\right)^{1/2} e^{i\frac{\delta t}{\hbar}\left[\frac{m}{2}\left(\frac{x_{j+1}-x_j}{\delta t}\right)^2 - V(x_j)\right]} \tag{2.12}$$

Plugging this into our expression for the propagator (eq. 2.9) gives

$$\langle x_F, t_F|e^{-i\hat{H}(t_F-t_I)/\hbar}|x_I, t_I\rangle = \left(\frac{-im\hbar}{2\pi\delta t}\right)^{N/2} \prod_{j=1}^{N-1} \int dx_j e^{i\frac{\delta t}{\hbar}\sum_{l=0}^{N-1}\left[\frac{m}{2}\left(\frac{x_{l+1}-x_l}{\delta t}\right)^2 - V(x_l)\right]} \tag{2.13}$$

Now we'll take some liberties to start massaging this into a more manageable form. First, we identify the quantity $\left(\frac{x_{l+1}-x_l}{\delta t}\right)$ as a discrete time derivative. Since we will be taking $\delta t \to 0$, we will make the following substitutions from discrete to continuous expressions:

$$\delta t \sum_{l=0}^{N-1} V(x_l) \to \int_{t_I}^{t_F} dt\ V[q] \tag{2.14a}$$

$$\delta t \sum_{l=0}^{N-1} \frac{m}{2}\left(\frac{x_{l+1}-x_l}{\delta t}\right)^2 \to \int_{t_I}^{t_F} \frac{m}{2}\dot{q}^2 \tag{2.14b}$$

With these substitutions, we can re-write our last expression for the propagator eq. 2.13 as

$$\langle x_F, t_F|e^{-i\hat{H}(t_F-t_I)/\hbar}|x_I, t_I\rangle = \lim_{N\to\infty}\left(\frac{-im\hbar}{2\pi\delta t}\right)^{N/2}\left(\prod_{j=1}^{N-1}\int dx_j e^{\frac{i}{\hbar}\int_{t_I}^{t_F} dt\left(\frac{m}{2}\dot{q}^2 - V[q]\right)}\right) \tag{2.15a}$$

$$\equiv \int \mathcal{D}x\, e^{\frac{i}{\hbar}\int_{t_I}^{t_F} dt L[q,\dot{q}]} \tag{2.15b}$$

$$= \int \mathcal{D}x\, e^{iS[q]/\hbar} \tag{2.15c}$$

In going from eq. 2.15a to eq. 2.15b, we have defined the integral over all paths as $\int \mathcal{D}x$ to hide the ugly $\lim_{N\to\infty}$ and $\prod_j \int dx_j$. We have also identified the phase term in the

---

[1] The gaussian integral $\int_{-\infty}^{\infty} \exp\left(\frac{1}{2}iax^2 + iJx\right)dx = \sqrt{\left(\frac{2\pi i}{a}\right)}\exp\left(-\frac{iJ^2}{2a}\right)$; see eq. 2.20 for generalization

integral of the exponential as the Lagrangian $L[q, \dot{q}]$. Finally, moving from eq. 2.15b to eq. 2.15c, we identify the integral of the Lagrangian as the action $S[q]$.

To make use of this for atom interferometry, we'll now make a some simplifications. First, note that paths that minimize the action S will contribute most to the integral. Paths with larger action cause the phase in the integral to oscillate rapidly, since $S \gg \hbar$, averaging their contribution to zero. Motivated by this observation, we can Taylor expand around the classical path. The classical path taken by a particle minimizes the action, and is found by solving the Euler-Lagrange equation:

$$\frac{d}{dt}\left(\frac{\partial L}{\partial \dot{q}}\right) - \frac{\partial L}{\partial q} = 0$$

We can now write a generic path $q(t)$ as an expansion about the classical path $q_c(t)$:

$$q(t) = q_c(t) + \delta q(t)$$

Recalling that we moved to the continuous variable q from the discrete $\{x_j\}$, this corresponds to making the transformations

$$x_j \rightarrow x_c(t_j) + \varepsilon_j \tag{2.16a}$$

$$dx_j \rightarrow \varepsilon_j \tag{2.16b}$$

This takes the discrete versions of our continous variables to

$$q_c(t) = \boldsymbol{q}_c = \{x_I, x_c(t_I + \delta t), \ldots, x_c(t_I + (N-1)\delta t), x_F\} \tag{2.17a}$$

$$\delta q(t) = \boldsymbol{\varepsilon} = \{0, \varepsilon_1, \ldots, \varepsilon_{N-1}, 0\} \tag{2.17b}$$

Substituting eqs. 2.16 into the expanded expression for the propagator eq. 2.15a, we get

$$\lim_{N\to\infty}\left(\frac{-im\hbar}{2\pi\delta t}\right)^{N/2}\left(\prod_{j=1}^{N-1}\int d\varepsilon_j e^{iS[q_c(t)+\delta q(t)]/\hbar}\right) \tag{2.18}$$

From here, we can expand the action in a multivariate power series around the classical path:

$$\begin{aligned} S[\boldsymbol{q}_c + \boldsymbol{\varepsilon}] &= \sum_{n=0}^{\infty}\frac{1}{n!}\left(\boldsymbol{\varepsilon}\cdot\boldsymbol{\nabla}\right)^n S[\boldsymbol{q}]\big|_{\boldsymbol{q}=\boldsymbol{q}_c} \\ &= S[\boldsymbol{q}_c] + \cancel{\left(\sum_{j=1}^{N-1}\frac{\partial S}{\partial x_j}\varepsilon_j\right)}\big|_{\boldsymbol{q}=\boldsymbol{q}_c} + \frac{1}{2}\left(\sum_{j=1}^{N-1}\sum_{k=1}^{N-1}\frac{\partial^2 S}{\partial x_j \partial x_k}\varepsilon_j\varepsilon_k\right)\big|_{\boldsymbol{q}=\boldsymbol{q}_c} + \mathcal{O}\left(\varepsilon^3\right) \end{aligned}$$

The first derivative term vanishes because the classical path, by definition, minimizes the action. Plugging this into eq. 2.18, our expression for the propagator now becomes

$$\lim_{N\to\infty}\left(\frac{-im\hbar}{2\pi\delta t}\right)^{N/2} e^{iS[\boldsymbol{q}_c]/\hbar}\left(\prod_{j=1}^{N-1}\int d\varepsilon_j \exp\left[\frac{i}{2\hbar}\sum_{j=1}^{N-1}\sum_{k=1}^{N-1}\frac{\partial^2 S}{\partial x_j \partial x_k}\varepsilon_j\varepsilon_k + \cancel{\mathcal{O}\left(\varepsilon^3\right)}\right]\right) \tag{2.19}$$

For a potential that is at most quadratic in x, the $\mathcal{O}\left(\varepsilon^3\right)$ terms are identically zero because third-order (and higher) derivatives of the action vanish. For higher order potentials, we assume the $\mathcal{O}\left(\varepsilon^3\right)$ terms are small.

To evaluate this integral, we can use a general expression for n-dimensional gaussian integrals (integrals of this type are common in quantum field theory, see Ref. [28]). For a real, symmetric $n \times n$ matrix A, and $n \times 1$ column vector J,

$$\int d^n x \exp(-\frac{i}{2} x \cdot A \cdot x + iJ \cdot x) = \sqrt{\frac{(2\pi i)^n}{\det A}} \exp\left(-\frac{i}{2} J \cdot A^{-1} \cdot J\right) \tag{2.20}$$

In our integral eq. 2.19, we identify $J = 0$, and $A = \frac{\partial^2 S}{\partial x_j \partial x_k}$ (which is real and symmetric). Using eq. 2.20 to evaluate eq. 2.19, we get our final expression for the propagator:

$$\langle x_F, t_F | e^{-i\hat{H}(t_F - t_I)/\hbar} | x_I, t_I \rangle = \lim_{N\to\infty} \frac{1}{\sqrt{2\pi i\hbar}} \left(\frac{m}{\delta t}\right)^{N/2} \frac{1}{\sqrt{\det A}} e^{iS[\boldsymbol{q}_c]/\hbar} \tag{2.21}$$

$$= \mathcal{Z} e^{iS[\boldsymbol{q}_c]/\hbar} \tag{2.22}$$

where we've wrapped up all of the potential weirdness from taking $\lim_{N\to\infty}$ into a normalization constant $\mathcal{Z}$, that for now, we're just hoping is sufficiently well-defined. Luckily, it is (see Refs. [27, 29] for more detail).

We've found that evaluating the propagator, up to a normalization constant, amounts to a phase given by the action along the classical trajectory divided by $\hbar$. We will now investigate a very simple matterwave interferometer. In doing so, we will use the beamsplitter from eq. 2.1.

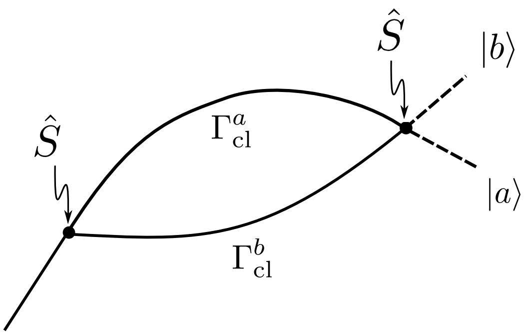

Figure 2.1: Simple Interferometer

Consider the trajectory shown in Fig. 2.1. A beamsplitter $\hat{S}$ is applied to split a matter wave along two classical trajectories Γ^a_{cl} and Γ^b_{cl}. When the trajectories overlap again, another beamsplitter $\hat{S}^\dagger$ recombines them. If we denote the state following paths Γ^a_{cl} and Γ^b_{cl} respectively as $|a\rangle$ and $|b\rangle$, we can write the state just after the first beamsplitter as

$$\begin{aligned}|\Psi(x_I+\varepsilon_x, t_I+\varepsilon_t)\rangle &= \hat{S}|a\rangle \\ &= \frac{1}{\sqrt{2}}\begin{pmatrix}1\\ i\end{pmatrix} = \frac{1}{\sqrt{2}}\left(|a\rangle + i|b\rangle\right)\end{aligned}$$

where ε_x and ε_t are tiny quantities just to indicate that this is *after* the beamsplitter.

From this chapter's calculation of the propagator, we know in the free evolution between beamsplitters, each arm acquires a phase given by the action. When the arms again overlap at $\{x_F-\varepsilon_x, t_F-\varepsilon_t\}$ the wavefunction is thus

$$\begin{aligned}|\Psi(x_F-\varepsilon_x, t_F-\varepsilon_t)\rangle &= e^{i\hat{H}(t_F-t_I)/\hbar}|\Psi(x_I,t_I)\rangle \\ &= \frac{1}{\sqrt{2}}\begin{pmatrix}e^{iS_a/\hbar}\\ ie^{iS_b/\hbar}\end{pmatrix}\end{aligned}$$

where $S_i = S[\Gamma^i_{\mathrm{cl}}]$ for $i=a,b$ (and we've taken the symbolic $\varepsilon_t \to 0$ in the exponential). The off-diagonal elements of the evolution operator $U(t_F,t_I) = e^{i\hat{H}(t_F-t_I)/\hbar}$ are zero by definition of the classical paths Γ^i_{cl} under the Hamiltonian; $|a\rangle$ and $|b\rangle$ are orthogonal eigenstates of $\hat{H}$.

Applying a final beamsplitter now reveals the interference. After the beamsplitter $\hat{S}^\dagger$, the state $|\Psi_{\mathrm{F}}\rangle$ is:

$$|\Psi(x_F,t_F)\rangle = \hat{S}^\dagger|\Psi(x_F-\varepsilon_x, t_F-\varepsilon_t)\rangle = \frac{1}{2}\begin{pmatrix}e^{iS_b/\hbar}+e^{iS_a/\hbar}\\ i\left(e^{iS_b/\hbar}-e^{iS_a/\hbar}\right)\end{pmatrix}$$

The probabilities to end up in either state are

$$\begin{aligned}\begin{pmatrix}P_a\\ P_b\end{pmatrix} &= \begin{pmatrix}\cos^2\left(\frac{S_b-S_a}{2\hbar}\right)\\ \sin^2\left(\frac{S_b-S_a}{2\hbar}\right)\end{pmatrix} \\ &= \begin{pmatrix}\cos^2\left(\frac{\phi_b-\phi_a}{2}\right)\\ \sin^2\left(\frac{\phi_b-\phi_a}{2}\right)\end{pmatrix}\end{aligned}$$

where we have defined $\phi_i \equiv S_i/\hbar$ for $i=a,b$. This result is identical to our results eq. 2.5 and eq. 2.6 from Sec. 2.1! We've simply identified how to calculate the free evolution phases.

More information and derivations underpinning matter wave interferometry can be found in Refs. [27, 29–31]. With this framework for interference developed, the next section will look into the atom-laser interactions used to actually perform the mirror and beamsplitter operations.

The key takeaway from this section is that the free evolution phase is calculated by integrating the Lagrangian along the classical path.

2.3 Atom-laser interactions

Mirrors and beamsplitters of a matter wave interferometer are performed with laser pulses in the aptly named "light pulse atom interferometer". Photon momenta are coherently exchanged with a matter wave to split, re-direct and recombine the wave along desired paths. Atom optics other than light pulses have also been demonstrated, such as material gratings [32] and magnetic field gradients [33], but are far less common. In this section, we quantitatively outline the atom-laser interactions behind the atom optics in this thesis, deriving the effect of these atom optics on the interferometer phase.

A Raman transition is a two-photon process that changes the hyperfine state of the atom and exchanges momentum with the light field. Bragg transitions, or Bragg diffraction, are also used extensively in atom interferometry. In these transitions, the matter wave is diffracted into various momentum states without changing the internal state. Bragg diffraction is briefly discussed in Section 2.3.4. However, we predominantly discuss Raman transitions, as they are used nearly exclusively in this experiment.

2.3.1 Raman transitions: the system

Consider the three-level system in Fig. 2.2.

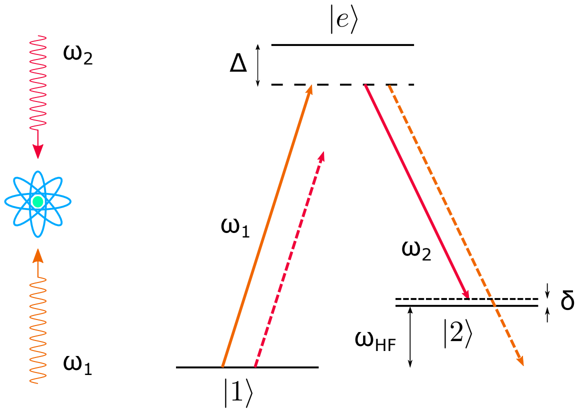

Figure 2.2: Three-level Raman system

The system consists of two ground states, $|1\rangle$ and $|2\rangle$, and an excited state $|e\rangle$. The ground states are separated in energy by $\hbar\omega_{\mathrm{HF}}$, and $|2\rangle$ is separated from the excited state by $\hbar\omega_{2\mathrm{e}}$. For cesium, the atom used in our experiment, $\omega_{\mathrm{HF}} = 2\pi \times 9.192631770$ GHz is a microwave frequency defining the second (for now), while $\omega_{2\mathrm{e}} \approx 2\pi \times 351.7$ THz is an optical frequency. Consider an atom with this level structure placed in the light field shown in Fig. 2.2: an upward propagating beam with frequency ω_1, and a counterpropagating beam with frequency ω_2. The Hamiltonian is

$$\hat{H} = \frac{\hat{\boldsymbol{p}}^2}{2m} + \hbar\omega_1^A|1\rangle\langle 1| + \hbar\omega_2^A|2\rangle\langle 2| + \hbar\omega_e^A|e\rangle\langle e| + \hat{V} \tag{2.23}$$

where $\hat{V}$ is the light field perturbation, and the superscript A is used for clarity to denote a property of the atom. Explicitly, the perturbation is

$$\hat{V} = -\hat{\boldsymbol{d}} \cdot \boldsymbol{E}$$

where $\hat{\boldsymbol{d}} = e\hat{\boldsymbol{r}}$ is the dipole operator. The electric field can be written as

$$\boldsymbol{E} = \boldsymbol{E}_1 \cos\left(k_1 z - (\omega_1 t - \varphi_1)\right) + \boldsymbol{E}_2 \cos\left(k_2 z + (\omega_2 t - \varphi_2)\right) \tag{2.24}$$

with wavevectors $|\boldsymbol{k}_i| = k_i = \omega_i/c$, and $\boldsymbol{k}_2 \approx -\boldsymbol{k}_1$. In the next section, we solve the Schrödinger equation for this Hamiltonian.

2.3.2 Solving the equation

Momentum transfer

In this section, we'll show that when an atom interacts with the light field, it gains or loses one photon's momentum. With the atom's momentum and internal states as the relevant degrees freedom, we follow Ref. [34] and propose as an ansatz for the solution:

$$|\psi\rangle = \int dp \sum_\alpha a_{\alpha,p}(t) e^{i\left(\omega_\alpha^A + \frac{p^2}{2m}\right)t} |\alpha, p\rangle \tag{2.25}$$

where $|\alpha, p\rangle \equiv |\alpha\rangle \otimes |p\rangle$ corresponds to an atom with internal state $\alpha \in \{1, 2, e\}$ and in momentum eigenstate $\psi_p(x) \sim e^{ipx/\hbar}$. Since $\hat{V}$ contains trigonometric terms, we will be interested in the operator $e^{\pm ik\hat{z}}$. More explicitly,

$$\langle \alpha, p|\hat{V}|\alpha', p'\rangle \sim \left(\langle\alpha| \otimes \langle p|\right) \hat{\boldsymbol{r}} \cdot \boldsymbol{E} \left(|\alpha'\rangle \otimes |p'\rangle\right) \ni \langle p|e^{\pm ik\hat{z}}|p'\rangle \tag{2.26}$$

Using the identities[2] $\mathbb{1} = \int dp\, |p\rangle\langle p| = \int dz\, |z\rangle\langle z|$, we can rewrite

$$e^{\pm ikz} = \int dp\, e^{\pm ikz} |p\rangle\langle p| \tag{2.27}$$

and

---

[2] These identities come from the orthonormality condition $\langle p|p'\rangle = \delta(p - p')$. This is, unfortunately, different than a convention used in quantum field theory, $\langle p|p'\rangle = 2\pi\delta(p - p')$, which explains eq. 2.10.

$$|p\rangle = \int dz\, |z\rangle\langle z|p\rangle = \frac{1}{\sqrt{2\pi\hbar}} \int dz\, e^{ipz}|z\rangle. \tag{2.28}$$

Plugging eqs. 2.27 and 2.28 into eq. 2.26, we can calculate

$$\langle p|e^{\pm ik\hat{z}}|p'\rangle = \langle p| \left(\int dq\, |q \pm \hbar k\rangle\langle q| \right) |p'\rangle = \delta_{p,p'\pm\hbar k} \tag{2.29}$$

So only momentum states separated by $\pm\hbar k$ are connected to each other by each $e^{\pm ikz}$ term. This shows that by interacting with a light field, an atom can gain or lose a photon's momentum, corresponding to absorption or stimulated emission. With this momentum ladder established, we can simplify our ansatz eq. 2.25 to three components:

$$|\Psi_p\rangle = \begin{pmatrix} a_{1,p} \\ a_{2,p+\hbar(k_2-k_1)} \\ a_{e,p+\hbar k_1} \end{pmatrix} \tag{2.30}$$

The three basis states then correspond to the atom's energy levels, with momenta connected by the light fields shown by the solid lines in Fig. 2.2.

Hamiltonian transformation

In this new basis, we can write the Hamiltonian as

$$\hat{H} = \begin{pmatrix} \frac{\boldsymbol{p}_1^2}{2m} + \hbar\omega_1^A & V_{12} & V_{1e} \\ V_{12}^* & \frac{\boldsymbol{p}_2^2}{2m} + \hbar\omega_2^A & V_{2e} \\ V_{1e}^* & V_{2e}^* & \frac{\boldsymbol{p}_e^2}{2m} + \hbar\omega_e^A \end{pmatrix} \tag{2.31}$$

where

$$V_{\alpha\beta} \equiv \langle\alpha|\hat{V}|\beta\rangle\,, \tag{2.32}$$

and $\boldsymbol{p}_2 = \boldsymbol{p}_1 + \hbar\left(\boldsymbol{k}_1 - \boldsymbol{k}_2\right)$, $\boldsymbol{p}_e = \boldsymbol{p}_1 + \hbar\boldsymbol{k}_1$ obey the momentum relations from the previous section. Furthermore, states $|1\rangle$ and $|2\rangle$ in the cesium hyperfine ground states have equal parity, so they are not connected by the dipole operator $\hat{d}$. Thus, $V_{12} = 0$.

We can simplify this Hamiltonian with a transformation $\hat{O}$ such that $\hat{O}^\dagger\hat{O} = \mathbb{1}$. If $|\Psi\rangle \to |\Psi'\rangle = \hat{O}|\Psi\rangle$, the Schrödinger equation then becomes

$$\begin{aligned} i\hbar\frac{\partial}{\partial t}\left(\hat{O}|\Psi\rangle\right) &= \hat{H}\left(\hat{O}|\Psi\rangle\right) \\ i\hbar\frac{\partial}{\partial t}|\Psi\rangle &= \underbrace{\left(\hat{O}\hat{H}\hat{O}^\dagger - i\hbar\hat{O}\frac{\partial}{\partial t}\hat{O}^\dagger\right)}_{\hat{H}'}|\Psi\rangle \end{aligned}$$

So making such a basis transformation simply changes the Hamiltonian to

$$\hat{H}' = \left(\hat{O}\hat{H}\hat{O}^\dagger - i\hbar\hat{O}\frac{\partial}{\partial t}\hat{O}^\dagger\right) \tag{2.33}$$

We can presciently choose a transformation:

$$\hat{T}_1 = \begin{pmatrix} e^{i\left[\frac{\boldsymbol{p}_1^2}{2m}+\hbar\omega_1^A\right]t} & 0 & 0 \\ 0 & e^{i\left[\frac{\boldsymbol{p}_2^2}{2m}+\hbar\omega_2^A\right]t} & 0 \\ 0 & 0 & e^{i\left[\frac{\boldsymbol{p}_e^2}{2m}+\hbar\omega_e^A\right]t} \end{pmatrix} \tag{2.34}$$

that factors out the fast oscillations in the Schrödinger equation from the atomic and kinetic energy. Specifically, the eigenvector amplitudes are transformed according to

$$\begin{pmatrix} b_1 \\ b_2 \\ b_e \end{pmatrix} = \hat{T}_1 \begin{pmatrix} a_{1,p} \\ a_{2,p+\hbar(k_2-k_1)} \\ a_{e,p+\hbar k_1} \end{pmatrix} = \begin{pmatrix} a_{1,p}e^{i\left[\frac{\boldsymbol{p}_1^2}{2m}+\hbar\omega_1^A\right]t} \\ a_{2,p+\hbar(k_2-k_1)}e^{i\left[\frac{\boldsymbol{p}_2^2}{2m}+\hbar\omega_2^A\right]t} \\ a_{e,p+\hbar k_1}e^{i\left[\frac{\boldsymbol{p}_e^2}{2m}+\hbar\omega_e^A\right]t} \end{pmatrix} \tag{2.35}$$

Plugging eq. 2.34 into eq. 2.33 gives the Hamiltonian in this new basis:

$$\hat{H}' = \begin{pmatrix} 0 & 0 & \tilde{V}_{1e} \\ 0 & 0 & \tilde{V}_{2e} \\ \tilde{V}_{1e}^* & \tilde{V}_{2e}^* & 0 \end{pmatrix} \tag{2.36}$$

where $\tilde{V}_{\alpha e} = V_{\alpha e}\exp\left(i\left[\left(\frac{\boldsymbol{p}_\alpha^2}{2m}+\hbar\omega_\alpha^A\right)-\left(\frac{\boldsymbol{p}_e^2}{2m}+\hbar\omega_e^A\right)\right]t\right)$. Working this out a bit further,

$$V_{\alpha e} = \langle\alpha|\hat{V}|e\rangle = \langle\alpha| - \hat{\boldsymbol{d}}\cdot\sum_{\nu=1,2}\boldsymbol{E}_\nu\left(\frac{e^{i(k_\nu z-\omega_\nu t+\varphi_\nu)}+\cancel{c.c.}}{2}\right)|e\rangle$$

where ν sums over the laser beams. By setting the complex conjugate term to zero, we explicitly consider only the solid lines in Fig 2.2 (including these terms simply shifts the energy levels $|1\rangle$ and $|2\rangle$, the so-called ac Stark shift, or light shift). See Ref. [35] for a more in-depth calculation. We now introduce the following quantities:

$$\Omega_{n\nu} \equiv -\frac{\langle n|\hat{\boldsymbol{d}}\cdot\boldsymbol{E}_\nu|e\rangle}{\hbar} \tag{2.37}$$

$$\Delta \equiv \left(\omega_e^A - \omega_1^A\right) - \omega_1 \tag{2.38}$$

$$\delta \equiv \left(\omega_e^A - \omega_2^A\right) - (\omega_2 + \Delta) \tag{2.39}$$

Δ and δ are the same as shown in Fig. 2.2, and are the bare single-photon detuning and bare two-photon detuning, respectively. In eq. 2.37, we have defined the Rabi frequency $\Omega_{n\nu}$ for the coupling of level $|n\rangle$ to the excited state $|e\rangle$ by laser beam ν. For cesium, the levels $|1\rangle$ and $|2\rangle$ correspond to the $|F=3\rangle$ and $|F=4\rangle$ hyperfine levels of the $6^2\mathrm{S}_{1/2}$ ground state. Their dipole matrix elements, and therefore single photon Rabi frequencies ($\Omega_{1\nu}$ and $\Omega_{2\nu}$) differ only by factors including Wigner 3-j symbols (Clebsch-Gordan coefficients) and 6-j symbols [36].

Combining these definitions, we can apply the "rotating wave approximation" (RWA). In the RWA, fast oscillating terms in the differential equations for $\dot{b}_\alpha$ are ignored, as they quickly average to zero. For example, consider a term like

$$\tilde{V} = \alpha\left(e^{i\left(\beta+(\omega_1+\omega_{e1}^A)t\right)} + e^{i\left(\beta+(\omega_1-\omega_{e1}^A)t\right)}\right) \tag{2.40}$$

where $\omega_{e1}^A \equiv \omega_e^A - \omega_1^A = \omega_1 + \Delta$. For the case of our cesium transitions, $\frac{\omega_{e1}^A}{\Delta} \sim 10^4$. Thus the first term in eq. 2.40 (the "counter-rotating" term) accumulates phase at a much faster rate than the second term (the "co-rotating" term). We can ignore the counter-rotating term, since its effect in the differential equations for the b_i will only be fast oscillations of $\dot{b}_i$ about the slow dynamics of the co-rotating term, and thus average to zero.

After applying the RWA to toss out the counter-rotating terms, we get

$$\begin{aligned}\tilde{V}_{1e} &= \frac{\hbar\Omega_{11}}{2} e^{-i\left(\left[\Delta+\underbrace{k_1 v}_{\text{Doppler}}+\overbrace{\frac{\hbar k_1^2}{2m}}^{\substack{\text{recoil}\\ \text{frequency}}}\right]t+\varphi_1\right)} \\ &= \frac{\hbar\Omega_{11}}{2} e^{-i\left(\tilde{\Delta}\,t+\varphi_1\right)}\end{aligned}$$

where $\tilde{\Delta} \equiv \Delta + k_1 v + \frac{\hbar k_1^2}{2m}$ combines the bare single photon detuning, the Doppler shift and the recoil frequency [36]. In this step, we've also squished the z-dependence into the laser phase φ, that is, $k_\nu z + \varphi_\nu \rightarrow \varphi_\nu$. Similarly, the analogous two-photon detuning

$$\tilde{\delta} \equiv \delta + \underbrace{(\boldsymbol{k}_1-\boldsymbol{k}_2)\cdot\boldsymbol{v}}_{2\gamma\text{-Doppler}} + \overbrace{\frac{\hbar(\boldsymbol{k}_1-\boldsymbol{k}_2)^2}{2m}}^{\substack{2\gamma\text{ recoil}\\ \text{frequency}}} \tag{2.41}$$

is useful to express $\tilde{V}_{2e}$ in a similar form:

$$\tilde{V}_{2e} = \frac{\hbar\Omega_{22}}{2} e^{-i\left((\tilde{\Delta}+\tilde{\delta})t-\varphi_2\right)} \tag{2.42}$$

Combining it all, we can write the transformed Hamiltonian as

$$\hat{H}' = \frac{\hbar}{2}\begin{pmatrix} 0 & 0 & \Omega_{11}\, e^{-i\left(\tilde{\Delta}\,t\,+\,\varphi_1\right)} \\ 0 & 0 & \Omega_{22}\, e^{-i\left((\tilde{\Delta}+\tilde{\delta})t\,-\,\varphi_2\right)} \\ \Omega_{11}^*\, e^{i\left(\tilde{\Delta}\,t\,+\,\varphi_1\right)} & \Omega_{22}^*\, e^{i\left((\tilde{\Delta}+\tilde{\delta})t\,-\,\varphi_2\right)} & 0 \end{pmatrix} \tag{2.43}$$

Writing out the Schrödinger equation with this Hamiltonian leads to a system of differential equations:

$$i\hbar\,\dot{b}_1 = \frac{\hbar}{2}\Omega_{11}e^{-i\left(\tilde{\Delta}\,t\,+\,\varphi_1\right)}b_e \tag{2.44a}$$

$$i\hbar\,\dot{b}_2 = \frac{\hbar}{2}\Omega_{22}e^{-i\left((\tilde{\Delta}+\tilde{\delta})\,t\,-\,\varphi_2\right)}b_e \tag{2.44b}$$

$$i\hbar\,\dot{b}_e = \frac{\hbar}{2}\Omega_{11}^*e^{i\left(\tilde{\Delta}\,t\,+\,\varphi_1\right)}b_1 + \frac{\hbar}{2}\Omega_{22}^*e^{i\left((\tilde{\Delta}+\tilde{\delta})t\,-\,\varphi_2\right)}b_2 \tag{2.44c}$$

Adiabatic elimination

The next step is to reduce this to a two-level system. This step is motivated by the idea that the excited state is only ever negligibly populated, an assumption that is justified if the single photon detuning Δ is large compared to natural linewidth Γ of the transition to the excited state. This implicitly ignores single photon scattering. Note that if $\Delta \gg |\Omega_{11}|, |\Omega_{22}|$, then the phase factors in eq. 2.44c, oscillate much faster than the Rabi frequencies at which b_1, b_2 oscillate (the relevant comparison is to how fast b_1 and b_2 themselves change, not the phase factors in their differential equations). We can thus directly integrate eq. 2.44c assuming b_1, b_2 to be constant with respect to the integration. Doing so,

$$\begin{aligned} b_e(t) &= \int_{t_0}^{t_0+t} dt'\,\dot{b}_e(t') \\ &\approx -\frac{1}{2\tilde{\Delta}}\left(\Omega_{11}^*e^{-i\left(\tilde{\Delta}\,t\,+\,\varphi_1\right)}b_1(t) + \Omega_{22}^*e^{i\left((\tilde{\Delta}+\tilde{\delta})t\,-\,\varphi_2\right)}b_2(t)\right) \end{aligned} \tag{2.45}$$

where we have used eq. 2.44c to compute eq. 2.45, and used that $\Delta \gg \tilde{\delta}$. Substituting the result back into eq. 2.44 gives our new set of differential equations:

$$\dot{b}_1 = \frac{i}{4\tilde{\Delta}}\left(|\Omega_{11}|^2 b_1 + \Omega_{11}\Omega_{22}^* b_2 e^{i\left(\tilde{\Delta}\,t\,+\,\varphi_1\right)}\right) \tag{2.46a}$$

$$\dot{b}_2 = \frac{i}{4\tilde{\Delta}}\left(\Omega_{11}^*\Omega_{22}e^{i\left((\tilde{\Delta}+\tilde{\delta})t\,-\,\varphi_2\right)}\right)b_1 + |\Omega_{11}|^2 b_2 \tag{2.46b}$$

$$\dot{b}_e = \frac{\hbar}{2}\Omega_{11}^*e^{i\left(\tilde{\Delta}\,t\,+\,\varphi_1\right)t}b_1 + \frac{\hbar}{2}\Omega_{22}^*e^{i\left((\tilde{\Delta}+\tilde{\delta})t\,-\,\varphi_2\right)}b_2 \tag{2.46c}$$

Note that the sign of $\dot{b}_e$ changes rapidly when Δ is large, as we have assumed. As a result b_e never changes appreciably from zero. We can thus ignore it from this stage, and move to a two-level system considering only b_1 and b_2.

Solving the two level system

To signify our jump from a three level system to a two-level system, we will change our component notation from b_i to c_i. The equation we are now trying to solve is

$$\begin{aligned} i\hbar \begin{pmatrix} \dot{c}_1 \\ \dot{c}_2 \end{pmatrix} &= \hat{H}_2 \begin{pmatrix} c_1 \\ c_2 \end{pmatrix} \\ i\hbar \begin{pmatrix} \dot{c}_1 \\ \dot{c}_2 \end{pmatrix} &= -\hbar \begin{pmatrix} \frac{|\Omega_{11}|^2}{4\tilde{\Delta}} & \frac{\Omega_{11}\Omega_{22}^*}{4\tilde{\Delta}} e^{i\left(\tilde{\delta}t-(\varphi_1-\varphi_2)\right)} \\ \frac{\Omega_{11}^*\Omega_{22}}{4\tilde{\Delta}} e^{-i\left(\tilde{\delta}t-(\varphi_1-\varphi_2)\right)} & \frac{|\Omega_{22}|^2}{4\tilde{\Delta}} \end{pmatrix} \begin{pmatrix} c_1 \\ c_2 \end{pmatrix} \\ &= -\hbar \begin{pmatrix} \Omega_1^{\mathrm{ac}} & \frac{\Omega_{2\gamma}}{2} e^{i\left(\tilde{\delta}t-\phi_{\mathrm{L}}\right)} \\ \frac{\Omega_{2\gamma}^*}{2} e^{-i\left(\tilde{\delta}t-\phi_{\mathrm{L}}\right)} & \Omega_2^{\mathrm{ac}} \end{pmatrix} \begin{pmatrix} c_1 \\ c_2 \end{pmatrix} \end{aligned} \tag{2.47}$$

where we have defined several new quantities. One is the effective laser phase, $\phi_{\mathrm{L}} = \varphi_1 - \varphi_2$. Temporarily re-including the spatial dependence hidden in φ_ν, we have $\phi_{\mathrm{L}} = \varphi_1 - \varphi_2 + (\boldsymbol{k}_1 - \boldsymbol{k}_2) \cdot \boldsymbol{z}$. We also define the effective wavevector $\boldsymbol{k}_{\mathrm{eff}} = \boldsymbol{k}_1 - \boldsymbol{k}_2$.

Another new quantity is the two-photon Rabi frequency:

$$\Omega_{2\gamma} = \frac{\Omega_{11}\Omega_{22}^*}{2\tilde{\Delta}}, \tag{2.48}$$

the rate at which the population oscillates between states $|1\rangle$ and $|2\rangle$ due to the driving light fields. The ac Stark shifts $\Omega_\alpha^{\mathrm{ac}}$ are the shift of level α due to the driving light fields. We previously ignored the dotted lines in Fig. 2.2, and stated that their effect is to change $\Omega_\alpha^{\mathrm{ac}}$ [35]. Inserting the full result here, the ac Stark shift for level $|n\rangle$ is

$$\Omega_n^{\mathrm{ac}} = \sum_{\nu=1,2} \frac{|\Omega_{n\nu}|^2}{4\tilde{\Delta}_{n\nu}}, \quad n = 1, 2 \tag{2.49}$$

where the sum runs over couplings $\Omega_{n\nu}$ and detunings $\tilde{\Delta}_{n\nu}$ for laser beam ν.

The general solutions to eq. 2.47 date back to the early days of atomic physics [37] from Norman Ramsey. Explicitly, they are

$$\begin{aligned} c_1(t_0+t) = e^{i\left(\Omega_1^{\mathrm{ac}}+\Omega_2^{\mathrm{ac}}\right)t/2} e^{i\tilde{\delta}t/2} \Bigg(& c_2(t_0) e^{i\left(\tilde{\delta}t_0-\phi_L\right)} \left[i \sin\Theta \sin\left(\frac{\tilde{\Omega}_{2\gamma}t}{2}\right)\right] \\ & + c_1(t_0) \left[\cos\left(\frac{\tilde{\Omega}_{2\gamma}t}{2}\right) - i\cos\Theta \sin\left(\frac{\tilde{\Omega}_{2\gamma}t}{2}\right)\right] \Bigg) \end{aligned} \tag{2.50a}$$

$$c_2(t_0+t) = e^{i\left(\Omega_1^{\mathrm{ac}}+\Omega_2^{\mathrm{ac}}\right)t/2} e^{-i\tilde{\delta}t/2}\Bigg(c_2(t_0)\left[\cos\left(\frac{\tilde{\Omega}_{2\gamma}t}{2}\right) + i\cos\Theta\sin\left(\frac{\tilde{\Omega}_{2\gamma}t}{2}\right)\right] \tag{2.50b}$$

$$+ c_1(t_0)e^{-i\left(\tilde{\delta}t_0-\phi_L\right)}\left[i\sin\Theta\sin\left(\frac{\tilde{\Omega}_{2\gamma}t}{2}\right)\right]\Bigg)$$

where Θ is defined by

$$\tan\Theta = \frac{\Omega_{2\gamma}}{\tilde{\delta}-\delta^{\mathrm{ac}}} \tag{2.51}$$

$$\cos\Theta = \frac{\tilde{\delta}-\delta^{\mathrm{ac}}}{\tilde{\Omega}_{2\gamma}} \tag{2.52}$$

$$\sin\Theta = \frac{\Omega_{2\gamma}}{\tilde{\Omega}_{2\gamma}} \tag{2.53}$$

with differential ac Stark shift δ^{ac} defined as

$$\delta^{\mathrm{ac}} = \Omega_1^{\mathrm{ac}} - \Omega_2^{\mathrm{ac}},$$

and with generalized off-resonant Rabi frequency

$$\tilde{\Omega}_{2\gamma} = \sqrt{|\Omega_{2\gamma}|^2 + (\delta^{\mathrm{ac}}-\tilde{\delta})^2}$$

.

This is the full solution that can be referenced for general cases. However, we can simplify considerably from the general solution eqs. 2.50. First, we notice the common factor $e^{i\left(\Omega_1^{\mathrm{ac}}+\Omega_2^{\mathrm{ac}}\right)t/2}$. This is a *common mode ac Stark phase shift*. As long as the ac Stark frequency shift does not vary across the wavefunction separation, this common global phase can be ignored. We will thus suppress it from here on out.

Second, let's assume we are right on two-photon resonance, i.e. $\tilde{\delta} = \delta^{\mathrm{ac}}$. This makes $\cos\Theta = 0$, $\sin\Theta = 1$, and $\tilde{\Omega}_{2\gamma} = \Omega_{2\gamma}$. In a mirror pulse, we choose a pulse duration t_π such that $\tilde{\Omega}_{2\gamma}t_\pi = \pi$ exactly. For this reason, a mirror pulse is also commonly referred to as a π pulse. See Ref. [38] for a quantitative analysis of the undesired phase shifts arising from violations of these detuning and pulse duration criteria.

Applying these simplifications, the solution for a π pulse of duration τ from eq. 2.50 then becomes

$$c_1(t_0+\tau) = ic_2(t_0)e^{i(\tilde{\delta}\,\tau/2+\tilde{\delta}\,t_0-\phi_L)} \tag{2.54a}$$

$$c_2(t_0+\tau) = ic_1(t_0)e^{-i(\tilde{\delta}\,\tau/2+\tilde{\delta}\,t_0-\phi_L)} \tag{2.54b}$$

or in matrix form,

$$\begin{aligned}\begin{pmatrix} c_1(t_0+\tau) \\ c_2(t_0+\tau) \end{pmatrix} &= i \begin{pmatrix} 0 & e^{i(\tilde{\delta}\,\tau/2+\tilde{\delta}\,t_0-\phi_L)} \\ e^{i(\tilde{\delta}\,\tau/2+\tilde{\delta}\,t_0-\phi_L)} & 0 \end{pmatrix} \begin{pmatrix} c_1(t_0) \\ c_2(t_0) \end{pmatrix} \\ \begin{pmatrix} c_1(t_0+\tau) \\ c_2(t_0+\tau) \end{pmatrix} &= \hat{M}(\tau, t_0) \begin{pmatrix} c_1(t_0) \\ c_2(t_0) \end{pmatrix} \qquad (2.55)\end{aligned}$$

where we have here defined the mirror operator $\hat{M}(\tau, t_0)$.

For a beamsplitter pulse, we choose a pulse duration $t_{\frac{\pi}{2}}$ such that $\tilde{\Omega}_{2\gamma} t_{\frac{\pi}{2}} = \frac{\pi}{2}$ (again reflecting the “beamsplitter” ↔ “$\frac{\pi}{2}$ pulse” nomenclature). Under the stated assumptions, a $\frac{\pi}{2}$ pulse with duration τ simplifies from eq. 2.50 to

$$c_1(t_0+\tau) = \frac{e^{i\tilde{\delta}\,\tau/2}}{\sqrt{2}} \left(c_1(t_0) + i c_2(t_0) e^{i(\tilde{\delta}\,t_0-\phi_L)} \right) \qquad (2.56a)$$

$$c_2(t_0+\tau) = \frac{e^{-i\tilde{\delta}\,\tau/2}}{\sqrt{2}} \left(c_2(t_0) + i c_1(t_0) e^{-i(\tilde{\delta}\,t_0-\phi_L)} \right) \qquad (2.56b)$$

or in matrix form,

$$\begin{aligned}\begin{pmatrix} c_1(t_0+\tau) \\ c_2(t_0+\tau) \end{pmatrix} &= \frac{1}{\sqrt{2}} \begin{pmatrix} e^{i\tilde{\delta}\tau/2} & i e^{i(\tilde{\delta}\tau/2+\tilde{\delta}t_0-\phi_L)} \\ i e^{i(\tilde{\delta}\tau/2+\tilde{\delta}t_0-\phi_L)} & e^{-i\tilde{\delta}\tau/2} \end{pmatrix} \begin{pmatrix} c_1(t_0) \\ c_2(t_0) \end{pmatrix} \\ \begin{pmatrix} c_1(t_0+\tau) \\ c_2(t_0+\tau) \end{pmatrix} &= \hat{B}(\tau, t_0) \begin{pmatrix} c_1(t_0) \\ c_2(t_0) \end{pmatrix} \qquad (2.57)\end{aligned}$$

where we have here defined the mirror operator $\hat{B}(\tau, t_0)$.

More comprehensive treatments of Raman transitions and their use in interferometers can be found in Refs. [34, 35, 37–39].

2.3.3 Laser phases in an interferometer

Optical Ramsey clock / interferometer

With our description of Raman transitions, we can construct an interferometer a few levels more complete than that from Section 2.1. We now replace our Platonic ideal of a beamsplitter eq. 2.1 with a real Raman beamsplitter eq. 2.57. The simple interferometer from eq. 2.4 now becomes an optical Ramsey clock! Acting on an initial state $|\Psi_{\mathrm{I}}\rangle = \begin{pmatrix} 1 \\ 0 \end{pmatrix} = |1\rangle$, the interferometry sequence then gives:

$$|\Psi_{\mathrm{F}}\rangle = \hat{B}(\tau, T+\tau)\hat{U}(\phi_a, \phi_b)\hat{B}(\tau, 0)|\Psi_{\mathrm{I}}\rangle \qquad (2.58)$$

where $|\Psi_{\mathrm{F}}\rangle$ is the final state after the interferometer sequence, and T is the free evolution time over which $\hat{U}$ operates. Multiplying out these matrices using eq. 2.57 for $\hat{B}$ and eq. 2.3 for $\hat{U}$ (we're not yet introducing the results of Section 2.2), we take the norms of components of $|\Psi_{\mathrm{F}}\rangle = \begin{pmatrix} c_{1,\mathrm{F}} \\ c_{2,\mathrm{F}} \end{pmatrix}$ as the probability to be in states $|1\rangle$ and $|2\rangle$. These quantities are:

$$\begin{pmatrix} P_1 \\ P_2 \end{pmatrix} = \begin{pmatrix} c_{1,\mathrm{F}}^2 \\ c_{2,\mathrm{F}}^2 \end{pmatrix} = \frac{1}{2} \begin{pmatrix} 1 + \cos(\tilde{\delta}\, T + (\phi_L^1 - \phi_L^2) + (\phi_b - \phi_a)) \\ 1 - \cos(\tilde{\delta}\, T + (\phi_L^1 - \phi_L^2) + (\phi_b - \phi_a)) \end{pmatrix} \tag{2.59}$$

where ϕ_L^i is the effective laser phase $(\varphi_1^i - \varphi_2^i)$ seen by the atom in pulse i. Keep in mind that the detuning $\tilde{\delta}$ is the difference between the laser beam frequencies $\omega_1 - \omega_2$ and $\frac{1}{\hbar}$ times the energy separation of the *bare* levels $|1, \boldsymbol{p}\rangle$ and $|2, \boldsymbol{p} + \hbar \boldsymbol{k}_{\mathrm{eff}}\rangle$. That is, when on the ac Stark-shifted two-photon resonance, $\tilde{\delta} \neq 0$. For convenience, from here on we will replace $\tilde{\delta}$ with δ (the symbol δ had previously referred to this same quantity, but neglecting the shift between levels due to the Doppler shift and recoil energy, see eq. 2.41).

The phases ϕ_a and ϕ_b are equal, since the internal energy difference $\hbar\left(\omega_2^A - \omega_1^A\right)$ during the free evolution time T is already accounted for in the solutions eqs. 2.50. We can also take the laser phase $\phi_L^1 - \phi_L^2 = 0$, as long as nothing fancy (e.g., frequency ramping, phase jump) is done to the lasers during T, and they continue to obey eq. 2.24. With these considerations, eq. 2.59 reduces to the familiar expression for a Ramsey clock:

$$\begin{pmatrix} P_1 \\ P_2 \end{pmatrix} = \frac{1}{2} \begin{pmatrix} 1 + \cos(\delta\, T) \\ 1 - \cos(\delta\, T) \end{pmatrix} \tag{2.60}$$

This analysis has neglected that in the time T, the two arms spatially separate from each other. However, if $\boldsymbol{k}_1 \approx \boldsymbol{k}_2$ [co-propagating], then $\boldsymbol{k}_{\mathrm{eff}} \approx 0$ (rather than $\boldsymbol{k}_{\mathrm{eff}} \approx 2\vec{k}_1$ for $\boldsymbol{k}_1 \approx -\boldsymbol{k}_2$ [counter-propagating]). Optical Ramsey fringes from performing this operation in our experiment can be seen in Fig. 4.11 in Chapter 4. To derive the full Ramsey fringe shape, including the contrast decay as increasing δ moves the Raman lasers off-resonance, imperfections involving Θ and its constituent trig relations eqs. 2.51 would have to be taken into account using the full solution eqs. 2.50.

Mach-Zehnder interferometer

The next entry in our interferometry toolkit is the *Mach-Zehnder* geometry, as seen in Fig. 2.3. We take $\boldsymbol{k}_1 \approx -\boldsymbol{k}_2$, giving $\boldsymbol{k}_{\mathrm{eff}} \approx 2\boldsymbol{k}_1$, and therefore spatial separation. After a free evolution time T, a mirror pulse $\hat{M}$ reverses the relative momentum of the two arms. After another free evolution time T, the two arms are again spatially overlapped, and interfered with a final beamsplitter pulse.

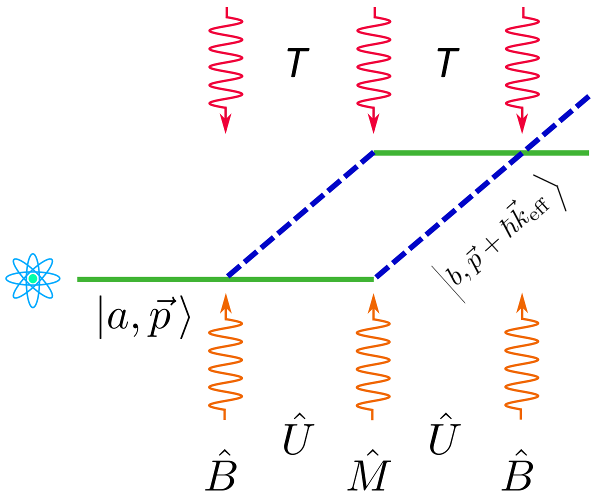

Figure 2.3: Mach-Zehnder schematic

In our operator notation, this process is represented by

$$\hat{O}_{\text{MZ}} = \hat{B}(\tau_3, \tau_2+\tau_1+2T)\hat{U}(\phi_c,\phi_d)\hat{M}(\tau_2,\tau_1+T)\hat{U}(\phi_a,\phi_b)\hat{B}(\tau_1,0)$$

Acting $\hat{O}_{\text{MZ}}$ on an initial state $|\Psi_{\text{I}}\rangle = \begin{pmatrix}1\\0\end{pmatrix} = |1\rangle$ gives the output state $|\Psi_{\text{F}}\rangle$:

$$|\Psi_{\text{F}}\rangle = \hat{O}_{\text{MZ}}|\Psi_{\text{I}}\rangle = \frac{1}{2}\begin{pmatrix} -e^{\frac{i}{2}(\delta(\tau_1+T+\tau_2+T+\tau_3)-2(\phi_L^2+\phi_L^3))}\left(e^{i(2\phi_L^2+\phi_a+\phi_d)} + e^{i(\phi_L^1+\phi_L^3+\phi_b+\phi_c)}\right) \\ e^{-\frac{i}{2}(\delta(\tau_1+T+\tau_2+T+\tau_3)-2\phi_L^2)}\left(e^{i(2\phi_L^2+\phi_a+\phi_d)} - e^{i(\phi_L^1+\phi_L^3+\phi_b+\phi_c)}\right)\end{pmatrix}$$

where, again, ϕ_L^i is the effective laser phase at pulse i, and ϕ_{a-d} represent various free evolution phases (which we have neglected to be specific about yet; see Section 2.4). The global phases on each of these components don't enter the probabilities when we take the norm of these components. The probabilities to end up in either state are then

$$\begin{pmatrix}P_1\\P_2\end{pmatrix} = \frac{1}{2}\begin{pmatrix}1+\cos(\phi_L^1-2\phi_L^2+\phi_L^3-\phi_a+\phi_b+\phi_c-\phi_d)\\1-\cos(\phi_L^1-2\phi_L^2+\phi_L^3-\phi_a+\phi_b+\phi_c-\phi_d)\end{pmatrix} \tag{2.61}$$

There are a few operational simplifications we can make here now that will make things easier. The first simplification is noticing that (in the case of our $\Theta = \frac{\pi}{2}$ assumption) δ doesn't enter into a physically measurable quantity. We will thus ignore it in the expressions eqs. 2.55 and 2.57. This is equivalent to having vanishing ac Stark shift ($\delta = \delta_{\text{ac}} = 0$), or assuming that the two-photon Rabi frequency is much larger than the ac Stark shift ($\Omega_{2\gamma} \gg \delta_{\text{ac}} = \delta$). With that, we can write simplified mirror and beamsplitter operations $\hat{M}_0$ and $\hat{B}_0$, respectively from eqs. 2.55 and 2.57:

$$\hat{M}_0 = i\begin{pmatrix}0 & e^{-i\phi_L^i}\\ e^{i\phi_L^i} & 0\end{pmatrix}, \qquad \hat{B}_0 = \frac{1}{\sqrt{2}}\begin{pmatrix}1 & ie^{-i\phi_L^i}\\ ie^{i\phi_L^i} & 1\end{pmatrix}. \tag{2.62}$$

For situations other than a very on-resonant, well-timed Mach-Zehnder, these simplifications will of course have to be revisited (e.g., as in Sec. 5.6). However, these versions of mirrors and beamsplitters make it very clear what's happening.

There is a clear analogy from $\hat{M}_0$ and $\hat{B}_0$ to the rotation operators $\hat{R}(\pi, -\hat{x})$ and $\hat{R}(\frac{\pi}{2}, -\hat{x})$ from eq. 2.2. The simplified Raman beamsplitter $\hat{B}_0$ is now quite similar to the idealized beamsplitter $\hat{S} = \hat{R}(\frac{\pi}{2}, -\hat{x})$ from eq. 2.1. The only difference is the addition of the laser phase $e^{\pm i\phi_L}$ on the off-diagonals. The mirror pulse $\hat{M}_0$ looks just like the rotation operator $\hat{R}(\frac{\pi}{2}, -\hat{x})$ with laser phase shifts $e^{\pm i\phi_L}$ on the off-diagonals. It inverts the states, and imparts a laser phase.

The off-diagonal terms represent the amplitude of a state that has undergone a Raman transition as a result of the operation. Thus, we see that when an arm interacts with the laser field, it picks up a phase $\pm\phi_L$. Furthermore, the sign is determined by the direction of the momentum kick: When the atom gains momentum $+\hbar\boldsymbol{k}_{\text{eff}}$, it acquires a phase shift of $+\phi_L$. When the atom loses momentum to the light field, changing its momentum by $-\hbar\boldsymbol{k}_{\text{eff}}$, it picks up a phase $-\phi_L$. That is, as a result of the pulses, we have:

$$|a, \boldsymbol{p}\rangle \to e^{+i\phi_L}|b, \boldsymbol{p} + \hbar\boldsymbol{k}_{\text{eff}}\rangle \tag{2.63}$$

$$|b, \boldsymbol{p} + \hbar\boldsymbol{k}_{\text{eff}}\rangle \to e^{-i\phi_L}|a, \boldsymbol{p}\rangle \tag{2.64}$$

This is in fact, general, and is derived and discussed in Ref. [31]. Armed with this fact, we can follow Ref. [31] to write a formula for the total laser phase shift $\Delta\phi_L$ in an atom interferometer:

$$\Delta\phi_L = \left(\sum_j \pm\phi_L(t_j, \boldsymbol{x}_u(t_j))\right)_{\text{upper}} - \left(\sum_j \pm\phi_L(t_j, \boldsymbol{x}_l(t_j))\right)_{\text{lower}} \tag{2.65}$$

where $\{t_j, \boldsymbol{x}_u(t_j)\}$ and $\{t_j, \boldsymbol{x}_l(t_j)\}$ are the locations of atom-laser interaction j for the upper and lower arms, respectively.

In summing up the laser phases, we have applied the solution eqs. 2.50 to the full superposition up to this point. However, it is common practice [38] to apply mirror and beamsplitter operators to individual arms of the interferometer as if they were not part of a superposition. That is, add up the laser phases along each arm individually, then subtract the phases of arms interfering with each other as in eq. 2.65. This is justified by linearity, that is,

$$\hat{H}\left(\alpha|0\rangle + \beta|1\rangle\right) = \alpha\left(\hat{H}|0\rangle\right) + \beta\left(\hat{H}|1\rangle\right).$$

From eqs. 2.50, we see that there can be other phase shifts for Raman pulses due to ac Stark shifts, detunings and pulse imperfections. These are less general, but are discussed, for example in Refs. [30, 38].

2.3.4 Bragg diffraction

In Bragg transitions, an atom coherently interacts with $2n$ photons to transition from a state $|a, \boldsymbol{p}\rangle$ to $|a, \boldsymbol{p} + 2n\hbar\boldsymbol{k}\rangle$. The external momentum state changes, but the internal state does not. A diagram of this process is shown in Fig. 2.4.

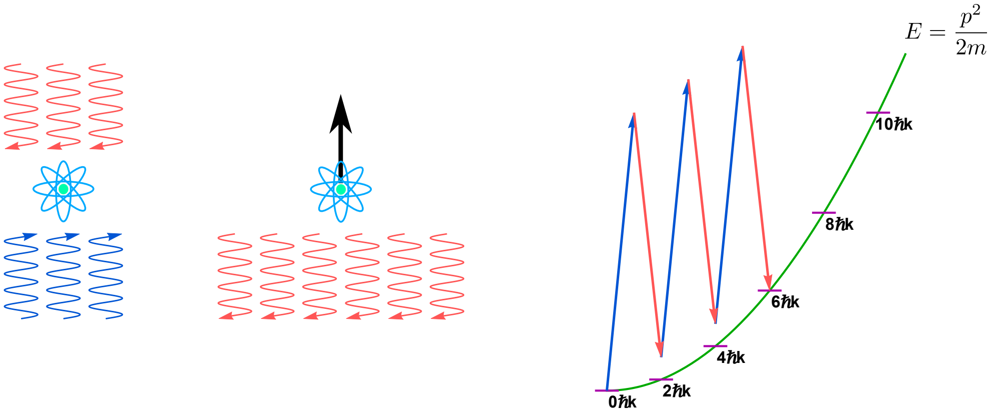

Figure 2.4: Bragg diffraction.

The Bragg resonance is met when the laser frequency difference is set such that both energy and momentum are conserved. Conservation of momentum enforces that the momentum lost by the light field is gained by the atom. That is,

$$n\hbar(\boldsymbol{k}_1 - \boldsymbol{k}_2) = m\Delta\boldsymbol{v}_A$$

where $\boldsymbol{k}_1 \approx -\boldsymbol{k}_2 \equiv \boldsymbol{k}$. As a result, the atom's velocity changes by $\Delta\boldsymbol{v}_A = 2nv_{\text{rec}}$, where $v_{\text{rec}} = \frac{\hbar k}{m}$ is called the recoil velocity. The kinetic energy gained by the atom in this process must also equal the energy lost from the light field. In the reference frame moving at the initial velocity of the atom, that requires

$$\frac{1}{2}m\Delta v_A^2 = n\hbar|\omega_1 - \omega_2|$$

The energy gained by the atom is $(2n)^2E_{\text{rec}}$, where $E_{\text{rec}} = \frac{\hbar^2k^2}{2m}$ is known as the *recoil energy*, and $\omega_{\text{rec}} = E_{\text{rec}}/\hbar$ is called the *recoil frequency*. This condition is satisfied when

$$|\omega_1 - \omega_2| = \frac{2n^2\hbar k^2}{m}$$

For cesium, as used in this work, the recoil velocity is $v_{\text{rec}} = 3.5225$ mm/s and the recoil energy is $E_{\text{rec}} = \hbar\omega_{\text{rec}} = h \times 2.0663$ kHz.

One advantage of Bragg diffraction is that it offers the possibility for large momentum transfer (LMT) by transferring $2n$, rather than just 2, photons' worth of momentum to the atom. This can increase the sensitivity of the interferometer, as the laser phase then becomes

$\phi_L \rightarrow n\phi_L$. Additionally, the kinetic energy increases with n^2, leading to quadratically increasing kinetic component ϕ_K to the free evolution phase (the Lagrangian is given by $L = K - U$). This quadratic scaling is useful, for example in measuring the fine-structure constant [5]. Having the atoms in the same hyperfine state also reduces sensitivity to unwanted phases such as differential Zeeman and ac Stark shifts.

The disadvantages primarily lie in the difficulty of implementing Bragg diffraction. The momentum spread of the atom sample must be small, at least sub-recoil. The many-state nature of the $2\hbar k$-separated momentum ladder means that the usual two level treatment can't be applied [40]. These additional levels also lead to complicated, difficult-to-control and undesired phase shifts [41]. Finally, while useful for suppressing systematic effects, the common hyperfine state sacrifices state-labeling of the interferometer arms, which complicates detection.

Far more extensive discussion of Bragg diffraction of matter waves can be found in, for example Refs. [20, 27, 40, 41].

2.4 The canonical example: gravity

We will now combine the results of the previous sections to calculate the phase shift for an atom interferometer under gravity. Consider the Mach-Zehnder geometry in a uniform gravitational field (Fig 2.5).

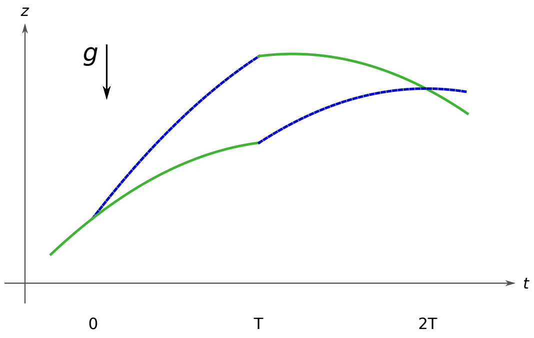

Figure 2.5: Mach-Zehnder light pulse interferometer

A $\frac{\pi}{2}$ pulse splits the atomic wavefunction along two paths at $t = 0$. After a free evolution time T, a π pulse redirects the arms towards each other. After another duration of T, when the two arms overlap again, a final $\frac{\pi}{2}$ pulse recombines the paths. The resulting interference determines the relative populations of the two output ports. From the previous two sections, the phase of this interferometer would be

$$\Delta\Phi = \Delta\phi_L + \Delta\phi_{\mathrm{FE}}, \tag{2.66}$$

where $\Delta\phi_{\mathrm{FE}}$ is the free evolution phase found by integrating the action (Sec. 2.2) and $\Delta\phi_L$ is the phase shift due to atom-laser interactions (Sec. 2.3). The end of this section will list a number of phase shifts that are not being considered in this example.

To calculate the action, we use the Lagrangian

$$\begin{aligned} L &= K - U \\ &= \frac{1}{2} m \dot{z}^2 - mgz \end{aligned} \tag{2.67}$$

with kinetic energy K and potential energy $U = mgz$, as is the case for a constant gravitational field, causing an acceleration g for a freely falling body.

To integrate this over the trajectories we start from the velocities

$$v_u(t) = \begin{cases} v_0(t) + 2v_r \\ v_0(t) \end{cases} \qquad v_\ell(t) = \begin{cases} v_0(t) \\ v_0(t) + 2v_r \end{cases} \qquad \begin{matrix} 0 \leq t \leq T \\ T < t < 2T \end{matrix} \tag{2.68}$$

where subscripts u and ℓ denote upper and lower paths, respectively. The recoil velocity $v_r = \frac{\hbar k}{m}$ is the velocity at which an atom recoils due to absorption or emission of a photon with momentum $\hbar k$. Finally, $v_0(t) = v_I - gt$ is the velocity profile the atom would take in the absence of the laser pulses. Integrating eq. 2.68 to get the positions gives

$$z_u(t) = \begin{cases} z_0(t) + 2v_r t \\ z_0(t) + 2v_r T \end{cases} \qquad z_\ell(t) = \begin{cases} z_0(t) \\ z_0(t) + 2v_r(t - T) \end{cases} \qquad \begin{matrix} 0 \leq t \leq T \\ T < t < 2T \end{matrix} \tag{2.69}$$

where $z_0(t) = z_I + v_I t - \frac{1}{2} g t^2$ is the trajectory the atom would take without any laser pulses. From these expressions, it's straightforward to turn the crank; integrating the Lagrangian eq. 2.67 along each path to get the difference in the actions:

$$\begin{aligned} S_u - S_\ell &= \frac{1}{2} m \int_0^{2T} dt\ \left(v_u(t)^2 - v_\ell(t)^2\right) - mg \int_0^{2T} dt\ \left(z_u(t) - z_\ell(t)\right) \\ &= \left(2mv_r g T^2\right) - \left(2mv_r g T^2\right) \\ &= 0 \end{aligned} \tag{2.70}$$

So in this case, the free evolution phase is zero! The actions along the upper and lower classical trajectories are equal, as the kinetic and potential terms cancel.

Any phase shift in the interferometer must therefore come from the laser phase. Using eq. 2.65 for the upper output port:

$$\Delta\phi_L^u = \sum \pm \phi_L^u - \sum \pm \phi_L^\ell$$

$$\begin{aligned}&= (+\phi_L(0, z^u(0)) - \phi_L(T, z^u(T)) + \phi_L(2T, z^u(2T))) - \big(0 + \phi_L(T, z^\ell(T)) + 0\big) \\ &\equiv \big(\phi_1^u - (\phi_2^u + \phi_2^\ell) + \phi_3^u\big) \qquad (2.71)\end{aligned}$$

where in the last line we have let $\phi_i^a \equiv \phi_L(t_i, z^a(t_i))$ be the laser phase seen by arm a for laser pulse i. Note that $\phi_j^u = \phi_j^\ell$ for $j = 1, 3$, since the arms are overlapped for these pulses. We did this calculation for the upper output port, but doing so for the lower output port gives the same answer (as it must, due to conservation of probability).

If we define the midpoint path $z_m(t) = \frac{1}{2}(z_u(t) + z_\ell(t))$, and let $\phi_i \equiv \phi_L(t_i, z^m(t_i))$, eq. 2.71 becomes

$$\Delta\phi_L = \phi_1 - 2\phi_2 + \phi_3 \qquad (2.72)$$

If the effective wavevector $\boldsymbol{k}_{\text{eff}}$ is constant, each phase can be expressed as $\phi_i = k_{\text{eff}} z_m(t_i)$. Making this substitution into eq. 2.72, we get

$$\Delta\phi_L = -k_{\text{eff}} g T^2 \qquad (2.73)$$

Combining eqs. 2.70 and 2.73 into eq. 2.66, we get our final expression for the phase of a Mach-Zehnder atom interferometer in a constant gravitational field:

$$\Delta\Phi = -k_{\text{eff}} g T^2 \qquad (2.74)$$

This geometry therefore, is a sensitive measurement of acceleration due to a gravitational field. The effective wavevector k_{eff} is a large scale factor ($\gtrsim 10^7$ m^{-1} for optical transitions) so that small changes in g have a large lever arm to change $\Delta\Phi$, and thus the population ratio of the output ports.

2.5 Adding a perturbation

Atom interferometers are often employed to measure small effects. While the formalism of Sec. 2.2 is useful for gaining intuition on how matter wave interference arises, it is cumbersome for anything beyond the simplest Lagrangians. In practice, a perturbative treatment is used instead. Suppose a small perturbation modifies a Lagrangian L_0 such that $L_0 \to L_0 + \epsilon L_1$. To first order in ϵ, the resulting phase shift is calculated by integrating the perturbation along the classical trajectory. That is,

$$\delta\phi^{(1)} = \epsilon \left(\int_{\Gamma_0^u} L_1 dt - \int_{\Gamma_0^\ell} L_1 dt \right)$$

where $\Gamma_0^{u(\ell)}$ is the classical trajectory of the upper (lower) interferometer arm.

As an example, consider the gravity gradient near the Earth's surface. The perturbation ϵL_1 to the Lagrangian L_0 from eq. 2.67 is

$$\epsilon L_1 = \frac{m}{2}\gamma z^2$$

For small distances z, the constant gravitational term ($g \approx 9.8\ \frac{\mathrm{m}}{\mathrm{s}^2}$) is much larger than the gradient term ($\gamma \approx 3 \times 10^{-6}\ \mathrm{s}^{-2}$). We can thus treat the gradient term as a perturbation. Integrating L_1 over the trajectories (eqs. 2.69) gives the resulting phase shift $\phi_\gamma^{(1)}$. From eq. 2.74, a phase shift implies a shift in the inferred value $g = \frac{\Delta\Phi}{k_{\mathrm{eff}}T^2} \to g_0 + \delta g_\gamma$. When $\Delta\Phi \to \Delta\Phi_0 + \phi_\gamma^{(1)}$ due to the presence of the gradient, the shift is

$$\delta g_\gamma = \gamma\left(\frac{7}{12}gT^2 - (T(v_0 + v_r) + z_0)\right)$$

As discussed in Section 2.2, this treatment is exact when the perturbing potential is of quadratic order or lower in the position (as is the case for the gravity gradient potential eq. 2.75). A more complete treatment covering introduction of a perturbation can be found in Ref. [29].

2.5.1 Other phase shifts

The above derivation gives a conceptual description of two major phase shifts: the laser phase, and the free evolution phase for an atom in a constant gravitational field. However, this discussion leaves out a number of other phase shifts. A few of them are briefly mentioned here, along with references to more complete descriptions.

Gravity gradient

In the presence of a gravity gradient γ, the gravitational potential U in the Lagrangian becomes

$$U = mgz + \frac{1}{2}m\gamma z^2 \tag{2.75}$$

This adds quadratic terms the Lagrangian, and thus new phase terms. This specific example was treated perturbatively in Sec. 2.5, but more information can be found in Refs. [27,29].

Finite pulse duration

We have also assumed that the laser pulses have zero duration. For a duration $\tau \ll T$, this is a good approximation. We can rewrite the phase in eq. 2.74 as $\Delta\Phi = k_{\mathrm{eff}}gT^2 \to \alpha k_{\mathrm{eff}}gT^2$, where $\alpha = 1$ for zero-length pulses. For square $\frac{\pi}{2}$ (π) pulses of duration $\tau(2\tau)$, the leading order correction is [42]

$$\alpha_{\mathrm{sq}} = 1 + \frac{\tau}{T}\left(\frac{4}{\pi} - 1\right) + \left(\frac{\tau}{T}\right)^2\left(\frac{2}{\pi} - \frac{3}{4}\right) + \mathcal{O}\left(\frac{\tau}{T}\right)^3$$

where T is defined as the separation between the centers of the pulses. In a typical experiment in this thesis, $\tau \approx 30\,\mu$s and $T \approx 50$ ms $\Rightarrow \frac{\tau}{T} \sim 10^{-3}$. This factor also changes with pulse shape. More information can be found in Refs. [30, 42].

Separation phase

If the interferometer arms do not properly close, there is an additional phase shift known as the separation phase. This could happen, for example, due to a force gradient, where the interferometer arms are displaced by different amounts. The separation phase is given by

$$\Delta\phi_{\text{sep}} = \bar{\boldsymbol{p}} \cdot \boldsymbol{\Delta z}$$

where $\boldsymbol{\Delta z} = z_\ell - z_u$ is the separation between the upper and lower arms at the time of the final recombination pulse. $\bar{\boldsymbol{p}}$ is the average classical momentum of the two arms being combined in a given output port in the final beamsplitter. More information can be found in Ref. [31].

Other real-life shifts

Many effects arise as systematics to the desired measurement. Examples include magnetic fields (Zeeman shifts), light shifts (ac Stark shifts), and misalignment of the laser wavevector with the acceleration wavevector. These individual systematics will be discussed as needed throughout the measurements described in this thesis (specifically, see Sec. 5.6).

2.6 Optical resonators

This section outlines some basics of optical resonators. Imagine two reflective surfaces facing each other, as in Fig. 2.6.

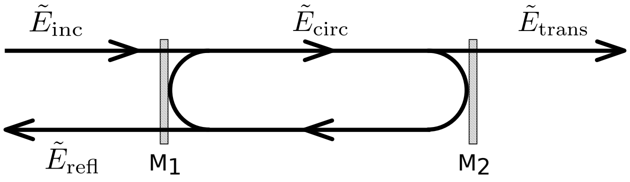

Figure 2.6: The two reflective surfaces facing each other constitute a *Fabry-Perot resonator* (or *cavity*). An electromagnetic wave $\tilde{E}_{\text{inc}}$ incident on the first surface splits into a reflected component $\tilde{E}_{\text{refl}}$ and a portion that contributes to the circulating field $\tilde{E}_{\text{circ}}$ inside the resonator. A transmitted field $\tilde{E}_{\text{trans}}$ exits the resonator at the second surface.

The mirrors M_i have field reflection (transmission) coefficients r_i (t_i), also known as Fresnel coefficients. The intensity reflection and transmission coefficients (the values typically spec'd on optics components) are $R_i = r_i^2$ and $T_i = t_i^2$, respectively.

This analysis follows closely the excellent textbook *Lasers* by Anthony Siegman [43], including the electrical engineering convention of using $j = \sqrt{-1}$. We first solve for the fields $\tilde{E}_{\text{circ}}$, $\tilde{E}_{\text{refl}}$, and $\tilde{E}_{\text{trans}}$ as a function of the input field $\tilde{E}_{\text{inc}}$. Quantities with a tilde, $\tilde{X}$ are complex-valued (that is, they have a phase). We write an expression for the circulating field just inside of the first mirror M_1 as a transmitted component of the incident wave, and the steady state circulating field that was reflected off the mirror one round trip earlier:

$$\tilde{E}_{\text{circ}} = jt_1\tilde{E}_{\text{inc}} + \tilde{g}_{rt}(\omega)\tilde{E}_{\text{circ}} \tag{2.76}$$

There is a 90° phase factor j in the transmitted portion of the incident beam due to choice of reference plane (see [43]). $\tilde{g}_{\text{rt}}$ is the (frequency-dependent) complex round-trip gain for one complete transit through the resonator. In general, it's given by

$$\tilde{g}_{\text{rt}}(\omega) = r_1 r_2 (r_3 ...) \exp\left(-\alpha_0 p - j\frac{\omega}{c}p\right)$$

where the product of r_i's gives reflection off all the mirrors involved in one round trip, α_0 represents losses, and p is the round trip path length in the resonator. Simplifying to our application of two mirrors in a vacuum chamber, we can set $\alpha_0 = 0$ and $p = 2L$, where L is the separation between the mirrors. The round trip gain is then

$$\tilde{g}_{\text{rt}} = r_1 r_2 \exp(-j2\omega L/c)$$

Rearranging eq. 2.76, we get the ratio of the circulating field to the input field:

$$\frac{\tilde{E}_{\text{circ}}}{\tilde{E}_{\text{inc}}} = \frac{jt_1}{1 - \tilde{g}_{\text{rt}}(\omega)} = \frac{jt_1}{1 - r_1 r_2 e^{-j2\omega L/c}} \tag{2.77}$$

where the first equation holds for the general $\tilde{g}_{\text{rt}}$ (for example, a ring cavity with more mirrors, or adding in loss) and the second specializes to our case of interest (lossless, two-mirror cavity).

The intensity ratio follows straightforwardly as the square of the field ratio. For our cavity, this gives

$$\frac{I_{\text{circ}}}{I_{\text{inc}}} = \frac{1 - r_1}{1 - 2r_1 r_2 \cos\left(2\omega L/c\right) + r_1^2 r_2^2} \tag{2.78}$$

where we have used the relation $r^2 + t^2 = 1$.

We can set up analogous equations to solve for the reflected and transmitted fields as well. The reflected field $\tilde{E}_{\text{refl}}$ consists of a reflected portion of the incident field, and a transmitted portion of the circulating field through M_1:

$$\tilde{E}_{\text{trans}} = r_1\tilde{E}_{\text{inc}} + jt_1\left(\frac{\tilde{g}_{\text{rt}}}{r_1}\tilde{E}_{\text{circ}}\right).$$

The resulting field ratio is therefore

$$\frac{\tilde{E}_{\text{refl}}}{\tilde{E}_{\text{inc}}} = \frac{r_1^2 - \tilde{g}_{\text{rt}}(\omega)}{r_1(1 - \tilde{g}_{\text{rt}}(\omega))}. \tag{2.79}$$

The transmitted field $\tilde{E}_{\text{trans}}$ consists of the transmitted portion of the circulating field through M_2:

$$\tilde{E}_{\text{trans}} = jt_2 \exp[-\alpha_0 p_1 - j\omega p_1/c]\tilde{E}_{\text{circ}}$$

where the exponential term represents the path (with length p_1) of the circulating field from the in-coupling mirror to the out-coupling mirror, and therefore isn't the full round-trip gain $\tilde{g}_{\text{rt}}$. The field ratio is

$$\frac{\tilde{E}_{\text{trans}}}{\tilde{E}_{\text{inc}}} = -\frac{t_1 t_2}{\sqrt{r_1 r_2}} \frac{\sqrt{\tilde{g}_{\text{rt}}(\omega)}}{1 - \tilde{g}_{\text{rt}}(\omega)} = -\frac{t_1 t_2 e^{-j\omega L/c}}{1 - r_1 r_2 e^{-2j\omega L/c}} \tag{2.80}$$

where the final equality again represents specialization to our two-mirror case.

Resonant behavior can be seen in, e.g., eq. 2.78. When the denominator is minimized ($\cos(2\omega_q L/c) = 1 \rightarrow \omega_q = 2\pi q \frac{c}{2L}$, for integer q), the intensity ratio can become large. For a modest mirror reflectivity of $r_1 = r_2 = 0.98$ the optical intensity of the circulating field is 50 times that of the incident field. We call this quantity the optical gain $\mathcal{G}$:

$$\mathcal{G} \equiv \frac{I_{\text{circ}}}{I_{\text{inc}}} \tag{2.81}$$

These field solutions are periodic. The phase factor $\exp[-j2\omega L/c]$ in $\tilde{g}_{\text{rt}}$ as the only frequency dependence indicates that the behavior of these fields has (angular) frequency periodicity $(2\pi)\frac{c}{2L}$, as the above equation for ω_q hinted. This period is known as the "free spectral range", or FSR, and is equivalent to the inverse of the round trip travel time t_{rt} of the light field in the resonator:

$$\text{FSR} = \frac{1}{t_{\text{rt}}} = \frac{c}{2L} \tag{2.82}$$

where again the first equality is the more general definition, and the final one specializes to the two-mirror case. The periodic and resonant behavior of the circulating field can be seen in Fig. 2.7. Circulating intensity is plotted for matched resonators ($r_1 = r_2 \equiv r$) for several mirror reflectivities.

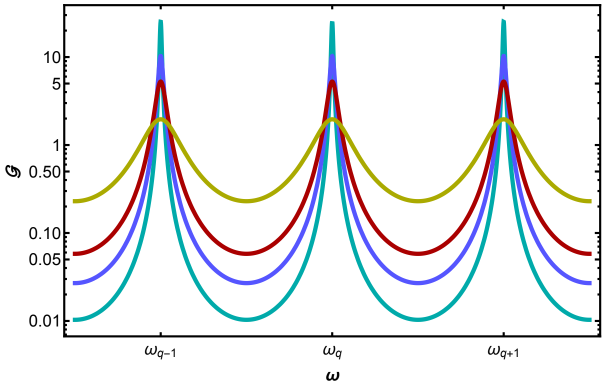

Figure 2.7: Optical gain in matched resonators. Three free spectral ranges are shown for resonators with r = 0.7, 0.90.0.95, 0.98. The vertical scale is logarithmic.

Looking at Fig. 2.7, it's clear that features get sharper with increasing mirror reflectivity. By how much? We define the full-width half-maximum linewidth γ_{FWHM} as the span between points on either side of a resonance peak where the circulating intensity has dropped to half its maximum value. From eq. 2.77, this amounts to finding the frequency where the denominator $|1-\tilde{g}_{rt}|^2$ doubles from its minimum value at resonance. For our lossless, two-mirror case, this minimum value is $(1-r_1r_2)^2$. We thus need to solve the following equation for γ_{FWHM}:

$$\begin{gathered}\left|1-\tilde{g}_{\text{rt}}\left(\omega_q+\frac{\gamma_{\text{FWHM}}}{2}\right)\right|^2=2\left|1-\tilde{g}_{\text{rt}}(\omega_q)\right|\\ 1-2r_1r_2\cos\left(\gamma_{\text{FWHM}}\frac{L}{c}\right)+r_1^2r_2^2=2(1-r_1r_2)^2\end{gathered}$$

After a decent bit of algebra (including using the relation $2\arcsin(\psi)=\arcsin(2\psi\sqrt{1-\psi^2})$ with $\psi=\frac{1-r_1r_2}{2\sqrt{r_1r_2}}$), we end up with the expression for the linewidth:

$$\gamma_{\text{FWHM}}=\frac{4c}{p}\arcsin\left(\frac{1-g_{rt}}{2\sqrt{g_{\text{rt}}}}\right)=4\ \text{FSR}\ \arcsin\left(\frac{1-r_1r_2}{2\sqrt{r_1r_2}}\right) \tag{2.83}$$

In the first equality, we've re-inserted the general case formulation with $g_{\text{rt}}=|\tilde{g}_{\text{rt}}|$, which it turns out holds true despite doing the above algebra with our specific, two-mirror case. Here, γ_{FWHM} is an angular frequency (since the arcsin returns radians).

Another important quantity in analyzing these resonators is the *finesse* $\mathcal{F}$. The finesse is a measure of the frequency-resolving power of the resonator. The most straightforward definition is the free spectral range over the linewidth. That is,

$$\mathcal{F}=\frac{\text{FSR}}{\Delta\nu_{\text{cav}}} \tag{2.84}$$

where $\Delta\nu_{\text{cav}} = \gamma_{\text{FWHM}}/2\pi$ is the full-width, half maximum of the resonance in [Hz] (to match the FSR units). There is some subtlety in the exact definitions used for the finesse, which are nicely and clearly explained in Ref. [44], and only briefly described below. These multiple definitions are all very nearly equivalent at reasonably high finesse, and the differences in definition only begin to matter at low reflectivities ($\lesssim 0.1$). With this caveat, the following expressions for the finesse are all appropriate:

$$\mathcal{F}_{\text{Airy}} = \frac{\pi}{2}\left[\arcsin\left(\frac{1-r_1r_2}{2\sqrt{r_1r_2}}\right)\right]^{-1} \tag{2.85}$$

$$\mathcal{F}_{\text{classical}} = \frac{\pi\sqrt{g_{\text{rt}}}}{1-g_{rt}} = \frac{\pi\sqrt{r_1r_2}}{1-r_1r_2} \tag{2.86}$$

$$\mathcal{F}_{\text{Lorentz}} = \frac{\pi}{-\ln(r_1r_2)} \tag{2.87}$$

$$\tag{2.88}$$

The Airy definition $\mathcal{F}_{\text{Airy}}$, in calculating eq. 2.84, uses the expression for the linewidth eq. 2.83. It gives the number of Airy lineshapes (produced by a single frequency in the resonator when considering all axial modes q [and not just the one it's closest to]) that can be spectroscopically resolved in one free spectral range. Here, spectroscopically resolved refers to the so-called "Taylor criterion", which dictates that two spectral lines are considered resolved if their normalized lineshapes cross at half-intensity or lower. Though a bit of a mouthful, this definition provides a conceptually clear interpretation.

The classical definition $\mathcal{F}_{\text{classical}}$ simply makes the approximation $\sin(x) \approx x$ in eq. 2.83 before plugging into eq. 2.84.

The Lorentz definition $\mathcal{F}_{\text{Lorentz}}$ comes from using the Lorentzian lineshape (which arises by considering photon lifetimes in the cavity) as the relevant linewidth in eq. 2.84. The Lorentzian cavity linewidth is given by $\Delta\nu_{\text{Lorentz}} = 1/(2\pi\tau_c)$, where $\tau_c = \frac{\sum_i -\ln(r_i^2)}{t_{\text{rt}}}$ is the $1/e$ photon decay time from the cavity.

While conceptually interesting and useful in unusual parameter regimes, this variety of definitions will go unappreciated in our work here. Since we will work with reasonably high reflectivities ($r \gtrsim 0.98$) we will justifiably consider them equivalent. It is also noteworthy that the finesse is approximately π times the optical gain; $\mathcal{F} \approx \pi\mathcal{G}$ (but to much less accuracy than the equivalence of the alternative finesse definitions).

One benefit of these resonators is the spatial mode filtering that they provide. In free space propagation, the transverse Hermite-Gaussian modes are frequency-degenerate. Thus, a beam can acquire a non-ideal shape (speckle, diffraction, etc.). In a resonator with boundary conditions, the Guoy phase shift breaks this degeneracy. The total phase accumulated along the resonator for Hermite-Gaussian transverse mode H_{mn} between mirror M_1 at position z_1 and mirror M_2 at position z_2 is

$$\phi(z_2 - z_1) = k(z_1 - z_2) - (n + m + 1) \times [\psi(z_2) - \psi(z_1)]$$

with Guoy phase shift $\psi(z) = \arctan(z/z_{\mathrm{R}})$. z_{R} is the *Rayleigh range*, given by

$$z_{\mathrm{R}} = \frac{\pi w_0^2}{\lambda} \tag{2.89}$$

where w_0 is the beam waist, and λ is the wavelength of the radiation. The Rayleigh range is a measure of divergence of a Gaussian beam; it is the distance from the waist at which the beam $\frac{1}{e}$ radius has increased by a factor of $\sqrt{2}$ (cross-sectional "area"[3] has doubled).

This Guoy phase breaks the degeneracy between the modes H_{mn}. After a lot of algebra, one can arrive at the expression

$$\psi(z_2) - \psi(z_1) = \arccos(\pm\sqrt{g_1 g_2})$$

where $g_i = 1 - \frac{L}{\mathrm{ROC}_i}$ and ROC_i is the radius of curvature of mirror M_i (the ± is chosen by the sign of the g_i [which must be the same]; see Ref. [43] for more detail). This phase shift therefore shifts the resonant frequency of the H_{mn} mode from the fundamental H_{00} mode by

$$\delta f_{mn} = \frac{\mathrm{FSR}}{\pi} \arccos(\sqrt{g_1 g_2}) \tag{2.90}$$

Since the Hermite-Gaussian modes are non-degenerate, a beam resonant with the cavity's H_{00} mode will primarily excite only that mode. The other spatial modes are suppressed according to eq. 2.78 by being δf_{mn} from resonance. A very clean H_{00} mode can therefore be excited within the cavity. Speckle, wavefront distortions, imperfect beam shaping, etc. are suppressed. It is in this sense that we refer to the cavity as a mode filter.

There are limiting cases in which this mode filtering does not apply. For a near planar situation (i.e., large radii of curvature), g_1, $g_2 \to 1$, so $\delta f_{mn} \to 0$. In this case, the degeneracy is restored, and mode-filtering is lost. For a near-concentric cavity (where the cavity length L differs from $\mathrm{ROC}_1 + \mathrm{ROC}_2$ by only a small amount), g_1, $g_2 \to -1$, so $\delta f_{mn} \to \mathrm{FSR}$. Again, the degeneracy is lost. Some care must therefore be taken in choosing mirror parameters if a cavity is to serve as a mode filter.

As we will be interested primarily in this fundamental Gaussian mode H_{00}, we will also be interested in its spatial size, specifically the waist w_0. For a stable Gaussian mode in the resonator, the curvature of the Gaussian beam $R(z) = z + z_{\mathrm{R}}^2/z$ must match the radius of curvature of the mirrors at the mirror positions. That is,

$$R(z_1) = z_1 + z_{\mathrm{R}}^2/z_1 = -\mathrm{ROC}_1 \tag{2.91a}$$

$$R(z_2) = z_2 + z_{\mathrm{R}}^2/z_2 = +\mathrm{ROC}_2 \tag{2.91b}$$

We can use $L = z_2 - z_1$ to eliminate z_2 from eq. 2.91b, then solve eq. 2.91a for z_1 to eliminate z_1 as well. The radii of curvature ROC_i can then be replaced by their respective

---

[3] This area has not been defined, but an area consideration explains the $\sqrt{2}$ factor in radius

g-factors, $\mathrm{ROC}_i = \frac{L}{1-g_i}$. This leaves a quadratic equation for the Rayleigh range z_{R}, which can be solved. Rearranging the solution using eq. 2.89 to get the the waist w_0, we find

$$w_0 = \frac{L\lambda}{\pi}\sqrt{\frac{g_1 g_2(1-g_1 g_2)}{(g_1+g_2-2g_1 g_2)^2}}. \tag{2.92}$$

Chapter 3

Experimental apparatus

In this chapter we'll describe the experimental setup on which the experiments in this thesis were performed. Details of sub-systems such as the vacuum chamber, the optical layout, and atom source preparation will be outlined.

3.1 Vacuum chamber

To maintain coherence in a quantum measurement, the system must be well isolated from the outside environment. This includes preventing collisions from background gas molecules. For this reason, atomic physics experiments are generally performed in ultrahigh vacuum (UHV). A rare, prehistoric picture depicting our vacuum setup before it was engulfed in optics can be seen in Fig. 3.1.

Our primary vacuum system consists of a vertically-oriented main chamber (Kimball Physics MCF600-SphOct-F2C8), whose top and bottom 2.75" CF flanges each connect to an auxiliary vacuum chamber (Kimball Physics MCF-450-SphCubeE6). Each auxiliary chamber houses one of the science cavity mirrors.

There is a specially-designed collar between the main and lower chambers housing a length ($\sim$ 6") of three layers of mu-metal magnetic shielding and a solenoid. This provides a uniform magnetic field over that region. This section has not yet been used, but could be important for future measurements. It's main result so far, however, has been to provide an undesired magnetic field gradient above it, which must be dealt with.

A small ion pump (2 L/s, Varian 919-0520) is connected to the bottom auxiliary chamber. The main chamber has a larger ion pump (20 L/s, Varian 919-1115). A turbo pump (Varian Turbo-V 81 M) is connected to the main chamber through a gate valve (Varian 9515027, $1\frac{1}{2}$" ID right angle valve), which is closed after baking. A dry scroll pump (Agilent IDP-2) is used between the turbo pump and atmosphere when pumping down from atmosphere, bringing the inlet pressure for the turbo to about 1 mbar.

An ion gauge (Varian UHV-24) and titanium sublimation pump are placed inside the chamber. The titanium sublimation pump (unknown part number, possibly Agilent 916-

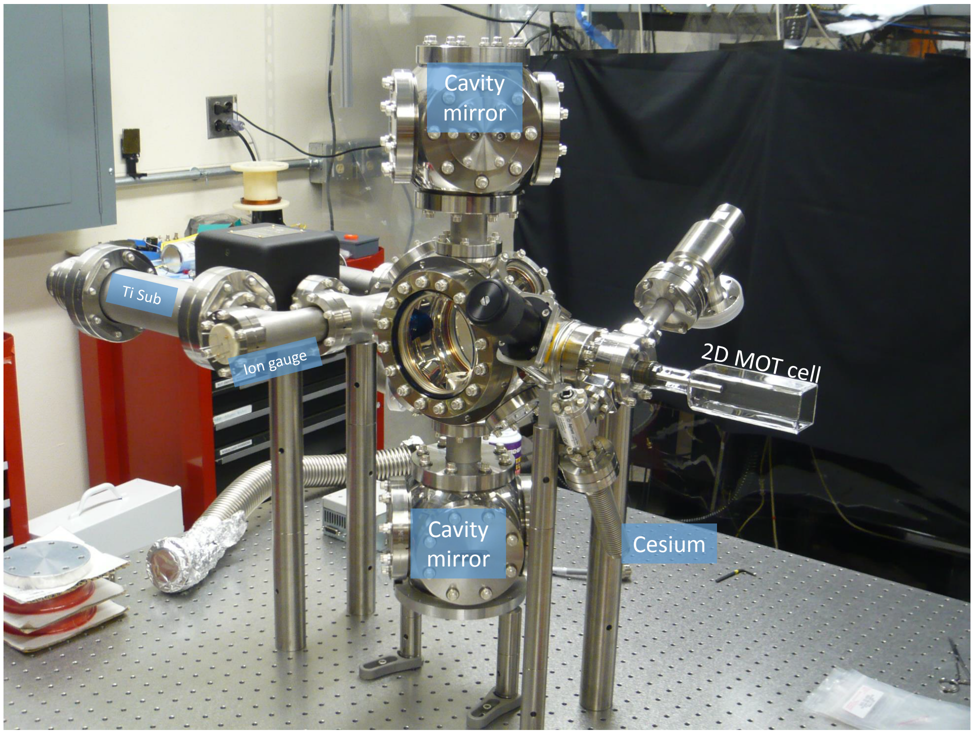

Figure 3.1: The vacuum chamber. The setup has since been surrounded my optics. Components have since been rearranged and added. For example, the visible ion pump (black cube) has been moved to make way for the wobble stick (see Ch. 5). This photo is courtesy of Brian Estey.

0050) can be fired at UHV by sending ~ 40 A of current through titanium-coated wires for ~ 1 minute at a time. This sputters titanium, which acts as a non-evaporative getter.

A differential pumping tube (unknown dimensions) connects the main chamber to a custom glass cell (Precision Glassblowing, 1.5" × 1.5" × 4" long; rotatable CF on $\frac{7}{8}$" tubing). A flexible bellows containing a cesium ampule connects to this cell via a small gate valve. The glass cell is used to load cesium from vapor pressure into a 2-dimensional magneto-optical trap (2D MOT). The differential pumping tube allows for a high cesium vapor pressure in the glass chamber for a high-flux 2D MOT, while maintaining low pressure in the main chamber. A gate valve (VAT mini-UHV gate valve, unknown part number) connecting the 2D MOT cell, and the reactive cesium, to the main chamber can be closed to keep the cesium in UHV when the main chamber is opened to atmosphere.

3.2 The science cavity

The science cavity is a half-symmetric resonator with one flat mirror and one curved mirror (see Fig. 3.2). Both mirrors are mounted on UHV compatible mirror mounts (Newport

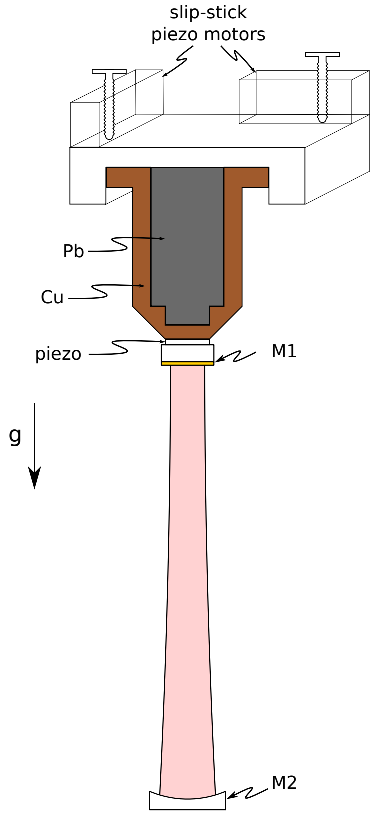

Figure 3.2: Schematic of the science cavity. The bottom mirror mount is also actuated by slip-stick piezo motors (not shown)

8817-6-UHV), whose three positioning screws have 6 mm of travel. Two of the mirror screws are actuated by slip-stick piezo motors (Newport Picomotors) that can be controlled electronically from outside of the vacuum chamber. The cavity mode is oriented along Earth's gravity. The upper mirror is mounted on a copper tube filled with lead to damp mechanical resonances [45], atop a ring piezo (Noliac NAC2123) for length stabilization. Transmission through the cavity is blocked by the lead filling in the current design.

Torr Seal is used as a UHV-compatible epoxy, and has not caused any problems. During bake-out, the slip-stick piezo actuators can slide out, both moving the mirror and preventing further actuation and thus cavity alignment. This shouldn't happen according to part specifications, but it has. We've added Torr Seal to each of the actuators. Even with a some Torr Seal, one of the lower mirror actuators has moved more than expected.

During baking, the mirrors can only get so hot. There is a lubricant inside the actuators that can bind if baked too hot (more information obtainable from Newport). We typically bake up to 100 C, though we have accidentally gone up to 15 C above that at parts of the vacuum chamber for short periods of time.

The mirrors of the science cavity are housed in the upper and lower bulbs of the vacuum chamber. On top of this coarse length imposition, we would like frequencies separated by

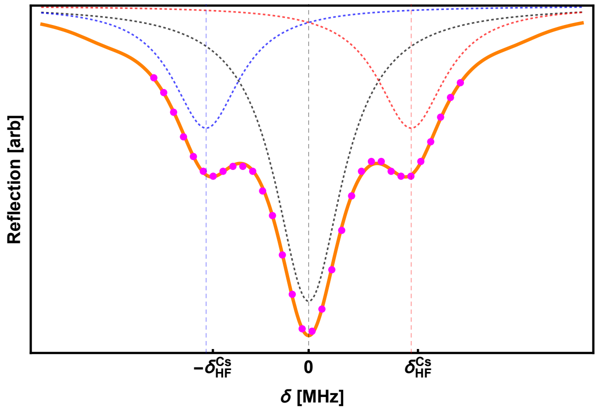

Figure 3.3: Free spectral range measurement. A laser is phase-modulated at the cesium hyperfine frequency $\omega_{\mathrm{HF}}^{\mathrm{Cs}}$. The reflected power is measured (magenta dots) as the cavity length is (and thus, resonance frequencies are) stepped. The data is fitted (shown in orange) to a sum of three Lorentzians with relative heights set by the modulation depth β (see eq. 4.9 Sec. 4.3.2). The central peak is the carrier, on resonance at axial mode q. The peak at negative (positive) cavity detuning is the blue (red) sideband, which has moved up (down) in frequency to be resonant with axial mode $q+23$ ($q-23$) if the cavity resonance frequency is shifted by -(+) $\delta_{\mathrm{offset}}^{\mathrm{HF}}$. Note that the sideband location is not exactly where one might expect from the total lineshape. The constituent carrier, blue and red sideband Lorentzian lineshapes are shown in dotted lines in black, blue and red respectively. Their peak locations are indicated by vertical dashed lines of the same color.

the cesium hyperfine transition ($\omega_{\mathrm{HF}}^{\mathrm{Cs}} =\approx 2\pi\times 9$ GHz) to simultaneously enter the cavity. A ∼9 GHz cavity linewidth however, would demand such low cavity finesse as to no longer be a resonator in any meaningful sense. The solution is to make the cavity free spectral range as close as possible to an integer divisor of the cesium hyperfine frequency $\omega_{\mathrm{HF}}^{\mathrm{Cs}}$.

The cesium hyperfine frequency is a bit less than 23 free spectral ranges. The remaining offset $\delta_{\mathrm{offset}}^{\mathrm{HF}}$ is defined by $\frac{1}{2\pi}\omega_{\mathrm{HF}}^{\mathrm{Cs}} + \delta_{\mathrm{offset}}^{\mathrm{HF}} = 23 \times \mathrm{FSR}$. We measure this offset by phase-modulating a laser at the cesium hyperfine frequency using an EOM, and seeing how far apart the carrier and ±1-order peaks are. The cavity can be locked to another laser (see Sec. 3.3.2) and stepped by known amounts to determine the spacing between these resonance peaks to high accuracy. An example of such a scan is seen in Fig. 3.3.

This procedure determines the cavity/hyperfine offset to be $\delta_{\mathrm{offset}}^{\mathrm{HF}} = 3.80$ MHz. The free spectral range of our cavity is then 399.845(2) MHz. From this measurement, the cavity length is determined with eq. 2.82 to be $L_0 = \frac{c}{2\times\mathrm{FSR}} = 37.4886(2)$ cm. Let $L_{n=23}$ denote the cavity length where 23 free spectral ranges exactly equals the cesium hyperfine frequency (i.e., $\delta_{\mathrm{offset}}^{\mathrm{HF}} = 0$). The mismatch in length $L_{n=23} - L_0$ is only 155 μm! That is, our cavity is 155 μm *short* of fulfilling this condition. We could therefore reduce $\delta_{\mathrm{offset}}^{\mathrm{HF}}$ somewhat by heating the vacuum chamber to thermally expand it. For a thermal expansion coefficient of steel $\alpha_T^{\mathrm{steel}} = 13 \times 10^{-6}$/C, the FSR changes by 5.2 kHz/C. The hyperfine offset frequency

$\delta^{\text{HF}}_{\text{offset}}$ changes by 23 times that, or 120 kHz/C. While we have not yet tried this (we'll see in Ch. 4 that setting $\delta^{\text{HF}}_{\text{offset}} = 0$ may not be desirable), being able to change $\delta^{\text{HF}}_{\text{offset}}$ by a several hundred kHz to a few MHz with some heating tape could prove to be useful in the future.

This excellent positioning is, frankly, lucky as there is no mechanism to change the in-vacuum mirror spacing from outside of the vacuum (besides something extreme like heating the chamber). The original intention of the experiment was to use Bragg diffraction, which does not have such a "FSR-matching" condition. The Raman FSR-matching condition was a nice feature to have, so the earlier experimenters aimed for it, but with large uncertainty on the positioning (since it wasn't critical to Bragg). After all the vacuum assembly and bake, we got sufficiently lucky that we can drive Raman transitions. This length is apparently reasonably robust, since the chamber has been reopened to atmospheric pressure, and baked/pumped down twice since then to put in source masses (see Chapter 5).

The mirror reflectivity was chosen as a compromise between bandwidth and optical power enhancement. High reflectivity mirrors would give a large cavity finesse, and thus high optical intensities. However, this would also increase the frequency selectivity of the cavity, decreasing its linewidth. Over the course of an interferometer sequence, the atoms experience a few MHz span of Doppler shifts ($\approx$23 kHz per ms of free fall time). To drive Raman transitions within the cavity throughout the atomic trajectory, these frequencies must fit within the cavity.

The top mirror (M1) is a 1/2" diameter gold-coated mirror. The mirror was chosen to be small to reduce its mass, giving a higher resonance frequency for its driving piezoelectric transducer (PZT). As a metal mirror, its reflectivity is roughly constant across wavelengths. The intensity reflectivity R_1 is spec'd to be ≈ 0.98. The field reflectivity, or Fresnel coefficient, is then $r_1 = \sqrt{R_1} = 0.99$. As a flat mirror, its nominal radius of curvature is infinity.

The bottom mirror (M2) is a 1" diameter curved dielectric mirror with a 10 m radius of curvature, with a wavelength-dependent reflectivity centered around 850 nm. Cavity parameters that are independent of wavelength are summarized in Table 3.1. The measured parameters and component specifications show good mutual agreement between each other (many of these quantities are cross-linked).

The reflectivity of the bottom, curved mirror at wavelength λ can be inferred by measuring the linewidth of the cavity for that wavelength (if we take $R_1 = 0.980$ as a given). We infer a reflectivity of $R_2 = 0.973$ at both $\lambda = 852$ nm and $\lambda = 866$ nm from such a measured linewidth. Wavelength-dependent cavity parameters are summarized in Table 3.2 for the wavelengths used in the experiment (852 nm, 780 nm and 866 nm).

The cavity parameters result in a 718 μm waist at 852 nm, the primary wavelength we use to interact with the atoms. The divergence is small, as the Rayleigh range z_R is large (1.9 m) compared to the cavity length ($\sim$37.5 cm). The beam radius is therefore approximately constant along the cavity length. For concreteness, from the flat mirror to the curved one, the beam has expanded from its 718 μm waist only to a spot size of 732 μm.

Table 3.1: Science cavity parameters that are (to good approximation) wavelength-independent.

Quantity	**Value**
FSR	399.845(2) MHz
Length	37.4886(2) cm
flat mirror reflectivity R_1	0.98
curved mirror radius of curvature	10 m
δf_{nm}	25.1 MHz
z_R	1.90 m

Table 3.2: Wavelength-dependent science cavity parameters for wavelengths used in the experiment.

λ [nm]	**w_0 [μm]**	**γ_{FWHM} [MHz]**	**R_2**	**Finesse $\mathcal{F}$**	**Optical gain $\mathcal{G}$**
780	687	12(1)	0.845	33	2.5
852	718	3.03(2)	0.973	132	36.1
866	724	3.03(2)	0.973	132	36.1

3.3 Laser system

A number of lasers are required to perform cooling and manipulations of the atoms. We will first look at the cooling lasers, then discuss the lasers required to perform interferometry. To show the optical layouts, we will borrow two sets of optical component drawings: one is from Brian Estey's PhD thesis [27], and the other is ComponentLibrary [46]. A table showing the meaning of the symbols used can be seen in Fig. 3.4.

3.3.1 Trap and cooling lasers

Alkali atoms have historically been used in atomic physics experiments because their single valence electron gives a comparatively simple level structure. The levels relevant for laser-cooling cesium are shown in Fig. 3.5.

The ground $6^2S_{1/2}$ state of cesium is split into two hyperfine levels, $|F=3\rangle$ and $|F=4\rangle$. The energy splitting of these states, $h\times$ (9 192 631 770 Hz), is currently the SI definition of the second, and therefore exact.

The transition used to laser-cool cesium is the D2 line ($^2S_{1/2} \to {}^2P_{3/2}$). The transition from $\left|{}^2S_{1/2}, F=4\right\rangle$ to $\left|{}^2P_{3/2}, F'=5\right\rangle$ is closed, and is the primary cycling transition (we denote hyperfine levels of the excited $^2P_{3/2}$ manifold by F', and from here on will drop the explicit $^2S_{1/2}$ and $^2P_{3/2}$ from our state notation). We call light exciting the $|F=4\rangle \to$

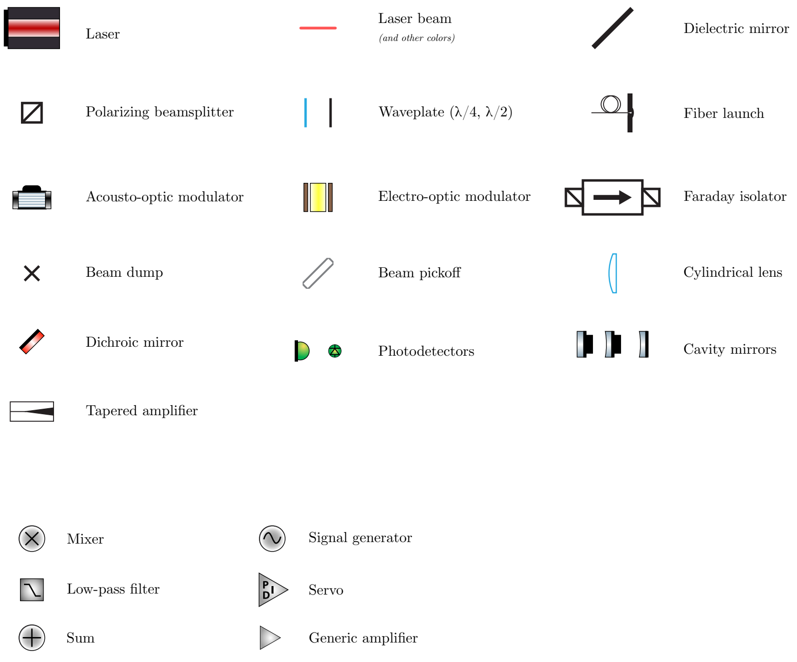

Figure 3.4: Optical and electronic components used in subsequent diagrams.

$|F' = 5\rangle$ transition *trap light*. Due to off resonant excitation of the $|F = 4\rangle \rightarrow |F' = 4\rangle$ transition however, for about 1 in every $\sim$ few hundred - 1000 photons scattered, the atom decays to the $|F = 3\rangle$ ground state. *Repump light* to bring such atoms back into the cooling cycle is therefore required. The repump light excites the $|F = 3\rangle \rightarrow |F' = 4\rangle$ transition. See Sec. 3.4 for more details on laser cooling and the atom source.

To cool the atoms we need both trap and repump light. The frequency stabilization scheme for these lasers is shown in Fig. 3.6, and discussed below.

The lock chain

A spectroscopy setup belonging to another experiment in our group [27] provides bedrock for stabilizing the laser frequencies and cavity lengths in our experiment. Light from an external cavity diode laser (ECDL) is frequency-stabilized ("locked") to the $|F = 3\rangle \rightarrow |F' = 2\rangle$ transition frequency via modulation transfer spectroscopy. Acousto-optic modulators (AOMs) shift that frequency by 352.5 MHz, delivering 300 μW of light to our experiment which is resonant with the $|F = 3\rangle \rightarrow |F' = 4\rangle$ transition frequency of the ^{133}Cs D2 line.

We generate trap and repump light from a *trap laser* and *reference laser*, respectively. The trap and reference lasers are both distributed feedback (DFB) diode lasers (Eagleyard EYP-DFB-0852-00150-1500-TOC03-0005). The reference laser is injection locked by this incoming 300 μW spectroscopy beam. All other laser and cavity locks in our experiment derive from this reference laser (hence the name). In injection locking [47,48], a small amount of seed power (in this case, the spectroscopy beam) is coupled into a lasing medium (the

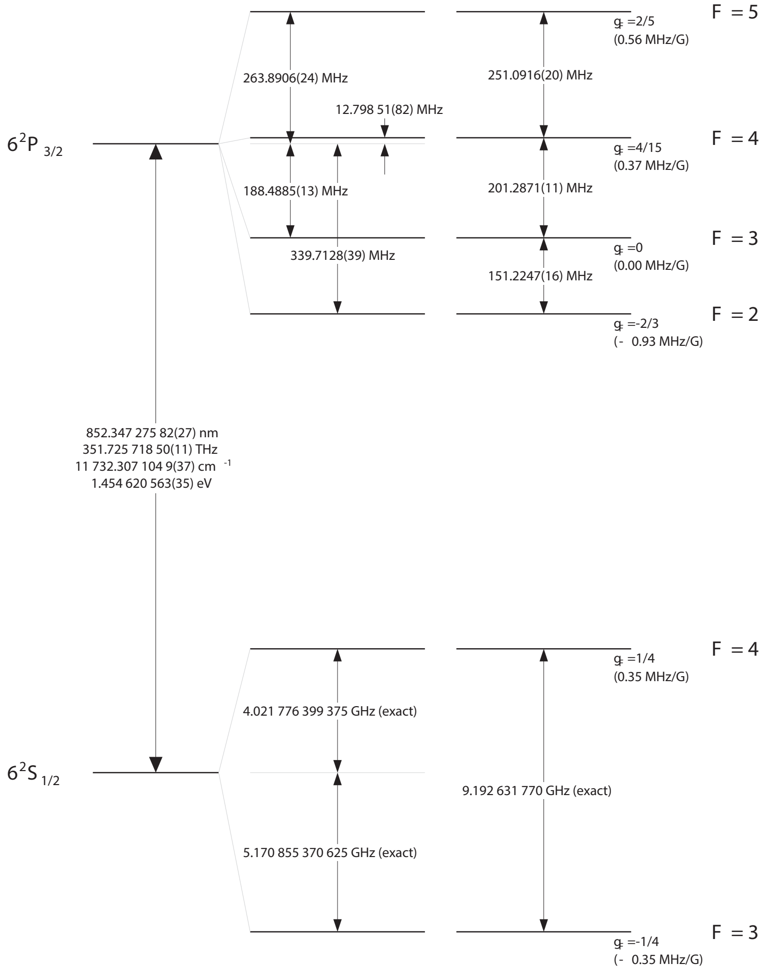

Figure 3.5: Hyperfine structure of the D2 line in cesium (taken from Ref. [36]).

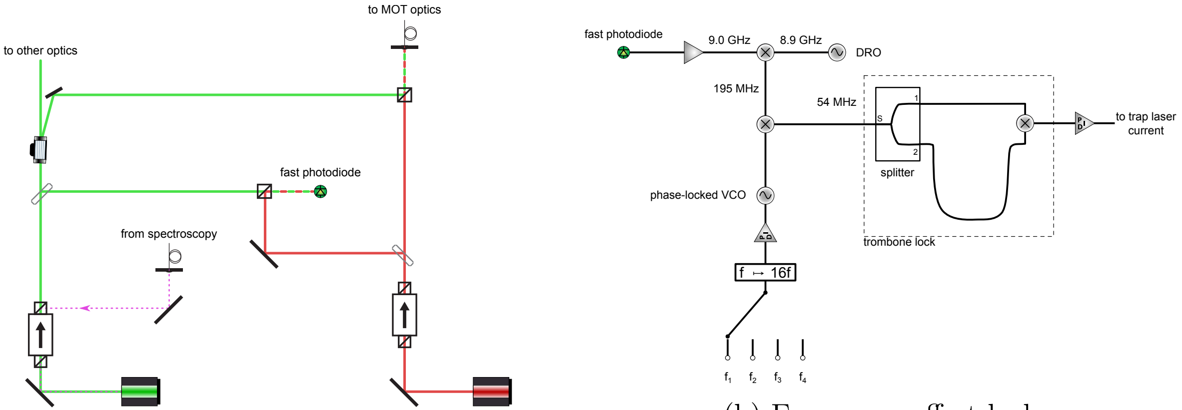

(a) MOT beam frequency locking

(b) Frequency offset lock

Figure 3.6: Locking scheme

reference laser). If the free-running frequency is close enough to the seed frequency, the lasing medium locks to that seed frequency. This condition is achieved by tuning the temperature and current (which modulates the carrier density, hence the effective path length of the semiconductor cavity) of our diode laser. The injection lock current range is about 1 mA. An injection lock allows use of a comparatively simpler Fabry-Perot diode, rather than an ECDL.

The trap laser is frequency stabilized to the D2 line with a frequency offset lock. A small amount of light (1.5 mW each) from both the reference laser and the trap laser are combined on a fast photodiode. For the trap laser to be resonant with the $|F = 4\rangle \rightarrow |F' = 5\rangle$ transition, their beatnote should be 8 941 MHz (see Fig. 3.5). An extra 80 MHz AOM downstream in the trap laser beam path means that we actually want it to be 9 021 MHz. The signal from the fast photodiode is amplified, and mixed with a dielectric resonator oscillator (DRO) at 8 826 MHz down to 195 MHz (See Fig. 3.6b). The 195 MHz signal is then mixed with a phase locked voltage-controlled oscillator (VCO) at 141 MHz.

Elsewhere, the VCO is divided by 16, and phase locked to one of 4 frequencies f_i. This allows the trap laser to lock to 4 different frequencies for different steps of the sequence (trapping, molasses, blowaway and imaging; see Sec. 3.4). As a result, the frequencies in the previous paragraph change slightly for these 4 purposes; the values above are for exact resonance of the trap light with the $|F = 4\rangle \rightarrow |F' = 5\rangle$ transition.

The resulting signal at 54 MHz then enters a “trombone lock”, where the lock condition is set by the cable path length. The signal is split (180° power splitter) and recombined. Upon recombining, the phase difference $\Delta\phi_{\mathrm{RT}}$ between the two arms for a signal at frequency f_{rf} is

$$\Delta\phi_{\mathrm{RT}} = k_{\mathrm{rf}} L = \frac{2\pi L}{v_p/f_{\mathrm{rf}}}$$

where $L \approx 1$ m is the cable path length and $v_p \approx \frac{2}{3}c$ is the speed of signal propagation in the cable. For the frequencies that give an odd multiple of $\frac{\pi}{2}$, $\Delta\phi_{\mathrm{RT}} = (2n+1)\frac{\pi}{2}$, the output of the final mixer is zero, which gives the lockpoint. For other frequencies, an error signal is generated. A proportional-integral (PI) servo then feeds back to the trap laser current to stabilize it to the correct frequency.

Power from the trap and repump lasers goes into an optical fiber to be delivered to a tapered amplifier chip (TA; m2k Laser, TA-0850-1500-CM). The optical fiber provides a clean mode and short path length for injection into the TA. About 20 mW (1 mW) of trap (repump) light is delivered to the TA, which amplifies the input to 700 mW at 2.12 A of pump current. The TA output then passes through optics for delivery to the atoms (2D MOT, 3D MOT, optical pumping). This is shown in Fig. 3.7.

Blowaway beams

Further downstream, some of the trap and repump light are each diverted to form blowaway beams for the $|F = 4\rangle$ and $|F = 3\rangle$ states, respectively. These beams are each resonant for

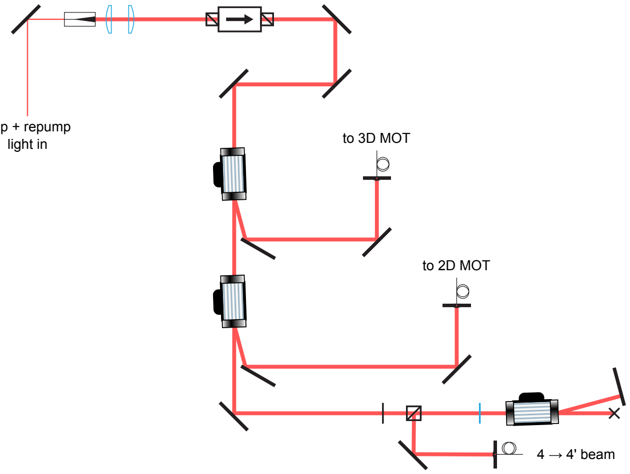

Figure 3.7: Generation and delivery of MOT light.

atoms in only one hyperfine state. This is useful, for example, in state preparation, where atoms in the wrong state can be blown away from the desired atom sample. They are also used in final readout, so the two hyperfine states can be spatially separated for imaging.

The trap light should be resonant with the $|F = 4\rangle \rightarrow |F' = 5\rangle$ transition. This $F = 4$ *blowaway beam* is controlled with an AOM.

The $F = 3$ *blowaway beam* is slightly more complicated. Selection rules restrict $\Delta F \in \{-1, 0, 1\}$ in scattering and decay events. Thus, if the excited manifold is populated in the $|F' = 4\rangle$ or $|F' = 3\rangle$ states, a decay to $|F = 4\rangle$ could occur, ruining the state-labeling and closed blowaway cycling. Thus, the $F = 3$ blowaway beam should be resonant with the $|F = 3\rangle \rightarrow |F' = 2\rangle$ transition. The beam is double passed through an AOM run at 176.25 MHz, giving the appropriate frequency shift.

There are 2 fewer Zeeman sub-levels in the $F' = 2$ manifold than in $F = 3$. There thus exist two dark states in the $F = 3$ manifold that comprise of linear superpositions of the constituent Zeeman states, depending on the polarization of the scattering light and the magnetic field setting the quantization axis. In practice, this just means we sometimes need to fiddle with the magnetic field if an $F = 3$ blowaway pulse doesn't seem to be working. The B field just needs to be such that the $F = 3$ atoms scatter enough photons to remove them from the sample cloud before falling into one of these dark states. This is achievable, but is less robust than the $F = 4$ blowaway.

The two blowaway beams are overlapped and coupled into a fiber port. The fiber is a 50/50 fiber splitter, allowing for two blowaway launches. This is useful, for example, because the atoms' trajectories can span about 2 cm, larger than the blowaway beam size.

3.3.2 Interferometry lasers and lock schemes

To perform interferometry, the laser pulses must be resonant with the cavity. However, the interferometry laser (the "science laser") can't be on at all times because it would introduce large light shifts during the free evolution time, and cause decoherence via single-photon scattering. As a result, we use a far off-resonant *tracer laser* to lock the cavity length. The lock scheme for keeping the science laser resonant with the science cavity is shown in Fig. 3.8

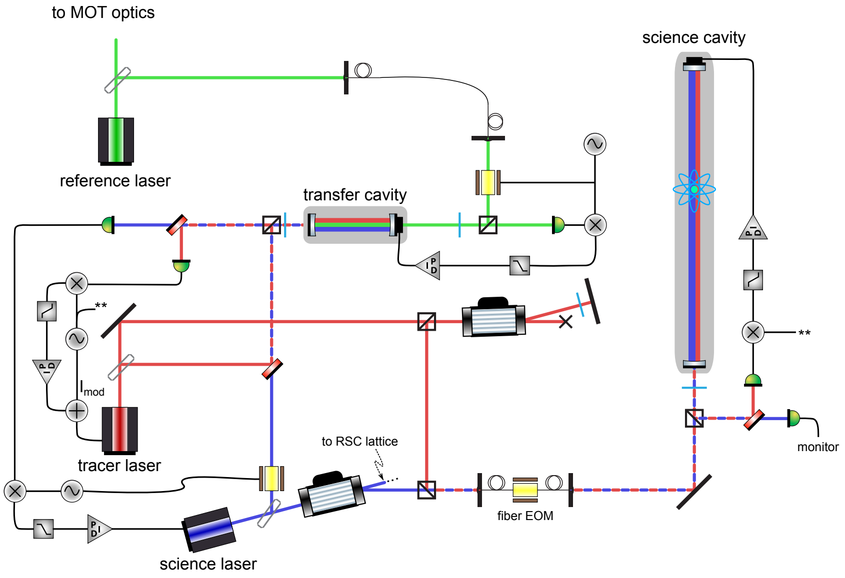

Figure 3.8: Science cavity locking scheme.

The science laser is an external cavity diode laser (ECDL; Toptica DL100 Pro), and the tracer laser is a DFB at 780 nm wavelength (Eagleyard, EYP-DFB-0780-00080-1500-TOC03-0000). A "transfer" cavity is used to transfer the long term stability of the reference laser onto the science and tracer lasers. The cavity is locked to the reference laser using a Pound-Drever-Hall (PDH) scheme [49]. The science and tracer lasers are each locked to the cavity, also via PDH. The current of the tracer laser is modulated to provide the phase modulation for its PDH lock, while the science laser passes through an EOM. The free spectral range (FSR) of the transfer cavity is ∼5 GHz, meaning the each of these laser wavelengths can be chosen only in increments of ∼5 GHz.

The transfer cavity spacer is made of Invar, a nickel-iron alloy with a low coefficient of thermal expansion ($\approx 1 \times 10^{-6}$ K^{-1}). This gives good enough length stability that it is easy to lock the cavity to the same free spectral range using the reference laser, despite several °C drifts in the lab temperature. This means the tracer and science lasers can easily be locked to the same frequency every day, rather than hunting for said frequency among a forest of 5 GHz separated lockpoints. This is particularly important for the science laser, whose single-photon detuning from the D2 line plays a critical role.

The science cavity is locked to the tracer laser. The same current modulation used for the tracer laser PDH lock to the transfer cavity also provides a PDH error signal for the science cavity to be locked to the tracer laser. Co-locking the tracer and science lasers to the transfer cavity ensures that $L_{\mathrm{txr}} = m\frac{\lambda_{\mathrm{sci}}}{2} = n\frac{\lambda_{\mathrm{trc}}}{2}$, where $L_{\mathrm{txr}} = 3.3$ cm is the length of the transfer cavity, $\lambda_{\mathrm{sci}} \approx 852$ nm is the science laser wavelength, and $\lambda_{\mathrm{trc}} \approx 780$ nm is the tracer laser wavelength. However, this does not provide co-locking on the science cavity, which has length $L_{\mathrm{sci}} \approx 37.5$ cm.

To co-lock both lasers on both cavities, the tracer laser passes through a high-bandwidth AOM (Brimrose TEF300-200-780). For fixed alignment we achieve about a 60 MHz range over which the diffracted power is approximately constant. This is less than one FSR of the science cavity (399.8 MHz), so it doesn't guarantee a co-locking point. However, choosing a different FSR of the transfer cavity for locking the tracer laser always enables us in practice find a point within the 60 MHz tunability range. A more convenient co-locking method has been implemented to add a third laser at 866 nm into the cavity, which is discussed in Chapter 8.

3.4 Atom source and preparation

As with many atomic physics experiments, ours runs in a shot-based manner. A sample of atoms is trapped, cooled, and used to perform interferometry. This sequence is repeated to make measurements. A shot of the experiment begins by loading a 3-dimensional magneto-optical trap (3D MOT) from a 2D MOT.

Doppler and sub-Doppler cooling

Without going into too much detail (see, e.g., Refs. [50–55] for information on laser cooling), laser cooling reduces the phase space density of a gas, compressing its position and momentum distributions. This is accomplished by getting atoms to preferentially scatter photons. We want atoms with small velocities, at the trap center, to scatter few photons. We want atoms with large velocity and/or large displacement from the trap center to scatter more photons. In this way, atoms will scatter their way to low velocities at positions close to the trap center.

Achieving compression in momentum space utilizes the Doppler shift. Pairs of counter-propagating beams are red-detuned from an atomic transition. If an atom has a large velocity in one direction, it will see that beam Doppler-shifted closer to resonance. It thus scatters more photons from that beam (emitting into random directions), reducing its momentum in that direction.

Position compression uses magnetic fields. An anti-Helmholz coil configuration generates a quadrupole field, giving zero field at the center of the geometry, and increasing in magnitude in all directions. If magnetic fields shift the atomic energy levels in the appropriate directions, then there will be increased scattering of photons for atoms further away from the trap center. This causes atoms to pile up in the center of the trap.

The 2D MOT is loaded in the glass cell of the vacuum chamber from cesium background vapor. To cover more area on the rectangular glass cell, the 2D MOT beams are large, elliptical beams formed with large cylindrical lenses. The atoms are cooled in the directions perpendicular to the path to the main chamber. This gives a transversally cooled beam of cesium atoms pointed through the differential pumping tube towards the 3D MOT.

The 3D MOT forms at the center of the chamber. Counter-propagating beams in all three dimensions provide cooling. While loading the MOT, the detuning of the beams is set to -2.2Γ, where $\Gamma \approx 2\pi \times 5.2$ MHz is the natural linewidth of the cesium D2 transition. After the MOT is loaded, the temperature of the atomic cloud is 110 μK. Next, polarization gradient cooling (PGC) is performed (also known as optical molasses or Sisyphus cooling; see Refs. [56,57]). The intensity is lowered and the detuning is further moved to -6.3Γ to reduce the scattering rate, and the magnetic field is set to zero. PGC reduces the temperature to 7 μK.

Magnetic fields are provided by current-controlled coils. The anti-Helmholtz coils generating the MOT fields comprise of 64 circular loops (wound into 8 rows of 8 wires), mounted on either side of the vacuum chamber. The wire used is $\frac{1}{8}$" × $\frac{1}{8}$" square hollow wire to allow for water cooling at high currents (which we typically do not need to use, as we only apply 8 A of current). The inner diameter of the loops is 6" (and the outer diameter is thus 8").

Bias fields are provided by auxiliary sets of coils. The $\hat{z}$ ($\hat{x}$) directions are provided by 40 square loops of wire with dimensions 20" × 20" (20" × 11"). These two sets of 40 loops are made by using a single pass of ribbon cable, with appropriate connection of the cable ends. The $\hat{y}$ direction coils are an unknown number of circular loops of wire with radius ≈ 6", and mounted just outside of, and concentric with, the MOT coils. These auxiliary coils are used, for example, to cancel out Earth's magnetic field, provide $\boldsymbol{B} = 0$ for PGC, and to provide a bias field in the vertical direction for interferometry. Each direction of the bias coils is in a Helmholtz arrangement to provide a spatially uniform $\boldsymbol{B}$ field.

Raman sideband cooling

The atoms are loaded into the cavity mode by adiabatically ramping on the science laser with the PGC beams still on. Repump light into the TA is extinguished so that the trap light pumps the atoms into $F = 3$. All MOT/PGC beams are then extinguished. Once the atoms are loaded into the cavity, two additional beams perpendicular to the cavity mode form a 3D lattice. These two running waves, approximately perpendicular to each other, also derive from the science laser and come from a single-pass bowtie beam path. Raman sideband cooling [58–60] is then performed. Fig. 3.9 shows a depiction of the Raman sideband cooling (RSC) configuration.

Atoms in the lattice are (to good approximation) in a harmonic oscillator, with energy levels given by

$$E_n = \left(n + \frac{1}{2}\right) \hbar\omega_{\text{trap}},$$

where ω_{trap} is the trap frequency. The idea behind Raman sideband cooling is to remove vibrational energy quanta from the atoms. A magnetic field is applied to make the Zeeman splitting ΔE_{Z} degenerate with the harmonic oscillator spacing. The Zeeman splitting for a state $|F, m_{\text{F}}\rangle$ in a weak magnetic field B is given by

$$\Delta E_{|F,m_{\text{F}}\rangle} = \mu_B \, g_F \, m_F \, B := m_{\text{F}} \, \Delta E_Z(B)$$

where μ_B is the Bohr magneton, g_F is the hyperfine Landé g factor, and we have defined $\Delta E_Z(B) = \mu_B \, g_F \, B$, i.e., the shift for the $m_{\text{F}} = +1$ level.

To make the harmonic oscillator and Zeeman splittings degenerate then, we require

$$\begin{gathered} \Delta E_Z = \Delta E_n \\ \mu_B \, g_F \, B = \hbar\omega_{\text{trap}} \end{gathered}$$

A small amount (in our case, 8 μW) of σ^+-polarized light resonant with the $|F = 3\rangle \rightarrow |F' = 2\rangle$ transition pumps atoms into the excited manifold. The σ^+ polarization enforces the selection rule $\Delta m_{\text{F}} = +1$, so this light pumps atoms towards $|F = 3, m_{\text{F}} = 2, 3\rangle$, which are dark states to this light. The beams forming the lattice drive degenerate Raman transitions between states $|m_{\text{F}} + 1, n + 1\rangle \leftrightarrow |m_{\text{F}}, n\rangle$, indicated by the curved arrows in Fig. 3.9.

For an atom starting in the dark state $|m_{\text{F}} = 2, n\rangle$, these Raman transitions can drive the atom to $|m_{\text{F}} = 1, n - 1\rangle$. From there, it can scatter a σ^+ photon, and decay back to the $F = 3$ ground manifold. In the tightly-bound Lamb-Dicke regime, the vibrational spacing E_n is much larger than the kinetic energy associated with scattering these two photons[1], so the vibrational quantum number can't change during the decay. An atom that decays to $F = 2$ thus atom loses one vibrational quantum over the round trip! This cycle is how the cooling proceeds.

Atoms pile up in the states that are still fully dark to the σ^+ light, even in the presence of the lattice Raman beams. These levels are $|m_{\text{F}} = 2, n = 0\rangle$ and $|m_{\text{F}} = 3, n = 0, 1\rangle$. An even smaller amount of π-polarized light introduces two of these states into the fold, leaving only $|m_{\text{F}} = 3, n = 0\rangle$ as the only dark state. In practice, this π-polarized light is produced by a small misalignment of the quarter-waveplate generating the σ^+ polarization. An additional beam resonant with the $|F = 4\rangle \rightarrow |F' = 4\rangle$ transition is also applied to address atoms that were not initially pumped into $F = 3$, or that scatter lattice beam photons.

As this process takes place, the atoms pile up in the vibrational ground state of the lattice, cooling the cloud. After 14 ms of Raman sideband cooling, the lattice is adiabatically released. This leaves the atoms in the stretched Zeeman state $|F = 3, m_{\text{F}} = 3\rangle$, and reduces the cloud temperature to 300 nK.

---

[1] That is, $E_n \gg \frac{\hbar^2 \boldsymbol{q}^2}{2m}$, where $\boldsymbol{q} = |\boldsymbol{k}_{\text{absorb}} - k_{\text{emit}}|$. For cesium on the D2 line, the maximum $q = 2k$ corresponds to a recoil energy of $4E_{\text{rec}} = h \times 8.3$ kHz. Our RSC trap frequency is about 30 kHz.

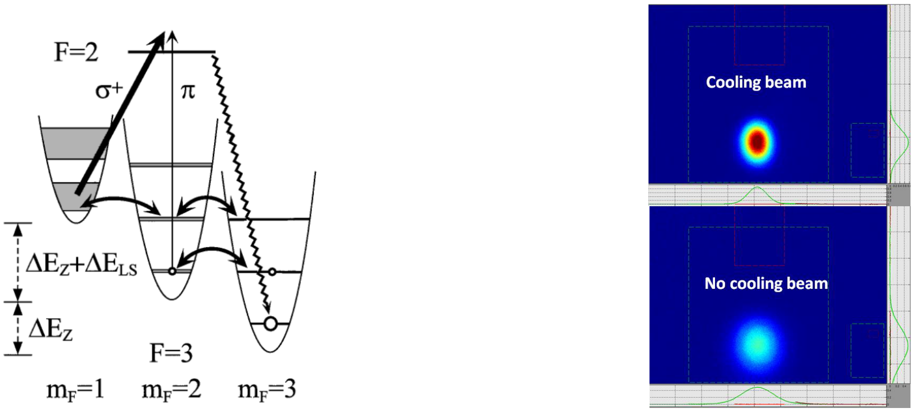

Figure 3.9: Raman sideband cooling. Left: Energy level diagram with relevant laser-driven transitions shown (reused with permission from Ref. [59]). See main text for description. Right: Atomic state preparation in our experiment with (above) and without (below) the RSC beam.

Microwave adiabatic passage

To efficiently transfer the atoms from the stretched Zeeman state to the magnetically insensitive $m_\mathrm{F} = 0$ state, adiabatic rapid passage with microwaves is used. Fig. 3.10 demonstrates this procedure. A quantitative description of adiabatic rapid passage is given in Ch 7. Microwaves are applied to the atoms using a horn waveguide.

A microwave pulse begins with a frequency $\omega_\mathrm{HF} + 5.5\,\Delta E_\mathrm{Z}/\hbar$. The frequency is then swept slowly (relative to the Rabi frequency) to $\omega_\mathrm{HF} + 0.5\Delta E_\mathrm{Z}/\hbar$. The atoms are efficiently transferred through the path shown by the solid arrows in Fig. 3.10: $|F = 3, m_\mathrm{F} = 3\rangle \rightarrow |F = 4, m_\mathrm{F} = 2\rangle \rightarrow |F = 3, m_\mathrm{F} = 1\rangle \rightarrow |F = 4, m_\mathrm{F} = 0\rangle$. The start and end values of the frequency ramp are chosen so that the $|F = 3, m_\mathrm{F} = 3\rangle \rightarrow |F = 4, m_\mathrm{F} = 3, 4\rangle$ transitions are not driven at the beginning of the pulse, and the $|F = 4, m_\mathrm{F} = 0\rangle \rightarrow |F = 3, m_\mathrm{F} = 0, -1\rangle$ transitions are not driven at the end of the pulse.

Selection rules dictate that $\Delta m_\mathrm{F} \in \{-1, 0, +1\}$. $\Delta m_\mathrm{F} = 0$ transitions are suppressed by setting the magnetic field in the experiment (and thus the atom's quantization axis) such that the polarization of microwave B field can't drive them (for example, the $|F = 4, m_\mathrm{F} = 2\rangle \rightarrow |F = 3, m_\mathrm{F} = 2\rangle$ at microwave frequency $\omega_\mathrm{HF} + 4\,\Delta E_\mathrm{Z}/\hbar$). After these three adiabatic passages, atoms remaining in the $F = 3$ state are blown away. A final (standard, not adiabatic passage) microwave pulse resonant with the clock transition drives the atoms from $|F = 4, m_\mathrm{F} = 0\rangle$ to $|F = 3, m_\mathrm{F} = 0\rangle$. Leftover atoms in $F = 4$ are blown away.

After these microwave manipulations, we have a 300 nK cloud of freely-falling atoms in the $|F = 3, m_\mathrm{F} = 0\rangle$ state.

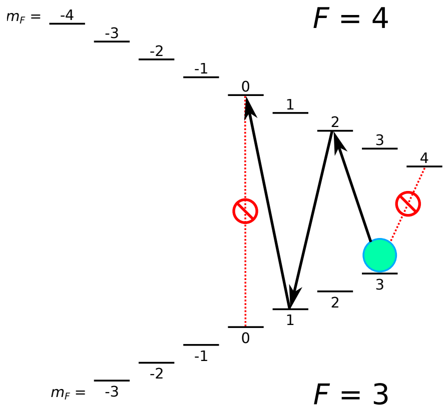

Figure 3.10: Microwave transfer to the magnetically insensitive state.

Vertical launch

The atoms are then launched upwards to provide time of flight to perform interferometry. This is done using a Bloch oscillations in a frequency chirped optical lattice (see Sec. 8.4 for more details on Bloch oscillations). Two tones are sent into an AOM, generating two optical frequencies $\omega \pm \delta$ (see Fig. 3.11). When these two beams hit the cavity (symmetrically centered), their sum can be written as

$$\begin{aligned}\mathbf{E} = \boldsymbol{E}_0 \Bigg(& \overset{(1)}{\sin\left[(\omega-\delta)(z-t)\right]} + \overset{(2)}{\sin\left[(\omega+\delta)(z-t)\right]} + \overset{(3)}{\sin\left[(\omega-\delta)(z+t)\right]} + \overset{(4)}{\sin\left[(\omega+\delta)(z+t)\right]} \Bigg) \\ &= 4\boldsymbol{E}_0 \left(\cos(\omega t)\sin(\omega z)\cos(\delta\cdot t)\cos(\delta\cdot x) - \sin(\omega t)\sin(\omega z)\cos(\delta\cdot t)\sin(\delta\cdot x)\right) \\ &\approx 4\boldsymbol{E}_0 \cos(\omega t)\sin(\omega z)\cos(\delta t) \qquad (3.1)\end{aligned}$$

where we've taken $c = 1$ for simplicity such that $\omega = k$, and in the last line used that $\delta\cdot z \sim 10^{-4}$ for this experiment ($\delta \sim 2\pi \times 100$ kHz, $z/c \sim 10^{-10}$ s), such that $\cos(\delta\cdot z) \approx 1$ and $\sin(\delta\cdot z) \approx 0$. In the first line, terms (1) and (2) represent the upward-running waves at frequencies $\omega - \delta$ and $\omega + \delta$, respectively. Terms (3) and (4) are the downward-running waves. Doing some trig sum/product rule rearrangement on eq. 3.1 and re-introducing c gives

$$\begin{aligned}\boldsymbol{E} = 4\boldsymbol{E}_0 \cos(\omega t)\overset{(i)}{\sin}(kz - \delta t) + 4\boldsymbol{E}_0 \cos(\omega t)\overset{(ii)}{\sin}(kz + \delta\cdot t) \qquad (3.2) \\ - 4\boldsymbol{E}_0 \cos(\omega t)\overset{(iii)}{\sin}(kz)\cos(\delta\cdot t)\end{aligned}$$

The terms in eq. 3.2 represent (*i*) an upward running lattice, (*ii*) a downward running lattice, and (*iii*) a stationary lattice with time-varying amplitude, respectively.

When the launch chirp starts, the atoms have been falling for about 10 ms. The laser field from Fig. 3.11 is adiabatically turned on in 400 μs. The atoms falling at velocity v see

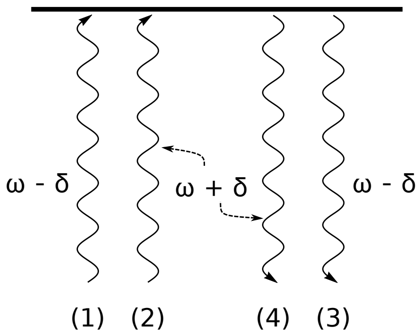

Figure 3.11: Laser field configuration in the cavity for the atomic launch. Beam labels correspond to eq. 3.1

beam j Doppler shifted by $\delta_{\mathrm{Dopp}} = \boldsymbol{k}_j \cdot \boldsymbol{v}$. For appropriately chosen $\delta = \frac{\delta_{\mathrm{Dopp}}}{2}$, the atoms are loaded into the downward running lattice (which is stationary in the atom's frame). The frequency δ is then ramped to zero, where all three terms in eq. 3.2 are degenerate, giving a simple standing wave in the lab frame.

The frequency ramp continues through zero, but this degeneracy causes a problem. For large enough δ, the atoms can be loaded into one lattice (say, the downward-running one), and pretty much ignore the other lattices. More technically, the atoms undergo Bloch oscillations in the ground band of one lattice, but Landau-Zener tunneling in a higher band of the other lattices. For more details on Bloch oscillations, see Sec. 8.4. However, near zero velocity this assumption doesn't hold. The result of ramping through zero velocity then, is that an approximately equal number of atoms are launched downwards, as are launched upwards, while another class of atoms remain trapped in the stationary, amplitude-modulated lattice. An image of the atomic cloud just after the launch, shown in Fig. 3.12, clearly shows these populations.

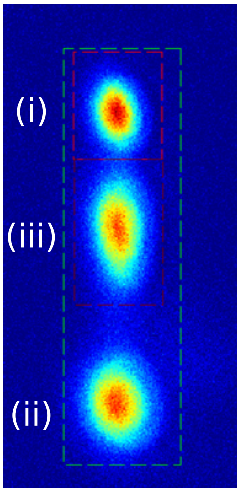

Figure 3.12: Atoms after the launch. Populations trapped in each of the lattices described in eq. 3.2 are visible.

We haven't found a good way to avoid the atom number loss associated with crossing zero velocity. It's possible that something like an adiabatic rapid passage Bragg pulse could allow a more efficient transition across zero velocity. Up to this point however, we just accept the hit in atom number.

By reversing the direction of the frequency chirp after the atoms' time of flight, they can be loaded into a downward moving optical lattice before being decelerated to rest. This catch provides spatial selection of the center of the cloud (atoms that have not expanded out of the beam), and slows the atoms down for improved imaging.

Imaging

To image the atoms after a sequence is performed, the 3D MOT beams are turned on. The atoms scatter photons, which are collected by a charge-coupled device (CCD) camera fitted with a lens tube. A background image is subsequently taken after the atoms have fallen away. The images are subtracted to give a picture of the atom cloud(s).

For interferometry detection, the $F = 4$ blowaway beam is flashed for about 10 μs to spatially separate the atoms in the $F = 4$ state from those in the $F = 3$ state. This allows for normalized detection via the population ratio.

Frankly, our imaging system is pretty crude. At low atom numbers $\lesssim$ a couple 10^5, imaging noise dominates. The MOT beams used for imaging give substantial unwanted reflections into the camera. The background subtraction removes most of this, but fluctuations between images contribute noise. That said, access to a two-dimensional image of the cloud is extremely helpful when setting things up and diagnosing what might be going wrong.

A broadly useful, solid bang-for-buck/time improvement to the experiment could be an upgraded imaging system. This could be a light sheet plus photomultiplier tube (PMT) that the atoms fall through [27], or even just a more careful and optimized fluorescence collection scheme. This could involve a CCD camera (detection via spatial resolution) or photodiode (detection via time resolution) and/or additional specialized imaging beam(s).

3.5 Additional details

3.5.1 Experimental control

Our experiment is controlled by *"A distributed, graphical user interface based, computer control system for atomic physics experiments"* developed at MIT [61]. It consists of a client-server architecture. The client, Cicero Word Generator (or just Cicero) is used to graphically build, modify, save and load sequences. The server, called Atticus, receives instructions from Cicero and communicates with the hardware (National Instruments cards, GPIB or serial devices, etc.).

We gratefully thank the creator(s) of Cicero; it has been fantastic for rapidly adding or modifying functionality in the experiment without sinking massive amounts of time into building and managing our own experimental control.

3.5.2 Raman signal generation

The Raman frequency is generated by phase-locking a dielectric resonant oscillator (DRO) near 9.2 GHz. A stable 10 MHz source, referenced to GPS, is multiplied up to 180 MHz, to which a VCO is phase locked. The VCO signal is then sent into a non-linear transmission line (Picosecond Pulse Labs LPN-7103) which generates many harmonics. The 51st harmonic at 9180 MHz is picked out using a narrow bandpass filter (Marki Microwave FB-0860) and amplified. This signal then serves as the local oscillator for a mixer, against which a pickoff of the DRO signal is beaten, giving a ∼12 MHz beatnote. A ∼12 MHz rf source is then mixed with this beatnote to close the phase lock loop (PLL). By choosing among several rf sources, the DRO can be moved and/or ramped between several frequencies for different purposes (for example, microwave state selection or interferometry pulses). The PLL is shown in Fig. 3.13.

The microwave signal from the DRO is amplified and used to drive either a microwave horn or an electro-optical modulator for two-photon Raman transitions. The $\sim$ 12 MHz source that ramps the Raman frequency to account for the changing Doppler shift due to gravity is provided by an Analog Devices AD9958 direct digital synthesizer (DDS) chip. The discrete nature of the ramp parameters means that we can't continuously tune the ramp rate as finely as we would like to perform gravity measurements. We get around this limitation by clocking the AD9958 with the output of a SRS DS345 function generator with 1 μHz frequency resolution. We program the AD9958 for a fixed frequency ramp rate, where it assumes it will receive a 10 MHz clock signal. We then provide the clock frequency required to achieve the actual ramp rate desired by setting the DS345 to output a signal appropriately offset (by a small amount) from 10 MHz.

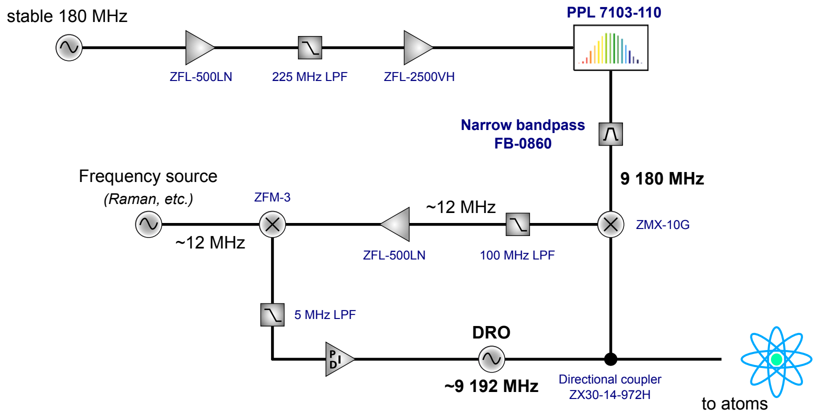

Figure 3.13: Phase lock loop for a DRO to generate the microwave frequencies necessary to manipulate the atoms.

Low microwave source phase noise is critical to the experiment because the laser phases are determined in part by the phase of the microwave signal. Phase noise on the DRO thus enters directly into the interferometer. The idea of the phase lock in Fig. 3.13 is to use the inherent excellent short-term phase stability of a DRO, and tie it down to a long-term stable source with a servo to provide stability out to long times. We can perform a microwave Ramsey experiment to tweak and lower the phase noise in the loop, using the atoms as natural clocks against which to measure our system's performance.

3.5.3 Inertial stabilization

Another important subsection of the experiment is the inertial control. The retro-reflection mirror in an atom interferometer determines the laser wavefront locations, so vibrations of that mirror are indistinguishable from movement of the atom in giving the laser phase $\Delta\phi_{\mathrm{L}}$ of the interferometer. In our setup, we can't just isolate a retro-reflection mirror. The cavity mirrors are both mounted in-vacuum, and ultimately connected to the vacuum chamber. As such, we attempt to stabilize the entire vacuum chamber.

To this end, the vacuum chamber is not mounted directly to the optical table. Instead, it is clamped onto a steel-reinforced rectangular aluminum frame. Each of the four corners of the frame rests atop a benchtop isolator (Thorlabs PWA090). These units are electronically-controlled pneumatic isolators which float a platform on an air pad upon which the load rests. A picture of this setup can be seen in Fig. 3.14. This provides additional vibration isolation from the optical table (which is itself floated on air pads to decouple it from ground vibrations).

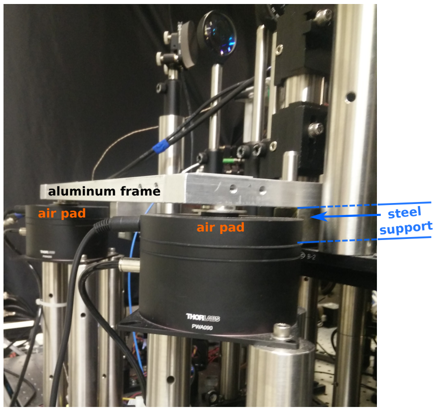

Figure 3.14: Passive vibration isolation. The vacuum chamber is to the right of the image, clamped to the steel-reinforced aluminum frame. Part of the aluminum frame and a tiny segment of the steel reinforcement are visible. Two of the four benchtop isolators can be seen. In the foreground, washers can be seen as spacers atop the floating pad of the benchtop isolator.

In addition to this passive isolation, we require active stabilization. Inspired by Ref. [62], we mount a seismometer on a platform atop the vacuum chamber. The seismometer measures vertical vibrations of the chamber, and its output is used to apply feedback to keep the system inertially quiet. As there is some shared academic lineage between this group and the authors of Ref. [62], I believe we're even using some of the literal same hardware components from that work.

3.5.3.1 Some control theory

The analog control loop for the vibration stabilization is a tricky one. A quick bit of control theory before getting into the specifics of this servo. Consider the system shown in Fig. 3.15.

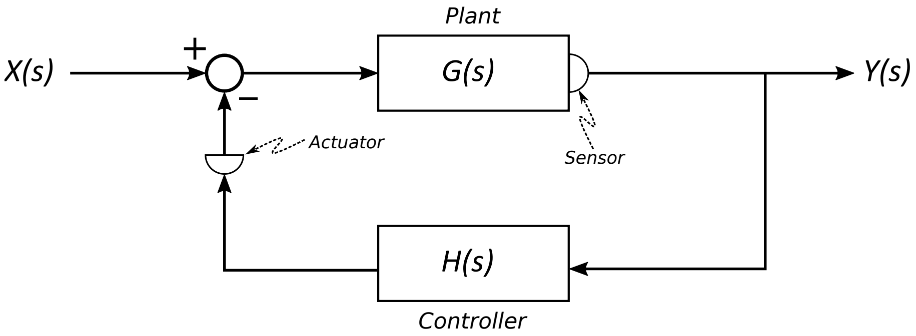

Figure 3.15: Basic control loop. $X(s)$ is the *input*, or disturbance. $Y(s)$ is the *output*, or sensor signal. $G(s)$ is the response (transfer function) of the system (often called the *plant*) to be controlled. The plant may refer inclusively to the *sensor* and/or *actuator* as well. $H(s)$ is the transfer function of the *controller*, which processes the sensor signal to drive the plant actuator. The output of the controller is used for negative feedback. The complex parameter $s = \sigma + i\omega$ is the independent variable after Laplace-transforming from the time domain. For our purposes, it's basically i times the frequency $s = i\omega$ ($\sigma \neq 0$ maintains the ability to deal with finite time intervals, transients, etc. in a more general framework).

A *transfer function* $\mathcal{T}(s)$ describes the output $Y(s)$ of a system as a function of its input $X(s)$ by

$$Y(s) = \mathcal{T}(s)X(s),$$

which is one of the advantages of working in the *s-domain*, after Laplace transforming from the time domain. Explicitly, convolution in the time domain (hard) becomes multiplication in the s-domain (easy). This allows us to stack transfer functions by multiplying them. Doing this to rearrange the transfer functions of Fig. 3.15, we can express the output/input ratio of the depicted system as

$$\mathcal{T}_{\mathrm{CL}}(s) := \frac{Y(s)}{X(s)} = \frac{G(s)}{1 + G(s)H(s)} \tag{3.3}$$

where $\mathcal{T}_{\mathrm{CL}}(s)$ is the *closed loop transfer function.* The $G(s)H(s)$ term in the denominator, sometimes denoted by $L(s) := G(s)H(s)$, is called the *open loop transfer function.* For a control loop to stabilize a system, the loop must be stable. What exactly does that mean? We will present two definitions of stability (each of which has its pros and cons): Bode stability, and Nyquist stability.

Bode stability

From eq. 3.3, we see that if

$$G(s)H(s) = -1, \tag{3.4}$$

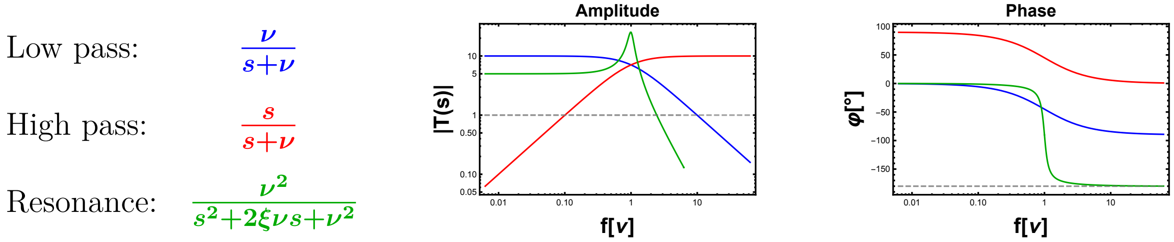

Figure 3.16: Simple Bode plots. Amplitude and phase response are shown for a low pass filter (blue), a high pass filter (red), and a resonance (green). For the resonance, the damping factor is $\xi = 0.1$. ν is equal for all the transfer functions, as can be seen from the roll-off points for the filters and the resonance peak.

the denominator blows up and we have a problem. In this case, the system becomes unstable and oscillates at the frequency for which this condition holds. Bode analysis typically works in the frequency domain, which we go to via the transformation $s \to j\omega$ ([2]).

A Bode plot for a transfer function $\mathcal{T}(s)$ plots the magnitude and phase of $\mathcal{T}(j\omega)$ as a function of frequency ω. Example Bode plots of three common elements are shown in Fig. 3.16.

The condition eq. 3.4 is satisfied if there exists a frequency for which the magnitude of the response is 1, and the phase shift is 180°. If there is a frequency for which this condition holds, the system is unstable.

We let ω_c denote the *critical frequency* for which the phase shift is $\pm 180°$, and ω_u denote the *unity gain frequency* for which the magnitude of the response is 1. The Bode stability criterion can then be stated as

Bode stability criterion

$$\omega_c \neq \omega_u \tag{3.5}$$

In practical control loops, this means scaling up the transfer function by a constant (increasing the gain) until the system oscillates once $\omega_c = \omega_u$, then backing that constant off by some safety margin (typically a factor $\lesssim 2$).

Nyquist stability

The Bode stability criterion above, while simply stated, does not cover all cases. In particular, it is not guaranteed to apply to transfer functions with more than exactly one value of ω_c and ω_u, a detail the previous section quietly swept under the rug. It also cannot be

---

[2] Control theory uses the convention $j = \sqrt{-1}$, which we adopt for this section.

applied to transfer functions with certain properties[3], including open-loop unstable systems (which can sometimes be made closed-loop stable). A more general condition called *Nyquist stability* can be used in this case.

First, it is useful to introduce a different view of what "stable" means. Note the following inverse Laplace transform:

$$\mathcal{L}^{-1}\left(\frac{1}{s-a}\right) = e^{at} \tag{3.6}$$

If $\mathrm{Re}(a) > 0$, this quantity blows up as $t \to \infty$. A transfer function $\mathcal{T}(s)$ can always be written in the form

$$\mathcal{T}(s) = \frac{N(s)}{D(s)} = \frac{a_n s^n + a_{n-1}s^{n-1} + \ldots + a_1 s + a_0}{b_m s^m + b_{m-1}s^{m-1} + \ldots + b_1 s + b_0},$$

that is, as a ratio of two polynomials in s. The roots of the numerator polynomial $N(s)$ are known as the *zeros* of $\mathcal{T}(s)$, denoted by z_i. Similarly, the roots of the denominator $D(s)$ are the *poles* of $\mathcal{T}(s)$, denoted by p_i. The transfer function can then be written as

$$\mathcal{T}(s) = \frac{a_n(s-z_1)(s-z_2)\cdots(s-z_n)}{b_n(s-p_1)(s-p_2)\cdots(s-p_n)}, \tag{3.7}$$

which can be decomposed into a sum of partial fractions[4] as

$$\mathcal{T}(s) = \frac{c_1}{(s-p_1)} + \frac{c_2}{(s-p_2)} \cdots + \frac{c_n}{(s-p_n)}, \tag{3.8}$$

where the constants c_i are called the *residues* of $\mathcal{T}(s)$, given by $c_i = \lim\limits_{s \to p_i} [(s-p_i)\mathcal{T}(s)]$. The Laplace transform (and its inverse) are linear, namely

$$\mathcal{L}\left(af(t) + gf(t)\right) = aF(s) + bG(s) \tag{3.9}$$

where $F(s)$ and $G(s)$ are the Laplace transforms of $f(t)$ and $g(t)$, respectively. Suppose a signal $u(t)$ is the input to the system represented by the transfer function $\mathcal{T}(s)$. If we want the output $v(t)$ to be stable (i.e., $v(t) \not\to \infty$ as $t \to \infty$), we can now state that more precisely:

> For the output of a system with transfer function $\mathcal{T}(s)$ to be stable, all poles $\mathcal{T}(s)$ must have negative real parts.

---

[3] The transfer function must also be strictly proper (more poles than zeros), and have no pole with real part ≥ 0 (which we will see implies open-loop instability).

[4] The following arguments require simple (i.e., non-repeated) poles, and $m > n$, but analogous arguments can be made if these conditions don't hold.

If this condition were not satisfied, then for some pole in the partial fraction eq. 3.8, we'd get a term like eq. 3.6 that blows up to ∞. So to determine a system's stability, we need to count the number of poles of its transfer function in the right half of the complex plane. If we are interested in a closed-loop transfer function of the form eq. 3.3, the number of poles of

$$\mathcal{T}_{\mathrm{CL}}(s) = \frac{G(s)}{1 + L(s)}$$

in the right half of the complex plane must be zero, where $L(s)$ is the open-loop transfer function. Poles of $\mathcal{T}_{\mathrm{CL}}$ satisfy the *characteristic equation*

$$1 + L(s) = 0 \tag{3.10}$$

Let us denote by Z the number of roots of the characteristic equation with real part ≥ 0. An abbreviated definition of the Nyquist stability criterion can now be presented:

Nyquist stability criterion

A closed-loop system with open-loop transfer function $L(s)$ is stable iff $Z = 0$, where Z is the number of roots of the characteristic equation $1 + L(s) = 0$ that lie to the right of the imaginary axis.

Nyquist stability also comes with some requirements[5] on the transfer function, but it is strictly more general than the Bode criterion. Apparently Z can be tricky or annoying to calculate, so we calculate it a fancy, roundabout way using results from complex analysis.

First, we introduce the *Nyquist contour* in the s-domain, Γ_s. The Nyquist contour is basically a way of encircling the right half of the complex plane. It consists of a path running along the imaginary axis from $-j\infty$ to $+j\infty$, and a semicircle of infinite radius enclosing the right half of the plane. The Nyquist contour can be seen in Fig. 3.17[6].

The *Nyquist plot*, or Nyquist diagram, for a transfer function $\mathcal{T}(s)$ is the curve produced by evaluating $\mathcal{T}(s)$ along the Nyquist contour. Conceptually, the Nyquist plot $\Gamma_{\mathcal{T}(s)}$ lives in a different complex plane than the Nyquist contour Γ_s (the *s-plane* for the latter, as opposed to the *$\mathcal{T}(s)$-plane* for the former).

Define the following integers (one of which has already been introduced) associated with an open loop transfer function $L(s)$:

---

[5] For example, Nyquist stability requires a linear time-invariant (LTI) system (as does Bode stability), and a proper (but not strictly proper) transfer function (number of poles $\geq$ number of zeros)

[6] Some care needs to be taken such that no poles of the transfer function being considered lie on the Nyquist contour, by taking tiny semicircular detours off the imaginary axis of radius $\epsilon \to 0$

Z - number of roots of the characteristic equation $1 + L(s) = 0$

P - number of poles of $L(s)$ in the right half of the s-plane

N - number of clockwise encirclements of the point $-1 + 0j$ by the Nyquist plot $\Gamma_{L(s)}$ in the $L(s)$-plane

Complex analysis tells us that $Z = N + P$ (specifically, using Cauchy's argument principle). This gives us a way to get at Z without doing a (perhaps messy) calculation! Note that most feedback loops are open-loop stable, which means $P = 0$. In that case, $Z = N$, and all we have to do is look at the Nyquist plot of a transfer function (specifically, its encirclements of the point $-1 + 0j$) to determine its stability. Nyquist plots for the simple transfer functions from Fig. 3.16 can be seen in Fig. 3.17.

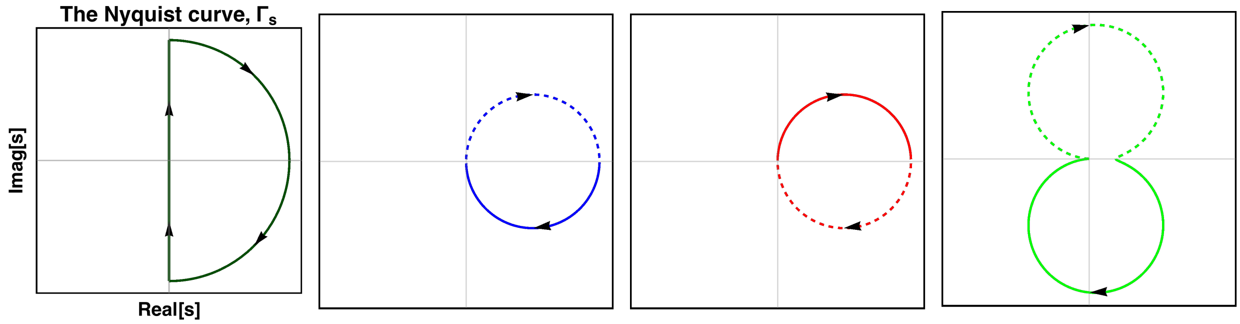

Γ_s $\frac{\nu}{s+\nu}$ $\frac{s}{s+\nu}$ $\frac{\nu^2}{s^2+2\xi\nu s+\nu^2}$

Figure 3.17: Simple Nyquist plots of the same transfer functions from Fig. 3.16. The Nyquist curve Γ_s is shown at left, in the s-plane. The next three plots are Nyquist diagrams (in the $\mathcal{T}(s)$-plane) for a low pass filter (blue), high pass filter (red), and resonance (green), whose transfer functions are shown below their respective plots. Arrows indicate the direction along which the Nyquist curve Γ_s is being traversed. Dotted (solid) lines in the Nyquist diagrams represent the negative (positive) imaginary axis portion of Γ_s, i.e., negative (positive) ω.

Next we'll make use of these concepts to analyze our vibration stabilization loop.

3.5.3.2 Vibration stabilization

The system

We will now apply the structure of the previous section to our setup. In our case, the cavity mirror mounting (and thus the whole vacuum chamber) is the plant, the object we wish to control. The seismometer atop the vacuum chamber is the sensor. Unwanted vibrations entering through the optical table are the disturbance. A voice coil between the vacuum chamber and a platform mounted to the optical table is our actuator. An electronic circuit (details to follow) is the controller that applies the appropriate correction to the voice coil based on the output of the seismometer. This loop is shown in Fig. 3.18.

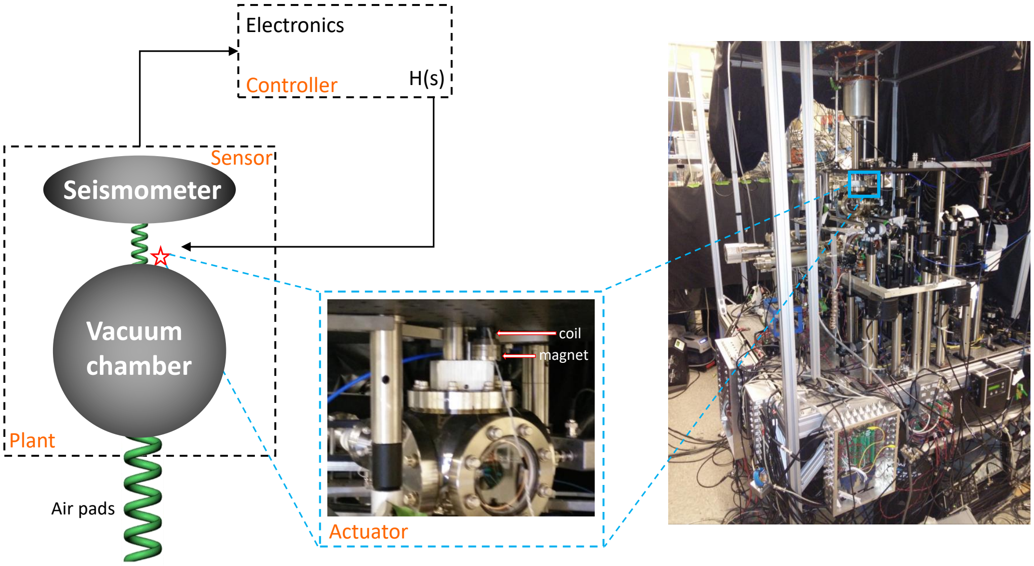

Figure 3.18: Vibration stabilization control loop.

The seismometer (Kinemetrics Ranger SS-1) is a heavy ($\sim$ kg) cylindrical magnet with a circular slot hanging on a spring. A many-turn coil, attached to the seismometer body, protrudes into the slot of the hanging magnet. When the seismometer body moves, the magnet-on-a-spring serves as an inertial test body which “stays still” as the coil moves. The changing magnetic flux through the output coil induces a current, which is read out as a voltage as the seismometer signal.

In order for the magnet to serve as an inertial test mass, the resonant frequency $\omega = \sqrt{\frac{k}{m}}$ of the mass-spring system (where m is the mass and k is the spring constant) must be low. For a mass-spring system supported against gravity, the spring force $F_s = k\Delta x$ (where Δx is the spring's extension from equilibrium) equals the gravitational force $F_g = mg$. The resonance frequency can thus be expressed as $\omega = \sqrt{\frac{g}{\Delta x}}$. Achieving a resonance frequency of $2\pi \times 100$ mHz would then require a spring 24.8 m in length, which is impractical. Low frequency inertial devices thus make use of *anti-springs*, where the spring constant is negative, in addition to the spring, to lower the resonance frequency. The seismometer uses an arrangement of bar magnets attached around the seismometer body as an anti-spring. Other applications, gravitational wave detectors in particular (e.g., Ref. [63] and references therein) use geometric anti-springs consisting of an arrangement of bent steel blades [64].

Transfer function of the plant

We will now derive the form of $G(s)$ for our system. We model our setup as a vacuum chamber of mass m_v attached to the optical table of infinite mass by a spring with stiffness k_v. It is located at position x_v, and experiences damping with coefficient β_v. The seismometer has mass m_s, and is modeled as being attached to the vacuum chamber by a spring of stiffness k_s. It is located at position x_s, and has damping coefficient β_s.

We drive the chamber with disturbing force F, and study the system's response. We assume that the seismometer is much lighter than the vacuum chamber, such that the back-action of the seismometer on the chamber is negligible. The equation of motion at fixed Fourier component ω is:

$$\begin{aligned} m_v\ddot{x}_v &= F - k_v x_v - \beta_v \dot{x}_v \\ -m_v\omega^2 x_v &= F - k_v x_v - i\omega\beta_v x_v \\ x_v &= \frac{F}{-m_v\omega^2 + k_v + i\omega\beta_v} \end{aligned} \tag{3.11}$$

The analogous equation for the seismometer position x_s is

$$\begin{aligned} m_s\ddot{x}_s &= -k_s(x_s - x_v) - \beta_s\frac{d}{dt}(x_s - x_v) \\ -m_s\omega^2 x_s &= -k_s(x_s - x_v) - i\omega\beta_s(x_s - x_v) \\ x_s &= x_v\frac{k_s + i\omega\beta_s}{-m_s\omega^2 + k_s + i\omega d_s} \end{aligned} \tag{3.12}$$

The seismometer measures a voltage V_s proportional to the relative velocity of its mass and the vacuum chamber; that is,

$$\begin{aligned} V_s &= \alpha(\dot{x}_s - \dot{x}_v) \\ V_s &= \alpha i\omega(x_s - x_v) \end{aligned} \tag{3.13}$$

For our seismometer, $\alpha = 260(10)\,\frac{\mathrm{V}}{\mathrm{m/s}}$.

With these equations, we can now write the seismometer output V_s ($Y(s)$ from Fig. 3.15) as a function of an input disturbance F ($X(s)$ from Fig. 3.15). Their ratio gives us the transfer function $G(\omega)$ of our plant. That is,

$$G(\omega) = \frac{V_s(\omega)}{F} = \frac{i\alpha m_\mathrm{s}\omega^3}{(k_\mathrm{v} - m_\mathrm{v}\omega^2 + i\omega\beta_\mathrm{v})(k_\mathrm{s} - m_\mathrm{s}\omega^2 + i\omega\beta_\mathrm{s})}$$

This can be recast into a more transparent form. First, we use the natural frequency of a mass-spring system, $\omega_\mathrm{n} = \sqrt{\frac{k}{m}}$, and the unitless damping ratio, related to the damping coefficient by $\xi = \frac{\beta}{2m\omega_\mathrm{n}}$. We then revert to the s-domain by taking $\omega \to s/i$. After this, the transfer function is given by

$$G(s) = -\frac{\alpha}{m_v} \frac{s^3}{\left(s^2 + 2s\xi_v\omega_{\mathrm{n},v} + \omega_{\mathrm{n},v}^2\right)\left(s^2 + 2s\xi_s\omega_{\mathrm{n},s} + \omega_{\mathrm{n},s}^2\right)}$$

Nyquist and Bode plots of this function are shown below in Fig. 3.19

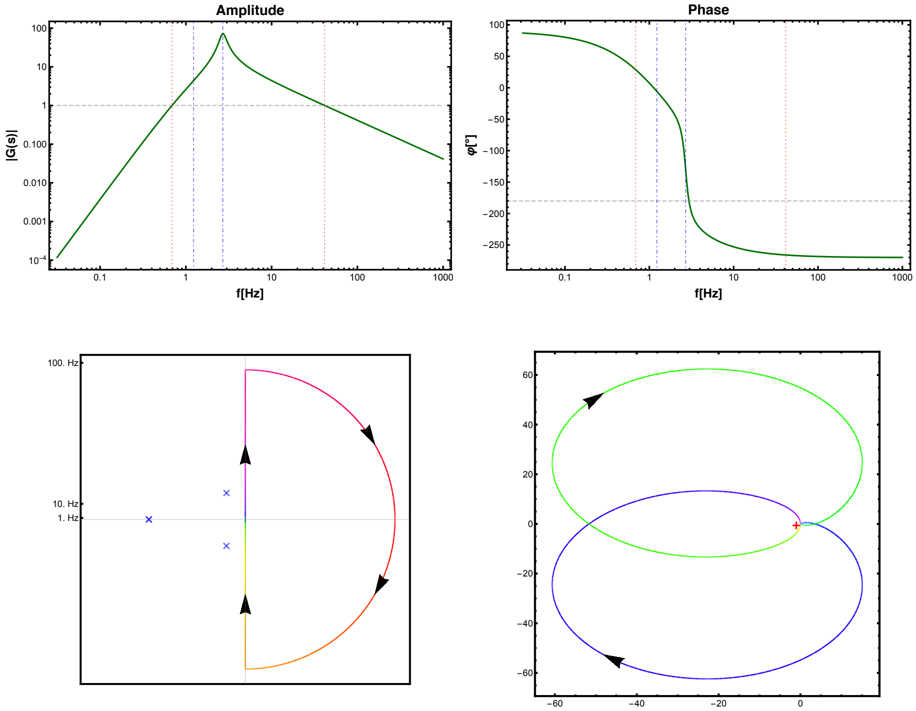

Figure 3.19: Mechanical response $G(s)$ to vibrations. Top row: Bode plots. Bottom row: Nyquist plots. See main text for description

The seismometer resonance is critically damped by appropriate choice of load resistance, so $\xi_s = 1$. The seismometer resonance frequency is measured to be $\omega_{n,s} = 2\pi \times 1.23$ Hz. The resonance frequency of the air pads is measured to be $\omega_{n,v} = 2\pi \times 2.7$ Hz. The damping ratio is inferred to be about $\xi_v = 0.09$ via the size of the resonance peak. We'll set $m_v = 1$ so we don't have to keep track of unit conversions.

The Bode plots give us intuition about what's going on. The undamped air pad peak is clearly visible, while the critically damped seismometer peak is more hidden. These resonance locations are indicated by dot-dashed blue lines. The response approaches these closely-spaced resonances from below as ω^3 and, far after the peaks, decreases via ω^{-1} (each resonance contributes ω^{-2} on top of the incoming ω^3). The phase shift far below the resonance is 90° (which is a reflection of the signal being proportional to the velocity, and not the position). Each resonance drops the phase by 180°; slowly across a decade or two for the critically damped seismometer resonance, and rapidly for the less-damped air pad resonance.

The horizontal dashed gray lines in the Bode plots show $|G| = 1$ and $\varphi = 180°$. The vertical dotted red lines show the two unity gain frequencies. Multiple ω_u is a disqualifier for using the Bode stability criterion (as is the triple pole on the imaginary axis at $s = 0$). Ignoring that, the Bode plot would predict stability for this system in a negative feedback loop, as there is not a unity gain frequency with 180° phase shift.

We need to go to the Nyquist picture to assess the stability. The Nyquist diagram is shown alongside a color-coded Nyquist curve[7] to help visualize which frequencies correspond to which points in the Nyquist diagram. The structure of the Nyquist diagram is dominated by frequencies around the ∼Hz level.

If we were to use the output of the seismometer directly as the negative feedback (i.e., a purely proportional controller), G would be the open loop transfer function. The four zeros of $G(s)$ (each indicated by with a blue x, including one double) all have negative real part $\iff$ are not contained within the Nyquist contour. The system is therefore open-loop stable $\iff$ $P = 0$. However, the point $-1 + 0j$ is encircled by the Nyquist diagram, in this case twice, giving $N = 2$. Therefore, $Z = 2$, and the system *would not be closed-loop stable.* This is in contradiction to the prediction of the (inapplicable) Bode stability criterion. We'll need a nontrivial controller transfer function for a stable closed loop, which we discuss in the next section.

Controller transfer function

The electronic controller alleviates the closed-loop instability of the bare mechanical response by applying its own transfer function $H(s)$. We use an analog control loop, so parameters of the system are tweaked in situ to optimize loop performance. Parameters used in this analysis will therefore be representative, but not exact.

The controller consists of two *lag compensators* preceded by a large-gain, inverting amplifier. A lag compensator has a flat frequency response, except in a specific frequency range where it acts as an integrator. Ours are made using an op amp in a configuration shown in Fig. 3.20, alongside the resulting transfer function.

The second line in eq. 3.14 is the general form of a lag compensator, and we identify $\omega_1 = 1/R_3C$ and $\omega_2 = 1/C(R_2 + R_3)$ for our circuit's realization. At very low frequencies ($\omega \ll \omega_2 < \omega_1$), the gain is given by K, and at high frequencies ($\omega \gg \omega_1$) it is given by $K \times \frac{\omega_2}{\omega_1}$.

Our setup has something like $\omega_1 \sim 2\pi \times 700$ mHz, $\omega_2 \sim 2\pi \times 30$ mHz for both circuits, but we haven't measured the final component values after tuning. This aspect could very likely be optimized, especially in a digital control loop where adding and changing feedback elements is far easier than in an analog circuit. This has been done, e.g., in Refs. [62, 65]. Optimizing the (and likely adding at least one more) lag compensators could probably improve system performance if needed.

Parameterized in terms of the frequencies $\omega_{i\alpha}$ where $i = 1, 2$ above, and $\alpha \in \{A, B\}$ for our two lag compensators, the total transfer function of our controller is

---

[7] Technically, there should be a semicircle around the origin of radius $\varepsilon \to 0$ so the curve does not pass through the poles at $s = 0$, but we'll just say that's too small to see on this scale. Also, the large semicircle should go from $+j\infty$ to $-j\infty$, but we set $2\pi \times 95$ Hz $= \infty$ for the sake of a (barely) discernible color scale.

$$\begin{aligned} H_{\mathrm{lag}} &= \frac{R_1}{R_2}\frac{1+sCR_3}{1+sC(R_2+R_3)} \\ &= K\,\frac{1+s/\omega_1}{1+s/\omega_2} \end{aligned} \tag{3.14}$$

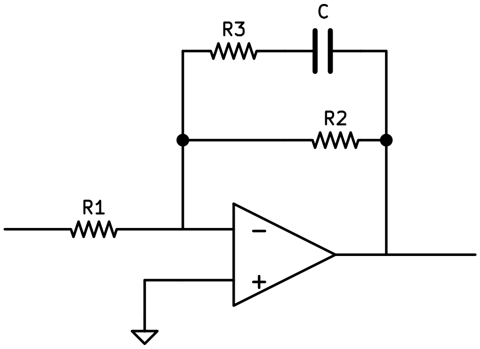

Figure 3.20: Op amp lag compensator

$$H(s) = -K_{\mathrm{tot}}\left(\frac{1+s/\omega_{1\mathrm{A}}}{1+s/\omega_{2\mathrm{A}}}\right)\left(\frac{1+s/\omega_{1\mathrm{B}}}{1+s/\omega_{2\mathrm{B}}}\right) \tag{3.15}$$

This transfer function $H(s)$ can be seen in Fig. 3.21. K_{tot} is positive, and we explicitly include the minus sign to indicate that there is an inverting amplifier (contributing a $-180°$ phase shift) as well.

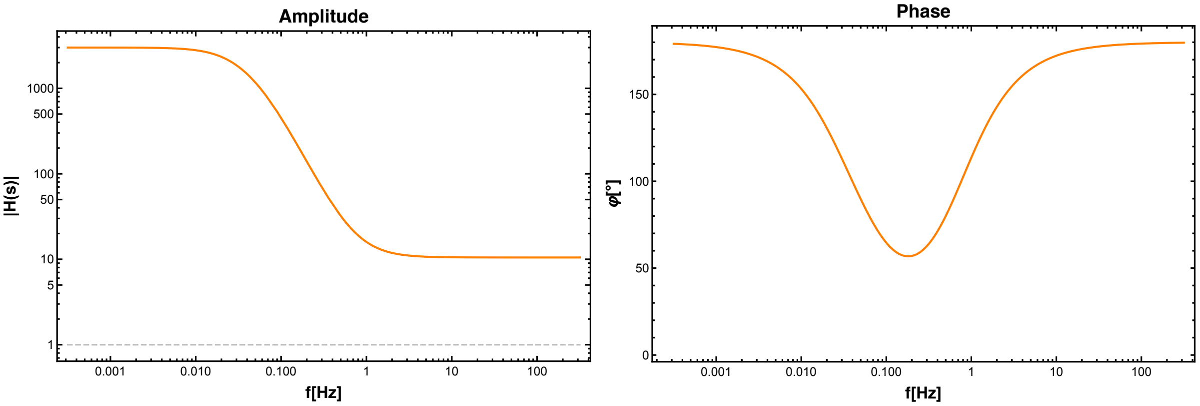

Figure 3.21: Controller transfer function $H(s)$. Note that this includes both lag compensators (as seen from the slope of the double-integrator region), which have similar ω_1 and ω_2.

The circuit for the full controller can be seen in Fig. 3.22:

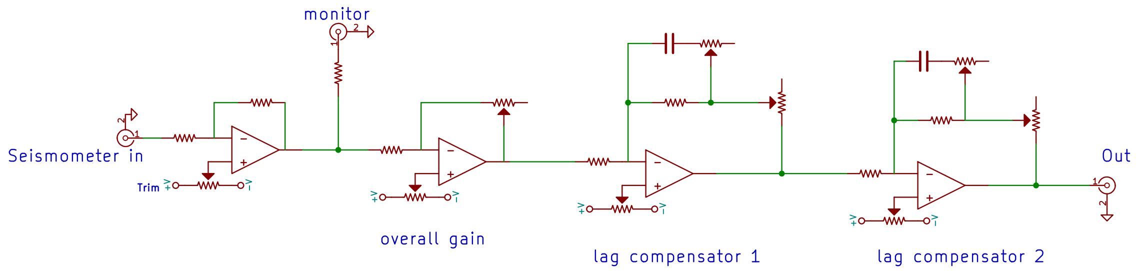

Figure 3.22: Controller circuit schematic. The extra potentiometer in the lag compensators is a trick to mimic a large variable resistor (larger than typically available potentiometers). In the actual setup, this is followed by an active twin-T notch filter to filter out a high-frequency mechanical resonance at 2 kHz.

Stability

The open-loop transfer function is now given by $L(s) = H(s)G(s)$. Fig. 3.23 shows Nyquist and Bode plots for $L(s)$.

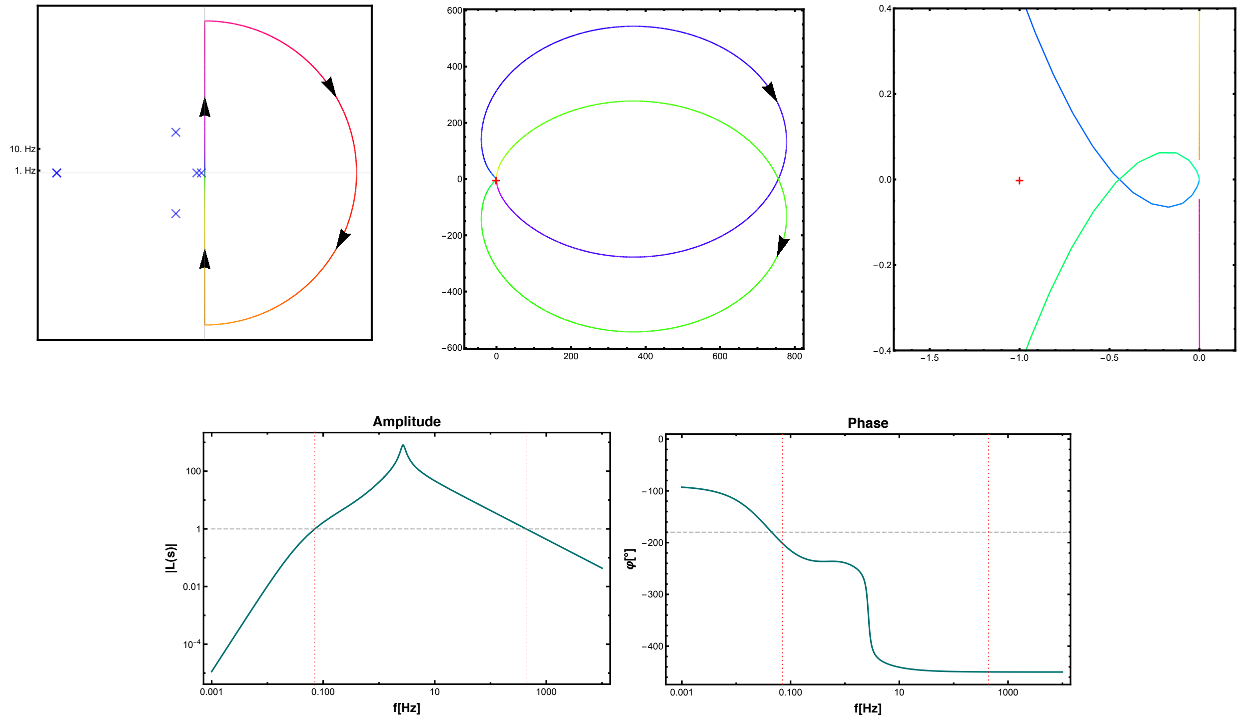

Figure 3.23: Nyquist and Bode plots for the open-loop transfer function $L(s)$.

We'll start with the Nyquist plots in the upper row of Fig. 3.23. Again, the color scale on the Nyquist curve is used to see which frequencies comprise which part of the Nyquist diagram. We see from the blue x's that $P = 0$ for $L(s)$. The middle plot of the top row shows the Nyquist plot for the open-loop system. The red + indicates the point $-1+0j$. We're too zoomed out to see if it's encircled because we've turned up the gain (K_{tot}, in eq. 3.15) so high. The rightmost plot zooms in, where we see that the point is not encircled! This particular parameter set is aggressive, giving a phase margin of only $\approx 20°$ (seen by literally rotating the Nyquist diagram). However, this increases quickly if turning down the gain, because the blue and green looped portions of the Nyquist diagram are curving strongly. Achieving the (conservative) typically-quoted phase margin for stability of 45° only requires reducing the gain by a factor of 2.5 from what is shown.

Since both $N=0$ and $P=0$,

$$\boxed{Z=0\text{, and our system is closed-loop stable!}}$$

The Bode plots below the Nyquist ones in Fig. 3.23 give a more interpret-able picture of what's going on. The full system's transfer function is given, as in eq. 3.3, by

$$\mathcal{T}_{\text{CL}}(s)=\frac{G(s)}{1+G(s)H(s)} \tag{3.16}$$

Bode plots of $\mathcal{T}_{\text{CL}}(s)$ are shown in Fig. 3.24, as is the amplitude $|\frac{\mathcal{T}_{\text{CL}}(s)}{G(s)}|$ showing how much the feedback loop attenuates vibrations as a function of frequency.

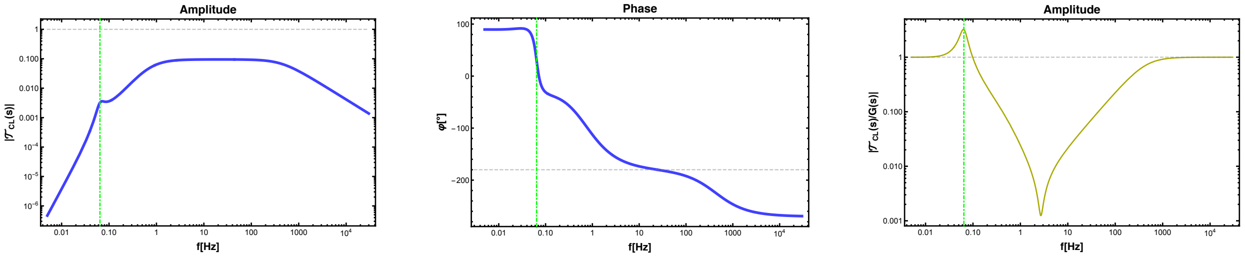

Figure 3.24: Bode plots for the closed-loop transfer function $\mathcal{T}_{\text{CL}}(s)$. Amplitude and phase plots for $\mathcal{T}_{\text{CL}}(s)$ are shown in the left and center panels, respectively. The right plot shows $|\frac{\mathcal{T}_{\text{CL}}(s)}{G(s)}|$ to visualize improvement over the unstabilized situation.

By inspecting the poles of $\mathcal{T}_{\text{CL}}(s)$, we find that the full system acts as if it were an underdamped system with resonance frequency $\omega_n = 2\pi \times 64$ mHz, and damping ratio $\xi = 0.18$, for the parameters used in Figs. 3.23 and 3.24. This effective resonance is indicated with a dot-dashed green line in the plots of Fig. 3.24. Turning down the gain raises the effective resonance frequency and the damping ratio, so there is likely an optimal setting somewhere.

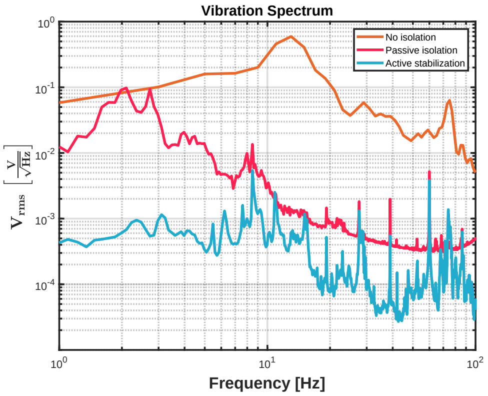

Figure 3.25: Vibration noise curves showing the in-loop seismometer signal with no isolation, passive isolation, and active stabilization (feedback loop engaged).

Full system and performance

After all that design, plus a little tweaking, the performance of the real-life vibration stabilization is shown in Fig. 3.25.

A quantitative description of Mach-Zehnder AI sensitivity to vibration noise can be found in Sec. 8.3. Glossing over those procedural details here, the spectra from Fig. 3.25 can be used to calculate the expected phase noise of the interferometer due to vibrations with and without stabilization. This is shown in Fig. 3.26.

Optimizations that have not yet been performed in our feedback loop (which could further improve the performance), plus limitations of the present realization, include the following:

- A more comprehensive lag compensator tuning
- The seismometer is not right at the retroreflection mirror. As such, the seismometer signal is not precisely representing the mirror vibrations. This transfer function is unknown.
- Despite putting the seismometer well above the vacuum chamber (possibly exacerbating the issue above), switching experimental magnetic fields do bounce the seismometer signal.
- There are unfortunate high frequency ($\sim$kHz) resonances that limit the gain of the control loop, despite use of some filters already
- The full vacuum chamber (rather than just a retroreflection mirror) is being stabilized. As a result, the voice coil actuator may be sub-optimal (e.g., its un-centered alignment).

Although these may limit the performance of the stabilization system, it has been sufficient for our purposes despite really having to shoehorn it into the existing setup due to

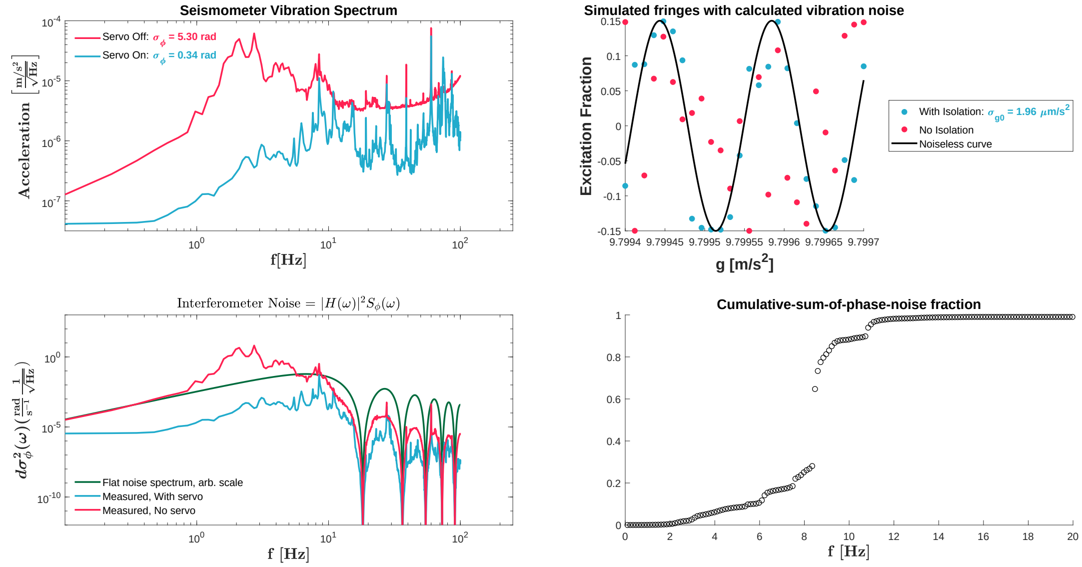

Figure 3.26: Interferometer vibration noise. Left: Seismometer outputs (a voltage measuring velocity) from Fig. 3.25 are converted to acceleration spectra. Right: Interferometer fringe simulations with phase noise due to the corresponding acceleration noise spectrum, and $T = 55$ ms. Without vibration stabilization, the phase noise has standard deviation σ_ϕ of nearly a full 2π, making it impossible to discern a fringe. With stabilization, this rms phase noise is reduced by a factor of ≈ 16, providing a clean fringe. These simulations match well to experimentally observed phase noise.

our lack of foresight. The reduction in vibrations demonstrated here is crucial for high-sensitivity accelerometry with a Mach-Zehnder atom interferometer. Without this active stabilization, vibration noise is high enough to fully wash out interferometry fringes, making a measurement impossible. A separate, surprising method to mitigate vibration-induced interferometer phase noise is also introduced in Sec. 8.3.

3.5.3.3 Tilt stabilization and vertical alignment

The laser phase $\phi_L = \boldsymbol{k} \cdot \boldsymbol{a} T^2$ includes the dot product of the atom's acceleration $\boldsymbol{a}$ and the laser wavevector $\boldsymbol{k}$. If these two vectors are misaligned by a small angle θ, the actual laser phase will be

$$\phi_L = \phi_L^0 \cos\theta \approx (1 - \theta^2)\phi_L^0$$

where $\phi_L^0 = kaT^2$ is the laser phase assuming perfect alignment of $\boldsymbol{k}$ and $\boldsymbol{a}$. Not only does this introduce a systematic shift in a measured value, but the becomes increasingly sensitive to small fluctuations in θ (since $\frac{d\phi_L}{d\theta} \approx -\theta\phi_L^0$).

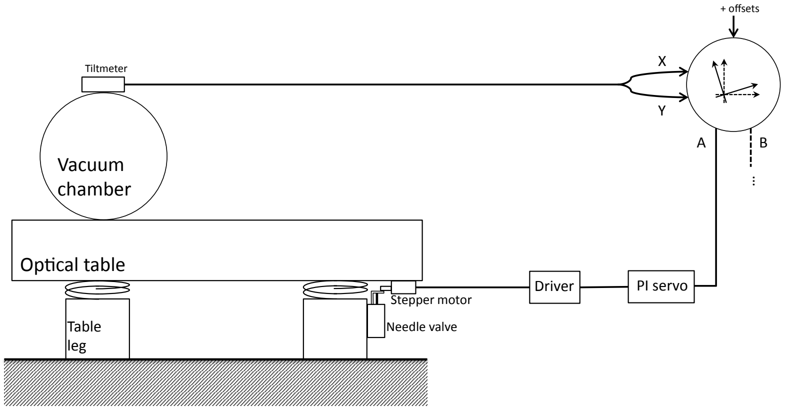

Figure 3.27: Tilt stabilization loop. The tiltmeter is mounted on the vacuum chamber on the optical table. A voltage proportional to its tilt along the two axes undergo a linear transformation from $\hat{x}$ and $\hat{y}$ to $\hat{A}$ and $\hat{B}$. This is necessary because the alignment and scale factors of the feedback axes do not necessarily align to the sensor axes. Each axis is then compared to its setpoint with a PI loop. The output of the PI loop then drives a servo motor via pulse width modulation to position an arm. That arm moves a lever attached to a needle valve controlling one leg of the floating optical table. Adjusting this arm changes the height at which that leg must sit to close the needle valve, thus tilting the optical table.

To avoid these problems, it is important to align the laser wavevector to Earth's gravitational field. We measure the tilt using an electronic bubble level (Applied Geomechanics 700-series) mounted to the vacuum chamber. The atom interferometer itself is used to find the angles θ_x and θ_y for each direction that align the cavity mode along gravity. See Sec. 5.6 for details and data about finding these setpoints.

However, once known, this alignment must be maintained. A feedback loop is used, which uses the tiltmeter signal as input, and stabilizes this signal to the setpoints discussed in the previous paragraph. This is especially important because the air pads upon which the vacuum chamber sits slowly but continuously lose air, and eventually need to re-level themselves. This however, is only done to a coarse level (for our air pad spacings, this corresponds to several hundred μrad tilt of the vacuum chamber). Fig. 3.27 shows the setup of our feedback loop.

The tiltmeter outputs are processed and used to control the position of two servo motors (one for each rotation axis) fitted with a rotation-to-translation attachments. Each motor is attached to the bottom of the optical table, with an arm attached. The arm presses against a lever to a needle valve controlling the height of that leg of the optical table. Translation of the arm via motion of the motor thus sets the height of the optical table leg. This setup can be seen in Fig. 3.28.

Needle valves have a small dead zone around their closed position for which a finite movement is required to open them in either direction. This nonlinearity means that a linear feedback loop would be unable to satisfy its setpoint condition, and would oscillate

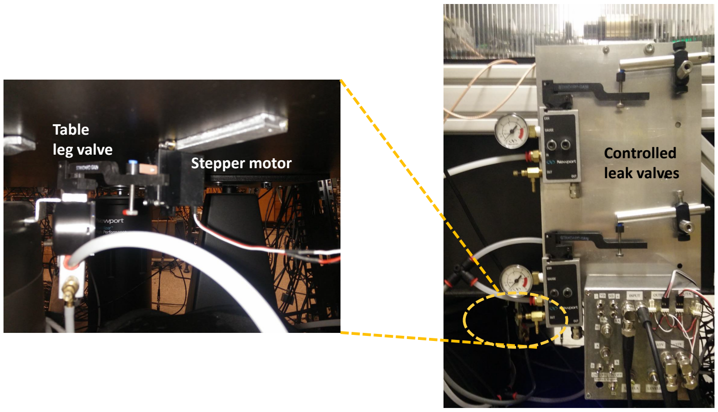

Figure 3.28: Left: Servo motor-controlled arm that opens/closes the optical table needle valve. Right: Each actuated leg also has a controlled leak applied, as discussed in the text. Valves for these leaks shown here. The box containing the linear transformation, PI loops, and motor drivers is visible in the lower right of the image.

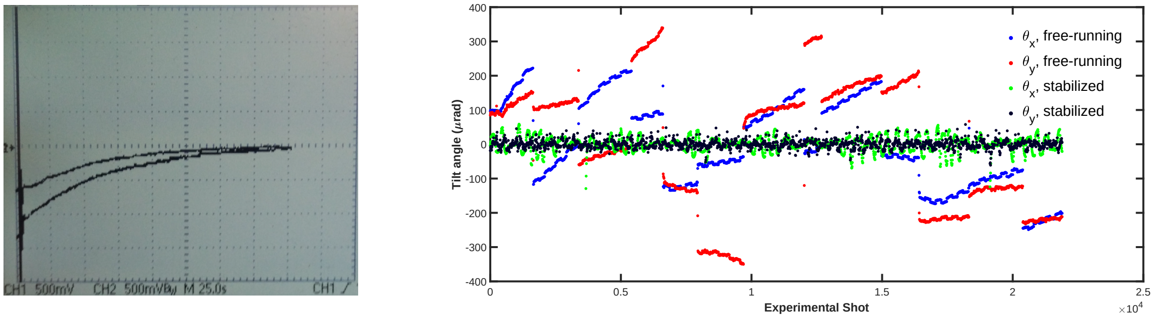

Figure 3.29: Tilt feedback performance. Left: Loop engaging and settling to equilibrium starting far from the setpoint. The time constant of about 1 minute set by the PI loop is observed. Oscilloscope traces show tilts θ_x and θ_y, at 25 s / div, and 500 mV / div (where 1 mV = 1 μrad of tilt. Right: Tilt stability with and without feedback engaged. Jumps in the unstabilized values are due to re-levels of the vacuum chamber air pads.

between opening the valve in alternating directions. A solution is to introduce a small, controlled leak [30]. This moves the equilibrium point of the loop into the linear regime of the valve's operation. The controlled leak valves for each axis of control can be seen in Fig. 3.28.

The performance of the loop can be seen in Fig. 3.29. The PI loop has an RC time constant of about 1 minute. This can be seen in the loop settling from an impulse in Fig. 3.29. The gain and slow time constant are set conservatively so that the feedback loop does not fight the re-leveling of the vacuum chamber air pads. It is important that the motor be attached to the bottom of the optical table. The table itself drifts, and if the motor is mounted to it, this effect automatically enters the feedback loop. If not, another time constant is introduced into the loop and performance degrades considerably.

Longer-term data is shown in Fig. 3.29. Red and blue points show tilts in the two rotation angles without the feedback loop, while green and navy points show the feedback engaged. Once initially set up, this feedback loop is pretty robust and painless, and stabilizes the tilts to the 10 μrad level.

Chapter 4

Interferometry in the cavity

The atom source provides a laser-cooled cloud of atoms that have just been launched upwards. The interferometry sequence can now begin. An overview of the Mach-Zehnder geometry was presented in Section 2.4, with constituent Raman pulses discussed in Section 2.3. These overviews glossed over many "real-world" details relevant to performing the necessary matter wave manipulations. We discuss such details in this chapter, with an emphasis on cavity-specific aspects.

Some of the motivations for putting an atom interferometer into an optical cavity have been mentioned previously (higher optical intensity, spatial mode filter), as have some potential difficulties. These benefits and difficulties are discussed here in further detail as well.

4.1 Cavity challenges

Beam size[1]

The cavity mode beam waist is 718 μm, set by the 10 m radius of curvature of the lower mirror of the science cavity. A larger radius of curvature gives a larger beam waist, but reduces the transverse mode spacing (see eq. 2.90), degrading spatial mode filtering. An attempt to address this trade-off using an intra-cavity lens has been made [66].

The small beam is comparable to the initial size of the atom cloud, since the cavity mode is used for the launch. As the atomic sample thermally expands, it begins to leave the beam. The atoms see a spread in Rabi frequencies across the transverse gaussian profile of the beam. This gives inhomogeneous π and $\frac{\pi}{2}$ pulse times across the atom sample. Pulses become less uniformly efficient, reducing interferometer contrast.

---

[1] The catch from Sec. 3.4 and the ARP pulses of Ch. 7 are attempts to address this problem.

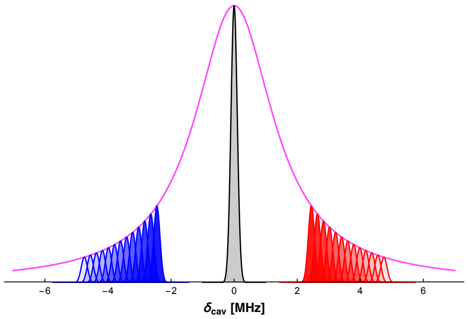

Figure 4.1: Raman frequency ramp in the cavity. The pink trace is the normalized cavity lineshape. The laser peak heights show the resonant enhancement in the cavity, not their actual intensity relative to each other (see Fig. 4.6 for that). They are shown in black (carrier), red (red sideband, ramping), and blue (blue sideband, ramping) with a 100 kHz linewidth. Only the ±1 orders are shown here. The shading of the sideband peaks darkens with increasing Doppler shift. For k^+ this means the sideband peaks move from light shading to dark over the interferometer duration. For k^-, they move from dark to light

Frequency selectivity

The science cavity has a full-width, half-maximum linewidth of $\gamma_{\mathrm{FWHM}} = 2\pi \times 3.03$ MHz at 852 nm. This frequency selectivity presents two problems.

First, the beams coupling the two hyperfine ground states of the atoms are separated in frequency by ~ 9.2 GHz, but must simultaneously be close to cavity resonance. This is solved by setting the cavity length such that the free spectral range is nearly an integer divisor of the cesium hyperfine frequency (see Sec. 3.2; that integer is 23 for our setup). In our case, the resulting mismatch is $\delta_{\mathrm{HF}}^{\mathrm{offs}} = \frac{1}{2\pi}\omega_{\mathrm{HF}}^{\mathrm{Cs}} - 23 \times \mathrm{FSR} = 3.80$ MHz. As outlined in Sec. 3.2, this is a somewhat lucky alignment mismatch of only $\sim 155\ \mu$m from a perfect free-spectral range matching length $L_{n=23} = c/\left(2 \times \frac{\omega_{\mathrm{HF}}^{\mathrm{Cs}}}{2\pi \times 23}\right)$.

The second problem is that these frequencies change over the duration of the interferometer by an amount comparable to γ_{FWHM}. For example, in a 100 ms interferometer, the Doppler shift of the atom changes by $\Delta\delta_{\mathrm{Dopp}} = k\,\delta v = k\,g\,\delta t = 2\pi\times$ 1.15 MHz. The shift in the two-photon Raman transition is twice that (since the atom sees each beam Doppler-shifted in a different direction). This means that in moving from say, a negative Doppler shift at the beginning of the launch to a positive Doppler shift on the way back down, the two-photon Raman resonance in the lab frame would have moved from $\delta_{\mathrm{HF}}^{\mathrm{offs}} - \delta_{\mathrm{Dopp}}$ to $\delta_{\mathrm{HF}}^{\mathrm{offs}} + \delta_{\mathrm{Dopp}}$. This is shown in Fig. 4.1.

4.2 Cavity benefits

Optical intensity enhancement

Perhaps the most straightforward benefit of the cavity is the higher optical power afforded by resonant enhancement. For fixed Rabi frequency, higher available intensity allows lower single photon scattering by increasing the single-photon detuning Δ; since Rabi frequency scales as $1/\Delta$, while single photon scattering scales as $1/\Delta^2$.

Additionally, high intensity raises the ceiling on performance for Bragg diffraction. For example, Bragg diffraction requires an intensity proportional to n^2 for constant pulse duration, or n^4 for a constant single-photon scattering rate via increased detuning [40]. With resonant enhancement in a cavity, we may achieve $n = 50 - 100$ photon Bragg transitions using tens of milliwatts of power from a standard diode laser, as opposed to the multiple watt systems recently developed [67, 68].

Mode cleaning

A more subtle benefit is the spatial mode filtering an optical cavity provides. Since higher order transverse modes are not frequency degenerate in the cavity (as they are in free space), light resonant with the fundamental mode of the cavity primarily excites only that mode. This ensures a clean gaussian transverse profile of the laser beam. Additionally, wavefront distortions not meeting the cavity resonance criterion destructively interfere themselves away when summing up the many reflections between cavity mirrors. This means that the phase fronts inside the resonator are very smooth.

This second quality will turn out to be quite important. Wavefront aberrations limit performance in several types of matter wave manipulations (see Chapters 7 and 8) that we overcome with this apparatus.

Reduced experimental complexity

Resonant enhancement of the optical intensity enables a fiber EOM to generate the Raman frequencies. Without a cavity, a second laser is usually phase-locked to a master laser to generate the Raman beam pair. The Raman phase noise is in general higher for phase-locked lasers than for a simple microwave source used to drive an EOM (in addition to requiring the extra laser plus optical phase lock loop).

Relative alignment of these multiple beams also needs to be well-controlled. Even alignment of a retro-reflection for precision measurement is non-trivial. In a cavity, counter-propagation of the interferometry beams is automatic.

For rotation sensors, mutual alignment of multiple beams is critical and tedious [17, 69]. Using multiple transverse spatial modes of the cavity could provide mutually self-aligned beams for a rotation sensor (see, e.g., Fig. 4.14 later in the chapter).

Well-defined beam parameters

Uncertainties due to optical wave front curvature, and Gouy phase shifts are leading systematics in precision experiments using atomic fountains [6–8, 41]. The well-defined geometry of an optical cavity reduces these: beam parameters can be determined precisely by measuring spectral features of the cavity, such as the transverse mode spacing (Sec. 3.2).

Many systematics are more easily controlled in a small volume, such as gravity gradients, electric and magnetic fields and gradients and source mass distribution. The combination of large momentum transfer (see Chapter 7) and long coherence times in an optical lattice (see Chapter 8) could provide high sensitivity in a compact area.

4.3 Raman pulses in a cavity

4.3.1 Finite-sized cloud in a finite-sized beam

An unavoidable feature of our experimental setup is that the atom cloud is approximately the same size as the interferometry beam. This is partly because the cavity mode is used to form the lattice for Raman sideband cooling, and partly because the cavity mode is used to launch the atoms.

Since the atom cloud's $\frac{1}{e}$ radius σ is comparable to the waist w_0 of the cavity mode, the atoms see a spread of beam intensities. We can assume a spherical gaussian atom distribution

$$n_{\text{atom}}(r) = \frac{N_0}{\pi^{3/2}\sigma^3} \exp\left(-\frac{r^2}{\sigma^2}\right), \tag{4.1}$$

where the normalization constant is such that $\int_0^\infty dr\, 4\pi r^2 n_{\text{atom}}(r) = N_0$, the total atom number. Note that r is the radial distance to the center of the cloud.

The gaussian beam meanwhile has intensity

$$\begin{aligned} I(\rho) &= I_0 \left(\frac{w_0}{w(z)}\right)^2 \exp\left(-\frac{2\rho^2}{w(z)^2}\right) \\ &\approx I_0 \exp\left(-\frac{2\rho^2}{w_0^2}\right), \end{aligned} \tag{4.2}$$

where ρ is the distance from the center of the beam transverse to the propagation axis. In the second line, we have used that our beam diverges weakly, so $w(z) \approx w_0$. The intensity, and thus the Rabi frequency (which we will ultimately be interested in), then depend only on ρ. The distribution of such quantities (i.e., that depend only on ρ) over the atom cloud is then given by integrating the atomic distribution around the azimuthal angle ϕ and along the propagation axis z:

$$n_{\text{atom, radial}}(\rho) = \int \rho\, d\phi\, dz\; n_{\text{atom}}(r)$$

$$= \frac{2N_0}{\sigma^2}\rho e^{-\rho^2/\sigma^2}, \tag{4.3}$$

This is the distribution of radial positions of the atoms, and is shown for a few values of σ in Fig. 4.2.

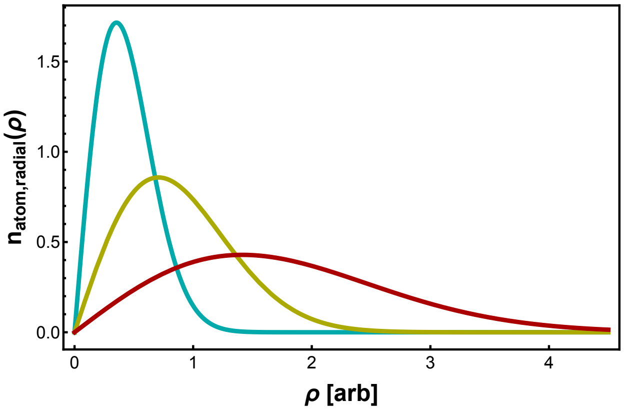

Figure 4.2: Radial distribution of atoms, eq. 4.3, plotted for $\sigma = 0.5, 1, 2$.

The resulting distribution in atom-laser couplings makes it difficult to uniformly address the atoms using the cavity mode. Specifically, π mirror pulses and $\pi/2$ beamsplitter pulses can only address some atom-averaged optimum, but not provide the π or $\pi/2$ condition for all atoms, reducing interferometer contrast. This effect worsens as the cloud thermally expands throughout its time-of-flight. Here, we quantitatively outline this spread in atom-laser coupling [2].

We first parameterize the intensity distribution with a unitless variable α:

$$I_{\text{atom},i} = \alpha_i I_0$$

where $I_{\text{atom},i}$ is the intensity seen by some atom i. Comparing explicitly with eq. 4.2, we see that $\alpha_i = \exp\left(-\frac{2\rho_i^2}{w_0^2}\right)$.

Let's introduce some notation. We will indicate the probability distribution function (pdf) of a continuous real random variable (rrv) X by $f_X(x)$. We indicate the cumulative distribution function (cdf) as $F_X(x)$, which is defined according to

$$F_X(x) = \int^x f_X(x')dx' \tag{4.4}$$

where the lower bound on the integration is the lower limit of the range X.

If we consider an atom's position to be a rrv drawn from the cloud according to eq. 4.3, the pdf is

---

[2] We have also developed a technique using adiabatic passage to address this inhomogeneous coupling problem, which is described in detail in Chapter 7

$$f_P(\rho) = \frac{2}{\sigma^2}\rho e^{-\rho^2/\sigma^2}, \tag{4.5}$$

where σ is again the $\frac{1}{e}$ radius of the atomic cloud. To get the distribution of intensity scaling α, we look at the laser intensities seen by this radial position distribution.

The laser intensity decreases with increasing radial coordinate ρ according to eq. 4.2, so $\alpha = 1$ at the center of the cloud. Then, $\alpha \in [0, 1]$ for all atoms in the cloud. α is now also a rrv with some distribution. The distribution can be found using the following steps:

1. Invert the relationship $\alpha(\rho)$ to get $\rho(\alpha)$
2. Integrate the pdf $f_P(\rho)$ to get the cdf $F_P(\rho) = \int_0^\rho f_P(\rho')d\rho'$
3. Evaluate the cdf of ρ for a given α to get the cdf of α: $F_A(\alpha) = 1 - F_P(\rho(\alpha))$
    i) Note: α is a *decreasing* function of ρ. For the cdf of α to be defined in the standard way (eq. 4.4), we therefore need the $1 - \ldots$
4. Take the derivative to get the pdf for α: $f_A(\alpha) = \frac{d}{d\alpha}F_A(\alpha)$

This procedure gives us the pdf for α:

$$f_A(\alpha) = x\alpha^{x-1} \tag{4.6}$$

where $x = \frac{w_0^2}{2\sigma^2}$, w_0 is the laser beam waist, and $\alpha \in [0, 1]$.

The atom cloud has a time-dependent σ. Assuming a gaussian distribution of velocities in the transverse directions (in addition to the gaussian position distributions), the size of the cloud follows [70]

$$\sigma(t) = \sqrt{\sigma_0^2 + \sigma_{\mathrm{v}}^2 t^2}, \tag{4.7}$$

where σ_0 is the initial size of the cloud and

$$\sigma_{\mathrm{v}} = \sqrt{\frac{k_{\mathrm{B}}T}{m_{\mathrm{Cs}}}}$$

is the velocity width as a function of temperature. The pdf $f_A(\alpha)$ thus changes over the atoms' time-of-flight (TOF), as can be seen in Fig. 4.3.

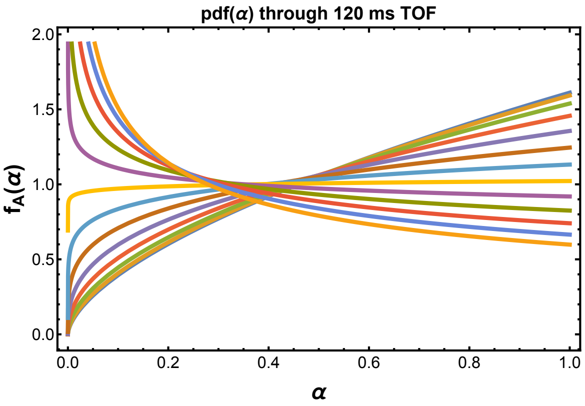

Figure 4.3: Intensity distributions for various TOF using our experimental values $w_0 = 718$ μm, $T = 300$ nK, and an initial cloud size of $\sigma_0 = 400$ μm. At early times, the distributions favor higher α near 1. As the cloud expands, more of it leaves the beam, and the distribution shifts towards α near 0. Times plotted range from $t = 0$ to $t = 120$ ms in increments of 10 ms.

This time-evolving distribution also implies a time-evolving average intensity seen by the cloud, as demonstrated by the expectation value $\bar{\alpha} := \langle \alpha \rangle$:

$$\bar{\alpha} = \int_0^1 d\alpha \, \alpha f_A(\alpha) = \frac{1}{1 + x^{-1}}$$

The average intensity across the cloud is seen in Fig. 4.4. Also shown is the standard deviation σ_α of α. The standard deviation is the square root of the variance $\mathrm{Var}(\alpha)$, which is given by

$$\mathrm{Var}(\alpha) = \int d\alpha \, (\alpha - \bar{\alpha})^2 f_A(\alpha) = \frac{1}{(1 + 2x^{-1})\,(1 + x)^2}$$

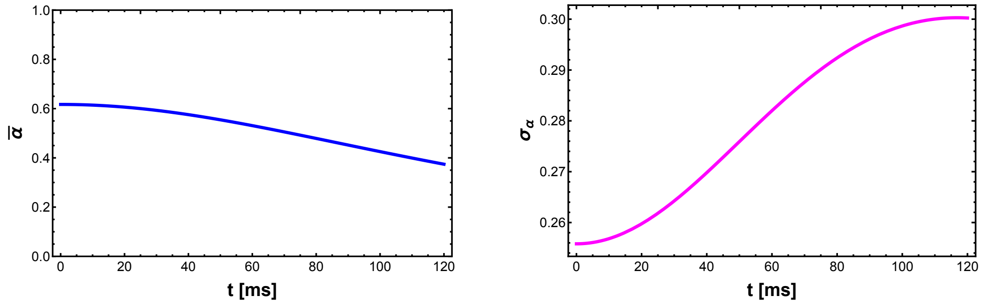

Figure 4.4: **a)** Average intensity $\bar{\alpha}$ and **b)** standard deviation $\sigma_\alpha = \sqrt{\mathrm{Var}(\alpha)}$, both using the same experimental parameters as in Fig. 4.4. Note the different vertical scales in the two plots.

Interestingly, this intensity distribution admits a closed form solution for Rabi flopping across the cloud. Each atom undergoes Rabi flopping according to

$$P(\alpha, t) = \frac{1}{2}\left(1 - \cos(\alpha\Omega t)\right)$$

where $P(\alpha, t)$ is the probability for atom with intensity scaling α to have undergone a transition after a pulse has been applied for a time t. The average probability P over the cloud can then be found by integrating over the α distribution:

$$\begin{aligned} P(t) &= \int_0^1 d\alpha\, f_A(\alpha) P(\alpha, t) \\ &= \frac{1}{2}\left[1 - {}_1F_2\left(\frac{x}{2};\ \frac{1}{2}, 1 + \frac{x}{2};\ -\frac{1}{4}\Omega^2 t^2\right)\right] \end{aligned} \tag{4.8}$$

This looks like a mess, but it's understandable. ${}_pF_q\left(a_1, ..., a_p; b_1, ..., b_q; z\right)$ is a *generalized hypergeometric function*. This is just a name for a particular class of power series, which will be briefly described below (but feel free to gloss over). The power series is defined by

$${}_pF_q\left(a_1, ..., a_p; b_1, ..., b_q; z\right) = \sum_{k=0}^{\infty} \frac{(a_1)_k \ldots (a_p)_k}{(b_1)_k \ldots (b_q)_k} \frac{z^k}{k!}$$

where $(q)_n$ is the rising Pochhammer symbol, defined by

$$(q)_n = \begin{cases} 1 & n = 0 \\ q(q+1)\cdots(q+n-1) & n > 0 \end{cases}$$

In our case, $p = 1$, $q = 2$, and we're only concerned with real $z = -\frac{1}{4}\Omega^2 t^2$. More information on generalized hypergeometric functions can be found in Chapter 16 of Ref. [71].

Eq. 4.8 is interesting because we now have an analytic solution to Rabi flopping of a finite sized beam in a finite-sized cloud. The solution has only one physical parameter: $\frac{\sigma}{w_0}$, the size ratio of the cloud and the beam. Fig. 4.5 shows plots for various values of $\frac{\sigma}{w_0}$.

It would be useful to incorporate a spread of detunings δ (due to ac Stark shifts and/or Doppler shifts) into eq. 4.8. At the moment, this behavior is not captured. One example where this would be useful is seeing the advantage of going to higher Rabi frequency Ω with such a detuning spread. Loosely speaking, higher Ω → shorter t_π → "worse" frequency resolution → higher bandwidth over which the pulse is efficient. Slightly more quantitatively, for higher Ω, the generalized Rabi frequency $\tilde{\Omega} = \sqrt{\Omega^2 + \delta^2}$ at which the population *really* oscillates (see eq. 2.50) is dominated by the Rabi frequency rather than the detuning.

A Doppler detuning spread would presumably behave differently than an ac Stark shift spread, since the latter is intensity-dependent like the Rabi frequency, while the former is not. That is, we could write the generalized Rabi frequency as something like:

$$\tilde{\Omega} = \sqrt{(\alpha\Omega)^2 + \left((\alpha - \alpha')\delta_{\mathrm{ac},\alpha'} + \delta_{\mathrm{Dopp}}\right)^2}$$

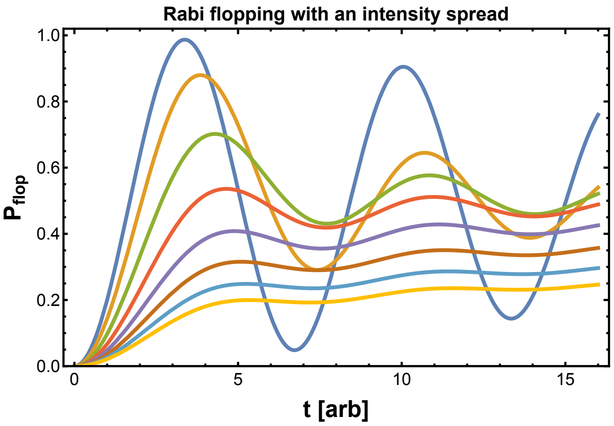

Figure 4.5: Analytic solutions for Rabi flopping of a finite-sized cloud in a finite-sized beam. Curves shown for $\frac{\sigma}{w_0}$ from 0.2 to 1.6 in steps of 0.2.

The above formula assumes the Raman frequency has been found by maximizing the transferred atomic population, corresponding to being exactly on-resonance for some α' (including ac Stark shift). A velocity distribution giving a pdf for δ_{Dopp} would also be used (probably symmetric about zero). An analytic form including these detuning effects would be nice to casually explore such questions, but we are not sure if it exists. If this type of question were to become important, Monte Carlo simulations could be performed.

4.3.2 Rabi frequency and ac Stark shift with multiple beams

To perform Raman pulses, light from the science laser passes through a fiber EOM. By modulating at frequency ω_{mod}, the science laser at frequency ω_L is phase modulated:

$$\begin{aligned} E_L e^{i\omega_L t} &\rightarrow E_L e^{i\omega_L t + \beta \sin(\omega_{\mathrm{mod}} t)} \\ &= E_L \sum_{n=-\infty}^{\infty} J_n(\beta) e^{i(\omega_L + n\omega_{\mathrm{mod}})t} \end{aligned} \tag{4.9}$$

where β is known as the modulation depth, and J_n is a Bessel function of the first kind. The second line uses an identity called the Jacobi-Anger expansion. The modulation depth is controlled by the amplitude of the modulation voltage into the EOM.

We see that phase modulation of the input optical beam gives an output spectrum with optical frequencies separated by the modulation frequency, whose strengths are given by Bessel functions. A pictorial representation of this beam incident upon the cavity is shown in Fig. 4.6.

An atom can absorb an upward-propagating photon and stimulated-emit into a downward-propagating field to undergo the two-photon Raman process. This preceding sentence holds true as well if "upward" and "downward" are interchanged. These two processes differ in the

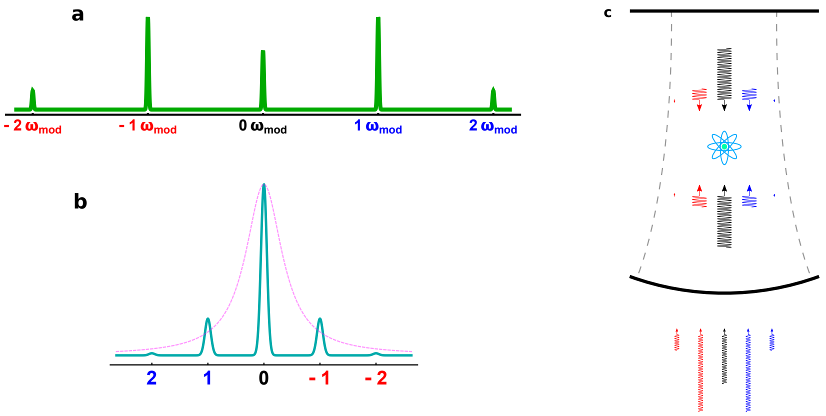

Figure 4.6: Raman beams incident on the cavity. The EOM phase modulates its input beam according to eq. 4.9. The resulting spectrum is shown in **(a)**, with modulation depth is $\beta = 1.6$ (a bit higher than typical experimental values $\beta \approx 1.2$ for better clarity in this figure). In **(b)**, the resonant enhancement of the cavity is taken into account. Here, $\omega_{\mathrm{mod}} = \omega_{\mathrm{HF}}^{\mathrm{Cs}}$. The carrier is centered on the cavity. $\omega_{\mathrm{HF}}^{\mathrm{Cs}}$ is $\delta_{\mathrm{HF}}^{\mathrm{offs}} = 3.80$ MHz short of 23 free spectral ranges, so the blue sideband has negative cavity detuning. The cavity lineshape is shown in the pink trace for reference. In **(c)**, the relevant beams to drive a Raman transition inside the cavity are shown. All beams propagate in both directions, and have circular polarization. The length of the wiggly lines indicates the intensity of the optical field at that frequency, as in **(a)** and **(b)**.

sign of their Doppler shift, and can thus be chosen via the appropriate sign detuning (though near zero velocity, they become degenerate and cannot be independently selected). We will refer to these different process as k^+ or k^-. We will use k^+ (k^-) to indicate the transition whose Doppler shift is increasing (decreasing) in time due to acceleration from gravity.

Sometimes the ± is used to refer to direction of the momentum kick. This is ambiguous, as the sign of the momentum kick depends on whether the transition is from $|F=3\rangle \rightarrow |F=4\rangle$ or vice versa. So in our definition, both k^+ and k^- can kick the atom in either direction, depending on the initial state.

To keep the Raman pair resonant with the atoms throughout their time of flight, the Raman frequency is ramped to account for the Doppler shift. This ramp rate α required is

$$\alpha = 2 \times \frac{d\delta_{\mathrm{Dopp}}}{dt} = 2\frac{g}{\lambda} = 23\frac{\mathrm{kHz}}{\mathrm{ms}},$$

where the extra factor of 2 comes from each of the counter-propagating beams seeing opposite Doppler shifts. We will refer to this Doppler-compensation frequency ramping as “gravity-ramping”, or “the gravity ramp”.

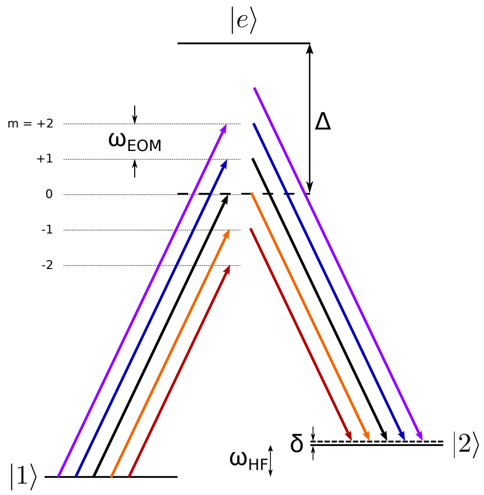

Figure 4.7: Atomic energy levels and laser frequencies with the output of an EOM incident on the cavity. m refers to the EOM sideband order, and $\omega_{\mathrm{EOM}} \approx \omega_{\mathrm{HF}}$.

4.3.2.1 Theory

Multiple orders from an EOM

The optical intensity afforded by the cavity allows use of a fiber EOM to generate the Raman beams. While reducing experimental complexity compared to an additional phase locked laser, it comes at the cost of additional unwanted frequency components (eq. 4.9). As seen from Fig. 4.1, the spacing of these frequency components relative to the cavity linewidth, the amount they move during an interferometer sequence, and the cavity linewidth itself are all comparable. This leads to complicated behavior.

Multiple beams separated by the Raman frequency provide multiple channels to drive the transition. These channels will interfere with each other, either constructively or destructively. To see how, we analyze a Raman transition in such a multi-chromatic field:

$$\boldsymbol{E} = \sum_{j,\text{upward}} E_j \cos\left(\omega_j t - \varphi_j - k_j z\right) + \sum_{\ell,\text{downward}} E_\ell \cos\left(\omega_j t - \varphi_j + k_\ell z\right) \tag{4.10}$$

$$= -2 \sum_i E_i \sin(\omega_i - \varphi_i) \sin(k_i z) \tag{4.11}$$

where in the second line we have assumed a perfect retroreflection such that there are an equal number of upward and downward propagating beams, $E_\ell = -E_j$ and $\omega_j = \omega_\ell$. The wavenumber k is given by $\omega = ck$. The sum is rewritten as a sum of standing waves in the second line of the equation.

The atomic energy levels and laser frequencies are shown in Fig. 4.7. The single photon detuning is Δ, and the ac Stark shift is δ_{ac}, both of which we take to be positive quantities for the arrangement shown here. Beams originating from an EOM are shown, and the modulation frequency is assumed to be on-resonant with the ac Stark-shifted target level. These equations make explicit the frequency relations shown in Fig. 4.7:

$$\omega_{L0} = \omega_{1e} - \Delta \tag{4.12}$$
$$\omega_{2e} = \omega_{1e} - \Delta_{\text{hfs}} \tag{4.13}$$
$$\omega_m = \omega_{L0} + m\omega_{\text{mod}} \tag{4.14}$$
$$\omega_{\text{mod}} = \Delta_{\text{hfs}} - \delta_{\text{ac}} - 2\delta_{\text{Dopp}} \tag{4.15}$$

δ_{Dopp} is the Doppler shift, ω_{L0} is the input laser frequency to the EOM and $\omega_{ij} = \frac{1}{\hbar}(E_i - E_j)$ represents the energy difference between levels i and j. Including $\delta_{\text{Dopp}} \neq 0$ provides for the selectivity between the $k^{\pm}$ transitions.

We can then use the machinery from Chapter 2 to solve the Schrödinger equation for the multichromatic field. A Hamiltonian is first written via eq. 2.31:

$$\hat{H} = \begin{pmatrix} E_1 & 0 & V_{1e} \\ 0 & E_2 & V_{2e} \\ V_{e1} & V_{e2} & E_e \end{pmatrix}$$

A transformation:

$$\hat{T} = \begin{pmatrix} e^{iE_1 t/\hbar} & 0 & 0 \\ 0 & e^{i(E_2-\delta_{\text{ac}})t/\hbar} & 0 \\ 0 & 0 & e^{iE_e t/\hbar} \end{pmatrix}$$

is then applied. We leave the δ_{ac} term in the phase because the light shift for a given field arrangement is not known a priori (though we will solve for it). $\hat{T}$ transforms the Hamiltonian, as in eq. 2.36, to:

$$\hat{H}' = \begin{pmatrix} 0 & 0 & \tilde{V}_{1e} \\ 0 & \delta_{\text{ac}} & \tilde{V}_{2e} \\ \tilde{V}_{e1} & \tilde{V}_{e2} & 0 \end{pmatrix}$$

The excited state $|e\rangle$ can then be adiabatically eliminated (see 2.3.2 for details, in particular equation 2.45):

$$b_e(t) = b_1\left(\int \tilde{V}_{e1}(t)\right) + b_2\left(\int \tilde{V}_{e2}(t)\right)$$

From here, the setup of the problem will follow Refs. [72, 73]. Substituting this expression for b_e back into the equations for b_1 and b_2 gives an effective two-level system:

$$\frac{d}{dt}\begin{pmatrix} c_1 \\ c_2 \end{pmatrix} = i\hat{W}\begin{pmatrix} c_1 \\ c_2 \end{pmatrix}$$

with

$$\hat{W} = \frac{1}{4}\begin{pmatrix} A & B \\ C & D \end{pmatrix} \tag{4.16}$$

where the elements of $\hat{W}$ are determined by V (in this case, the laser beams we apply), and the change from b_i to c_i signifies that we have reduced the three-level system to a two-level system. Eq. 4.16 is equivalent to the differential equation

$$\begin{aligned} &\ddot{c}_1(t) + i\frac{A+D}{4}\dot{c}_1(t) + \frac{AD-BC}{16}c_1(t) = 0 \\ &\ddot{c}_2(t) = -\frac{4i}{B}\dot{c}_1(t) - \frac{A}{B}c_1(t) \end{aligned}$$

If $c_1(0) = 1$, $c_2(0) = 0$ (i.e., the system starts in $|1\rangle$), this system has the solution

$$\begin{aligned} c_1(t) &= 1 - \Lambda \sin^2\left(\frac{\Omega_R}{2}t\right) \\ c_2(t) &= \Lambda \sin^2\left(\frac{\Omega_R}{2}t\right) \end{aligned}$$

with

$$\Lambda = \frac{4BC}{(A-D)^2 + 4BC}$$

and

$$\Omega_R = \frac{1}{4}\sqrt{(A-D)^2 + 4BC}$$

where Ω_R is the two-photon Rabi frequency. Full contrast between the two states is achieved by maximizing $\Lambda \to 1$ by having $A = D$. This condition is achieved with the appropriate δ_{ac}, telling us the ac Stark shift.

The problem then boils down to constructing this $\hat{W}$ matrix from a given field arrangement. Applying the rotating wave approximation makes the expressions tractable. This provides the quantities of interest: the Rabi frequency Ω_R and the ac Stark shift δ_{ac}.

Mathematica can be used to churn through this algebra. For anyone that doesn't want to do that, the results for up to 3rd order EOM sidebands are below. The formulas have many terms, but each term has a clear physical interpretation and follows a pattern. The full formulas will be presented first, followed by the physical interpretation and generalization into a pattern. This greatly simplifies the expression, and we posit that the pattern extends beyond 3rd order sidebands.

The single photon Rabi frequency for the mth sideband is denoted by Ω_m. While up to third order is given, typical modulation depths $\beta \sim 1.2$ give small enough contributions to higher order sidebands that they can be ignored (by setting some $\Omega_m = 0$). Terms involving only carrier and first-order sidebands will be shown in black, those that involve second-order are shown in violet, and those with third-order appear in dark green.

The ac Stark shift is found by setting $A = D$. We make use of $\delta_{\rm ac} \ll \Delta, \Delta_{\rm hfs}$ to solve for $\delta_{\rm ac}$:

$$\begin{aligned}\delta_{\rm ac} = &\left(\frac{\Delta_{\rm hfs}}{4\Delta(\Delta-\Delta_{\rm hfs})}\right)\Omega_0^2 + \left(\frac{\Delta_{\rm hfs}}{4(\Delta-2\Delta_{\rm hfs})(\Delta-\Delta_{\rm hfs})}\right)\Omega_1^2 + \left(\frac{\Delta_{\rm hfs}}{4\Delta(\Delta+\Delta_{\rm hfs})}\right)\Omega_{-1}^2 \\ &+ \left(\frac{\Delta_{\rm hfs}}{4(\Delta-3\Delta_{\rm hfs})(\Delta-4\Delta_{\rm hfs})}\right)\Omega_2^2 + \left(\frac{\Delta_{\rm hfs}}{4(\Delta+\Delta_{\rm hfs})(\Delta+2\Delta_{\rm hfs})}\right)\Omega_{-2}^2 \\ &+ \left(\frac{\Delta_{\rm hfs}}{4(\Delta-4\Delta_{\rm hfs})(\Delta-3\Delta_{\rm hfs})}\right)\Omega_3^2 + \left(\frac{\Delta_{\rm hfs}}{4(\Delta+2\Delta_{\rm hfs})(\Delta+3\Delta_{\rm hfs})}\right)\Omega_{-3}^2 \end{aligned} \tag{4.17}$$

Each beam contributes a term to the ac Stark shift which can be seen to reflect that beam's intensity (Ω_m^2) and the product of its detunings from the atomic transition ($\Delta - m\omega_{\rm mod} \approx \Delta - m\Delta_{\rm hfs}$) between the excited state and the each of the two hyperfine ground states being coupled.

The Rabi frequency is more complicated, but the terms also follow a pattern:

$$\begin{aligned}4\Omega_R^2 = &\frac{\Omega_1^2\Omega_0^2}{(\Delta-\Delta_{\rm hfs})^2} + \frac{\Omega_0^2\Omega_{-1}^2}{\Delta^2} + \frac{\Omega_2^2\Omega_1^2}{(\Delta-2\Delta_{\rm hfs})^2} + \frac{\Omega_{-1}^2\Omega_{-2}^2}{(\Delta+\Delta_{\rm hfs})^2} + \frac{\Omega_3^2\Omega_2^2}{(\Delta-3\Delta_{\rm hfs})^2} + \frac{\Omega_{-2}^2\Omega_{-3}^2}{(\Delta+2\Delta_{\rm hfs})^2} \\ &+ \frac{2\Omega_1\Omega_0^2\Omega_{-1}\cos(2k_{\rm rf}z+\varphi_1-2\varphi_0+\varphi_{-1})}{\Delta(\Delta-\Delta_{\rm hfs})} \\ &+ \frac{2\Omega_2\Omega_1^2\Omega_0\cos(2k_{\rm rf}z+\varphi_2-2\varphi_1+\varphi_0)}{(\Delta-2\Delta_{\rm hfs})(\Delta-\Delta_{\rm hfs})} + \frac{2\Omega_0\Omega_{-1}^2\Omega_{-2}\cos(2k_{\rm rf}z+\varphi_0-2\varphi_{-1}+\varphi_{-2})}{\Delta(\Delta+\Delta_{\rm hfs})} \\ &+ \frac{2\Omega_2\Omega_1\Omega_0\Omega_{-1}\cos(4k_{\rm rf}z+\varphi_2-\varphi_1-\varphi_0+\varphi_{-1})}{\Delta(\Delta-2\Delta_{\rm hfs})} + \frac{2\Omega_1\Omega_0\Omega_{-1}\Omega_{-2}\cos(4k_{\rm rf}z+\varphi_1-\varphi_0-\varphi_{-1}+\varphi_{-2})}{(\Delta-\Delta_{\rm hfs})(\Delta+\Delta_{\rm hfs})} \\ &+ \frac{2\Omega_3\Omega_2^2\Omega_1\cos(2k_{\rm rf}z+\varphi_3-2\varphi_2+\varphi_1)}{(\Delta-3\Delta_{\rm hfs})(\Delta-2\Delta_{\rm hfs})} + \frac{2\Omega_{-1}\Omega_{-2}^2\Omega_{-3}\cos(2k_{\rm rf}z+\varphi_{-1}-2\varphi_{-2}+\varphi_{-3})}{(\Delta+\Delta_{\rm hfs})(\Delta+2\Delta_{\rm hfs})} \\ &+ \frac{2\Omega_3\Omega_2\Omega_1\Omega_0\cos(4k_{\rm rf}z+\varphi_3-\varphi_2-\varphi_1+\varphi_0)}{(\Delta-3\Delta_{\rm hfs})(\Delta-\Delta_{\rm hfs})} + \frac{2\Omega_0\Omega_{-1}\Omega_{-2}\Omega_{-3}\cos(4k_{\rm rf}z+\varphi_0-\varphi_{-1}-\varphi_{-2}+\varphi_{-3})}{\Delta(\Delta+2\Delta_{\rm hfs})} + \\ &+ \frac{2\Omega_1\Omega_0\Omega_{-2}\Omega_{-3}\cos(6k_{\rm rf}z+\varphi_1-\varphi_0-\varphi_{-2}+\varphi_{-3})}{(\Delta-\Delta_{\rm hfs})(\Delta+2\Delta_{\rm hfs})} + \frac{2\Omega_2\Omega_1\Omega_{-1}\Omega_{-2}\cos(6k_{\rm rf}z+\varphi_2-\varphi_1-\varphi_{-1}+\varphi_{-2})}{(\Delta-2\Delta_{\rm hfs})(\Delta+\Delta_{\rm hfs})} + \frac{2\Omega_3\Omega_2\Omega_0\Omega_{-1}\cos(6k_{\rm rf}z+\varphi_3-\varphi_2-\varphi_0+\varphi_{-1})}{\Delta(\Delta-3\Delta_{\rm hfs})} \\ &+ \frac{2\Omega_3\Omega_2\Omega_{-1}\Omega_{-2}\cos(8k_{\rm rf}z+\varphi_3-\varphi_2-\varphi_{-1}+\varphi_{-2})}{(\Delta-3\Delta_{\rm hfs})(\Delta+\Delta_{\rm hfs})} + \frac{2\Omega_2\Omega_1\Omega_{-2}\Omega_{-3}\cos(8k_{\rm rf}z+\varphi_2-\varphi_1-\varphi_{-2}+\varphi_{-3})}{(\Delta-2\Delta_{\rm hfs})(\Delta+2\Delta_{\rm hfs})} \\ &+ \frac{2\Omega_3\Omega_2\Omega_{-2}\Omega_{-3}\cos(10k_{\rm rf}z+\varphi_3-\varphi_2-\varphi_{-2}+\varphi_{-3})}{(\Delta-3\Delta_{\rm hfs})(\Delta+2\Delta_{\rm hfs})} \end{aligned} \tag{4.18}$$

First, each resonant pair contributes a non-negative term; these terms are listed in the first line. The rest of the terms represent interference between different *pairs* of beams driving transitions. Whether this interference is constructive or destructive depends on the differences of phases φ_i (which are space- and time-independent) between the beam pairs, and spatial location (since the total phase differences do vary in space). An interference term $\tilde{R}_{mn}$ has the form

$$\tilde{R}_{mn} = \frac{\Omega_m\Omega_{m-1}\Omega_n\Omega_{n-1}}{(\Delta-m\Delta_{\rm hfs})(\Delta-n\Delta_{\rm hfs})}\cos\left(2|m-n|k_{\rm rf}z+\varphi_m-\varphi_{m-1}-\varphi_n+\varphi_{n-1}\right). \tag{4.19}$$

$k_{\mathrm{rf}} = \Delta_{\mathrm{hfs}}/c$ is the wavevector of the hyperfine frequency Δ_{hfs}; for cesium it is $\frac{2\pi}{3.26\ \mathrm{cm}}$. Noticing that this expression with $m = n$ also describes the non-interference terms in the first line of eq. 4.18, we can write the much-simplified expression

$$4\Omega_R^2 = \sum_{m,n=-N+1}^{N} \tilde{R}_{mn} \tag{4.20}$$

where N is the highest order of EOM sidebands being considered. This expression has been algebraically verified up to $N = 3$. Given the clear physical interpretation of each aspect of the terms in eq. 4.18, however, it seems reasonable to assume its validity beyond that.

If we take the same liberties in defining and extrapolating for δ_{ac}, we can define

$$\begin{aligned}\tilde{S}_m &= \frac{\Delta_{\mathrm{hfs}}}{4}\frac{\Omega_m^2}{(\Delta - m\Delta_{\mathrm{hfs}})(\Delta-(m+1)\Delta_{\mathrm{hfs}})} \\ &= \frac{\Omega_m^2}{4}\left(\frac{1}{\Delta-(m+1)\Delta_{\mathrm{hfs}}} - \frac{1}{\Delta - m\Delta_{\mathrm{hfs}}}\right)\end{aligned} \tag{4.21}$$

With this expression, the total ac Stark shift from eq. 4.17 simplifies, and can be seen as just the sum of the differential ac Stark shifts from each individual beam:

$$\delta_{\mathrm{ac}} = \sum_{m=-N}^{N} \tilde{S}_m. \tag{4.22}$$

Adding the cavity

We now make these beams incident on a cavity. As a function of cavity detuning δ, the circulating power in the cavity scales with a factor

$$s(\delta) = \frac{(\gamma/2)^2}{\delta^2 + (\gamma/2)^2}$$

where the above is normalized to unity on resonance, and γ defines the full-width half maximum of the Lorentzian. We will use the convention for cavity-related frequencies to be cyclical, i.e., measured in Hz (as opposed to angular). As a result, the Rabi frequency Ω_R^m for the mth sideband out of the EOM is

$$\Omega_R^m = J_m(\beta)\sqrt{s(\delta_{\mathrm{cav}}^m)}\,\Omega_{00}$$

where δ_{cav}^m is the detuning of the mth sideband from cavity resonance, and Ω_{00} is given by eq. 2.37 for the full electric field strength E_{00} of the beam before modulation into several frequency components. There is a square root because the Rabi frequency is proportional to the electric field, while $s(\delta)$ describes the intensity.

The zeroth order (carrier) is offset from cavity resonance by an amount δ_{cav}. Where the sidebands fall on the cavity lineshape depends on the free spectral range and the EOM modulation frequency. The offset from cavity resonance for sideband m is

$$\delta_{\text{cav}}^m = \delta_{\text{cav}} + \left(m\frac{\omega_{\text{mod}}}{2\pi} - \text{FSR} \times \text{round}\left(\frac{m\omega_{\text{mod}}/(2\pi)}{\text{FSR}}\right)\right). \tag{4.23}$$

where FSR = 399.845 MHz for our cavity. The formula captures the sign dependences discussed in Sec. 3.2 (where more details on the FSR-matching can be found). For example, at $\delta_{\text{cav}} = 0$ and $\omega_{\text{mod}} = \omega_{\text{HF}}^{\text{Cs}}$, the blue sideband has negative cavity detuning, $\delta_{\text{cav}}^{+1} < 0$. Note that the detuning δ_{cav}^m is a function of time, due to the gravity ramp.

Finally, the phases of the beams φ_m also depend on the detuning from cavity resonance (Sec. 2.6). That dependence is

$$\varphi_m = \arg\left(\frac{\tilde{E}_{m,\text{ circ}}}{\tilde{E}_{m,\text{ inc}}}\right) = \arctan\left(\frac{-r_1 r_2 \sin\left(2\pi\frac{\delta_{\text{cav}}^m}{\text{FSR}}\right)}{1 - r_1 r_2 \cos\left(2\pi\frac{\delta_{\text{cav}}^m}{\text{FSR}}\right)}\right),$$

as can be derived from the equations in Sec. 2.6, or from the presentation in Ref. [43].

Note that it is typical for phase-modulated sidebands to be considered to have intrinsic phases. For example, the carrier and +1 sideband have phase equal to 0, while the -1 order has π phase (reflecting that the beatnote between the carrier and the 1st order sideband is π out of phase with the beatnote at the same frequency of the carrier and the -1st order sideband). Here, we carry that dependence in the sign of the Bessel function $J_n(\beta)$, so it doesn't enter into φ_i.

These expressions provide the single photon Rabi frequencies Ω_m and the phases φ_m necessary to calculate the Rabi frequency and ac Stark shift for the output of a modulated EOM incident on a cavity using eqs. 4.20 and 4.22.

4.3.2.2 Comparison with experiment

We now present several comparisons between experiment and the preceding theory. In the following plots, parameters that are known and fixed are: EOM modulation frequency, atomic trajectory in the cavity, cavity linewidth and cavity offset. The initial position of the atoms relative to the cavity beatnote (that is, z_0 in $2k_{\text{rf}}z_0$) is fixed across all plots.

Some parameters are allowed to vary slightly. The free spectral range was most recently measured to be 399.845 MHz, but allowed to vary by up to 20 kHz between datasets. This accounts for thermal expansion; for a thermal expansion coefficient of steel $\alpha_T^{\text{steel}} = 13 \times 10^{-6}$/C, the FSR changes by 5.2 kHz/C. The cavity's ring piezo has a free stroke of 3.3 μm. This distance changes the cavity FSR by about 3.5 kHz, and so can be ignored with reasonable safety. That is, the fact that the cavity is locked to different integer numbers of 780 nm half-wavelengths is subdominant to temperature changes of the vacuum chamber when considering these Raman transition dynamics in the cavity.

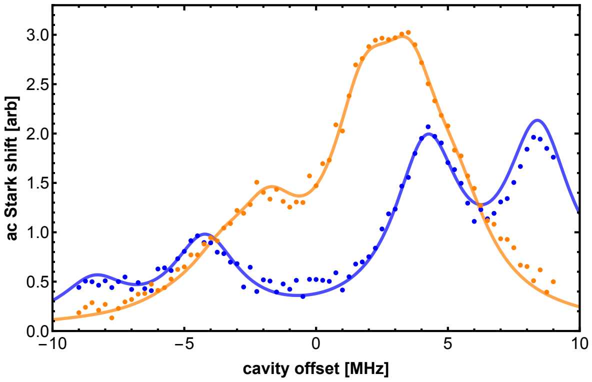

Figure 4.8: ac Stark shift vs. cavity offset for modulation depth $\beta = 2.37$. Two different EOM modulation frequencies are shown, $f_1^+ = f_{\mathrm{HF}}^{\mathrm{Cs}} - 1.4$ MHz and $f_3^+ = f_{\mathrm{HF}}^{\mathrm{Cs}} + 1.0$ MHz. $f_j^\pm$ were chosen to correspond to the jth pulse in a $k^\pm$, $T = 55$ ms Mach-Zehnder interferometer (see Sec. 5.6 for measurement details). Points are experimental data, and lines are theory with an overall scaling.

The modulation depth β is known to the few % level, but could be measured more accurately if needed.

Finally, a linear scaling $x' = mx$ for $x \in \{\Omega_R, \delta_{\mathrm{ac}}\}$ is applied to the measured values for comparison with theory. The absolute scale was not the point of the measurement; rather, variation with position and cavity offset was. Theory curves are fit by eye to the data via this linear scaling. A forthcoming publication will present similar measurements in more detail.

These data were measured before we had a complete understanding of what was happening in the cavity, hence the somewhat strange parameter collection. If this data were to be taken again, one could now do a much more consistent job of verifying the model. Spatial selection using the cavity catch could be used to suppress the effect of cloud expansion. Fitting unknown parameters, rather than "by-eye" choice would be preferable. Parameters could be more carefully controlled, for example, keeping positions exactly the same between $k^\pm$ transitions despite those velocity selection pulses kicking the atom cloud in opposite directions. Finally, ac Stark shift variation with cavity offset shifts the true resonance frequency. Off-resonant driving artificially increases the measured Rabi frequency (as the contrast simultaneously decreases). A more careful measurement would account for this effect.

4.4 Interferometry and results

With the properties of these intracavity pulses fleshed out: interferometry works! The historical time-ordering of these events was not linear; interferometry was performed in the

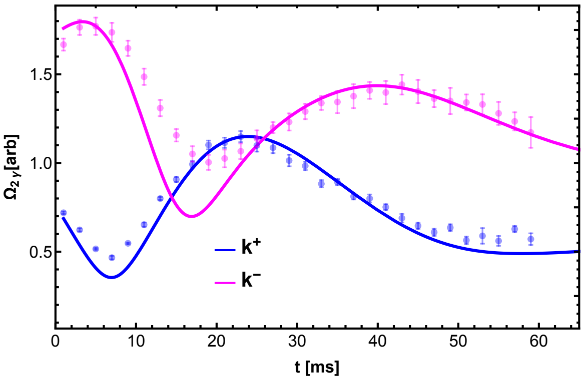

Figure 4.9: Spatial beatnote of the Rabi frequency for both k^+ and k^- transitions. Measurement was taken with $\beta = 0.9$, and at cavity offsets of 1.5 (-1.74) MHz for the $k^+(k^-)$ transition. There's no significance to these values being different, it's just where these particular datasets were taken. The inferred phase of the spatial beatnote at the initial position of the atoms is $2k_{\mathrm{rf}}z_0 \approx 0.5$ rad. At low contrast (which occurs at low Rabi frequencies), the Rabi frequency fit is less accurate.

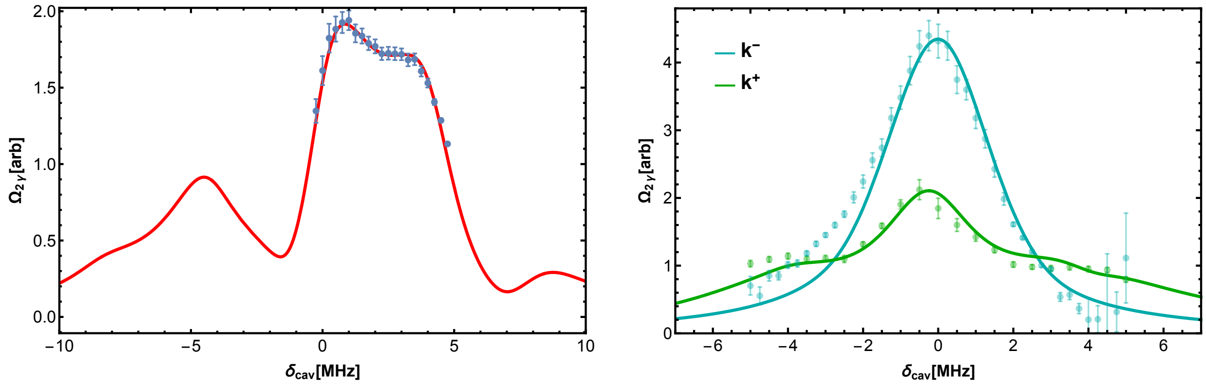

Figure 4.10: Rabi frequency vs. cavity offset. Left: k^+ transition 23 ms after the launch ($v_0 \approx 60$ cm/s just after the launch). Right: Both k^+ and k^- transitions, which differ in frequency, 0.5 ms after the launch. Both left and right use $\beta = 1.20$. Rabi frequency is inferred as in Fig. 4.9 caption.

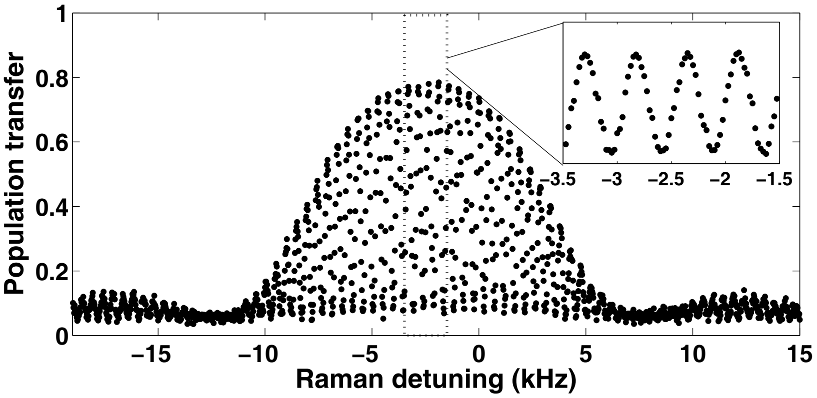

Figure 4.11: Optical Ramsey fringes with $T = 2$ ms. The ac Stark shift of the Raman pulses used is measured to be $\delta_{\mathrm{ac}} = -2.35$ kHz by the offset of the zero fringe from the cesium hyperfine frequency $\omega_{\mathrm{HF}}^{\mathrm{Cs}}$ (which corresponds to 0 on the x-axis). Inset shows the sinusoidal behavior predicted by eq. 2.60. Sufficiently far from resonance, contrast decreases as the pulses become off-resonant. This statement is made quantitative by carrying through the full pulse imperfection terms involving Θ from eqs. 2.50 into a more complete formula (fewer assumptions) for the beamsplitter operator $\hat{B}$.

cavity (about five years) before the properties in the preceding section were fully understood. In this section, we'll show some of our first data, representing the first realization of an atom interferometer inside an optical cavity [74].

As a first demonstration, we run an optical Ramsey clock in the cavity (see Sec. 2.3.3 for a derivation of this procedure). Raman transitions with a co-propagating pair of photons are velocity-insensitive, and transfer negligible momentum to the atoms. Two such Raman $\frac{\pi}{2}$ pulses between the clock states $|F = 3, m_{\mathrm{F}} = 0\rangle \to |F = 4, m_{\mathrm{F}} = 0\rangle$, spaced by a pulse separation time of $T = 2$ ms generate the Ramsey fringes shown in Fig. 4.11. The high contrast demonstrates good coherence of the process across the atomic cloud, despite the comparable size of the cloud and the interferometry beams. This is an optical version of a cesium fountain clock.

Finally, we demonstrate an atom interferometer. We perform a gravity measurement by a $\frac{\pi}{2} - \pi - \frac{\pi}{2}$ combination of three velocity-sensitive Raman pulses, forming a Mach-Zehnder interferometer. The Raman frequency is gravity-ramped at a rate of $k_{\mathrm{eff}} a_{\mathrm{eff}} \approx 2\pi \times 23$ kHz/ms for $a_{\mathrm{eff}} \approx g = 9.8$ m/s^2. We detect the interferometer outputs separately by first pushing atoms in $F = 4$ to the side with a blowaway beam, and then using fluorescence detection on a CCD camera to spatially resolve the two populations. After normalization to take out atom-number fluctuations, we obtain the interference fringes shown in Fig. 4.12 by scanning the Raman frequency ramp rate, parameterized by a_{eff}. When the ramp rate perfectly matches the acceleration, the interferometer phase, $k_{\mathrm{eff}}\left(g - a_{\mathrm{eff}}\right) T^2$, is zero independent of the pulse separation time T.

Additionally, we have used as little as 87 μW of power (at a smaller single photon

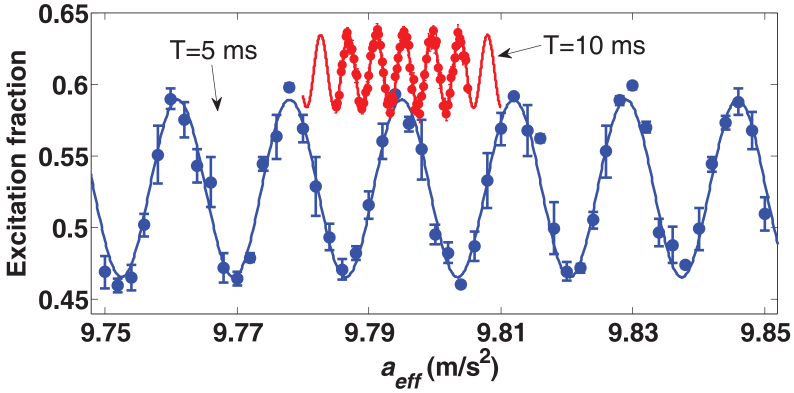

Figure 4.12: First fringes from the cavity interferometer: Mach-Zehnder fringes of a $\frac{\pi}{2} - \pi - \frac{\pi}{2}$ pulse sequence with pulse separation times $T = 5$ ms (blue) and $T = 10$ ms (red).

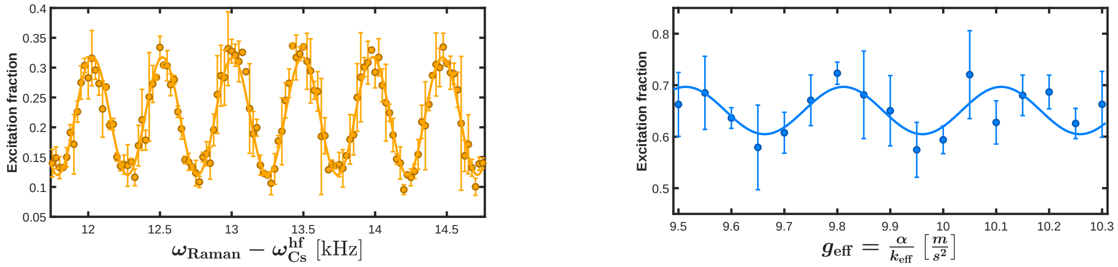

(a) 50 μW optical Ramsey clock, $T = 2$ ms.

(b) 87 μW Mach-Zehnder, $T = 1$ ms.

Figure 4.13: Low power interferometry

detuning $\Delta = 2$ GHz) to obtain fringes with $> 10\%$ contrast, as shown in Fig. 4.13b. To our knowledge, this is the lowest incident optical power ever used in an atom interferometer. At this detuning, we also obtained optical Ramsey fringes with 50 μW of optical power (Fig. 4.13a).

With these basic atom optics now demonstrated inside of an optical cavity, we can begin exploring a range of applications. For example, Fig. 4.14 shows a possible realization of a rotation sensor using the self-aligned transverse modes of the cavity, alongside a demonstration of atoms loaded into such modes. While we have not addressed this particular application, we have realized several others.

Since our first demonstration of atom interferometry in an optical cavity [74], we have improved our apparatus and techniques considerably. We have made science measurements, and developed new atom interferometer technologies. Each of the following chapters in this thesis provides an in-depth look at one such application. So with the groundwork of cavity atom interferometry finally laid, keep reading for the good stuff!

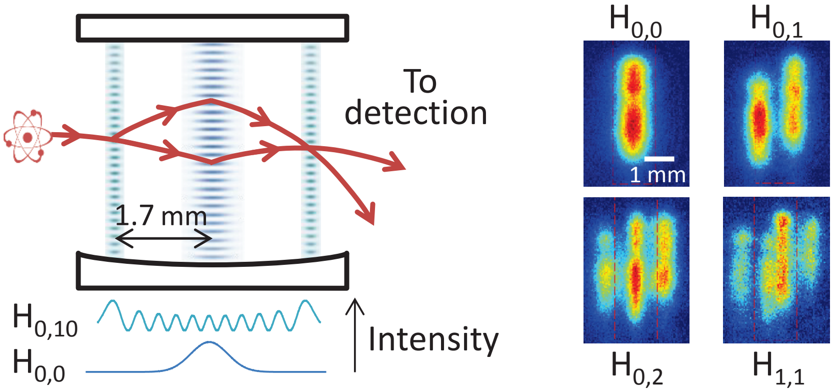

Figure 4.14: Higher order cavity modes for rotation sensing. Left: Possible implementation of a rotation-sensitive interferometer enclosing a spatial area using transverse cavity modes. Atoms enter the cavity from the side and are split by a pulsed standing wave in the Hermite-Gaussian $H_{0,10}$ cavity mode, reflected by a pulse in the fundamental $H_{0,0}$ mode,and interfered on the far side with a second pulse of the $H_{0,10}$ mode. Right: Fluorescence images of atoms in optical lattices formed by transverse modes of the optical cavity.

Chapter 5

Gravity and dark energy with a source mass

In this chapter, we use the cavity atom interferometer to measure the gravitational attraction between cesium atoms and a small, in-vacuum source mass. By observing only a gravitational interaction between the two, we constrain "screened field" models of dark energy, which would give rise to an anomalous force. Such models propose a dynamical scalar field to explain the observed accelerated expansion of the universe.

5.1 What is dark energy, and how do we know it's there?

General relativity, while over 100 years old, is our best understanding of gravity. The theory describes gravity as a curvature of spacetime due to the presence of matter, whose movement is in turn dictated by that curvature. As the adage goes, "spacetime tells matter how to move, and matter tells spacetime how to curve". The quantification of this statement is given by the Einstein field equation(s):

$$G_{\mu\nu} + \Lambda g_{\mu\nu} = 8\pi T_{\mu\nu} \tag{5.1}$$

The Einstein tensor $G_{\mu\nu} = R_{\mu\nu} - \frac{1}{2} R\, g_{\mu\nu}$ consists of the metric $g_{\mu\nu}$, the Ricci tensor, $R_{\mu\nu}$, and the Ricci scalar $R = g^{\mu\nu} R_{\mu\nu}$, also known as the curvature scalar. The Ricci tensor is itself a contraction of the Riemann curvature tensor $R_{\mu\nu} = R^{\alpha}{}_{\mu\alpha\nu}$. The Riemann tensor (redundantly) encodes the curvature of spacetime, or more generally, that of a Riemannian manifold. Both of these quantities, however, ultimately derive from the metric $g_{\mu\nu}$, which contains the geometric information about the spacetime, such as curvature, distances and angles. For a deep trip down the differential geometry rabbit hole in the context of general relativity, see the textbooks Refs. [75, 76].

$T_{\mu\nu}$ is the "energy-momentum" tensor. The distribution and dynamics of matter / energy density live within $T_{\mu\nu}$. The spacetime geometry, defined by the metric $g_{\mu\nu}$ and the connection on that metric, is encoded in the Einstein tensor $G_{\mu\nu}$. By linking these quantities (spacetime geometry and matter), to each other, eq. 5.1 motivates the aforementioned adage. Units are used where the gravitational constant G (not the Einstein tensor) and the speed of light c are normalized, $G = c = 1$, so that the simple presentation of eq. 5.1 can hide the considerable difficulty of unpacking and interpreting this tensor equation

The constant Λ has been conspicuously absent from the discussion thus far. Λ has been associated with the energy density of empty space, and therefore dubbed the "cosmological constant". The cosmological constant has a storied and confused history. Originally, it was introduced by Einstein into eq. 5.1 so that there could exist a static universe solution. Edwin Hubble in 1929 then published the discovery of our expanding universe [77], and Einstein's static universe solution was found to be unstable against perturbations anyways. The cosmological constant was then famously dubbed a "blunder", more confusion ensued, and much later Λ was experimentally found to be nonzero [78,79]. For a look into this confusing history, the introduction of Ref. [80] is a good start (and written before the discovery that $\Lambda > 0$, providing an interesting vantage point).

What effect does a non-zero cosmological constant have on the evolution of spacetime? Consider the Friedmann-Lemaître-Robertson-Walker (FLRW) metric:

$$-ds^2 = -dt^2 + a(t)d\Sigma^2 \qquad \Rightarrow \qquad g_{\mu\nu} = \begin{pmatrix} -1 & 0 & 0 & 0 \\ 0 & a(t) & 0 & 0 \\ 0 & 0 & a(t) & 0 \\ 0 & 0 & 0 & a(t) \end{pmatrix} \tag{5.2}$$

where the spacetime distance element ds^2 is composed of unchanging time-like separation dt^2, and a space-like separation $d\Sigma^2$. The space-like separation is uniform and isotropic, but has a time-dependent scale factor $a(t)$. This is equivalent to the metric $g_{\mu\nu}$ shown on the right. Let's take a matter distribution that is similarly uniform and isotropic,

$$T^{\mu}{}_{\nu} = \begin{pmatrix} \rho & 0 & 0 & 0 \\ 0 & -p & 0 & 0 \\ 0 & 0 & -p & 0 \\ 0 & 0 & 0 & -p \end{pmatrix} \tag{5.3}$$

where ρ is the mass-energy density, and p is the pressure. This matter distribution is commonly referred to as a "perfect fluid". The FLRW universe (the metric [eq. 5.2] plus the matter distribution [eq. 5.3]) is frequently used in cosmology; even being dubbed the "Standard Model of present-day cosmology" [81].

Pushing this metric and energy-momentum tensor through the Einstein equations 5.1 gives

$$\frac{\dot{a}^2 + kc^2}{a^2} = \frac{8\pi G\rho + \Lambda c^2}{3} \tag{5.4a}$$

$$\frac{\ddot{a}}{a} = -\frac{4\pi G}{3}\left(\rho + \frac{3p}{c^2}\right) + \frac{\Lambda c^2}{3} \tag{5.4b}$$

where $k = \{+1, 0, -1\}$ for positive, zero, or negative curvature respectively in the uniform spacetime. These are the so-called *Friedmann equations*. The Friedmann equations describe the time evolution of the scale factor $a(t)$ in the FLRW universe. $H := \dot{a}/a$ is the *Hubble parameter*, which is frequently used.

From the second of these equations, we can see that positive energy density ρ and pressure p decrease $\ddot{a}$, leading to an (eventual) reduction in the scale factor $a(t)$. A positive Λ however, increases $\ddot{a}$, leading (eventually) to an accelerated expansion of the universe. It is this accelerated expansion that has been experimentally observed, and dubbed dark energy.

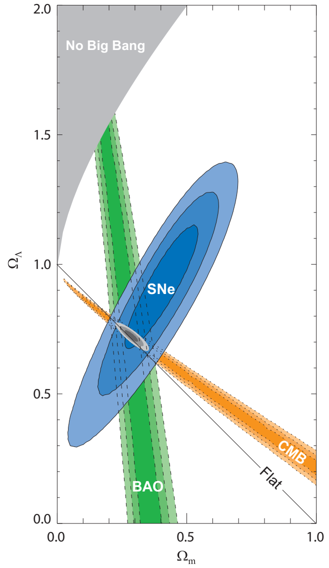

Figure 5.1: Constraints on Ω_M^0 and Ω_Λ^0. The superscript 0 indicates values for the present epoch. Figure taken from Ref. [82], though constraints have tightened in the decade since.

The observation of dark energy comes from a number of independent lines of astrophysical evidence. The accelerated expansion of the universe was first discovered by using Type Ia supernovae (Sne) [78, 79, 83]. Measurements of the cosmic microwave background (CMB) radiation provide further evidence for dark energy [84–86], and increasingly precise determinations of cosmological parameters. Baryon acoustic oscillation (BAO) meaurements (e.g., [87, 88]) provide yet another independent technique implying the presence of a dark-energy-like component of our universe.

The joint constraints on the matter density Ω_M and dark energy density Ω_Λ in our universe are shown in Fig. 5.1, which demonstrates the complementarity of these measurement types

(Sne, CMB, BAO). The density parameters Ω_i are the ratio of energy density of component i to the *critical density* ρ_c, the energy density in a flat ($k = 0$), dark-energy-less ($\Lambda = 0$) universe that is exactly on the knife's edge between a forever-expanding and a forever-contracting universe. That is, $\Omega_i = \rho_i/\rho_\mathrm{c}$, where the critical density is found from eqs. 5.4 to be $\rho_\mathrm{c} = 3H^2/8\pi G$.

The currently accepted measurement for the amount of dark energy in the universe is $\Omega_\Lambda = 0.68$. This corresponds to an energy scale of 2.4 meV in natural units (found by expressing the energy density with units [energy][length]$^{-3}$ in natural units [eV]^4). Since our universe is at least very close to flat, the sum of energy densities is approximately the critical density, thus $\sum \Omega_i \approx 1$. That is, dark energy makes up about 68% of our universe.

The composition of dark energy is unknown. From eqs. 5.4, we see that accelerated expansion can be explained either by a positive cosmological constant $\Lambda > 0$, or the presence of a negative-pressure fluid satisfying $p < -\frac{\rho c^2}{3}$. It is this second possibility what we have been able to address in our experiment, and whose motivations and characteristics are discussed in the next section.

5.2 Quintessence: scalar fields as dark energy

5.2.1 Motivation

As explained in the previous section, dark energy is the name scientists have given to whatever is driving the late-time accelerated expansion of the universe. The most common explanation for dark energy is that of a positive cosmological constant. The positive energy density associated with empty space is interpreted as the vacuum energy of the standard model of particle physics. While we are used to thinking of vacuum energies as shift-able to zero (because "only energy differences matter!"), we can't do that anymore once we think about energy density gravitating.

The famous cosmological constant problem [80] is that the zero-point energy of the standard model produces a cosmological constant that is 10^{120} times too large. Supersymmetric considerations can arguably reduce this number to "only" $\sim 10^{60}$ times too large. Even worse, this number isn't meant to cancel to zero (a nice, symmetric number) to match experimental values: It's supposed to cancel to a tiny, non-zero number! This is quite serious fine-tuning.

For a cosmological constant to explain dark energy, an *additional* fine-tuning is also required [89]. From the previous section, we saw that the energy density of matter in today's universe, $\Omega_{\mathrm{M},0}$ is of the same order as today's density of dark energy, $\Omega_{\Lambda,0}$; they're within a factor of ~ 2. However in the post-inflation expansion of our universe, Ω_M has dropped by many orders of magnitude, while Ω_Λ has by definition remained constant. This also seems like quite the coincidence for us to live in the epoch in which the two are nearly equal

In light of these issues with taking the cosmological constant to be the identity of dark energy, alternatives have been proposed. Dark energy could instead consist of a scalar field, and give rise to accelerated expansion not through the $\frac{\Lambda c^2}{3}$ term in eq. 5.4, but by having sufficiently negative pressure $p < -\frac{\rho c^2}{3}$. In this picture, dark energy is dynamic, with accelerated expansion driven by the underlying field. This proposal, dark energy as a dynamic scalar field, has been dubbed "quintessence" [90].

5.2.2 A force arises (and is screened)

Let's explore the idea of a scalar field composing the dark energy. It has been proven that a finite number of static scalar fields cannot solve the fine tuning problem (Weinberg's "no-go" theorem [80]). As such, the most promising route explored has been to look at a dynamic field (rather than an infinite number of static fields, which just seems wasteful).

In order to still be in non-equilibrium today, 10^{10} years after the Big Bang, a new field must be very light. This can be seen from the evolution equation of a homogeneous scalar field ϕ in an expanding universe [91]:

$$\ddot{\phi} + 3H\dot{\phi} + \frac{1}{2}m_\phi^2\phi = 0$$

where $H = \frac{\dot{a}}{a}$ is the Hubble parameter; $a = a(t)$ is the scale factor of the FLRW universe. The mass m_ϕ of the field is given by the curvature of the field's potential $V(\phi)$: $m_\phi^2 = \frac{\partial^2 V(\phi)}{\partial \phi^2}$. In order for the dynamics (i.e., time-dependence) to be relevant to the observation today so that $\Omega_\Lambda \sim 1$, the drag term $3H\dot{\phi}$ must be of the same order as the mass term $m_\phi^2\phi$. In that case, m_ϕ must be of the order of the Hubble parameter in the present epoch, $H_0 \sim 10^{-33}$ eV. Another statement of this claim is that the mass of the scalar field must be "at most comparable to present day Hubble parameter" or else it "could be integrated out and would be irrelevant to the low energy dynamics" [92].

This leaves us with a dynamic scalar field which must be extremely light. From such a field, we would generically expect a Yukawa potential of the form

$$V_{\text{Yukawa}} \sim \alpha \frac{e^{-m_\phi r}}{r} \tag{5.5}$$

due to the field ϕ. That is, the field would mediate a force, and with such a low mass, this force should be long-ranged. Should the force couple differently to bodies of different composition, this would lead to apparent violation of the equivalence principle (EP). However, EP tests (for example, torsion pendula [93, 94], lunar laser ranging [95]) have seen no such difference. EP violation can be characterized by the Eötvös parameter η:

$$\eta(A, B) = \frac{2(a_\text{A} - a_\text{B})}{a_\text{A} + a_\text{B}}$$

with a_A and a_B being the free-fall accelerations of test bodies A and B. The *MICROSCOPE* mission has recently presented the most stringent limits on an Eötvös parameter, measuring $\eta(\text{Ti, Pt}) \lesssim 10^{-14}$ for titanium and platinum test bodies [96].

Alternatively, fifth force / inverse square law tests can probe for new forces as deviations from Newtonian gravity. They place bounds on the strength α, and the range $\lambda \sim \frac{1}{m_\phi}$ parameters of the Yukawa potential 5.5. Such searches [97–99] have also not observed any new, unknown forces.

It would seem then that this dynamic field dark energy candidate is sunk at this point, since the force it predicts has not been observed. However, in regions of high matter density, the behavior of a field can be suppressed, or "screened". A field for which this happens is called a *screened field*. There are a variety of mechanisms through which a particle can have its behavior suppressed. Since the initial discovery [100,101] of a screening mechanism, many more have been explored; see [92] for a review.

Screening generally arises from a coupling of the field to baryonic (normal) matter. In the vast majority of the universe, with mean density $\sim 10^{-30}$ g/cm^3, a well-motivated field would be unscreened. The Earth's density of ~ 5 g/cm^3, thirty orders of magnitude larger, would suppress effects due to the field. The Earth therefore, wouldn't experience the full interaction we might expect from the Yukawa potential eq. 5.5. A screened field can thus avoid detection in EP tests, while still being the dark energy culprit.

So far we have entirely glossed over what this mysterious "screening" actually is, or how it arises. To make this behavior more concrete, we take a deeper look into one screening mechanism in the next section: the chameleon mechanism.

5.2.3 The chameleon mechanism

Screening arises from an interaction of a field ϕ with baryonic, or "normal" matter. An effective field potential $V_{\text{eff}(\phi)}$ can be expressed as

$$V_{\text{eff}}(\phi) = V(\phi) + V_{\text{int}}(\phi)$$

where $V(\phi)$ is the self-interaction term (i.e., the bare potential of the field itself) and V_{int} is the field's interaction with normal matter. For the simple chameleon model we will consider here, we take the self-interaction potential to be

$$V(\phi) = \Lambda^4 e^{\Lambda^n/\phi^n} \simeq \Lambda^4 + \frac{\Lambda^{4+n}}{\phi^n} + \dots \tag{5.6}$$

This is an example of a so-called "tracker" potential [102, 103] commonly used in cosmology, in which the late-time behavior of a slow-rolling field is largely insensitive to the initial conditions of the field. Λ is a parameter of this self-interaction potential with units of energy. The coupling to normal matter V_{int} takes the form

$$V_{\text{int}}(\phi) = \frac{\phi\rho}{M}$$

where ρ is the local density of normal matter, and M describing the coupling strength is a second parameter of the model. With these expressions, the basis of the chameleon mechanism becomes apparent and can be seen in Figure 5.2

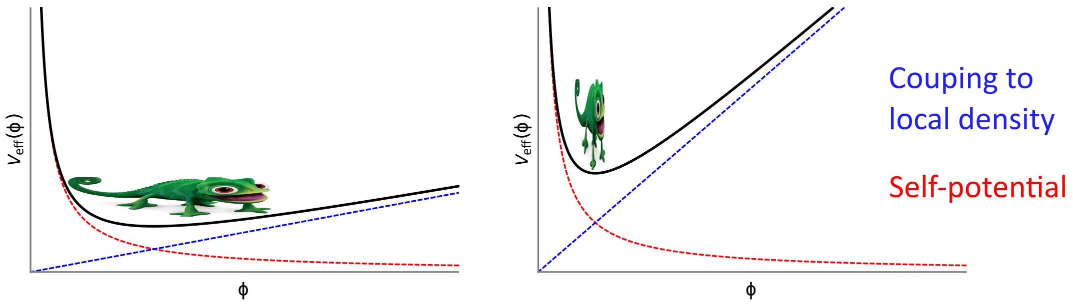

Figure 5.2: Chameleon potential. At low densities, the coupling to the local density in the interaction potential, $V_{\text{int}}(\phi) = \frac{\phi\rho}{M}$, has a shallow slope. This leads to and a broad, shallow minimum in the effective potential V_{eff}, and thus a low chameleon mass. In high ambient densities ρ, the effective potential acquires a sharply curved minimum, and a correspondingly high chameleon mass.

In regions of low density ρ, the interaction potential V_{int} is small. When summed with the tracker potential $V(\phi)$, the effective potential V_{eff} thus has a broad, shallow minimum. Excitations about that minimum have a low mass, since the curvature is low (remember, $m_\phi^2 = \frac{\partial^2 V_{\text{eff}}}{\partial \phi^2}$). The expected Yukawa interaction due to the chameleon is free to be long-ranged with this low mass. In regions of high density, however, the slope of the interaction potential is large. This leads to a sharp minimum with a correspondingly large mass. The range of its Yukawa potential therefore becomes very small. The thirty-order-of-magnitude differences in ρ for macroscopic objects compared to empty space makes this effect dramatic. In this way, the chameleon acquires a large mass in regions of macroscopic density, suppressing its effects.

5.2.4 Chameleon hunting

How are we to detect these fields if they are seemingly designed to hide (hence, the eponymous lizard) from experiments? Ref. [104] presented a clever proposal to use an atom interferometer. The idea capitalizes on the ultra-high vacuum typical of atomic physics experiments to "unsuppress" the chameleon field. While strongly suppressed in the stainless steel walls of a vacuum chamber, the chameleon field becomes approximately free to approach its empty-space value as one moves further into the UHV region.

The atoms of the interferometer serve as nearly-ideal test particles to probe the chameleon field: they experience interaction with the field, but are not dense enough to suppress it. Introducing a source mass to the center of the vacuum chamber, one can now re-suppress the chameleon field, changing the potential seen by the atoms. This effect can be measured by performing an atom interferometer in the affected region.

A word about the parameters in this chameleon theory: The parameters Λ and M both have the dimension of mass. If the field is to describe the observed cosmic acceleration, Λ

should take the dark energy value $\Lambda_{\mathrm{DE}} = 2.4$ meV (though such a particle could still exist for other values, and just not be the driver for dark energy).

M was fairly unconstrained before the experiments in this thesis. It should plausibly be below the reduced Planck mass $M_{\mathrm{Pl}} = (\hbar c/8\pi G)^{1/2} \approx 2.4 \times 10^{18}$ GeV/c^2. Before 2014, the best lower bound came from hydrogen spectroscopy at $M > 10^4$ GeV/c^2 [105]. A different convention also seen in the literature is to use $\beta = M_{\mathrm{Pl}}/M$ instead of M.

The field distribution

Getting into a bit more detail let's first take a look at the effect a source mass has on a chameleon field. Specializing the tracker potential eq. 5.6 to the $n = 1$ case, the effective potential is

$$V_{\mathrm{eff}}(\phi) = \Lambda^4 + \frac{\Lambda^5}{\phi} + \frac{\rho}{M}\phi$$

In a region of uniform density ρ, the chameleon field takes the value ϕ_{eq} that minimizes the potential:

$$\frac{\partial V_{\mathrm{eff}}(\phi)}{\partial \phi}\Big|_{\phi=\phi_{\mathrm{eq}}} = 0 = -\frac{\Lambda^5}{\phi_{\mathrm{eq}}^2} + \frac{\rho}{M} \tag{5.7}$$

$$\rightarrow \phi_{\mathrm{eq}} = \left(\frac{\Lambda^5 M}{\rho}\right)^{1/2} \tag{5.8}$$

and the mass of the excitation about this minimum is

$$m_\phi = \sqrt{\frac{\partial^2 V_{\mathrm{eff}}}{\partial \phi^2}}\,\Bigg|_{\phi=\phi_{\mathrm{eq}}} = \sqrt{2}\left(\frac{\rho^3}{M^3\Lambda^5}\right)^{1/4} \tag{5.9}$$

The Compton wavelength of the field is $\lambda_\phi = m_\phi^{-1}$. Equations 5.8 and 5.9 and show the density-dependence of the equilibrium value of the field and its mass, respectively, in a uniform density environment.

For a non-constant density distribution, we must solve the chameleon field equations of motion [100, 106] to find the field's distribution:

$$\nabla^2\phi = \partial_\phi V_{\mathrm{eff}}(\rho_m, \phi) \tag{5.10}$$

for a given matter density distribution $\rho_m(\boldsymbol{x})$. This nonlinear Poisson-Boltzmann equation is reminiscent of the Poisson equation in electrostatics where one solves for the potential (voltage) for a given charge distribution, an analogy which is discussed in [107].

The thin-shell effect

Consider a spherical object of macroscopic density $\rho_{\rm obj}$ and radius R in a dilute background environment of density $\rho_{\rm bg} < \rho_{\rm obj}$, as seen in Fig. 5.3. If both the object and the environment are large, then far from the density border, the field approaches its equilibrium values, $\phi_{\rm obj}$ and $\phi_{\rm bg}$, in each medium. However, near the border some sort of transition must happen.

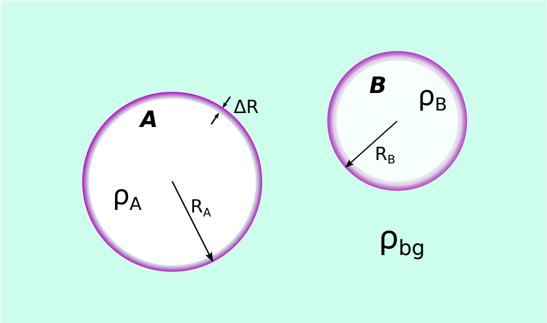

Figure 5.3: Two bodies interacting via the chameleon potential.

This transition happens in most cases of macroscopic density in a thin shell around the exterior of the object [101]. In this thin shell, the field value changes from its exterior value ($\approx \phi_{\rm bg}$) to its interior value ($\approx \phi_{\rm obj}$) rapidly. The interior of the object, all but that thin shell exterior, is thus shielded from chameleon effects in the outside world.

To push the electrostatics comparison, this thin-shell effect is analogous to a conducting sphere: the chameleon "charge" all accumulates near the surface of the chameleon "conductor". Another way of looking at this is that once inside the macroscopically dense object, the chameleon field acquires a large mass and thus a short Compton wavelength. It is thus able to change its value on a short spatial length scale to approach its equilibrium value. The thickness of this shell ΔR is given by [106]:

$$\Delta R = \frac{M\phi_{\rm bg}}{\rho_{\rm obj} R} \tag{5.11}$$

As an example, for the parameter set $\{\rho_{\rm obj} = 10\ {\rm g/cm}^3,\ \rho_{\rm bg} = 10^{-10}$ Torr of hydrogen, $R = 1$ cm, $\Lambda = \Lambda_{\rm DE}$, $M = 10^{-6} M_{\rm Pl}\}$, the thin shell thickness evaluates to $\Delta R \approx 26$ nm.

Outside of the object, in the lower density $\rho_{\rm bg}$, the field acquires a lower mass (and thus longer Compton wavelength), and approaches its equilibrium value more slowly. In general, for a given mass distribution, the differential equation 5.10 must be numerically solved to capture the exact behavior of the field. This can be a fairly computationally expensive and difficult procedure. An in-depth discussion, including simulation of the chameleon field for our own experimental geometry, can be found in Ref. [106].

A sample numerically calculated field distribution can be seen in Fig. 5.6 in the next section.

The atom-field interaction

Now let's look at an atom interacting with the chameleon field. Since the atom has mass, it couples to the chameleon field by $V_{\mathrm{int}} \propto \phi$. A spatial gradient in the field ϕ therefore leads to a gradient in their interaction energy, and thus a force. This force is given by

$$\boldsymbol{a}_\phi = \frac{1}{M} \boldsymbol{\nabla} \phi$$

where a_ϕ is the acceleration experienced by the atom due to the chameleon field. We can cast this acceleration / force into a form that looks similar to gravity (because gravitational strength is the expected, "natural" scale for this interaction).

Consider two bodies A and B with densities ρ_A and ρ_B, and masses M_A and M_B. Interacting at a distance r via both gravity and their mutually sourced chameleon field, the force between the bodies is

$$F_{\text{gravity}} + F_{\text{chameleon}} = \frac{G M_A M_B}{r^2} \left[1 + 2\lambda_A \lambda_B \left(\frac{M_{\mathrm{Pl}}}{M} \right)^2 \right]$$

M is the parameter from V_{int}, and M_{Pl} is the Planck mass. The λ_i parameters are screening factors [104] given by:

$$\lambda_i = \begin{cases} 1 & \rho_i R_i^2 < 3M\phi_{\mathrm{bg}} \\ \frac{3M\phi_{\mathrm{bg}}}{\rho_i R_i^2} & \rho_i R_i^2 > 3M\phi_{\mathrm{bg}} \end{cases}$$

which, for a thin-shell situation (eq. 5.11), can be more simply interpreted as

$$\lambda_i = \frac{\text{thin shell mass}}{\text{test mass}}$$

For a macroscopic object, these screening factors can be quite tiny, strongly suppressing the chameleon force. For example, in the parameter example of the previous section, giving a thin shell thickness $\Delta R = 26$ nm for a sphere of radius 1 cm, the screening factor is $\lambda \approx 8 \times 10^{-6}$. For two such objects, one would need to measure their gravitational attraction at the 10^{-11} level to see the chameleon force! This level of precision is impractical, as a 10^{-4} gravitational measurement of non-planetary source masses is already very impressive.

The idea from Burrage et al. [104] is to replace one of the source masses with an atom. An atom is small, so for a large parameter range, $\lambda_{\text{atom}} \approx 1$. This gives a big boost in sensitivity to the chameleon force. With this picture in mind, we will discuss the specifics of our setup for chameleon-searching.

5.3 Source mass and interferometer geometry

Our experiments took place in two iterations. The first used a spherical aluminum source mass, while the second used a tungsten cylinder. Both had a vertical bore allowing the cavity mode to pass through the source mass. These geometries are shown in Fig. 5.4 with relevant dimensions

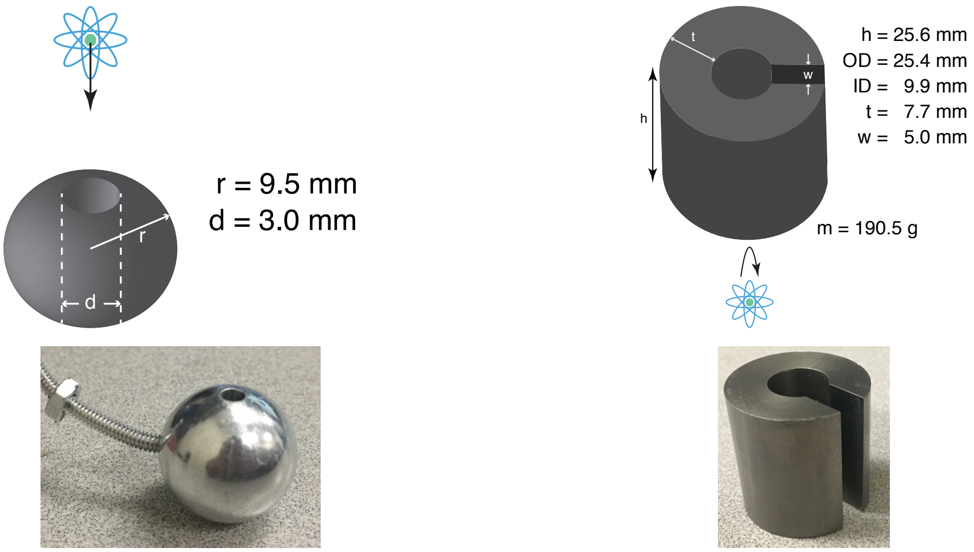

Figure 5.4: Source masses

The first source mass used a spherical geometry, which was simpler to calculate the expected chameleon profile (especially without use of the numerical simulations, which were developed later). Made of aluminum, this source mass was also simple to machine.

The cylindrical tungsten source mass was used in the second generation experiment. Tungsten was used for its high density to provide a large mass in the hopes of measuring the gravitational attraction between the atoms and the source mass (see Sec. 5.4). Tungsten however, is difficult to machine due to its hardness, which partially dictated the shape. Cylindrical tungsten is commercially available. Electric discharge machining (EDM) was used to slice out the borehole via a slot. The slot in the side of the borehole allows the source mass to be moved in and out of the cavity without interrupting the mode volume, and thus the cavity lock. This important feature was not present in the previous source mass, and it made data taking much simpler.

Both source masses had a threaded hole to mount the mass on a threaded rod. Using a mechanical vacuum feed-through, or “wobble stick” (Nor-Cal Products WBL-275-3) allowed the position of the source mass to be moved around from outside of vacuum. With the spherical source mass, the MOT was formed 2.55 cm above the source mass center, and allowed to fall towards it, during which interferometry was performed. This geometry is shown in Fig. 5.5.

Numerical simulations of the chameleon fields resulting from each source mass were performed in [106]. A representative figure is shown in Fig. 5.6.

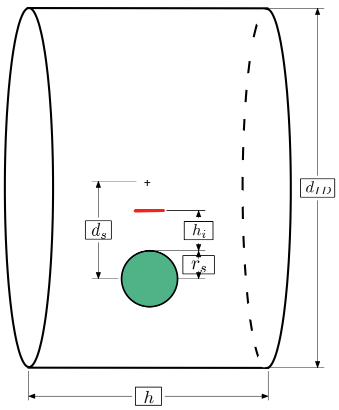

Spherical source radius	r_s	0.95 cm
Diameter of bore through source	d_{bore}	0.30 cm
Location of spherical source	d_s	2.55 cm
Location of interferometer	h_i	0.88 cm
Inner diameter of vacuum chamber	d_{ID}	12.2 cm
Vacuum chamber height	h	7.1 cm

Figure 5.5: Placement of the aluminum sphere source mass within the vacuum chamber (taken from Ref. [106]). A Mach-Zehnder interferometer with $T = 15.5$ ms began at the red line as the atoms fell towards the sphere.

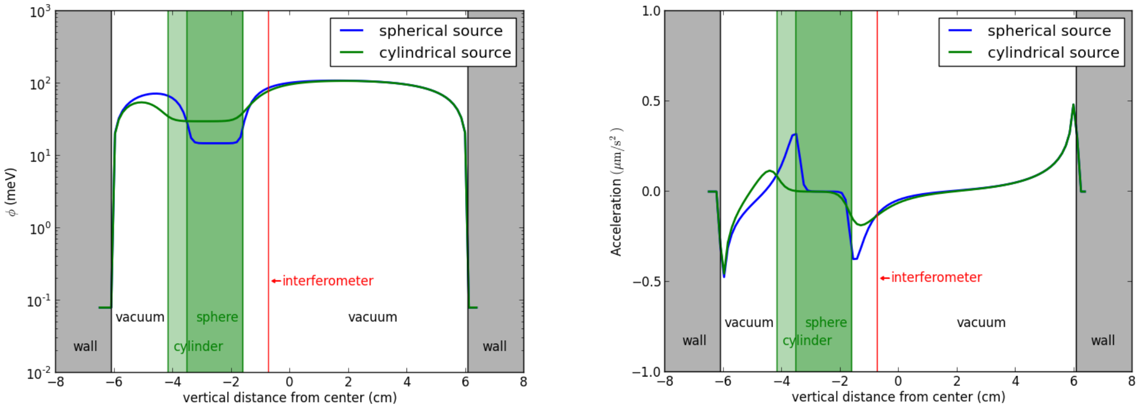

Figure 5.6: Chameleon profiles resulting from each of the two source masses (taken from Ref. [106]). Source mass is placed in the vacuum chamber as in Fig. 5.5, and the chameleon field is simulated along the vertical central axis of the chamber and source mass (which are aligned) as per eq. 5.10. The field is seen to plummet upon entering the steel vacuum chamber walls, an example of the thin-shell effect. This isn't seen in the source mass region (green shading) because the masses' boreholes are accounted for in the simulation; thus there is no abrupt density discontinuity.

A much more complete discussion of the experimental geometry, and the numerical simulations of the resultant chameleon fields can be found in Ref. [106]. We will not dwell too much on it here, since the geometry was changed for the higher-sensitivity second version of the measurement.

5.4 Gravitational attraction measurement

From our first measurement of chameleon fields [108] to our second [109], a number of experimental improvements were made that enabled a sensitivity improvement of > 100x. This improvement enabled a measurement of the gravitational attraction between the probe cesium atoms and the second-generation, tungsten source mass. We discuss that gravitational measurement in this section.

A number of experimental improvements were implemented to enable this increase in sensitivity. Important examples of these improvements are summarized below.

Raman sideband cooling. As outlined in Sec. 3.4, Raman sideband cooling was implemented. This narrowed the momentum distribution of the atomic sample both transverse to the interferometry beam (more time before leaving the beam) and along it (narrower Doppler spread)

Launch. With the narrower velocity spread along the laser beam axis, a sufficient number of the atoms can fall within the first Bloch band of the lattice. The launch from Sec. 3.4 could then be efficiently implemented to provide increased time-of-flight for longer interrogation times. This provides higher sensitivity, as the phase accumulated in the Mach-Zehnder geometry due to a constant acceleration scales quadratically with the pulse separation time T.

New source mass. The second generation source mass increased by more than an order of magnitude from a ~ 10 g aluminum sphere to a 190 g tungsten cylinder. This increases the source mass's gravitational pull. Additionally, with the increased time of flight due to the launch, the source mass was now positioned above the MOT, so that the apex of the atomic trajectory was near the source mass. This allowed the interferometer to spend more time sampling the region close to the source mass, where interactions with it are strongest.

Inertial stabilization. Along with increased sensitivity to accelerations comes increased sensitivity to vibrations (which are just accelerations of the separation between the freely falling atoms and the reference plane retro-reflection mirror). The vibration isolation + stabilization and tilt stabilization outlined in Sec. 3.5.3 were installed in the experiment.

Catch. Implementing the catch at the end of the sequence spatially selects only atoms remaining in the interferometry beam at the end of the time of flight. This improves the contrast, and thus the signal to noise (since non-participating atoms simply fall away)

Intensity stabilized beams. Intensity stabilization was introduced for the interferometry pulses.

Numerical simulations. The numerical simulations of Ref. [106] were performed between generations 1 and 2 of this experiment, which informed and confirmed design choices of the source mass geometry.

Data taking

We perform a differential measurement to isolate effects of the source mass on the atoms. This is a powerful technique because absolute measurements are hard. Rather than knowing all phase shifts (Earth's gravitational pull, Zeeman shifts, ac Stark, etc) to the accuracy of the desired result, we must only be confident that these quantities do not change with the source mass position.

To this end, we measure the phase shift in the atom interferometer with the source mass in *near* and *far* positions. The source mass position is automatically toggled between these positions using two translation stages (Thorlabs MTS50-Z8) to actuate the wobble stick. Due to the slot in the wall of the cylindrical vacuum chamber, the cavity remains locked throughout these movements. [1]

The interferometer phase is measured for ∼ 5 minutes before the position is toggled. The difference $\delta\phi_{\text{cyl}} = \delta\phi_{\text{near}} - \delta\phi_{\text{far}}$ between the interferometer phase in the near position ($\delta\phi_{\text{near}}$) and the phase in the far position ($\delta\phi_{\text{far}}$) then gives the phase shift due to the presence of the source mass. Many measurements of $\delta\phi_{\text{cyl}}$ can then be taken to average down noise. Data representing this process is shown in Fig. 5.7.

In the absence of any anomalous forces, we would expect $\delta\phi_{\text{cyl}}$ to arise only from the gravitational interaction of the atoms and the source mass. The expected phase shift can be found by treating the gravitational field of the source mass as a perturbation (see Sec 2.5) and integrating the gravitational potential from the source mass along the atomic trajectory. Doing this calculation as a function of source mass height h above the interferometer gives the result in Fig 5.8.

The phase shift can be converted into an "effective" acceleration of the atoms due to the presence of the source mass. This is done via the Mach-Zender interferometer phase shift formula, $\Delta\Phi_{\text{MZ}} = k_{\text{eff}} a T^2$, such that

$$a_{\text{eff, cyl}} = \frac{1}{k_{\text{eff}} T^2} \delta\phi_{\text{cyl}} \tag{5.12}$$

This conversion is shown on the right vertical axis in Fig. 5.8.

After subtracting the much smaller (∼ 10%) phase shift $\delta\phi_{\text{far}}$ for the cylinder's far position, the expected result for our gravitational signal is $a_{\text{eff, cyl}} = 65\ \text{nm/s}^2$ (corresponding to a ∼ 3 mrad phase shift).

After about 170 hours of data taking over three weekends, our final measured result was

$$a_{\text{cyl, meas}} = (74 \pm 19_{\text{stat}} \pm 15_{\text{syst}})\ \text{nm/s}^2,$$

---

[1] In the first generation, with the un-slotted aluminum source mass, a TTL-driven servo motor mounted on optics posts was used to turn a potentiometer to unlock the cavity while the source mass was being moved. The servo motor was then driven in the opposite direction to re-lock the cavity once the move was complete. As one might imagine, this method was less robust in staying locked for hours at a time, since the cavity was being un- and re- locked every few minutes.

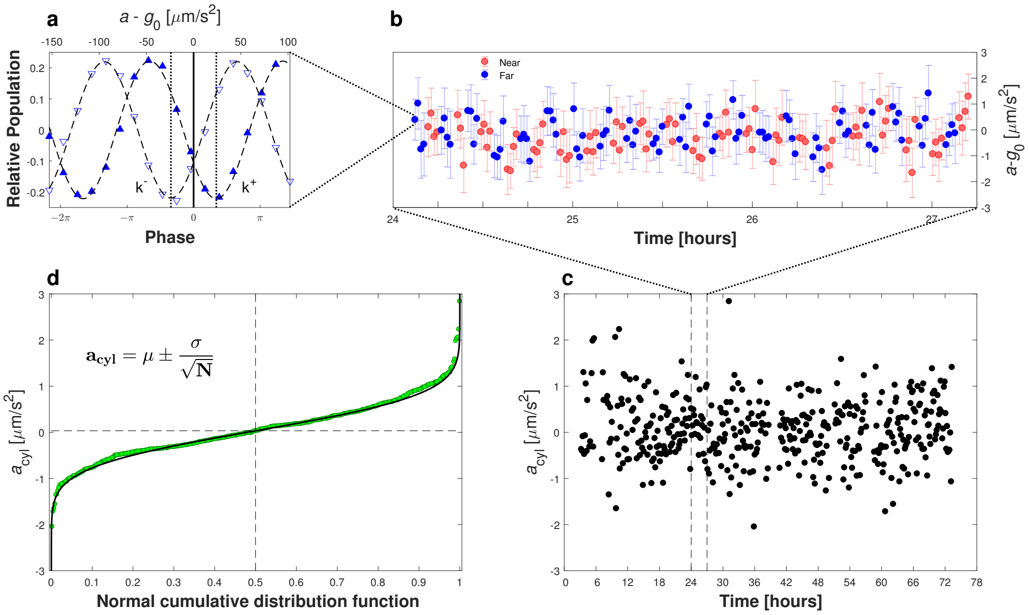

Figure 5.7: Gravitational attraction to the source mass. A differential measurement is performed by toggling the source mass between the near and far positions. **a)** Interferometer fringes for each wavevector direction k^+ and k^-. Combining these two measurements gives one data point out of 3,215 taken over 68 h. **b)** A 3-hour section of data. Four measurements are taken at each source mass position, which are then averaged. Blue points indicate that the source mass is in the far position; red points indicate the near position. An overall offset g_0 is subtracted for clarity. The difference between subsequent measurements after toggling the source mass position gives one measurement of a_{cyl}. Error bars represent 1-σ standard deviation (statistical). **c)** A single determination of a_{cyl} takes ~500 s. The full dataset (one of three) is shown here. **d)** The set of a_{cyl} measurements are fitted to the cumulative distribution function of a normal distribution with mean μ and standard deviation σ. N is the number of individual measurements. This least-squares fit (solid black line) gives a_{cyl} for the dataset.

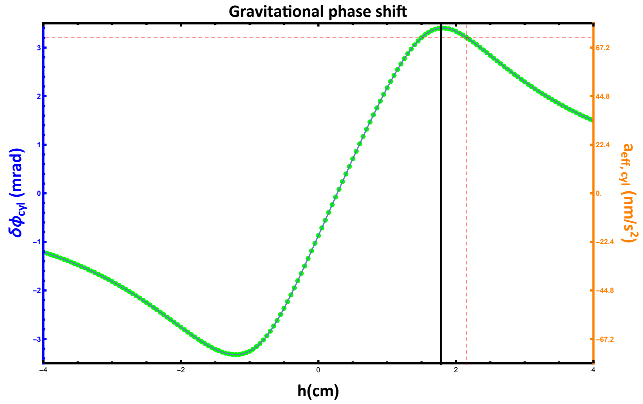

Figure 5.8: Gravitational phase shift due to the source mass. The atoms' initial position is $z(t = 0) = 0$. The atoms are launched upwards at 59.1 cm/s, and an interferometer of duration $2T = 110$ ms is used. $h = 0$ corresponds to the bottom surface of the cylinder being at $z = 0$. Our experiment used $h = 2.15$ cm, indicated by the dashed red cross-hairs. The black line indicates the height h where the bottom surface of the cylinder would be at apex of the atomic trajectory. The left axis shows the expected phase shift, and the right axis the effective acceleration.

which is consistent with the expected gravitational signal. The first uncertainty represents statistical uncertainty, and the second value systematic uncertainty. More information on the specifics of this measurement can be found in [109].

At the total uncertainty of 24 nm/s^2, this measurement resolves the gravitational pull of a 190 gram mass on a cesium atom at 2.7σ (standard deviations). To our knowledge, this is the smallest source mass gravitationally detected with an atom interferometer. Though other interferometers (e.g., [7,8]) have achieved comparable or better gravitational sensitivity to a source mass, the physical small-ness of the source is important in that it allows for placement inside the vacuum chamber. We will see the importance of this factor in the next section, where we discuss constraints on screened fields implied by this measurement.

5.5 Constraints on screened fields [2]

Observation of a phase shift consistent with gravity alone places limits on how strongly the atom and source mass can interact with each other via some other unaccounted-for way. We can thus constrain interactions between the two mediated by screened fields.

The chameleon mechanism was discussed in Sec. 5.2.3. We will discuss one other screened field example, the symmetron, before showing the constraints on these models implied by our measurements.

---

[2] Much of this section is taken from the supplementary information of Ref. [109]

5.5.1 Symmetrons

A symmetron scalar field has an effective potential symmetric under $\varphi \to -\varphi$, whose multiple minima in a low-density environment break this symmetry, and whose matter interaction restores it at high densities. A simple example is the w-shaped double well potential shown in Fig. 5.9. At low densities, the field picks one of the minima, and thus breaks the symmetry. As we will show, the symmetron's interaction with a small test particle is proportional to its field value. Thus in this "asymmetric phase", with a nonzero field value, the symmetron mediates a fifth force between test masses. The simplest interaction term V_{int} is a v-shaped term quadratic in φ, also shown in Fig. 5.9. At high densities, this dominates, and the entire effective potential becomes v-shaped, making the symmetric value $\varphi = 0$ the minimum of the potential. In this "symmetric phase", small changes to the density no longer alter the field value, and the fifth force vanishes. Thus the symmetron "hides" its fifth force by restoring its symmetry in high-density regions. The above statements follow from the effective symmetron potential V_{eff} which, as with the chameleon, is the sum of a bare potential V and an interaction potential V_{int}. We treat V_{eff} as a quantum effective potential already including all quantum corrections, as is common [104]. The simplest effective symmetron potential, which we study to illustrate the mechanism, takes the form

$$V_{\text{eff}} = \frac{\lambda}{4!}\varphi^4 + \frac{1}{2}\left(\frac{\rho_{\text{m}}}{M_{\text{S}}^2} - \mu^2\right)\varphi^2$$

in which λ is the self-coupling, M_{S} is the matter coupling suppression scale, and μ is the bare potential mass scale. λ is dimensionless, while M_{S} and μ have units of energy. This model can also be constructed in a way that is radiatively stable with well-behaved quantum corrections [110].

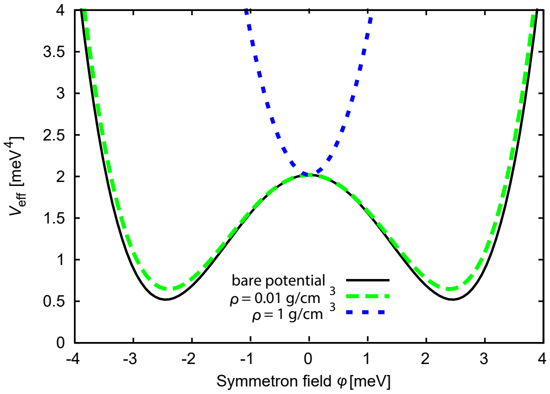

Figure 5.9: Symmetron potentials. At low and high densities for $\lambda = 1$, $\mu = 1$ meV, and $M_{\text{S}} = 1$ TeV. At low density, the field chooses one of the symmetry-breaking minima of the double-well potential. At high density, the symmetry-restoring minimum of the potential causes the effective matter coupling to vanish.

Fig. 5.9 shows this potential for matter densities lower and higher than the characteristic density $\mu^2 M_\mathrm{S}^2$, which is 0.23 g/cm^3 for the parameters shown. In regions of low density, the field minimizes the potential by choosing one of the two minima $\pm\mu\left(\frac{6}{\lambda}\right)^{1/2}$, breaking the $\varphi \to -\varphi$ symmetry. At high density, it settles at the symmetry-preserving value $\varphi = 0$. Symmetron screening is illustrated by linearizing the symmetron equation of motion [111] about a constant background field value, $\varphi = \bar{\varphi} + \delta\varphi$. In the static, non-relativistic case,

$$\nabla\delta\varphi = \frac{\bar{\varphi}}{M_\mathrm{S}^2}\rho_\mathrm{m} + 2\mu^2\delta\varphi$$

which is analogous to the Poisson equation for the gravitational potential but with an additional mass term and an effective matter coupling $\beta_\mathrm{sym}(\varphi) = \varphi M_\mathrm{Pl}/M_\mathrm{S}^2$. In the low-density limit, this approaches $6.0\,\lambda^{-\frac{1}{2}}\left(\frac{\mu}{\mathrm{meV}}\right)\left(\frac{M}{\mathrm{TeV}}\right)^{-2}$. At high density, $\rho_\mathrm{m} > \mu^2 M_\mathrm{S}^2$, the field sits at $\varphi = 0$, and the effective matter coupling vanishes. Thus fifth forces are suppressed at high ρ_m.

In the general case, the field profile due to a source mass is found by solving the non-linear Poisson equation $\nabla^2\varphi = \partial V_\mathrm{eff}/\partial\varphi$ just as with chameleons. Given that source field, we can describe the acceleration of an atom using the effective coupling $\beta_\mathrm{sym}(\varphi)$ and a screening parameter λ_a which we must determine. Using the correspondence between the linearized symmetron equation and the Poisson equation for a linear test particle, we see that $\delta\varphi = 2M_\mathrm{Pl}^2 M_\mathrm{S}^{-2}\bar{\varphi}\Psi$, where Ψ is the gravitational potential due to the test particle. This linear treatment breaks down when $|\delta\varphi| = \bar{\varphi}$, corresponding to $\Psi = \frac{M_\mathrm{S}^2}{2M_\mathrm{Pl}^2} = 8.4 \times 10^{-32}\left(\frac{M_\mathrm{S}}{\mathrm{TeV}}\right)^2$. Thus λ_a will be nearly unity as long as the gravitational potential of the atomic nucleus is smaller than this value. Approximating the cesium nucleus as a uniform-density sphere of radius $r = 1.25\ \mathrm{A}^{1/3}$ fm with $A = 133$, we find a gravitational potential $\Psi = 2.6 \times 10^{-38}$, meaning that $\lambda_\mathrm{a} = 1$ is accurate for M_S greater than 1 GeV. Below $M_\mathrm{S} = 1$ GeV, the atomic nucleus is partially screened. To obtain the screening factor λ_a, we divided the expression for the scalar charge [112, 113] by itself in the unscreened limit. This yields a value between zero (strongly screened) and one (unscreened).

5.5.2 Exclusions

We focus on chameleon and symmetron fields for concrete exclusion limits. Our first generation measurement [108] provided the most competitive lower bound on the chameleon coupling M to date. These lower bounds are complementary to macroscopic bounds set by torsion balance experiments [99, 111]. Our second generation measurement presented in the previous section improved previous limits [108, 112, 113] on these models by more than two orders of magnitude. Figure 5.10 shows excluded parameter ranges for these models.

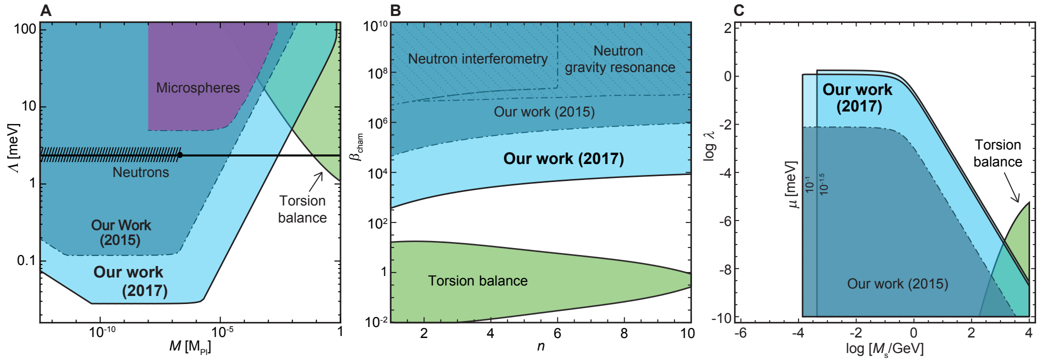

Figure 5.10: Constraints on screened scalar fields. **a**, Chameleon field: the shaded areas in the $M - \Lambda$ plane are ruled out at the 95% confidence level. M_{Pl}/M gives the coupling strength to normal matter in relation to gravity; $\Lambda = \Lambda_0 \approx 2.4$ meV (indicated by the black line) could drive cosmic acceleration today. A comparison is made to previous experiments: neutron interferometry [114] / neutron gravity resonance [115], microsphere force sensing [116], and torsion balance [99, 111]. **b**, Chameleon limits in the $n\beta_{\text{cham}}$ plane with $\Lambda = \Lambda_0$, showing the narrowing gap in which basic chameleon theories could remain viable. n is the power law index describing the shape of the chameleon potential; $\beta_{\text{cham}} \equiv M_{\text{Pl}}/M$ is the strength of the matter coupling. **c**, Symmetron fields: constraints by atom interferometry complement those from torsion pendulum experiments [112, 113] (shown with $\mu = 0.1$ meV) for the range of μ considered. For $\mu < 10^{-1.5}$ meV, the field vanishes entirely inside the vacuum chamber, leaving this parameter space unconstrained. The same effect produces the sharp cutoff in our limits at low M_{S}.

For chameleon fields with Λ at the dark energy value $\Lambda_0 = 2.4$ meV and $n = 1$, we exclude up to $M < 2.8 \times 10^{-3} M_{\text{Pl}}$, narrowing the gap to torsion pendulum constraints [99, 111]. One can see that these fields are nearly ruled out, with only a one order of magnitude range left for the coupling strength M. Furthermore, for all $\Lambda > 5.1$ meV, this gap is fully closed, ruling out all such models. Our symmetron limits are complementary to torsion pendula [99, 112, 113] as well. We improve previous constraints on λ by two orders of magnitude throughout the entire range of M_{S} and μ probed by our experiment. Our constraint is strongest in the regime where the atom is screened, where for $\mu = 0.1$ meV we rule out $\lambda < 1$.

Tests of gravity in the ultraweak-field regime with a miniature, in-vacuum source mass probe screened field theories with the potential to explain the accelerated expansion of our universe. In the future, technologies such as lattice interferometry ([117, 118], and Ch. 8) in our optical cavity and large momentum transfer beam splitters (e.g., in Ch. 7) will allow us to hold quantum probe particles in proximity to a miniature source mass, evading geometric constraints from the source mass' small size,and boosting sensitivity. With modest improvements, chameleon fields at the cosmological energy density will be either discovered or completely ruled out.

5.6 Systematic effects [3]

Taking the difference of measurements with the source mass near and far from the interferometer cancels systematic phase shifts that are independent of the source mass position. Such effects include Earth's gravity and gravity gradients. Also included are deviations of the phase of our laser beam from that of a hypothetical perfect plane wave, e.g., from the Gouy phase and wavefront curvature. The cavity mode ensures retroreflection alignment (i.e., that $\boldsymbol{k}_1$ and $\boldsymbol{k}_2$ are anti-parallel). The remaining systematic effects are discussed below and summarized in Table 5.1.

Table 5.1: Systematic effects table for the gravity / screened field measurement

Quantity	**Correction [nm/s^2]**	**Uncertainty [nm/s^2]**
Zeeman shift	-2.5	11
ac Stark shift	-	8
Tilt (vertical alignment)	-	0.2
Drift	-	3
dc Stark shift	-	0.8
Source mass gravity	65	5
Total	62.5	15

Many systematics can be suppressed by wavevector reversal. If $\boldsymbol{k} \to -\boldsymbol{k}$ (i.e., k^+ rather than k^-), the sign of the acceleration phase $\Delta\phi_{\text{acc}} = \boldsymbol{k}_{\text{eff}} \cdot \boldsymbol{a} T^2$ changes but certain systematic phases, such as Zeeman shifts and ac Stark shifts (to first order) do not. We can invert the sign of the effective laser wavevector ("wavevector reversal or k-reversal") by changing the frequency difference of the Raman beams, the Doppler detuning δ_{Dopp}. Averaging acceleration measurements for both k^+ and k^- allows us to subtract out Zeeman and ac Stark phase shifts, leaving only the acceleration phase.

Zeeman shifts

A Zeeman shift dependent on the source mass position could cause a phase shift mimicking an acceleration. Zeeman shifts can enter into the interferometer phase through the cesium hyperfine energy splitting $\alpha_{\text{B}} = 2\pi \times 427.45$ Hz/G^2 in a magnetic field, though only quadratically since we are using first-order magnetically insensitive states. The Zeeman phase $\Delta\phi_{\text{Zeeman}}$ is calculated by integrating the classical action along the trajectory of the two interferometer arms. The tungsten source mass should be non-ferromagnetic, but impurities or eddy currents could still cause small magnetic fields. We therefore measure the magnetic field along the trajectory for both positions of the source mass, with the same

---

[3] Much of this section is taken from the supplementary information of Ref. [109]

experimental timing, so that MOT eddy currents are included. To do so, we measure the magnetically-sensitive $|F = 4, m_{\mathrm{F}} = 4\rangle \rightarrow |F = 3, m_{\mathrm{F}} = 3\rangle$ microwave transition using the atoms as a local probe. The individual measurements vary with source mass position only by $\lesssim 0.1\%$. We fit the field measurements to a linear field $B = B_0 + B_1 z$, where z is a spatial coordinate, as in Fig. 5.11. This gives the magnetic field parameters B_0 and B_1, which are used to calculate $\Delta\phi_{\mathrm{Zeeman}}$.

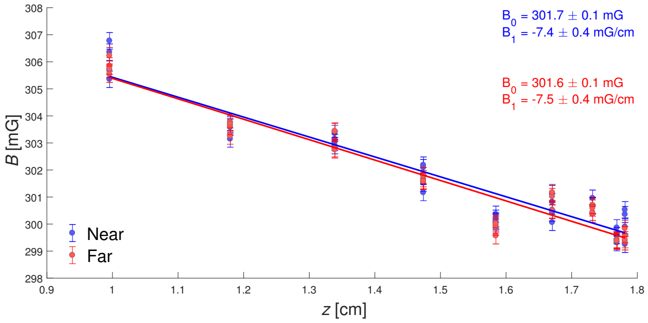

Figure 5.11: Magnetic field determination. The magnetic field is measured for both positions of the source mass along the atomic trajectory. Error bars represent 1-σ standard deviation (statistical).

We calculate $\Delta\phi_{\mathrm{Zeeman}}$ for our atomic trajectory in the measured field for both wavevector directions $k^{\pm}$. The expression for $\Delta\phi_{\mathrm{Zeeman}}$ is non-reversing under the transformation $\boldsymbol{k} \rightarrow -\boldsymbol{k}$, unlike the acceleration phase $\Delta\phi_{\mathrm{acc}}$ that we are interested in. Cancellation is imperfect, however, because the k-reversed interferometers are kicked in opposite directions, leading to slightly different classical trajectories. We cancel $\sim 90\%$ of $\Delta\phi_{\mathrm{Zeeman}}$ using k-reversal. The difference in Zeeman phase with source mass position($\Delta\phi^{\mathrm{near}}_{\mathrm{Zeeman}} - \Delta\phi^{\mathrm{far}}_{\mathrm{Zeeman}}$) after k-reversal is (167 ± 490) μrad, corresponding to a (4 ± 11) nm/s^2 shift in the measured acceleration.

There is also a force arising from the gradient in the second order Zeeman shift, whose acceleration is given by $a_{\mathrm{Zeeman}} = 2\frac{h}{m_{\mathrm{Cs}}}\alpha_{\mathrm{B}} B \frac{dB}{dx}$. The phase shift arising from this effect can be evaluated following Ref. [119]. For the magnetic field profile in Fig. 5.11, this evaluates to ~ 58 nm/s^2. However, we measure only the differential signal between the two source mass positions. This differential component is only (-1.5 ± 2) nm/s^2.

The total Zeeman shift is the sum of these two mechanisms, (2.5 ± 11.2) nm/s^2.

ac Stark shift

The ac Stark shift causes differential energy shift of the cesium $F = 3$ and $F = 4$ levels in a light field. This shift is opposite during interferometer pulses 1 and 3 (when the arms are in different states), which leads to a phase difference. This phase cancels in the symmetric Mach-Zehnder geometry if pulses 1 and 3 are identical. However, asymmetry between these pulses (due to thermal expansion of the cloud, changing δ_{Dopp}, etc.) results in a net shift in the interferometer phase. If this phase shift changes with source mass position, it would manifest as a false acceleration signal.

Clipping. Effects from the source mass on the cavity mode are negligible because the hole in the source mass, through which the cavity mode passes, is >16 waists wide. A radially symmetric steel clamp holds the source mass-moving translation stages onto the steel vacuum chamber flange. This minimizes torques on the vacuum chamber body as the source mass moves. No effect on the cavity linewidth or coupling efficiency could be observed by placing the source mass in the near position. This corresponds to a $<$ 2 mV change on a 500 mV transmission dip signal as seen in reflection on a photodiode. A change of this magnitude in cavity intensity would change the ac Stark shift by only ~ 20 μrad.

However, the source mass slightly clips two MOT beams due to geometric constraints, which could lead to a difference in the radial distribution of the launched atoms. This would lead to a difference in ac Stark shifts. This problem is exacerbated by the 718 μm waist of our cavity mode. Since the beam waist is of order the size of the atom cloud, the spatial dependence of ac Stark shifts across the cloud is non-negligible. These shifts can be suppressed by k-reversal, but the cavity complicates this.

Cavity effects. (See also erratum below)

The Raman frequency pair is generated by an electro-optic modulator (EOM) phase modulating the Raman laser, creating sidebands. The cesium hyperfine frequency (9 192 631 770 Hz) is just short of 23 cavity free spectral ranges. This situation is discussed in Sec. 3.2. During the interferometer, we ramp the frequency difference of the Raman beams by 2.42 MHz to compensate the free fall Doppler shift. In a cavity of linewidth $\Gamma_{\text{FWHM}} = 3.03$ MHz, this means that the third pulse (if naively locking the cavity to carrier resonance) creates a different light field within the cavity than the first pulse.

Applying the cavity transfer function to the incident beams (carrier and sidebands from the EOM) gives intensities and phase shifts that are in general quite different from each other. Furthermore, inverting the wavevector inverts the direction of the Doppler-compensation ramp. Without careful attention, the ac Stark phases $\Delta\phi_j^{\pm}$ from pulses $k_j^{\pm}$ will not be equal (where j = 1, 3 indicates the pulse number in an interferometer with wavevector $k^{\pm}$). For k-reversal to effectively cancel ac Stark phases, the $\Delta\phi_j^{\pm}$ should be made approximately equal.

We solve this problem by offsetting the cavity resonance from the carrier such that pulses $k_j^{\pm}$ give the same ac Stark shifts. Our protocol to measure the ac Stark shift is shown in Fig. 5.12. This measurement is performed as a function of cavity offset to find offsets at which the ac Stark shifts are made to be equal.

The phase shifts $\Delta\phi_j^{\pm}$ as a function of cavity offset from carrier resonance δ_{cav} are shown in Fig. 5.12c. The red circle indicates the point where pulses k_1^- and k_3^- impart the same phase shifts. Operating the k^- interferometer here minimizes the ac Stark phase shift ($\Delta\phi_3^- - \Delta\phi_1^-$). We find the analogous cavity offset for k^+ as

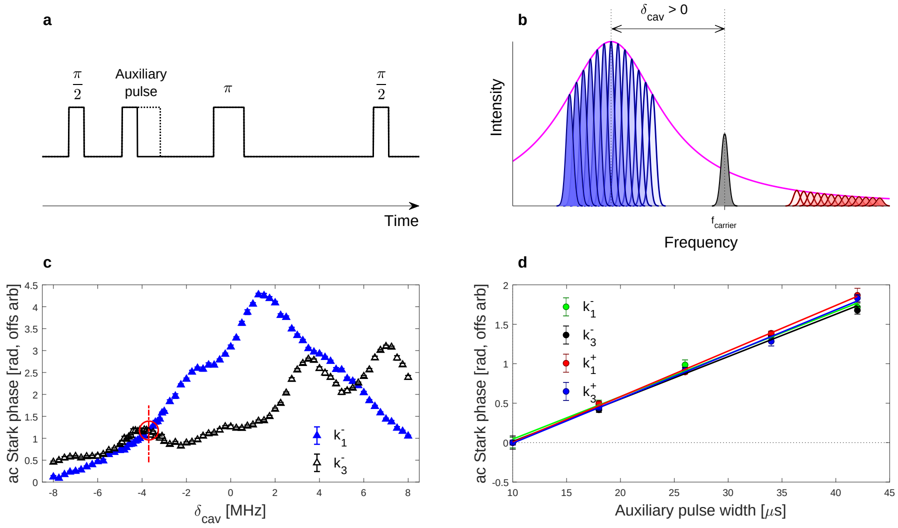

Figure 5.12: ac Stark shifts. **a)** ac Stark measurement protocol. An auxiliary pulse of variable length during a Mach-Zehnder interferometer is used to measure the ac Stark shift. The atoms are launched at a smaller velocity for this measurement. The auxiliary pulse thus does not drive transitions due to a large Doppler detuning from Raman resonance. **b)** Beams within the cavity. Cavity lineshape shown in magenta and the carrier beam shown in black. Blue (red) indicates the +(-)1 order sideband. The height of each laser lineshape indicates its intensity gain inside the cavity. For k^-, the Doppler compensation ramp moves the sidebands from transparent to opaque lineshapes. For k^+, the ramp moves in the opposite direction. **c)** Auxiliary pulse ac Stark phase vs. cavity offset δ_{cav}. The traces shown are for a single wavevector direction k^- for pulses 1 and 3. The point where they intersect is the cavity offset used for k^- in the actual measurement of a_{cyl}. **d)** ac Stark shift for the four relevant interferometer pulses. The ac Stark shift $\Delta f_j^{\pm}$ is given by the slope of the linear fit. The relative misalignment of the lines gives our k-reversal inefficiency ε_{ac}. The cavity offset used was -3.6 MHz (-4.1 MHz) for k^- (k^+). All error bars represent 1-σ standard deviation (statistical).

well. The ac Stark shifts $\Delta f_j^\pm$ are shown in Fig. 5.12d. The mismatch of the $\Delta f_j^\pm$ for these four pulses, $\varepsilon_{\text{ac}} = \frac{\text{range}(\Delta f_j^\pm)}{\text{mean}(\Delta f_j^\pm)}$ is $< 10\%$.

Uncertainty. The estimated error in the acceleration measurement arising from the ac Stark shift can then be given by

$$\Delta a_{\text{ac}} \lesssim \varepsilon_{\text{ac}} \times \frac{1}{k_{\text{eff}} T^2} \left\{ \Delta\phi_{\text{ac}}^{\text{near}} - \Delta\phi_{\text{ac}}^{\text{far}} \right\}$$

where $\Delta\phi_{\text{ac}}^i$ is the ac Stark phase for the interferometer when the source mass is in position i. We can infer the bracketed quantity from a given dataset using the measured data:

$$\left\{ \Delta\phi_{\text{ac}}^{\text{near}} - \Delta\phi_{\text{ac}}^{\text{far}} \right\} = k_{\text{eff}} T^2 \times \left\{ (a_{\text{near}}^+ - a_{\text{far}}^+) + (a_{\text{near}}^- - a_{\text{far}}^-) \right\},$$

where $a_i^\pm$ is the measured acceleration for wavevector $k^\pm$, with source mass position i. In short, we cancel source mass-dependent ac Stark shifts with inefficiency ε_{ac}. This varies somewhat across datasets, but a weighted average across datasets gives 8 nm/s^2 uncertainty.

Erratum In writing this thesis, it was discovered that the wrong modulation depth β (i.e., a different β than used for the interferometry pulses) was used to measure the ac Stark shift vs. cavity offset as per the above process. A calibration using the correct β would increase interferometer contrast and further reduce ac Stark uncertainty.

Tilt (vertical alignment)

Since the measured acceleration is $\boldsymbol{k} \cdot \boldsymbol{a} = ka\cos\theta$, ensuring that $\theta = 0$ gives the true acceleration, as well as reduces sensitivity to tilt fluctuations. Around $\theta = 0$, tilt changes affect the measurement only quadratically as $a \to a \cdot (1 - \theta^2)$. Toggling the source mass could introduce a systematic tilt, which could be mistaken for an acceleration signal. We stabilize the cavity mode wavevector along Earth's gravity using a feedback loop with a $\sim$ 1-minute time constant. This is faster than the source mass toggling, but slow compared to the experimental cycle time. Details of the control loop are discussed in Sec. 3.5.3.3. The setpoint of the feedback was determined by mapping the measured acceleration as a function of θ_x and θ_y (the tilt angles along the two axes) and finding the maximum. An example is shown in Fig. 5.13:

The feedback is necessary, e.g., to compensate for the drift of the pneumatic vibration isolation. In our datasets, the tilt data from the bubble level differ with source mass position by under 5 μrad for each dataset, corresponding to a systematic effect of < 0.2 nm/s^2.

Drifts

Environmental effects such as tides, laser power drifts, or temperature changes can cause the measured accelerations to drift on long time scales. If we always measure {near, far} in

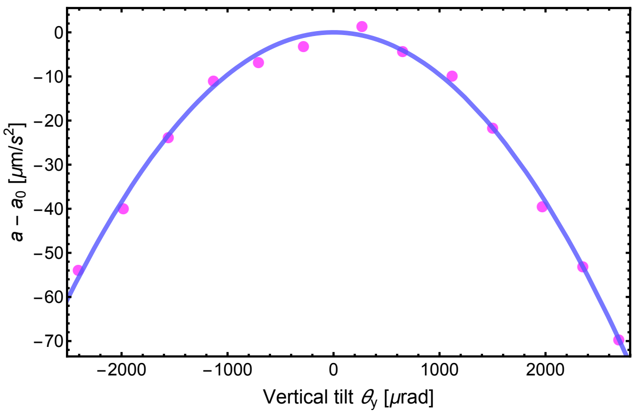

Figure 5.13: Tilt calibration. The measured acceleration varies $\propto \cos\theta_y \approx (1-\theta_y^2)$ for tilt angle θ_y.

the same order it is conceivable that a long, slow drift could cause the second position to produce a systematically different result (e.g., slightly higher for a drift upwards). The effect is largely suppressed for sufficiently fast toggling of the source mass position. No measured parameters (e.g., cavity coupling, temperature at multiple points in the experiment) vary at the 2 mHz toggling frequency. The MOT and interferometry beams are intensity stabilized, and thus should not drift much, it at all. Remaining effects are quantified by fitting a polynomial to the acceleration measurements with source mass in the far position only. We then subtract this polynomial from all the data. A weighted average of the absolute value of these drift corrections across datasets results in a 3 nm/s^2 shift, which we conservatively quote as a drift uncertainty.

dc Stark shift

The source mass is electrically grounded. However, thin films of surface oxidation $\sim$ 10 nm thick may form an insulating layer, allowing a voltage to build up. These films may have a dielectric strength of up to several MV/cm, allowing for surface voltages of up to 10 V. From the ground state dc polarizability of cesium, even this maximal voltage would cause a maximum acceleration of only 0.8 nm/s^2.

Source mass gravity

We model the source mass as a hollow cylinder with a wedge subtending an angle θ removed. We integrate the potential along the atomic trajectories to calculate the expected gravitational phase shift. The characterization of the source mass dimensions reproduces the density of tungsten to within $< 1\%$. Thus, the largest source of error in the gravitational pull is the positioning. Even assuming a large positioning error of 2 mm, the resulting phase shift changes only by 5%, $\sim$ 3 nm/s^2. To be even more conservative, accounting for transverse positioning, etc., we use 5 nm/s^2 as the uncertainty in the gravitational attraction of the source mass.

Chapter 6

Blackbody radiation: a new force mediator

Thermal radiation has had a storied history in physics. Infrared radiation from the Sun was the first form of electromagnetic radiation other than visible light to be discovered [120]. Max Planck's description of thermal radiation using quantized packets of energy [121] resolved the "ultaviolet catastrophe" stemming from the Rayleigh-Jeans law [122, 123], which predicted classically that the amount of energy thermally-radiated diverges to infinity. Planck's result is viewed as the first major step towards a quantum description of nature. In more recent times, the discovery [124, 125] and increasingly precise probes [85, 126, 127] of the cosmic microwave background, blackbody radiation from the time of recombination in the early universe, has provided insight toward myriad astrophysical purposes.

6.1 A force due to blackbody radiation

6.1.1 Qualitatively

A *blackbody* is a perfect emitter and absorber of radiation at all wavelengths. Many objects approximate a blackbody sufficiently closely (or at least can be scaled in magnitude with an emissivity ϵ) that "blackbody radiation" is commonly used as a synonym for thermal radiation.

Though known for over a century, blackbody radiation (BBR) has relevance even in modern atomic physics. For many leading modern atomic clocks, blackbody radiation presents an every-day struggle [128, 129]. Typical room temperature BBR spectra are far-detuned from the clock transitions used, and the frequency shifts induced are on the $\sim 10^{-14}$ level. For clocks operating at the 10^{-18} level of sensitivity however, this is a massive effect. Indeed, uncertainty on determining the exact size of this shift is a leading systematic in absolute clock measurement uncertainty [129].

Are the effects of these atomic energy level shifts confined to ultra-precise time-keeping?

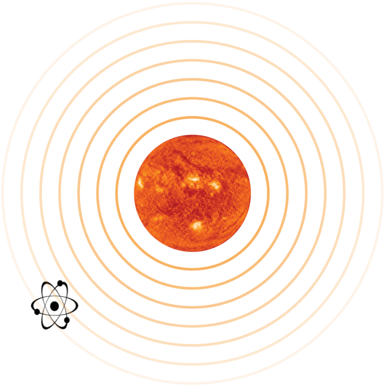

Figure 6.1: Cartoon of an atom near a hot, thermally-radiating object. Representative photo of the Sun from ESA/NASA [130].

Consider a ground-state alkali atom near an object hotter than room temperature, as in Fig. 6.1. The blackbody radiation emitted by the hot object can interact with the atoms in two ways. The first is through single-photon scattering. If the object is very hot, some of the emitted light will be resonant with the atom's optical transitions. The atom can scatter these photons, resulting in a repulsive radiation pressure. At room temperature, however, a cesium atom (for example) scatters on average less than one BBR photon every 10^8 years. For temperatures within a few hundred to a few thousand degrees above room temperature, this is a very rare process indeed. The blackbody radiation spectrum is shown in Fig. 6.2 along with the nearest cesium transitions.

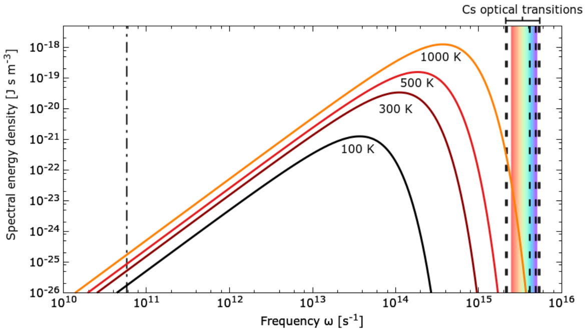

Figure 6.2: Blackbody radiation spectra. The spectra of blackbody radiation for various temperatures compared with transition frequencies of ground-state cesium indicated by vertical lines. The dash–dotted line on the left refers to the hyperfine splitting of the ground state used in the current definition of the second. The dashed lines on the right are strong optical absorption lines of cesium, starting from the D1 transition $6^2S_{1/2} \rightarrow 6^2P_{1/2}$ at 894 nm. The colored band indicates the visible spectrum as a guide for the eye.

The second interaction mechanism is via the same energy level shift from the discussion of atomic clocks. Blackbody radiation from the emitting object propagates outward. In doing so, the radiated power spreads out over a larger and larger surface area at increasing distance. The intensity of the blackbody radiation is thus reduced. This spatial gradient of the BBR intensity causes a spatial gradient in the atomic energy level shift. This gradient causes a force. This unexpected force was first proposed to exist by Sonnleitner et al. in Ref. [131].

In a slightly different framing, this force is actually familiar in atomic physics: it's the dipole force, which is routinely used to trap atoms in far-detuned laser beams [132]. Optical tweezers [133] operate through this mechanism as well. While we are accustomed to this concept in the strong, coherent, monochromatic beam cases of the previous two examples, the same principle applies to weak, incoherent and broadband thermal radiation. Since it's so far detuned from the optical transitions of the atom, the atom sees the thermal radiation as just weak, far red-detuned light. The thermal radiation thus mediates an *attractive* potential between the atom and the thermal emitter.

Even if the above arguments follow conceptually, the atomic clock energies shift only at the 10^{-14} level. Surely, a spatial gradient in this force would only contribute a negligible, if conceptually interesting, inertial effect on a real-life atom. It turns out that this force is not necessarily small. In the next section, we calculate the force quantitatively. We then present a measurement of the blackbody radiation-mediated force in Sec. 6.2.

6.1.2 Quantitatively

Since the blackbody radiation for temperatures within a few thousand Kelvin from room temperature are far-detuned from the optical transition in cesium, it is a good approximation to use the static polarizability α_0 of the atom to calculate the energy shift. This is very convenient, because including the effect of resonances (excited states) in the calculation complicates things considerably [128, 134, 135]. The energy level shift δE from the (time-averaged) electric field squared $\langle E^2 \rangle$ of the light is then

$$\delta E = -\frac{\alpha_0}{2} \langle E^2 \rangle,$$

where $\langle E^2 \rangle$ is found by integrating Planck's law to obtain

$$\langle E^2 \rangle = \frac{4\sigma T^4}{\varepsilon_0 c}$$

where T is the temperature, c is the speed of light, ε_0 is the permittivity of free space, and $\sigma = \pi^2 k_B^4/(60\hbar^3 c^2) \approx 5.67 \times 10^{-8}$ W m^{-2} K^{-4} is the Stefan-Boltzmann constant.

We now have the energy level shift for an atom immersed in isotropic thermal radiation at a temperature T. However, if there is a nearby blackbody source object at temperature T_S in an ambient environment at temperature T_0, the energy level shift becomes

$$\delta E(\boldsymbol{r}) = -\frac{2\alpha_0\sigma}{\varepsilon_0 c} \left(\frac{\Omega_\mathrm{S}(\boldsymbol{r})}{4\pi} T_\mathrm{S}^4 + \frac{4\pi - \Omega_\mathrm{S}(\boldsymbol{r})}{4\pi} T_0^4 \right) \tag{6.1}$$

where $\Omega_\mathrm{S}(\boldsymbol{r})$ is the solid angle covered by the source blackbody as seen by the atom at position $\boldsymbol{r}$. If $T_\mathrm{S} \neq T_0$, there will be a position-dependent energy level shift $\delta E(\boldsymbol{r})$. The gradient of this shift gives rise to a force $\boldsymbol{F}_\mathrm{BBR}$ on the atom,

$$\boldsymbol{F}_\mathrm{BBR}(\boldsymbol{r}) = -\boldsymbol{\nabla}\left(\delta E(\boldsymbol{r})\right) = \frac{\alpha_0 \sigma}{2\pi\varepsilon_0 c}\left(T_\mathrm{S}^4 - T_0^4\right)\boldsymbol{\nabla}\Omega_\mathrm{S}(\boldsymbol{r}) \tag{6.2}$$

As an example, for a spherical source of radius R with the atom at a distance $r > R$ from its center, the solid angle taken up by the source from the point of view of the atom is $\Omega_\mathrm{S}(r) = 2\pi(1 - \sqrt{r^2 - R^2}/r)$ [131]. The force from eq. 6.2 is then

$$F_\mathrm{BBR}(r) = -\frac{\alpha_0 \sigma}{\varepsilon_0 c}\left(T_\mathrm{S}^4 - T_0^4\right)\frac{R^2}{r^2\sqrt{r^2 - R^2}} \tag{6.3}$$

Let's put in some numbers. The static polarizability of cesium is $\alpha_0^\mathrm{Cs} = h \times 0.998\ \frac{\mathrm{Hz}}{(\mathrm{V/cm})^2}$. For a sphere at temperature $T_\mathrm{S} = T_0 + 100$ K of radius $R = 1$ cm in an ambient environment at room temperature $T_0 = 300$ K, a cesium atom (mass $m_\mathrm{Cs} = 2.2 \times 10^{-25}$ kg) located 3 mm from the surface ($r = 1.3$ cm) will experience an acceleration due to this blackbody radiation force of $a_\mathrm{BBR} = 800\ \mathrm{nm/s}^2$. This is well over an order of magnitude larger than the gravitational attraction towards such a body!

In the previous Chapter 5, we measured the gravitational attraction between a slotted cylinder and cesium atoms. In the next Section 6.2, we present a measurement of the blackbody radiation force $\boldsymbol{F}_\mathrm{BBR}$ between these two objects.

6.2 Measuring the blackbody radiation force

6.2.1 Modeling and predictions

The previous section calculated that the blackbody radiation force for a sphere about the same size as our cylindrical source mass is significant compared to the size of the gravitational signal measured in Ch 5. Motivated by this estimate, we now make predictions more specific to our actual experiment and source mass. For the calculations in this section, we are indebted to Matthias Sonnleitner, our collaborator in this work.

Radiative heat transfer

Much of the radiative heat transfer framework that follows is taken from the textbook Ref. [136], and its distillation into relevance to our experiment by Sonnleitner [137]. In particular, we follow closely the manuscript by Sonnleitner [137].

Our equation 6.2 assumes a perfect blackbody source object. In reality, objects have an emissivity $\epsilon_\lambda(\phi, \theta, T) \leq 1$, where thermal radiation at wavelength λ is emitted by the object at temperature T in the direction defined by azimuthal and polar angles ϕ and θ, respectively. A *gray* emitter is defined by having the same emissivity at all wavelengths,

$\epsilon_\lambda(\phi,\theta,T) \to \epsilon(\phi,\theta,T)$. A *diffuse gray* object has the further condition that the emission is isotropic, $\epsilon(\phi,\theta,T) \to \epsilon(T)$. In our model, we will assume that the cylinder is a diffuse gray emitter, and even further that there is no temperature dependence. The single parameter ϵ is thus the only quantity we will use to characterize the thermal emission from a surface of the source mass.

The energy flux J coming off an opaque, gray, diffuse surface at temperature T is thus the sum of its emitted radiation $\epsilon\sigma T^4$ and the the reflected portion of the incoming radiative flux G:

$$J = \epsilon\sigma T^4 + (1-\epsilon)G \tag{6.4}$$

Using eq. 6.4 we can convert eq. 6.1 to refer to a diffuse gray emitter, rather than a true blackbody:

$$\delta E(\boldsymbol{r}) = -\frac{2\alpha_0\sigma}{\varepsilon_0 c}\left(\frac{\Omega_\mathrm{S}(\boldsymbol{r})}{4\pi}\left(\epsilon T_\mathrm{S}^4 + (1-\epsilon)T_0^4\right) + \frac{4\pi - \Omega_\mathrm{S}(\boldsymbol{r})}{4\pi}T_0^4\right) \tag{6.5}$$

In this equation, we have eliminated the assumption of a perfect blackbody in favor of a diffuse gray emitter. We still, however, have two geometric assumptions of: (i) a perfect and homogeneous ambient temperature T_0 (by using $G = \sigma T_0^4$ to put eq. 6.4 into eq. 6.5), and (ii) no multiple reflections of radiation from the source mass.

To remove these two assumptions requires some geometry, and calculating *configuration factors* F_{1-2} between surface areas A_1 and A_2. The configuration factor is a geometrical property of two surfaces that describes the relative solid angle covered by surface A_1 as seen from surface A_2. Details on configuration factors, and the specific factors relevant to our experiment, can be found in Ref. [136] and Refs. [137, 138].

Configuration factors are reciprocal in that $A_1F_{1-2} = A_2F_{2-1}$. Furthermore, if surfaces $A_1, \ldots, A_N$ form an enclosure, then $\sum_{j=1}^N F_{i-j} = 1$ for $i \in \{1,\ldots,N\}$. The total radiative energy arriving at the ith surface can then be expressed as

$$A_iG_i = \sum_j A_jF_{j-i}J_j$$

where J_j is the radiative flux leaving surface j (note that $F_{i-i} \neq 0$ for a concave ith surface). Using the reciprocity of the configuration factors, we can solve for the radiation G_i arriving at surface i in terms of the configuration factors F_{i-j} and the radiation leaving the surfaces J_j:

$$G_i = \sum_j \frac{A_j}{A_i}F_{j-i}J_j = \sum_j F_{i-j}J_j \tag{6.6}$$

Plugging eq. 6.6 into eq. 6.4 for a configuration of N diffuse, gray emitters with emissivities ϵ_i and temperatures T_i ($i \in \{1,\ldots,N\}$) we obtain a set of N coupled energy flux relations:

$$J_i = \epsilon_i \sigma T_i^4 + (1 - \epsilon_i) \sum_{j=1}^{N} F_{i-j} J_j \tag{6.7}$$

The energy shifts on the atom can now be written with the geometric assumptions removed:

$$\delta E(\boldsymbol{r}) = -\frac{2\alpha_0 \sigma}{\varepsilon_0 c} \frac{1}{4\pi} \sum_{j=1}^{N} \Omega_j(\boldsymbol{r}) J_j. \tag{6.8}$$

Our cylinder

A schematic and parameterization of our cylinder is shown in Fig. 6.3

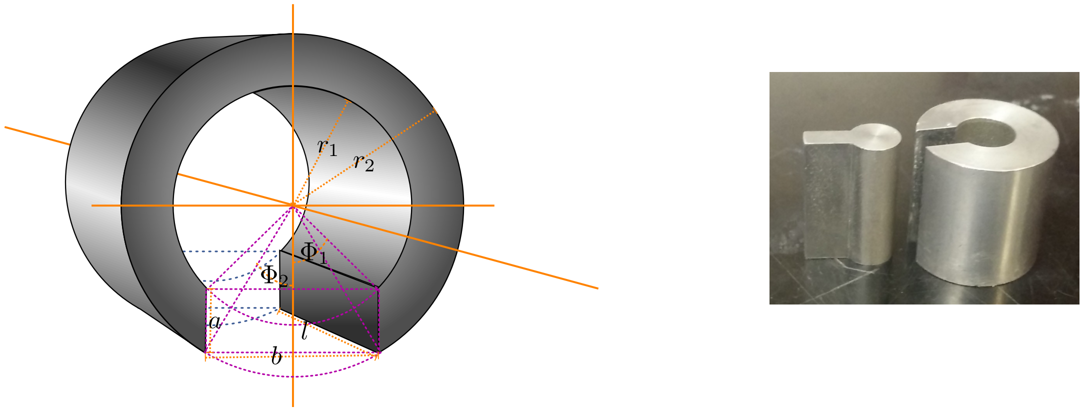

Figure 6.3: Cylinder parameterization for radiative heat transfer calculation. Left: Illustration (not to scale) of the open cylinder source mass used in our experiment.The cylinder has a length l and and inner and outer radius of r_1 and r_2, respectively. The slot cut from the cylinder has a width b such that the cylinder is missing an angle $2\Phi_1$ on the inside, $2\Phi_2$ on the outside. The atoms' trajectory enters the cylinder along the central axis. (figure and description from Matthias Sonnleitner [137]) Right: Real life photo of the cylinder, and the piece that was cut out of it.

The parameterization in Fig. 6.3 is used to calculate the configuration factors F_{i-j} and the outgoing radiation J_i for each surface i using equations 6.7. The resulting solutions are long and complicated, and detailed in Ref. [137]. However, they have a closed form, and can be put into a calculation program like *Mathematica* to solve for the energy shifts via eq. 6.8.

The resulting potential U_{BBR} is shown in Fig. 6.4, alongside the resulting acceleration ($a_{\text{BBR}} = -\frac{1}{m_{\text{Cs}}} \nabla U_{\text{BBR}}$). The details of the potential and acceleration profiles are discussed in the figure caption.

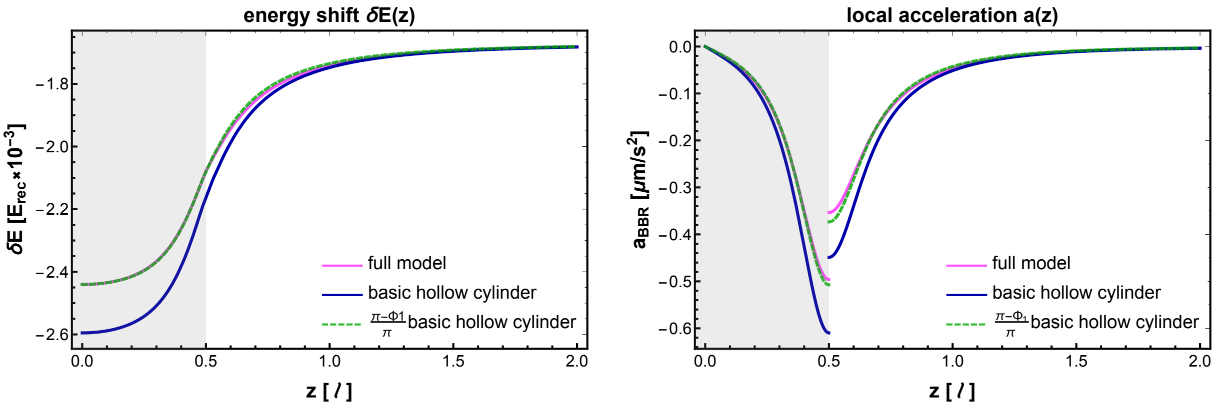

Figure 6.4: Blackbody radiation potential. The energy shift δE (left) and acceleration a_{BBR} (right) as a function of position. Position is measured in units of the cylinder height $l = 25.6$ mm. The energy shift is measured in cesium recoil energies, $E_{\mathrm{rec}} = \hbar\omega_{\mathrm{rec}}$. The shaded region indicates the source mass; the bottom surface of the mass is at $z = 0.5\, l$. Plots are shown for (i) a basic hollow cylinder (no slot) model, (ii) the full model in which the rectangular slot cutout is taken into account via configuration factors, and (iii) a model in which the simple cylinder model is just scaled by the angle missing from the inner surface of the cylinder $2\Phi_1$. We can see that this would be a reasonable simplification to make. The discontinuity in the acceleration is also visible as a discontinuity in the slope of the potential (if you look closely). This discontinuity comes from the abrupt change in solid angles Ω_i of various surfaces as seen by the atom as it enters the cylinder. In real life, imperfections would smooth this out. Plots are shown for $T_{\mathrm{S}} = 350$ K, $T_0 = 300$ K, and $\epsilon = 0.3$.

From the potential, we can calculate the phase shift by treating U_{BBR} as a perturbation, and integrating that potential along the atom interferometer trajectories. Doing so we can calculate the expected phase shift as a function of temperature, which is shown in Fig. 6.5.

6.2.2 Measurements

Emissivity

We determined the emissivity of the source mass. Experimental setup and representative image from an IR camera can be seen in Fig. 6.6.

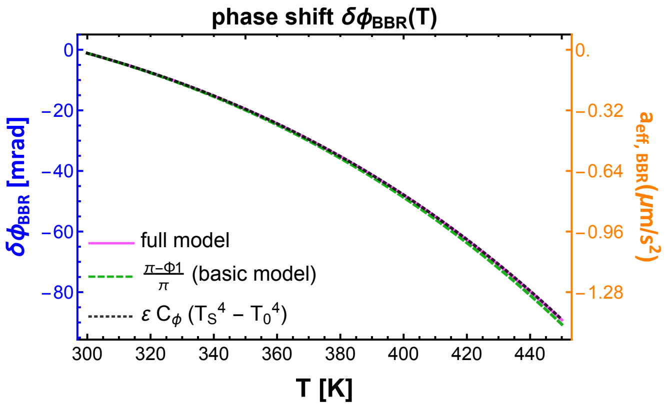

Figure 6.5: Blackbody radiation phase shift $\delta\phi_{\mathrm{BBR}}$ as a function of temperature. The models shown are the full model, the angularly cutout model, and a fit to the functional form $\epsilon C_\phi(T_{\mathrm{S}}^4 - T_0^4)$, with $C_\phi = 8.9\times10^{-12}\frac{\mathrm{rad}}{\mathrm{K}^4}$. The right vertical axis shows the effective acceleration (the constant acceleration that would give the same phase shift, see eq. 5.12). Parameters used correspond to the actual experiment, and are $T_0 = 296$ K and $\epsilon = 0.3$. The negative acceleration indicates acceleration *towards* the source mass, opposite the acceleration g due to Earth's gravity.

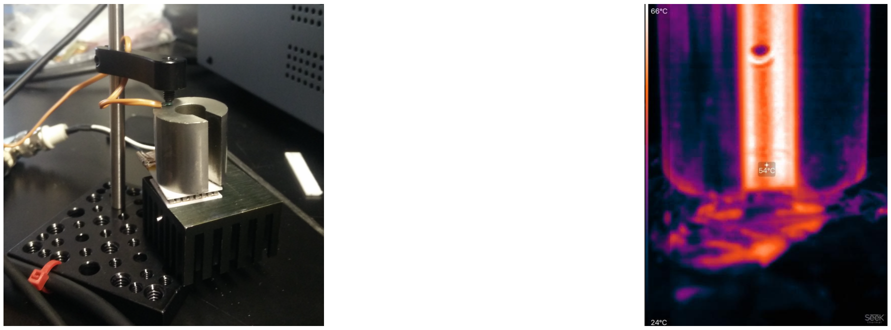

Figure 6.6: Emissivity measurement. Left: A Peltier element was used to heat the source mass from the bottom, and a thermocouple was used to measure the temperature. A thermal IR camera (Seek Thermal Compact XR) imaged the object, and inferred a temperature based on its assumed emissivity of $\epsilon_{\mathrm{a}} = 0.95$. From that, the true emissivity could be backed out (see text). In the actual experimental setup, aluminum foil was placed between the Peltier element and the source mass, as well as surrounding the full setup. This ensured a more uniform ambient temperature, since the aluminum foil has a low emissivity, and is thus mostly a reflector of the room's radiation, rather than an emitter of its own radiation. Right: An image into the slot of the cylinder from the IR viewer. Multiple reflections can be seen as bright vertical stripes to the sides of center. Since our model already includes these multiple reflections via the configuration factors, we want to use the region with a direct line of sight (and thus predominantly emitted radiation, not reflected), seen as the "cooler" central stripe.

The IR camera sensor assumes an emissivity of $\epsilon_{\mathrm{a}} = 0.95$, and no reflected background radiation. Accounting for these effects, we can back out the true emissivity ϵ from the sensor reading T_{sr} of an object at true temperature T_{true} (measured by the thermocouple), while also accounting for the ambient background radiation at temperature T_{bg}:

$$\epsilon(T_{\mathrm{sens}}, T_{\mathrm{true}}) = \epsilon_{\mathrm{a}} \frac{T_{\mathrm{sr}}^4 - T_{\mathrm{bg}}^4}{T_{\mathrm{true}}^4 - T_{\mathrm{bg}}^4}$$

The upper, lower and inside surfaces of the source mass were rough, as they had been electric discharge machined. These surfaces all had emissivities of 0.30(2). The outside cylindrical surface is polished, and thus has a lower emissivity of 0.08(4). However solid angle associated with this outer surface, as seen by the atoms, is always 0, so its emissivity doesn't impact the measurement.

Heating the source mass

To heat the source mass from outside the vacuum chamber, we shine a strong Nd:YAG fiber laser at 1064 nm (IPG Photonics YLR-100-1064LP, up to 100W output power, not single-frequency) into its slot. Within 12 min at a laser power of 8 W, we heat the cylinder from room temperature to about 460 K.

Outgassing from the source mass increases the background pressure with increased source mass temperature. Initially, outgassing of the cylinder at 460 K caused a pressure increase to about 10^{-7} Torr from a room-temperature vacuum of about 10^{-10} Torr (measured by an ion gauge about 50 cm away from the cylinder). After several heating cycles, this pressure increase was reduced to under 10^{-9} Torr.

An IR temperature sensor (Omega OS150 USB2.2, spectral response 2.0–2.4 μm) is then used to read out the source mass temperature through the vacuum chamber windows. The windows are made of fused silica and have a transmission cutoff just under $\lambda \approx 3$ μm, hence the specialized sensor. The infrared sensor works across a temperature range of $320 - 440$ K; outside of this range, we determine the cylinder temperature by extrapolation.

The temperature is extracted as a voltage from the sensor, and extrapolated to temperature as follows. We first take the differential equation for heat loss via conduction (through the threaded rod holding the source mass) and radiation. The differential equation is

$$T' + \alpha(T - T_{\mathrm{env}}) + \beta(T^4 - T_{\mathrm{env}}^4) = 0 \tag{6.9}$$

where the α and β terms represent conduction and radiation, respectively. We take calibration curves, and find the parameters $\{\alpha, \beta, T_{\mathrm{env}}\}$ by fitting these measured cooling curves to numerical solutions of this differential equation. This calibration is performed for several long cooling curves, and a weighted average of these fits is taken to determine the parameters of our system. A sample calibration curve is shown in Fig. 6.7:

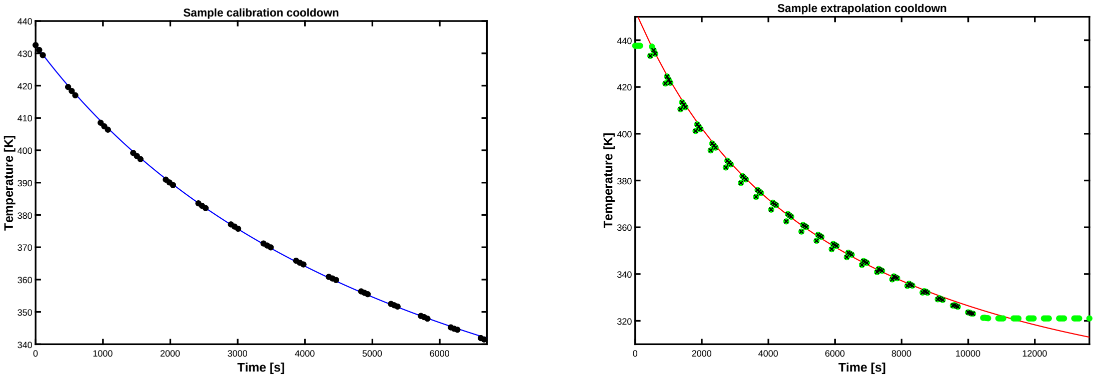

Figure 6.7: Cooling curves. Left: Calibration curve. The measured data points are fitted by solving eq. 6.9 to extract α, β, and T_{env}. The resulting curve is shown in blue. Right: Interpolated and measured temperatures for a data run (see text). Green points represent sensor output, and black x's indicate that a point is within the sensor's dynamic range. Each point represents one fringe, and gaps are data-taking with the source mass in the *far* position. The first point of each bunch being systematically too low is a technical shortcoming that has to do with undesired inclusion of measured points with the source mass in the far position (and thus measure room temperature). Using the extrapolated temperature (continuous red curve) means this doesn't cause a problem.

As stated earlier, the IR sensor works only from $320 - 440$ K, which does not include our highest or lowest (room) temperatures. As a result, we need to interpolate temperatures to include data in that range. An sample interpolation of a data cool-down curve is shown in Fig. 6.7 (left). This continuous red curve (right) is *not* a fit. Rather, it is a zero-parameter solution to the differential equation 6.9 using the parameters from the (separate) calibration curves. It is fed only an initial value, after with eq. 6.9 is integrated forward and backward in time to give the rest of the curve. We use these extrapolated temperatures for data analysis.

Results

From the launched atom source, we run a Mach-Zehnder atom interferometer with pulse separation time $T = 65$ ms. At the apex of their trajectory, the atoms enter 3.7 mm into the hollow cylinder. At the start of each experimental run, we heat the cylinder to a temperature of about 460 K with the fiber laser, which is subsequently switched off. We then measure the acceleration of the atoms during the cool-down period of up to 6 h, while monitoring the temperature with the IR sensor. When the source mass has cooled to near room temperature, we reheat it to start another run. We toggle the source mass' position between *near* and *far* positions, just as when measuring the gravitational attraction to the source mass in Ch 5. This again provides a differential mode measurement, allowing us to separate forces induced by the source mass from other forces, in particular the $>$ million-fold larger one from Earth's gravity. The *near* position exposes the atoms to blackbody radiation arising from the source, while the *far* position serves as a reference. We then investigate the temperature dependence of the interferometer phase difference between the near and far positions. A schematic of the measurement is shown in Fig. 6.8

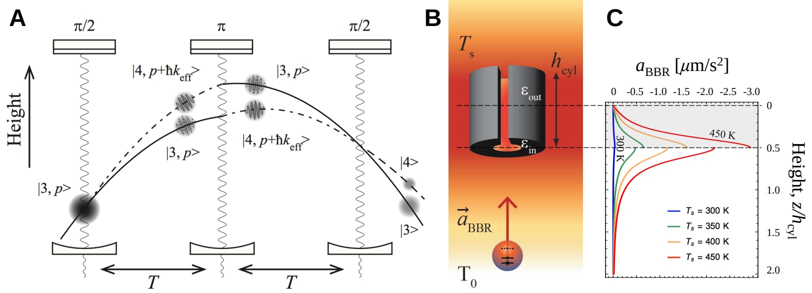

Figure 6.8: Measurement setup. **A)** Space–time diagram of each atom's trajectories in our Mach–Zehnder interferometer. **B)** Representation of the intensity gradient of blackbody radiation surrounding a heated, hollow cylinder that causes a force on atoms. **C)** Predicted acceleration of cesium atoms (as in Fig. 6.4) due to blackbody radiation, a_{BBR}, as a function of the distance z along the cylindrical axis. The vertical axis is taken from the center of the source mass. The light gray shaded area marks the region inside the hollow core of the cylinder.

Fig. 6.9 shows the measured effective acceleration $a_{\text{eff,cyl}}$ as a function of the source mass temperature T_{S} with a comparison to the theory from Sec. 6.2.1. The red dotted line in Fig. 6.9 shows the predicted acceleration $a_{\text{eff,cyl}} = a_{\text{eff,BBR}} + a_{\text{eff,grav}}$ as a sum of the gravitational pull $a_{\text{eff,grav}}$ and the blackbody interaction $a_{\text{eff,BBR}} = \epsilon C_{\text{a}}(T_{\text{S}}^4 - T_{\text{env}}^4)$ (from Fig. 6.5) of the atoms with the source mass. Here, $a_{\text{eff,grav}} = -66\frac{\text{nm}}{\text{s}^2}$ is calculated, and $T_{\text{env}} = 296$ K is the measured ambient temperature. C_a is the acceleration scale factor corresponding the phase scale factor $C_\phi = 8.9 \times 10^{-12}\frac{\text{rad}}{\text{K}^4}$ from Fig. 6.5 in Sec. 6.2.1:

$$C_a = \frac{1}{k_{\text{eff}}T^2}C_\phi = 4.7 \times 10^{-11}\frac{\mu\text{m}}{\text{s}^2\text{K}^4}$$

where T is the Mach-Zehnder pulse separation time.

Systematic effects

It is important to rule out artifacts that could partially mimic a blackbody-induced acceleration. A discussion of systematic effects largely overlaps with that of Sec. 5.6. Here we discuss a few potential effects specific to the blackbody measurement.

Outgassing and radiation pressure

The pressure applied by hot background atoms from outgassing of the heated source mass removes a substantial fraction of the cold atoms from the detection region at its highest

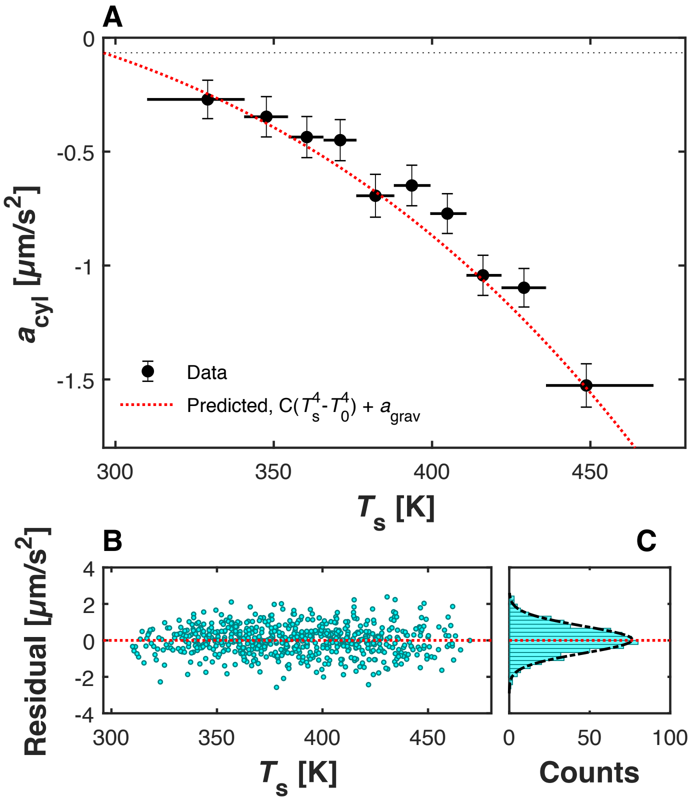

Figure 6.9: Blackbody acceleration data. Measured acceleration as a function of the source mass temperature T_{S}. A quartic dependence on T_{S} is observed for the acceleration experienced by cesium atoms towards the source mass. **A)** Data from 63 thermal cycles, about $2-5$ h each, are binned by temperature with $N_{\mathrm{bin}} = 65$ measurements per bin. The black dots represent the weighted mean of each bin. Vertical error bars show the 1-σ statistical uncertainty on the weighted mean. Systematic effects have been considered in detail and show no significant contributions to the error bars [138]. Horizontal bars show the temperature spread of the N_{bin} measurements in the bin. The red dotted line is a calculation of the effective acceleration $a_{\mathrm{eff,cyl}}$ the atoms experience during interferometry. The error for this theoretical prediction is dominated by the approximately 10% uncertainty of the source mass emissivity. The gravitational pull of the cylinder gives the room-temperature offset of the acceleration, indicated by the black dotted line at $a_{\mathrm{eff,grav}} = -66\frac{\mathrm{nm}}{\mathrm{s}^2}$. **B)** Residuals from the bulk acceleration data (cyan) to the zero-parameter theory model. **C)** A histogram of the bulk residuals is well described by a normal distribution. A Gaussian fit to the histogram (black dot–dashed curve) has mean compatible with zero within the standard error of $29\frac{\mathrm{nm}}{\mathrm{s}^2}$. Note that this standard error is less than half of $a_{\mathrm{eff,grav}}$, which therefore must be included for the measurement to be consistent with known effects. One may even venture to consider this a second measurement of the gravitational attraction to the source mass, in addition to the BBR force.

temperatures, so it is conceivably a component of the measured force on the remaining atoms. This, however, can be ruled out by multiple observations. First, this pressure should push the atoms away from the source, while the observed acceleration is towards the source. Second, it would depend exponentially on the source mass temperature; such an exponential component is not evident in the data. Finally, any scattering of hot background atoms with cesium atoms that take part in the interferometer would be incoherent, and would reduce the visibility of our interference fringes. Fig. 6.10, however, shows that the visibility is constant over our temperature range, ruling out scattering. This observation also confirms that absorption or stimulated emission of incoherent blackbody photons is negligible (see also Fig. 6.2). As with outgassing, absorption of the blackbody photons is additionally ruled out by the sign of the measured force.

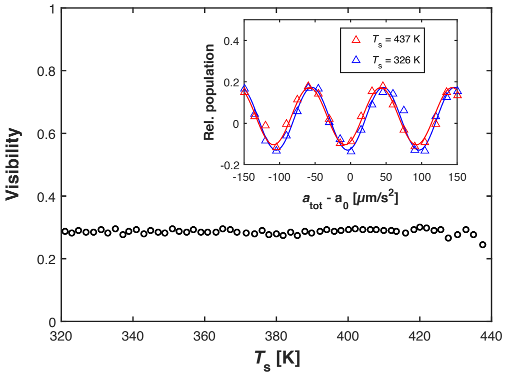

Figure 6.10: Visibility as a function of temperature, averaged in bins of 2 K for clarity. Scattering or absorption of photons would lead to a dephasing of the atomic ensemble, resulting in a reduction of visibility. No obvious loss of visibility is a strong indication that the contribution of scattering and absorption events is negligible. The inset shows interference fringes taken at $T_{\mathrm{S}} = 437$ K and $T_{\mathrm{S}} = 326$ K. Each fringe consists of 80 experimental runs with a cycle time of 1.2 s. The fitted fringe phase gives an acceleration measurement, contributing a data point to the bulk data seen in Fig. 6.9.

Constant a.c. Stark shifts.

Spatially constant energy-level shifts induced by the blackbody radiation (rather than an a.c. Stark shift gradient, which produces a force) can be ruled out because they would be common to both interferometer arms, and thus cancel out. In addition to this cancellation between interferometer arms, spatially constant a.c. Stark shifts from blackbody radiation would also be very nearly common to both ground hyperfine states, canceling out even within each arm. This is because the blackbody radiation is very far detuned from any optical transition in the atom, and thus causes (very nearly) the same energy-level shift to both hyperfine ground states. To verify, we ran the interferometer with opposite-sign wave-vector $\pm k_{\mathrm{eff}}$, implementing so-called “k-reversal” [14]. This inverts the signal $\boldsymbol{k}_{\mathrm{eff}} \cdot \boldsymbol{a}_{\mathrm{tot}} T^2$ arising from acceleration $\boldsymbol{a}_{\mathrm{tot}}$ but would not invert this constant a.c. Stark phase. We observe that the effect inverts sign with k_{eff}, as expected for a force. Our results in Fig. 6.9 include data runs for both directions of the wave-vector, performed independently, confirming a real acceleration.

Thermal expansion.
Heating of the cylinder eventually transfers heat to the vacuum chamber, potentially causing thermal expansion. This could affect the interferometer by, for example, changing the cavity length. Such thermal expansion is avoided using a slow temperature feedback loop acting on the vacuum chamber to allow the cavity PZT (which has limited dynamic range) to hold the cavity distance constant throughout the experiment.

Surface effects.
Near-field interactions such as Casimir–Polder forces [139] are suppressed, since the atoms never come closer to the source-mass surface than about 2 mm, and these forces decay at a length scale of the thermal wavelength, $\lambda_{\mathrm{T}} = \hbar c/k_{\mathrm{B}}T$. $\lambda_{\mathrm{T}} < 50$ μm for $T > 300$ K.

Differential a.c. Stark shifts, dc Stark shifts, Zeeman shifts, etc.
The setup in this work (this chapter, or Ref. [138]) is nearly identical to the chameleon / gravitational measurements in Ch. 5 (Ref. [109]) as far as these effects are concerned. They are discussed in detail for that measurement in Sec. 5.6.

Implications for future experiments

Just as blackbody radiation affects atomic clocks, the acceleration due to the blackbody field gradient observed here influences any high-precision acceleration measurements employing polarizable matter, including atomic and molecular interferometers, experiments with nanospheres and potentially measurements of the Casimir effect and gravitational wave detectors. For example, inside a thin cylindrical vacuum chamber, the thermal radiation field nearly follows the local temperature $T(z)$ of the walls, inducing an acceleration a of an atom:

$$a(z) = \frac{1}{m_{\mathrm{at}}}\frac{\partial}{\partial z}\frac{2\alpha_{\mathrm{at}}T(z)^4}{c\varepsilon_0},$$

where m_{at} and α_{at} are the atom's mass and static polarizability. Simulations confirm this approximation for thin cylinders, even for walls with percent-level emissivity. For cesium atoms, for example, a linear temperature gradient of $T'(z) = 0.1\ \frac{\mathrm{K}}{\mathrm{m}}$ around a base of 300 K would result in $a \approx 10^{-11}\frac{\mathrm{m}}{\mathrm{s}^2}$, non-negligible in, for example, terrestrial and space-borne high-precision measurements including tests of the equivalence principle, gravity measurements and gradiometers or gravitational wave detection with atom interferometry. The acceleration can be mitigated by monitoring and/or equalizing the temperature across the vacuum chamber, or (as shown by our simulations) by using wide, highly reflective vacuum chambers, wherein multiple reflections make the thermal radiation more isotropic. On the other hand, blackbody radiation can be used to simulate potentials. For example, heated test masses could be used to calibrate an atom interferometer for measuring the gravitational Aharonov–Bohm effect [140].

Chapter 7

Spin-dependent kicks for adiabatic passage in atom interferometers

In Sec. 4.3.1, we worked out the consequences of having our atom cloud and interferometry beam of comparable sizes. The result is that we address the atoms non-uniformly, precluding straightforward, highly efficient atom optics. We have developed a technique using adiabatic passage to address this inhomogeneous coupling problem. In adiabatic passage, a slowly changing Hamiltonian is used to manipulate the state of a quantum system with high fidelity. Motivated by the intensity spread seen by the atomic sample, these efforts resulted in highly efficient matter wave manipulations allowing for flexible and novel interferometers. The rest of this chapter describes implementation of the technique into a variety of high-fidelity interferometer geometries.

7.1 Adiabatic passage

7.1.1 The basics

The idea behind adiabatic passage (AP) is to slowly vary a Hamiltonian such that the state of a system is reliably transported from an initial state to a target state. This mapping is best seen visually on the Bloch sphere, and mathematically by using two bases: the bare basis and the dressed basis.

Consider a two level system that, in the absence of a driving Hamiltonian, has basis states $|0\rangle$ and $|1\rangle$. These two states constitute the *bare basis*. On the Bloch sphere, $|0\rangle$ corresponds to a vertical state vector pointing at the south pole, and $|1\rangle$ corresponds to a vertical state vector pointing towards the north pole.

Using the formalism we arrived at in Sec. 2.3.2, we enter just after adiabatically eliminating the (optically) excited state, forming an effective two-level system. A driving Hamiltonian H, in the form of eq. 2.47, couples the two levels:

$$\hat{H} = \begin{pmatrix} -\Delta & \Omega \\ \Omega & \Delta \end{pmatrix} \tag{7.1}$$

where Δ is the detuning, and Ω is the Rabi frequency. We now introduce the *dressed basis*, consisting of states $|-\rangle$ and $|+\rangle$, related to the bare basis by a rotation (see eq. 2.2):

$$\begin{aligned} \begin{pmatrix} |-\rangle \\ |+\rangle \end{pmatrix} &= \hat{R}(\theta, \hat{y}) \begin{pmatrix} |0\rangle \\ |1\rangle \end{pmatrix} \\ &= \begin{pmatrix} \cos\frac{\theta}{2} & -\sin\frac{\theta}{2} \\ \sin\frac{\theta}{2} & \cos\frac{\theta}{2} \end{pmatrix} \begin{pmatrix} |0\rangle \\ |1\rangle \end{pmatrix} \end{aligned} \tag{7.2}$$

where θ is defined in terms of the Hamiltonian parameters by $\tan\theta = \frac{\Omega}{\Delta}$. This rotation is chosen because in the case of constant Δ and Ω, it diagonalizes the Hamiltonian (when $\hat{H}$ is transformed to $\hat{H}'$ according to eq. 2.33) to

$$\hat{H}' = \frac{1}{2} \begin{pmatrix} -\tilde{\Omega} & 0 \\ 0 & \tilde{\Omega} \end{pmatrix},$$

where $\tilde{\Omega} = \sqrt{\Omega^2 + \Delta^2}$ is the generalized Rabi frequency. Converting $\hat{H}'$ to the form above requires making use of the other trig relations implied by the definition of θ. Explicitly, these relations are:

$$\sin\theta = \frac{\Omega}{\tilde{\Omega}} \qquad \cos\theta = \frac{\Delta}{\tilde{\Omega}} \qquad \tan\theta = \frac{\Omega}{\Delta} \tag{7.3}$$

Using this parameter θ that diagonalizes the Hamiltonian has a nice, clear interpretation on the Bloch sphere. The drive vector $\tilde{\boldsymbol{\Omega}}$ has vertical and transverse components Δ and Ω, respectively, and its tilt from the vertical is given by θ. This setup is shown in Fig. 7.1

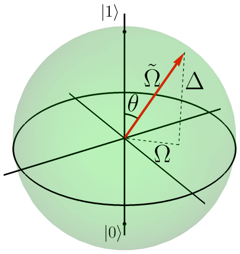

Figure 7.1: Driving Hamiltonian on the Bloch sphere

The effect of such a drive on the state vector $|\psi\rangle = c_0|0\rangle + c_1|1\rangle$ was first cast into an intuitive geometric form in Ref. [141]. This "Feynman picture" combines real and imaginary parts of c_0 and c_1 into a vector $\boldsymbol{R}$:

$$\boldsymbol{R} = \begin{pmatrix} c_0c_1^* + c_0^*c_1 \\ i(c_0c_1^* - c_0^*c_1) \\ |c_0|^2 - |c_1|^2 \end{pmatrix}$$

The evolution of $\boldsymbol{R}$ due to the drive can then be written in a simple equation resembling a torque:

$$\frac{d\boldsymbol{R}}{dt} = \tilde{\boldsymbol{\Omega}} \times \boldsymbol{R} \tag{7.4}$$

where the vector $\tilde{\boldsymbol{\Omega}} = (\mathrm{Re}(\Omega), \mathrm{Im}(\Omega), \Delta)^{\mathrm{T}}$. In this way, we have constructed on the Bloch sphere a vector described by the relationships eqs. 7.3. This picture is equivalent to the Bloch sphere picture [50], and we identify $\boldsymbol{R}$ as the familiar Bloch vector. Eq. 7.4 tells us that the Bloch vector $\boldsymbol{R}$ will *precess* around the drive vector $\tilde{\boldsymbol{\Omega}}$. This precession on the Bloch sphere can be visualized later in the chapter (spoiler alert) in Fig. 7.4.

With this intuition, we can present the basic idea of adiabatic passage. Suppose the initial state is $|1\rangle$, such that the Bloch vector $\boldsymbol{R}$ points to the north pole of the Bloch sphere. If we apply a strong drive $\tilde{\boldsymbol{\Omega}}$ also pointing at the north pole (or, a tiny angle ε away), the Bloch vector will rapidly precess around the drive vector. Now, if $\tilde{\boldsymbol{\Omega}}$ begins to slowly tip towards the south pole, the Bloch vector will continue precessing, and follow the slow tipping. Eventually, the drive will have tipped all the way to the south pole, and the state will have been transferred from $|1\rangle$ to $|0\rangle$.

Importantly, this procedure does not depend critically on the exact strength of the drive. As long as the drive is strong enough for precession to continue, the state is transferred with high fidelity. We will see that this *adiabaticity condition* requires that the Rabi frequency be much faster than the tipping; $\tilde{\Omega} \gg \dot{\theta}$, where $\dot{\theta}$ is the time derivative of the angle θ between the drive and the vertical.

Having this qualitative procedure motivated by the torque equation 7.4, we return to the bare basis Hamiltonian eq. 7.1 to quantify. The quantities in this equation ($\hat{H}$, Δ, Ω) are now understood to be time-dependent. This means that the transformation to the dressed basis, eq. 7.2, is also time-dependent. The Hamiltonian $\hat{H}'$ in the dressed basis (again using eq. 2.33), then becomes

$$\hat{H}' = \frac{1}{2}\begin{pmatrix} -\tilde{\Omega} & -i\dot{\theta} \\ i\dot{\theta} & \tilde{\Omega} \end{pmatrix}, \tag{7.5}$$

such that the evolution of a state $|\psi\rangle = A_-|-\rangle + A_+|+\rangle = \begin{pmatrix} A_- \\ A_+ \end{pmatrix}$ in the dressed basis (taking $\hbar = 1$) is given by

$$\frac{d}{dt}\begin{pmatrix} A_- \\ A_+ \end{pmatrix} = \frac{i}{2}\begin{pmatrix} \tilde{\Omega} & i\dot{\theta} \\ -i\dot{\theta} & -\tilde{\Omega} \end{pmatrix}\begin{pmatrix} A_- \\ A_+ \end{pmatrix} \tag{7.6}$$

Here we see the adiabatic criterion fall out nicely: if we can ignore $\dot{\theta}$, there is no coupling between the dressed state eigenstates. Thus, we require $\tilde{\Omega} \gg \dot{\theta}$ for the quantity to be adiabatic. For this reason, adiabatic passage is often also called "adiabatic rapid passage" (ARP) to indicate fast precession ($\tilde{\Omega}$) relative to an adiabatic process ($\dot{\theta}$).

7.1.2 Constructing a pulse

We will now introduce some machinery to derive our pulse shape. Much of what follows in deriving the pulse shape comes from Ref. [142]. To quantify how (non-)adiabatic a given pulse profile is, we construct an adiabatic parameter [143] $Q(t)$ and its reciprocal $\epsilon(t)$:

$$Q(t) = \frac{1}{\epsilon(t)} = \frac{\tilde{\Omega}}{\dot{\theta}}$$

Large Q (small ϵ) means an adiabatic process. Our goal will be to derive a pulse with constant (non-)adiabaticity as a function of time, i.e., $\epsilon(t) = \epsilon_0$. We call t_h the time at which the drive vector $\tilde{\boldsymbol{\Omega}}$ is horizontal (i.e. - $\Delta = 0$). from these relations, we can write:

$$\begin{aligned} \cos\theta(t) &= \cos\theta(t) - \cos\theta(t_h) \\ &= -\int_{t_h}^{t} \sin\theta(t')\dot{\theta}(t')dt' \\ &= \int_{t}^{t_h} \epsilon(t')\Omega(t')dt' \equiv \Gamma(t) \end{aligned} \tag{7.7}$$

where the above defines $\Gamma(t) = \cos\theta(t)$ for convenience. Using the trig relations 7.3, we can then write the detuning $\Delta(t)$ in terms of the Rabi frequency profile $\Omega(t)$:

$$\begin{aligned} \Delta(t) &= \frac{\Omega(t)}{\tan\theta(t)} \\ &= \frac{\pm\Omega(t)\Gamma(t)}{\sqrt{1-\Gamma(t)}} \end{aligned} \tag{7.8}$$

Up to now, no approximations or mentions of an atom have been made; the preceding manipulations simply relate geometric properties on the Bloch sphere to one another. The real, experimentally-causal chain is that amplitude and detuning profiles $\Omega(t)$ and $\Delta(t)$ define a path on the Bloch sphere followed by the vector $\tilde{\boldsymbol{\Omega}}(t)$, at angle $\theta(t)$ from the vertical, implying a non-adiabaticity $\epsilon(t)$. Now however, we will specialize to the pulses used in our experiment.

The pulse amplitude should be a smoothly varying shape, such that the dressed state eigenstates smoothly map out of and back into the free space eigenstates. There are several such commonly used shapes that have been studied in great depth in the field of NMR (e.g., see [144, 145]). For our purposes, we use the cosine-squared pulse, with a time-dependent two-photon Rabi frequency given by:

$$\Omega(t) = \Omega_0 \cos^2\left(\frac{\pi t}{2\tau}\right) \tag{7.9}$$

where $t \in \{-\tau, \tau\}$ gives the total pulse duration of 2τ. For a given Rabi frequency profile $\Omega(t)$ such as this one, we can evaluate $\Gamma(t)$ via eq. 7.7 by taking the desired constant adiabaticity $\epsilon(t) = \epsilon_0$. The detuning $\Delta(t)$ is then found using eq. 7.8. The resulting curves $\Omega(t)$, $\Delta(t)$ for the constant-adiabaticity cosine-squared pulse are shown in Fig. 7.2:

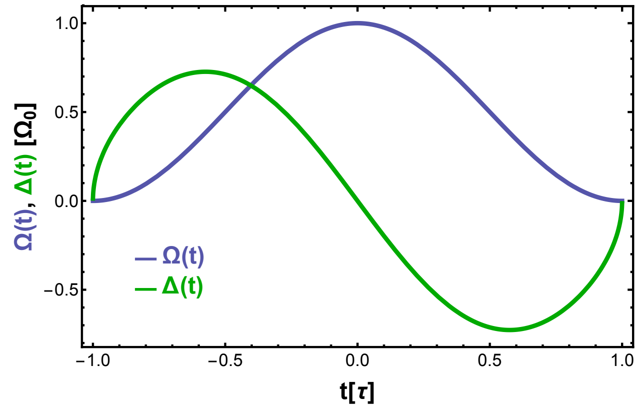

Figure 7.2: Amplitude $\Omega(t)$ and detuning $\Delta(t)$ for a constant adiabaticity cosine-squared pulse.

7.1.3 Applying the pulse to an atom

A small tweak can made to the detuning profile, as suggested by Ref. [142]. When both the intensity and detuning go to zero, as is the case for the *exact* cosine-squared pulse shown in Fig. 7.2, small errors can cause wild, undesired behavior of the drive vector $\tilde{\Omega}$ as $\theta = \arctan\frac{\Omega}{\Delta}$ changes with the small errors. Rather than using the *exact* detuning profile then, we can use a *robust* detuning profile that maintains large detunings at the beginning end of the pulse where the Rabi frequency is small. This keeps the drive vector vertical at the beginning and end of the pulse, even in the face of small errors and fluctuations. The robust and exact detuning profiles are shown in Fig. 7.3.

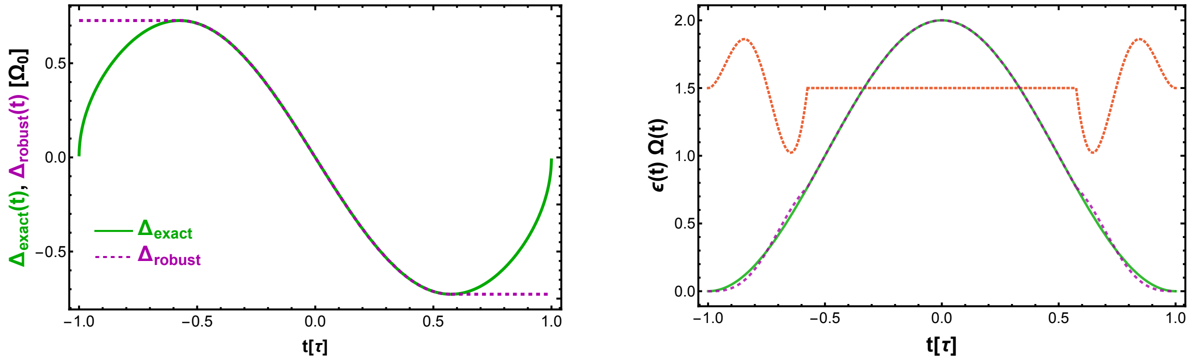

(a) Detuning profiles

(b) $\epsilon(t)\Omega(t)$

Figure 7.3: Robust and exact detuning profiles. In both plots, the exact profile is shown in solid green, and the robust profile is shown in dashed purple. **a)** The robust and exact detuning profiles. The robust profile is simply the exact profile between extrema of the pulse, but stays at the extremal detunings for times not between the extrema. **b)** $\epsilon(t)\Omega(t)$ for both detuning profiles. Their difference (arbitrarily multiplied by 10x and offset by 1.5 for visibility) is shown in dotted orange, illustrating that an increase in $\epsilon(t)\Omega(t)$ somewhere in the pulse necessitates a decrease elsewhere, as per eq. 7.11

The *robust* detuning is given explicitly by

$$\Delta_{\text{robust}}(t) = \begin{cases} 0.727\,\Omega_0 & t \leq -0.575\tau \\ \Delta(t) & \text{abs}(t) < 0.575\tau \\ -0.727\,\Omega_0 & t \leq 0.575\tau \end{cases} \tag{7.10}$$

where the numerical values just reflect the location and values of the extrema in the exact detuning profile $\Delta(t)$ (i.e., $\Delta(\pm 0.575) \approx \pm 0.727\,\Omega_0$ are the extrema). The robust detuning profile changes the adiabaticity by only a small amount, $\lesssim 10\%$. A relevant, interesting geometric property of a pulse profile on the Bloch sphere can be seen by defining the time t_v at which the Bloch vector is vertical. We can then write

$$\begin{aligned} \Gamma(t_v) &= 1 \\ \Rightarrow \int_{t_v}^{t_h} \epsilon(t)\Omega(t) &= 1 \end{aligned} \tag{7.11}$$

This is another geometric property, and thus doesn't rely on some adiabatic approximation, or care about the particular system. A plot demonstrating this relation for the robust and exact detuning profiles is shown in Fig. 7.3b. For the case of our cosine-squared π pulse, $t_v = -\tau$, and $t_h = 0$.

We have not actually implemented this robust detuning profile in the experiment, as it came to our attention after we had already performed our work. However, it may by useful to implement it in the near future, for the reasons discussed above. Using the robust detuning was useful in simplifying numerical hiccups in pulse simulations.

To obtain an arbitrary detuning profile in the experiment, we program a trigger-able arbitrary waveform generator (AWG, Tektronix AFG3022C) in burst mode. There is a subtlety in programming the instantaneous frequency of a sinusoid, defined as the time-derivative of the phase, $2\pi f_{\text{inst}} = \frac{d}{dt}\varphi(t)$. For a linear frequency chirp, for example, the phase is quadratic, given by $\varphi(t) = 2\pi\mu t^2 + 2\pi f_0 t + \varphi_0$. A subtle (at least to me) factor of 2 comes from the time derivative of the t^2 term, without which the frequency ramp covers twice the range one might (I did) expect. An IQ mixer (Marki IQ4509LXP) operated as a single sideband mixer is inserted into the output of the Raman frequency loop discussed in Sec. 4.3.2, Fig. 3.13. The frequency of the Raman loop DRO is dropped by 4 MHz. The AWG then puts out a signal with time-dependent frequency $f(t) = 4\ \text{MHz} + \delta(t)$. It is split into quadratures by a 90° splitter and used to drive the IQ mixer, up-converting it into the Raman frequency that drives the transitions.

If we can truly take the adiabatic limit, where $\dot{\theta} = 0$, the differential equations 7.6 are not coupled, and can be read out as having the solutions

$$\begin{pmatrix} A_-(t) \\ A_+(t) \end{pmatrix} = \begin{pmatrix} e^{i\phi/2} & 0 \\ 0 & e^{-i\phi/2} \end{pmatrix} \begin{pmatrix} A_-(0) \\ A_+(0) \end{pmatrix} \tag{7.12}$$

where

$$\phi = \int_0^t \tilde{\Omega}(t')dt' \tag{7.13}$$

is called the *dynamic phase*. This dynamic phase reflects the precession of the Bloch vector about the drive vector.

Though the dressed basis states simply acquire a phase, the transition can be seen by converting back to the bare basis states by inverting the transformation 7.2. The evolution of the dressed and bare basis states over the duration of a pulse are shown in Fig. 7.4

In a real experimental setup however, $\dot{\theta}$ is not identically zero. To apply our actual pulse to the atom, we put our specific amplitude and detuning profiles into eq. 7.6. For a constant adiabaticity cosine-squared pulse, we can use eq. 7.11 to show that

$$\epsilon_0 = \frac{2}{\Omega_0 \tau}$$

Finite available laser power means that Ω_0 cannot be arbitrarily high, and avoiding single-photon scattering means that τ can't be arbitrarily long. In our setup, we typically use $\Omega_0 \sim 2\pi \times 125$ kHz and $2\tau \approx 200\ \mu$s, which imply $\dot{\theta} = \varepsilon_0 = 0.025$. Equivalently, our pulses have adiabaticity $Q \approx 40$.

Other pulse imperfections include a spread of detuning offsets (due to the Doppler width of the atomic sample) and a spread in Rabi frequency (since the atomic cloud is about the same size as the cavity mode, as discussed earlier in this chapter). It is thus useful to

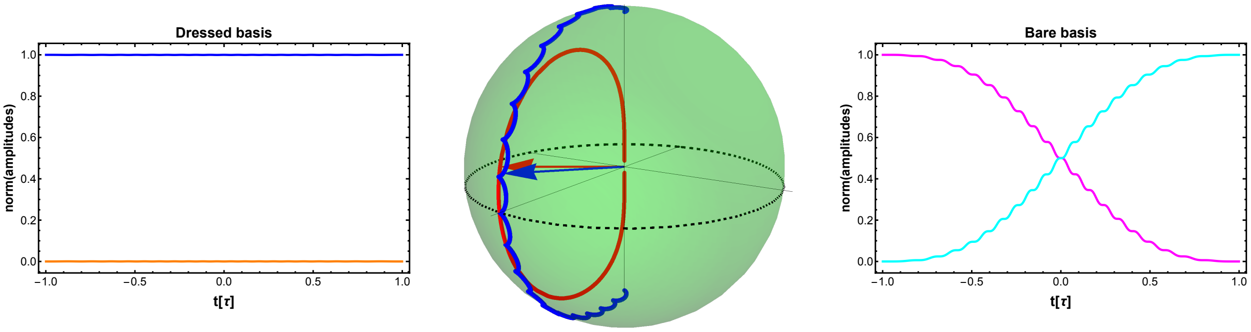

Figure 7.4: **a)** Dressed and **c)** bare state evolution during adiabatic passage. Adiabatic passage with non-adiabaticity $\epsilon_0 = 0.025$ is solved by numerically integrating eq. 7.6 for an atom initially in state $|1\rangle$ (Bloch vector pointing at the north pole) using the "exact" detuning profile, as in the experiment. The path on the Bloch sphere is shown in **b)**. The path of the drive $\tilde{\boldsymbol{\Omega}}$ (red arrow) over the pulse duration is shown in red, and the path of the Bloch vector (blue arrow) is shown in blue. The arrows show a snapshot of these vectors' locations during the pulse. Using the "robust" detuning profile smooths out the wiggles in the bare basis curves, suppressing the corresponding arcs in the state's path on the Bloch sphere.

numerically integrate the Schrödinger equation 7.6 for a given pulse. To investigate these effects, we parameterize the detuning offset and Rabi frequency spread according to:

$$\Omega(t) \rightarrow \alpha\Omega(t) \tag{7.14}$$

$$\Delta(t) \rightarrow \Delta(t) + f\Omega_0 \tag{7.15}$$

In this parameterization, α represents the spread in Rabi frequency, and f gives the detuning offset in units of the peak (unmodified) Rabi frequency Ω_0. A "perfect" pulse has $\{\alpha, f\} = \{1, 0\}$. Fig. 7.5 shows the results of pulses in this two-dimensional parameter space.

From the amplitude (left) plot, we see that there is a spread of detunings over which the pulse is highly efficient, whose width grows roughly linearly with increasing peak Rabi frequency (increasing α). From the phase (right) plot, we see that at fixed detuning f, the phase increases roughly linearly with α (as we'd expect from eq. 7.13). We also see that the dynamic phase as a function of detuning f at fixed α shows a quadratic relationship, especially where the pulse is efficient. That is,

$$\varphi(\alpha, f) \approx \alpha\phi_0 + a(\alpha)f^2$$

This behavior will be discussed in more detail later in the chapter. With that background, we will now discuss application of these pulses in our experiment.

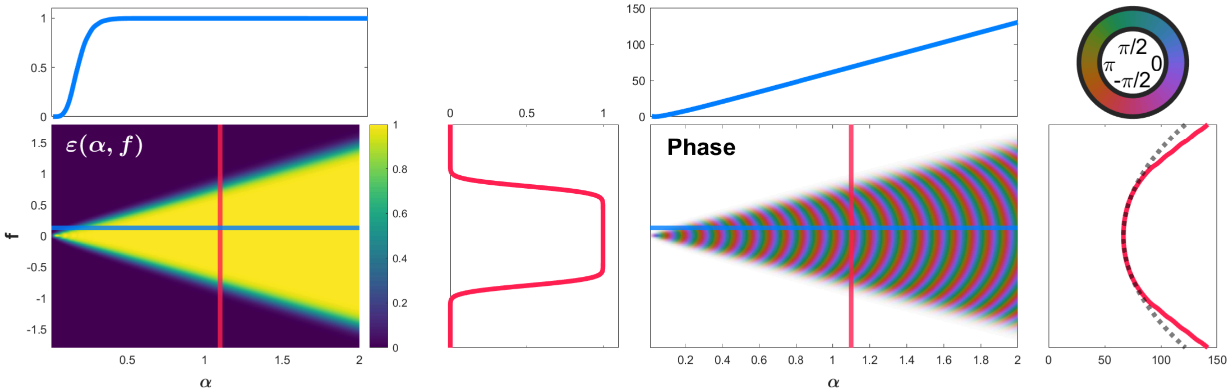

Figure 7.5: Numerical solution of imperfect ARP pulses. An initial state $|0\rangle$ evolves under an imperfect pulse with parameters $\{\alpha, f\}$ (as in eq. 7.14) meant to transfer it to the target state $|1\rangle$. The pulse uses a cosine-squared envelope, and the robust detuning profile, with non-adiabaticity parameter $\epsilon_0 = 0.025 \to Q = 40$. Left: The left color plot shows $\varepsilon(\alpha, f) := |\langle\psi_{\mathrm{f}}|1\rangle|^2$, where $|\psi_{\mathrm{f}}\rangle$ is the final state after the pulse. $\varepsilon(\alpha, f)$ indicates the pulse efficiency. Right: Phase of the arm in the target state $|1\rangle$ (that is, $\arg(\langle\psi_{\mathrm{f}}|1\rangle)$), shown using a cyclical color map. The opacity of this plot is set to $\varepsilon(\alpha, f)$, i.e., the value in the left plot, so that we see the phase behavior where the pulse is efficient. Both plots also show slices along constant α and constant f in red and blue, respectively, in the sidebars. The phase-at-constant-α sidebar also shows, in dashed gray, a quadratic curve $\phi = af^2 + \phi_0$, fitted with parameter a to the detunings f where the pulse is efficient above a threshold (here, $\varepsilon(\alpha, f) > 0.7$). ϕ_0 is the phase at $f = 0$.

7.2 Splitting the beamsplitter

From the introduction of our first beamsplitter in eq. 2.1, we have treated the beamsplitter as a single operation. This is of course well-motivated; our Raman beamsplitter pulse coherently and continuously splits the atomic wavefunction into two arms over its duration. However, the Raman beamsplitter is performing two tasks in parallel: (i) superposing the spin state, and (ii) entangling the spin state with the atom's external momentum. We typically don't think of Raman beamsplitters this way because we hide this underlying two-step by exclusive use of the basis states $|a, \boldsymbol{p}_0\rangle$ and $|b, \boldsymbol{p}_0 + \hbar\boldsymbol{k}_{\mathrm{eff}}\rangle$. We don't usually consider the states $|a, \boldsymbol{p}_0 + \hbar\boldsymbol{k}_{\mathrm{eff}}\rangle$ and $|b, \boldsymbol{p}_0\rangle$ because they are not coupled to the initial state by the Raman beams.

Once seeing these two functions of the Raman beamsplitter, we can imagine performing them separately. For example, we can first generate a spin-state superposition by performing a microwave $\frac{\pi}{2}$ pulse. The external momentum can then be entangled with the spin state using our usual velocity-sensitive (counter-propagating) Raman transitions. Suppose a given configuration of Raman beams couple

$$|a, \boldsymbol{p}_0\rangle \leftrightarrow |b, \boldsymbol{p}_0 + \hbar \boldsymbol{k}_{\text{eff}}\rangle,$$

it follows that

$$|b, \boldsymbol{p}_0'\rangle \leftrightarrow |a, \boldsymbol{p}_0' - \hbar \boldsymbol{k}_{\text{eff}}\rangle$$

are also coupled, simply by reversing the order of the first relationship and taking $\boldsymbol{p}_0' = \boldsymbol{p}_0 + \hbar \boldsymbol{k}_{\text{eff}}$, where $k_{\text{eff}} = 2k$ for a 2-photon velocity-sensitive Raman transition, and k is the laser wavevector.

A finite bandwidth δf of the pulse makes the pulse efficient for a range of Doppler spreads, and a corresponding range of $\boldsymbol{p}_0$. If the pulse bandwidth is sufficiently larger than the recoil frequency shifts involved, we can consider the pulse to have efficiency independent of momentum over that range. That is, we can rewrite the levels being coupled as

$$|a, \boldsymbol{p}_0\rangle \leftrightarrow |b, \boldsymbol{p}_0 + \hbar \boldsymbol{k}_{\text{eff}}\rangle \tag{7.16}$$

$$|b, \boldsymbol{p}_0\rangle \leftrightarrow |a, \boldsymbol{p}_0 - \hbar \boldsymbol{k}_{\text{eff}}\rangle \tag{7.17}$$

where the only difference from the previous state-couplings is that we've let $\boldsymbol{p}_0' \to \boldsymbol{p}_0$ by the assumption that the pulse bandwidth is sufficiently larger than the recoil shifts. To be a little more specific about that assumption, we define $\nu_{\text{sw}} \approx 8.3$ kHz as the frequency shift required to produce a standing wave moving at the recoil velocity $v_{\text{rec}} = \frac{\hbar k}{m_{\text{Cs}}}$. That is,

$$\nu_{\text{sw}} = \frac{1}{2\pi} \frac{2\hbar k^2}{m_{\text{Cs}}} \tag{7.18}$$

This is the relevant frequency shift because, as with a standing wave, an atom moving at v_{rec} sees the counter-propagating (velocity-sensitive) two-photon Raman transition frequency shifted by ν_{sw} (since each beam is Doppler shifted with opposite sign).

Note that the maximum difference in external momentum of the states involved in eq. 7.16 is $2\hbar k_{\text{eff}} = 4\hbar k$. The velocity difference between those states is then $4v_{\text{rec}}$. For our cesium atoms, this means our $\boldsymbol{p}_0' \to \boldsymbol{p}_0$ assumption is explicitly

$$\delta f \gtrsim 4\nu_{\text{sw}} \approx 33.1 \text{ kHz},$$

This is not always the case, but it can usually be accomplished. We will see that it certainly holds for our adiabatic passage pulses.

What we've explicitly found here is that the direction of the kick depends on the initial state. This is the reason for our somewhat convoluted definition of k^+ and k^- transitions in Chapter 4.3.2. Since the direction of the kick depends on the spin state, we will follow Refs. [146, 147] and call these transitions *spin-dependent kicks*, or SDKs.

We can now split the Raman beamsplitter into a two-part operation: (i) superpose the spin-state of the atom with a microwave $\frac{\pi}{2}$ pulse, and (ii) entangle the external momentum with the spin degree-of-freedom using an SDK π pulse. This process is shown, and compared

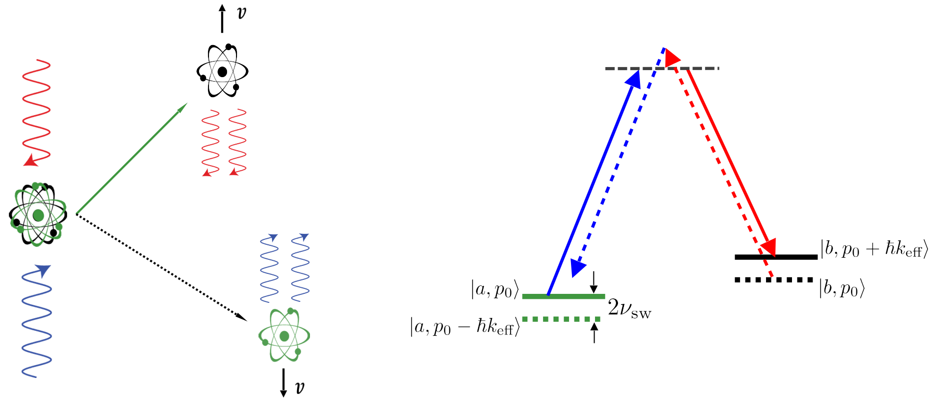

Figure 7.6: An atom initially in a spin superposition receives a spin-dependent kick. State $|a\rangle$, shown in green, is kicked up into state $|b\rangle$. An atom initially in state $|b\rangle$ however, is kicked down into $|a\rangle$. These two processes are shown on the atoms' energy levels at right in solid and dashed lines, respectively. The latter process is Doppler shifted to a different resonance frequency, since the atom sees opposite-sign Doppler shifts ($\pm 2\nu_{\mathrm{sw}}$) for the upward- and downward- traveling beams.

to a standard Raman beamsplitter, in Fig. 7.7.

Figure 7.7: SDK beamsplitter. The initial spin state $|a\rangle$ is shown in solid blue lines and the other spin state $|b\rangle$ is shown in dashed red lines. The horizontal (vertical) axis is time (position), so a state's momentum can be inferred from the slope of the line showing its path. Each operation is shown with a dashed black vertical line. The left schematic shows a standard $2\hbar k$ Raman $\frac{\pi}{2}$ pulse. The right shows a two-step SDK beamsplitter, where the spin-superposition and momentum-entanglement are performed in separate steps.

This new beamsplitter, the *SDK beamsplitter*, can then be used in an atom interferometer in place of the standard Raman beamsplitter. Note that the spin superposition could be also performed with a velocity-insensitive (co-propagating) Raman $\frac{\pi}{2}$ pulse instead of a microwave pulse.

A similar split beamsplitter has been proposed in Refs. [15, 148] for atoms. Analogous beamsplitters have been demonstrated in Refs. [146] using trapped ions, [33] with magnetic beamsplitters and [149] for temperature measurement, but these have not yet been applicable to precise atom interferometry measurements.

So far "splitting the beamsplitter" has seemed like an elaborate lateral move that, while mildly interesting, doesn't really gain us much. It turns out that the SDK beamsplitter has a number of advantages in atom interferometry applications. We discuss these advantages and present interferometer realizations in the next section.

7.3 SDK interferometry

Interferometers can be realized by combining SDKs. The simplest case, shown in Fig. 7.8, is one SDK beamsplitter, followed by two π pulses to invert the direction of the interferometer arms, and a SDK re-combiner to interfere the two arms. The SDK re-combiner is just the beamsplitter in reverse; the arms are brought to relative rest with a SDK pulse, then interfered with a microwave $\frac{\pi}{2}$ pulse.

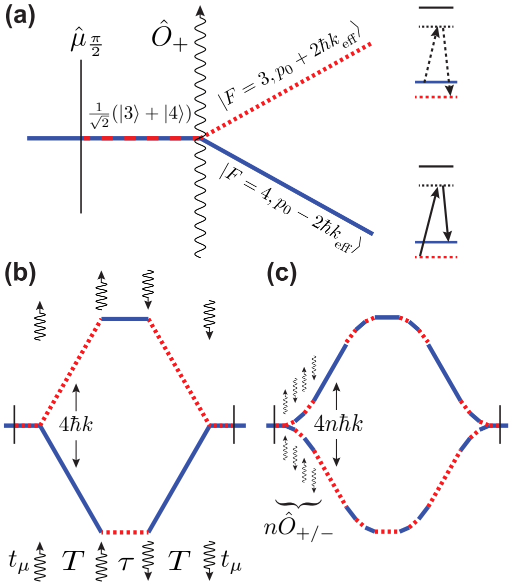

Figure 7.8: SDK interferometry. **a)** SDK beamsplitter. A microwave $\frac{\pi}{2}$ pulse $\hat{\mu}_{\pi/2}$ puts the atom into a superposition of hyperfine states. A Raman adiabatic passage $\hat{O}_+$ then delivers a spin-dependent kick to each arm of the superposition. The energy level diagrams at right show the transitions for both arms. **b)** Basic SDK interferometer. During the wave packet separation time T, the arms have $4\hbar k$ momentum separation, while τ denotes the time between halves of the SDK mirror pulse sequence, where the arms are at rest relative to each other. **c)** Large momentum transfer (see Sec. 7.3.3 in the main text). Inverting the laser wave vectors kicks the arms in opposite directions, $\hat{O}_-$. Since both laser frequencies travel in both directions, either operation can be chosen (a large enough Doppler shift breaks the degeneracy).

To this point, it has been unclear why we spent the first section of this chapter going through a lengthy description of adiabatic passage. It will turn out that the SDK interferometer is particularly amenable to the use of adiabatic passage.

We denote by $\hat{O}_\pm$ an adiabatic passage on the $k_\pm$ transition. For our cosine-squared pulses, atoms with a detuning in the range $\sim \pm\Omega_0/2 \approx 2\pi \times \pm 125$ kHz/2 are transferred with a measured efficiency of 96% ($\pm \sim 1\%$,depending on the intensity used). While we use adiabatic passage for the optical π pulses, this is not necessary for SDK operation; standard Raman π pulses would also work. A representative scan of our adiabatic passage efficiency as a function of detuning and amplitude can be seen in Fig. 7.9.

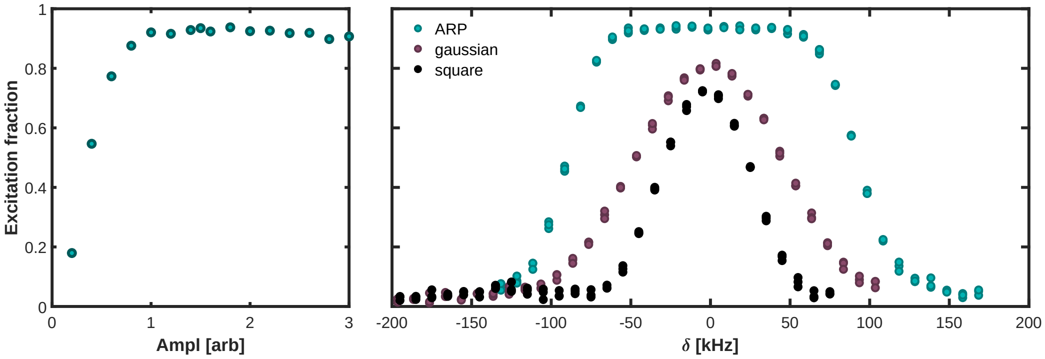

Figure 7.9: Adiabatic passage parameter scan. Pulse amplitude (left) and detuning offset (right) are scanned. Efficiency driving the transition $|0\rangle \rightarrow |1\rangle$ is measured. Detuning scans for (non-ARP; fixed frequency) pulses with Gaussian and square intensity profiles are shown as well. The increased efficiency and bandwidth provided by the ARP pulse is clearly seen.

In considering the adiabatic passage pulses acting on a superposition state during the interferometer, it is sufficient to consider the action on the basis states alone (since the Hamiltonian is, of course, linear: $\hat{H}(\alpha|0\rangle + \beta|1\rangle) = \alpha(\hat{H}|0\rangle) + \beta(\hat{H}|1\rangle)$). Thus, as with standard Raman interferometers, we can calculate phases along each arm independently to calculate the phases for an SDK interferometer.

7.3.1 SDK advantages

The split beamsplitter has a number of advantages over the traditional Raman beamsplitter that are not immediately obvious. We outline several of them here.

Exclusive use of efficient atom optics

The SDK beamsplitter is particularly amenable to the use of adiabatic passage. Though this has been attempted before in atom interferometry [150, 151], technical limitations persisted in previous methods. We will show in Sec. 7.3.2 that the SDK beamsplitter, especially in conjunction with an optical cavity, nicely mitigates these technical limitations.

Using microwaves to generate superposition is generally a more-easily uniform way to address the atomic cloud than using a laser beam. Since the atom cloud is much smaller than the wavelength of microwave radiation (but not optical radiation), achieving homogeneous coupling is easier with microwaves, which makes their use efficient over the cloud.

By using only microwave $\frac{\pi}{2}$ pulses and adiabatic passage π pulses, an interferometer can be composed exclusively of efficient manipulations of the matter wave.

Large momentum transfer

There is another clear difference between the beamsplitters shown in Fig. 7.7: the SDK beamsplitter has $4\hbar k$ momentum separation between the interferometer arms, which is twice the standard $2\hbar k$ Raman interferometer! We will see in Sec. 7.3.3 that SDK pulses can be cascaded, providing $4n\hbar k$ separation.

This benefit shows a merging of some benefits of both Bragg and Raman transitions. The SDK beamsplitter provides the state labeling and high bandwidth (relative to Bragg) of Raman transitions, and the large momentum transfer (LMT) and ac Stark insensitivity of Bragg transitions. Adiabatic passage further increases pulse bandwidth.

Reduced experimental complexity

The benefits above typically come at the cost of great experimental complexity. Efficient atom optics require uniformly addressing an atom cloud, which typically requires a large beam, and thus high laser power (up to 43 W [68]).

The velocity spread in the direction of the laser beam also must be very small for Bragg diffraction ($\sim 0.1\hbar k$). This comes at the cost of either complicated atom sample preparation (e.g., BEC, delta kick cooling, long cycle times up to 20 s) or a severe velocity selection, which greatly reduces the atom number.

The SDK interferometers in our experiment however, require < 0.5 s of atom sample preparation, no evaporation, and only ~ 10 mW of incident laser power for interferometry pulses. Despite this, the geometry allows for LMT interferometers, as well as other many-pulse geometries.

Suppressed ac Stark shifts

As explained briefly in Chapter 2 and in more detail in Ref. [38], optical π pulses are significantly less sensitive to ac Stark shifts than optical $\frac{\pi}{2}$ pulses. Use of an SDK beamsplitter allows all optical pulses to be π pulses, and thus suppresses ac Stark phase shifts. The cartoon-ish (but still mostly correct) way of looking at it is that each arm spends half of each optical pulse in each spin state. As long as not much changes over the pulse duration, the differential ac Stark phase shift between the interferometer arms vanishes. Contrast this to the case of standard Raman beamsplitters in a Mach-Zehnder. In that case, ac Stark cancellation occurs between the beamsplitter pulses, which can be separated by hundreds of milliseconds ($\sim 10^3$ times longer than typical pulse durations). This suppressed ac Stark sensitivity is particularly welcome in our cavity interferometer, where ac Stark shifts are complicated (see Sec. 4.3.2).

Fig. 7.10 demonstrates this suppressed sensitivity.

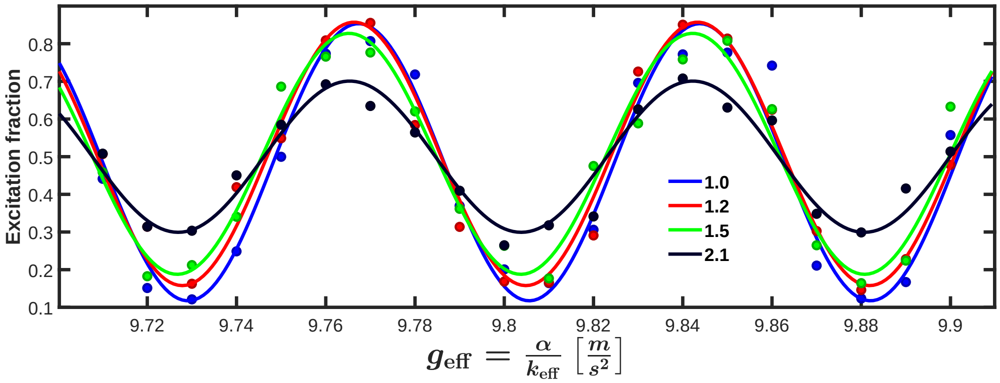

Figure 7.10: Suppressed ac Stark sensitivity. A basic $4\hbar k$ SDK interferometer is run varying the pulse amplitude beyond the minimum region where the pulses are first very efficient. Fringes shown have have relative pulse amplitudes of 1, 1.2, 1.5, 2.1 (arb. units), respectively. The fringes do not shift despite varying the pulse amplitude of all four SDK pulses by over a factor of 2, indicating statistically insignificant ac Stark phase shift. $T = 0.5$ ms was used.

State labeling

Simply put, this method maintains the state labeling inherent of Raman transitions, keeping the simplified detection and interferometer readout. This is not an advantage over a traditional Raman beamsplitter, but is a convenient feature that is preserved despite adding LMT capability and suppressed ac Stark sensitivity.

Equal velocity outputs

In previous sections, we've described the chirped lattice used to catch the atoms after their time of flight. Atoms whose transverse motion have taken them outside the cavity mode don't see the laser and continue falling.

The catch acts as a $2\hbar k$ momentum filter (if the lattice depth is low enough that only the first Bloch band is caught). Atoms that missed transitions, and therefore have the wrong velocity, are not caught and fall away. So the catch is both a spatial *and* velocity filter. However, in traditional Raman or Bragg interferometers, the final output ports are separated by at least $2\hbar k$, and thus cannot both be caught with high efficiency.

The SDK output ports, however, have the same velocity. They are thus particularly well-situated to take advantage of this benefit. The catch substantially improves SDK interferometer contrast, for reasons discussed in Sec. 7.4.2.

7.3.2 The dynamic phase

Before moving on, it is worth addressing the main technical hurdle that limited previous attempts at adiabatic passage atom optics: the dynamic phase ϕ from eq. 7.13. There's no free lunch [152], and adiabatic passage is not a magic bullet. The problem ARP addresses is that the inhomogeneous atom-laser coupling gives a spread in Rabi frequencies. Thus, atoms at different radial positions want different t_π times for a π pulse. ARP converts this "efficiency spread" into a phase spread, as the dynamic phase ϕ is proportional to the Rabi frequency. For some applications, this is of no consequence, but it matters for a phase-measuring atom interferometer.

Adiabatic passage converts the spread in Rabi frequencies (due to the laser beam waist, eq. 4.3) to a spread in the dynamic phase ϕ. A look at the top phase sidebar of Fig. 7.5 (blue, constant detuning) shows that ϕ is of order tens of π, so the spread in dynamic phase will be at least several π. Averaging over the atom cloud completely washes out any interference contrast, seemingly ruining any hope of an interferometer.

However, unlike an efficiency spread, a phase spread can be reversed. If two pulses are applied in quick succession with alternating sign of ϕ (determined by initial state (eq. 7.12) and sweep direction), the dynamic phase cancels. The contrast of our interferometer vanishes if such cancellation does not occur, for example if the sweep direction of one ARP pulse is intentionally inverted. The basic idea though, is that if not much changes between pulses whose dynamic phases are meant to cancel, then the two arms of an interferometer will receive dynamic phases from the first pulse of $\pm\phi(\rho)$, and from the second pulse of $\mp\phi(\rho)$. Thus, regardless of radial position ρ, the net dynamic phase will be 0, and the contrast will not wash out.

We use several methods for effective re-phasing. First, we intensity-stabilize interferometry pulses to minimize optical power drifts or fluctuations. Second, we avoid large radial motion of the atoms by catching only the center of the atom cloud (Sec. 3.4). Third, because the intra-cavity intensity changes with Raman frequency (Chapter 4), we adjust the input intensity of pulse pairs such that their Rabi frequencies are equal and thus their dynamic phases cancel.

The largest source of re-phasing errors in previous interferometers [151] was cited to be beam quality. In our apparatus, the optical cavity acts as a mode filter [153], providing very clean wave fronts. It is unclear, however, if the cavity is a requirement for effective SDK interferometer operation: measuring the wavefront distortion of the in-vacuum cavity mode, or running the apparatus without the cavity mode, are both prohibitively difficult. The work in Ref. [151] also used a larger, hotter atom cloud.

For more details than you ever wanted to know about the dynamic phase and its effective cancellation, see Sec. 7.4.

7.3.3 Large momentum transfer

Momentum transfer even higher than $4\hbar k$ can be achieved by cascading SDKs as shown in Fig. 7.8c. Alternating between $\hat{O}_+$ and $\hat{O}_-$ pulses allows momentum transfer in the same direction, as the spin state is toggled between $|F=3\rangle$ and $|F=4\rangle$. This alternating could be avoided by inserting microwave π pulses between the optical pulses, but this proved less efficient overall in our apparatus. A $4n\hbar k$ interferometer ($n = 1, 2, 3, \ldots$) is realized by consecutive pulses to first accelerate the arms away from each other, then invert relative momentum, and finally recombine.

The phase difference between the arms of this interferometer can be evaluated following the procedures in Ch. 2, and is given by

$$\Delta\phi = 4n(\boldsymbol{k} \cdot \boldsymbol{a})T(T + \tau) \tag{7.19}$$

where $\boldsymbol{a}$ is the acceleration experienced by the atom, and the times T, τ are defined in Fig. 7.8.

Performance of the SDK interferometer at large momentum transfer is shown in Fig 7.11. We have demonstrated interferometers with up to $20\hbar k$ momentum splitting (Fig. 7.11 shows up to $16\hbar k$). The momentum separation in our current setup is limited by the use of the same laser frequencies to address both interferometer arms (we will return to this in more detail later in this section).

We observe excellent contrast out to $T = 44$ ms (Fig. 7.11), limited only by the available free-fall time. SDK interferometers shown include a time $\tau \approx 20$ ms centered around the apex of the trajectory to avoid degeneracy between $\hat{O}_+$, $\hat{O}_-$ and the velocity-insensitive Raman transitions. The upper dashed line indicates the contrast of a Ramsey clock (i.e., only the $\hat{\mu}_{\pi/2}$ pulses) measured for various timings. Our interferometer with the largest scale factor ($16\hbar k$, $T = 44$ ms, $\tau = 18$ ms) acquires a phase shift of 3.4 Mrad due to Earth's gravity. A traditional $2\hbar k$ Raman Mach-Zehnder interferometer with the same $T = 44$ ms would have a phase of 0.28 Mrad, so this represents over an order of magnitude improvement.

To use large momentum transfer in an SDK interferometer, many pulses must be applied. A $4n\hbar k$ interferometer as in Fig.7.8c requires $4n$ optical pulses. This means each pulse must be very efficient for the matter wave to follow the entire interferometer. This is where using adiabatic passage presents a large advantage over Raman pulses.

Each pulse imparts $4\hbar k$ momentum transfer. For our $\sim 96\%$ efficient ARP pulses, this gives an efficiency of 99% per $\hbar k$. To achieve an overall efficiency $\geq 10\%$, use of adiabatic SDK pulses increases the total possible momentum transfer by over an order of magnitude compared to traditional Raman pulses, from $12\hbar k$ (6 Raman pulses, each 70% efficient) to $260\hbar k$ (65 adiabatic SDK pulses). This efficiency improvement is limited only by available laser power limiting Ω_0, and thus the non-adiabaticity ϵ_0. Because of a fiber EOM damage threshold, only 12 mW are incident on the cavity in our work.

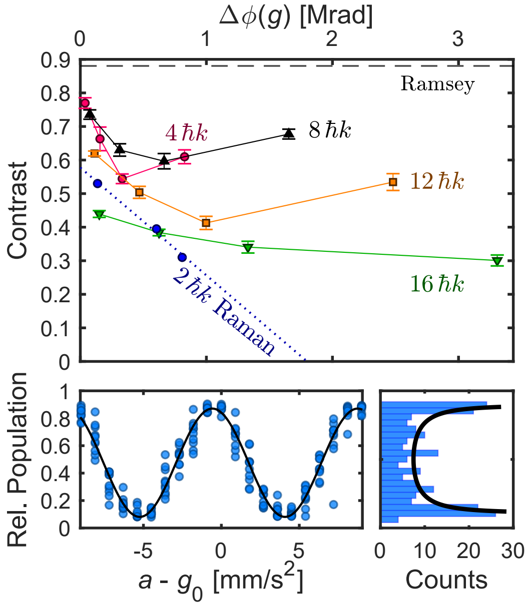

Figure 7.11: Large momentum transfer interferometers. Top: SDK interferometer contrast as a function of gravity phase $\Delta\phi$, measured for various orders of momentum transfer at wave packet separation times $T = 5$, 15, 25, and 44 ms. The gravity phase $\Delta\phi(g)$ is due to the acceleration from Earth's gravity, $g \approx 9.8\frac{\text{m}}{\text{s}^2}$. High visibility fringes are observed for $\Delta\phi \lesssim 0.5$ Mrad, above which vibration noise dominates. Contrast is therefore determined by fitting histograms of ~ 200 interferometer outputs to an arcsine probability distribution function [18]. Error bars represent the 1σ statistical uncertainty in the contrast fit parameter. The blue dotted line provides a comparison to traditional $2\hbar k$ Raman Mach-Zehnder interferometers in our apparatus with $T = 22$, 55, and 65 ms. Bottom: The fringe for a $4\hbar k$ interferometer with $T = 1$ ms, $\tau = 26$ ms is shown, along with its contrast histogram. Each point in the top panel of this figure comes from such a fitted histogram.

7.3.4 Single source gradiometer

The SDK toolkit enables novel and flexible interferometer geometries. As an example, we realize a single-source gradiometer (see Fig. 7.12). A SDK beam splitter is used to separate two arms of the atomic wave function. Once separated, they are brought back to equal velocity and used to perform two SDK interferometers simultaneously. These interferometers can then measure a relative phase, where common-mode noise (vibrations, laser phase noise) is rejected [16]. We demonstrate the gradiometer by measuring a phase induced by a transverse laser beam incident on only the lower SDK interferometer. The upper and lower interferometers have the same velocity and the same internal states, reducing systematic effects. Additionally, the gradiometer baseline is known to high precision, since it is determined only by the photon momentum and wave packet separation time.

The primary limitation on this interferometer was achieving the same Rabi frequency

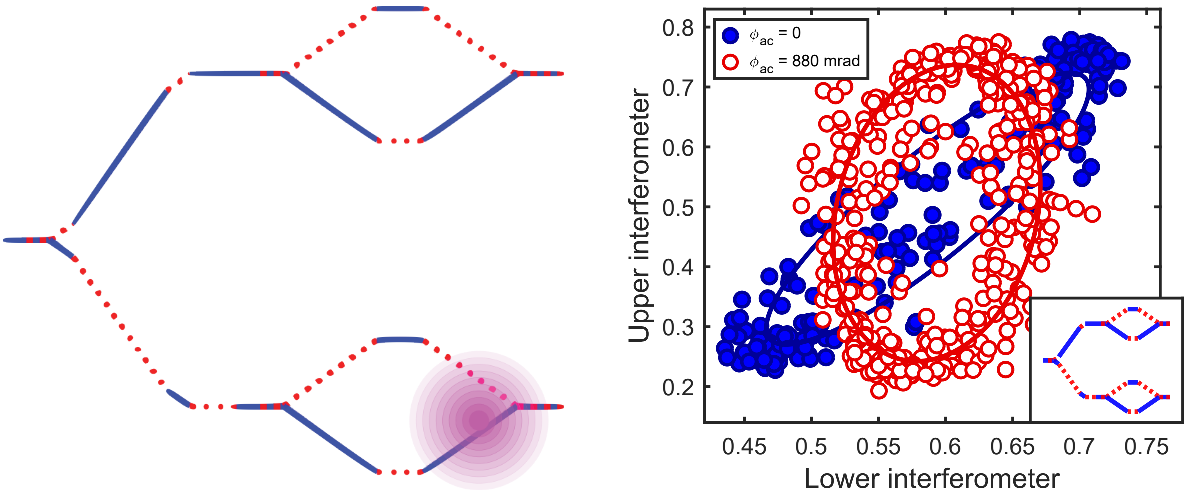

Figure 7.12: Single-source gradiometer. A schematic of the arm trajectories is shown at left, and in the inset at right. The first half of an $8\hbar k$ SDK interferometer separates two arms. Once brought back to relative rest, the actual interferometer sequence begins, simultaneously addressing both arms. The phases of the two interferometers can then be read out using the four output ports. The main plot shows gradiometer data. The two interferometers have a fixed phase difference independent of common mode phase noise. When plotted parametrically, the interferometer outputs form an ellipse whose shape is determined by this relative phase difference. Ellipses are plotted both with (red, hollow) and without (blue,filled) a transverse laser beam applied to phase shift the lower interferometer by ϕ_{ac}. For this data, the atoms separated for 63 ms, giving 1.764 mm of separation to the gradiometer. $T = \tau = 0.3$ ms was then used for the interferometers.

in the two spatially-separated interferometers for the microwave $\frac{\pi}{2}$ pulses $\hat{\mu}_{\pi/2}$. The spatial profile of microwave Rabi frequency is complicated due to multiple reflections of the radiation by the metal vacuum chamber. This effect could be alleviated by several methods, such as using a fractional adiabatic $\pi/2$ pulse [142], using a velocity-insensitive optical $\frac{\pi}{2}$ in the cavity mode (instead of $\hat{\mu}_{\pi/2}$), or even just a more deliberate alignment of the microwave horn.

7.3.5 Looped interferometer for ac signals

As a further example, we demonstrate a tunable detector for accelerations that oscillate with fixed periodicity. Such "resonant" atom interferometers have been proposed to search for gravitational waves [154] or oscillating forces due to light dark matter [155]. As shown in Fig. 7.13, lock-in ac detection is achieved by having the wave function enclose several loops ($m = 3$ are shown). The sensitivity function reverses in each loop, as the arms are kicked in alternating directions. A requirement for such a detector is the efficient application of many pulses. Performing many loops increases the frequency selectivity ("quality factor" Q) of the resonant detector, and therefore its noise suppression at other frequencies. The frequency

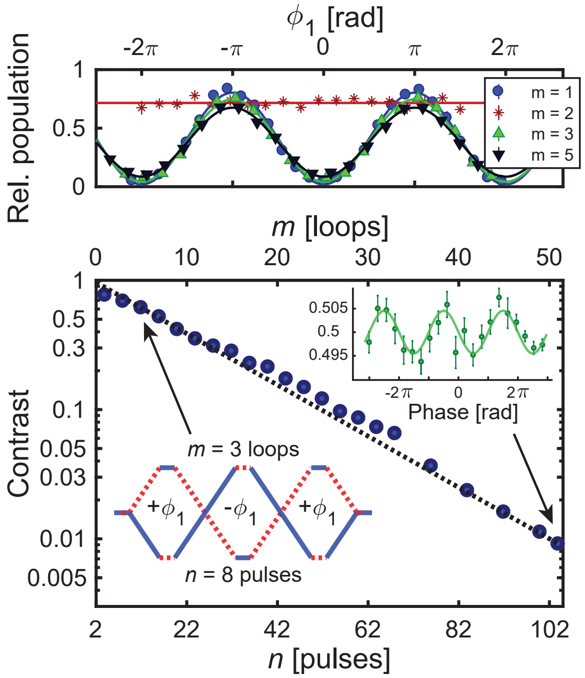

Figure 7.13: Resonant atom interferometer. Top: Interference fringes for different number of loops m, as the phase per loop is varied. Bottom: Contrast decay is shown as both a function of the number of loops m, and corresponding number of optical pulses n. Resonant interferometer geometry for $m = 3$ loops is illustrated in the lower left. The dotted line represents a model with no free parameters, using only the independently measured Ramsey contrast (88%) and ARP pulse efficiency (96%), and the calculated single photon scattering (1% per pulse). Agreement with the data indicates negligible sources of additional contrast loss. A stable fringe is observed even after 51 loops.

probed is set by the duration of each loop, which is easily tuned. The sensitivity function of this geometry is discussed in detail in Ref. [154]. We demonstrate a proof of principle for a scalable resonant scheme (up to three loops had been previously demonstrated [14]). The top panel of Fig. 7.13 confirms the expected behavior of such a resonant interferometer: for even m, dc effects (such as gravity and laser phase per loop φ_1) cancel, and the interferometer phase remains zero regardless of φ_1. For odd m the net interferometer phase is that of a single loop, φ_1. For this demonstration, contrast data were taken with loop sizes of $T = \tau = 10$ μs at $4\hbar k$ splitting to allow over 100 pulses of 200 μs duration to fit within the available free-fall time (including avoiding the times around the apex where $k^{\pm}$ transitions are degenerate with each other and the velocity-insensitive co-propagating transition). A stable fringe is observed at each loop order, whose fitted amplitude matches the histogram-fitted contrast of Fig. 7.13. LMT could also be implemented in each loop to increase sensitivity.

7.4 Real world issues

This section gets really into the nitty-gritty about how adiabatic passage pitfalls are avoided in our setup. For a deeper look into the technical details, please keep reading!

7.4.1 Doppler separation

A simplification that we glossed over previously to obtain eqs. 7.16 was assuming that the pulse bandwidth is greater than the recoil-induced Doppler shift between the states involved. This is a good assumption for our ARP pulses (~ 125 kHz bandwidth) in an SDK beamsplitter (same initial momentum → 33.1 kHz separation). However, as more pulses are added, the detuning of the arms grows by $\pm 2\nu_{\rm sw}$ with each additional LMT order.

Consider a SDK beamsplitter applied to an initial state $|\psi_0\rangle = \frac{1}{\sqrt{2}}(|a, p_0\rangle + |b, p_0\rangle)$. Suppose the ARP pulse $\hat{O}_+$ couples $|a, p_0\rangle \leftrightarrow |b, p_0 + 2\hbar k\rangle$. Let δ_+ be the detuning of the "upper" arm transition $|a, p_0\rangle \leftrightarrow |b, p_0 + 2\hbar k\rangle$, and δ_- be the detuning of the "lower" arm transition $|b, p_0\rangle \leftrightarrow |a, p_0 - 2\hbar k\rangle$. We can choose the center of the detuning profile such that $\delta_\pm = \pm 2\nu_{\rm sw}$. For the nth-order pulse, which couples the momentum states $|p_0 \pm 2(n-1)\hbar k\rangle \leftrightarrow |p_0 \pm 2n\hbar k\rangle$ (while also changing the hyperfine state), the detuning $\delta_\pm^{(n)}$ is

$$\delta_\pm^{(n)} = \pm 2n\nu_{\rm sw} \approx \pm n \times 16.5 \text{ kHz}$$

Note that the Doppler separation *between* the arms is twice that. This situation is illustrated in Fig. 7.14. For our cosine-squared ARP pulse bandwidths of ~ 125 kHz (see Fig. 7.9) then, a 4th adiabatic passage acting on a superposition is attempting to simultaneously address transitions separated by 132 kHz, which already begins to violate the assumption. For our pulse parameters, this is about the limit; there is a sharp decline in efficiency after about 4th order. This limit could be pushed further with a higher peak Rabi frequency, and corresponding detuning profile.

The results of this effect can be seen by looking at the numerical simulations, as in Fig. 7.15.

7.4.2 More dynamic phase

We just saw that the Doppler separation, when too large, hurts interferometer performance by lowering efficiency of the SDK pulses. There *is* another effect arising from this detuning: increased dynamic phase. Fig. 7.5. We can write

$$\phi(\alpha, \delta) \approx a(\alpha)\delta^2 + \alpha\phi_0 \tag{7.20}$$

This is an approximate relation, but fits well in the region where the pulse is efficient. The coefficient $a(\alpha)$ depends on the pulse intensity α. ϕ_0 is the dynamic phase for a "perfect" pulse, $\{\alpha, \delta\} = \{1, 0\}$. The atoms have a spread in momentum $\lesssim 2\hbar k$ that gives a spread

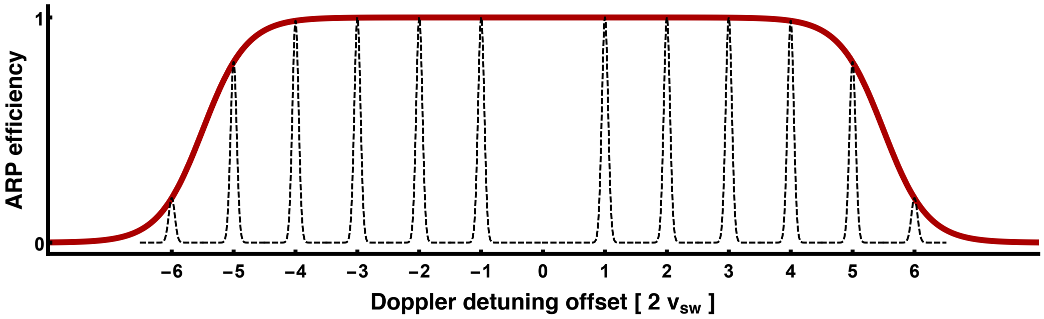

Figure 7.14: Doppler separation for nth order SDK pulse. As the pulse order n increases, so does the relative momentum between the two interferometer arms. This separation is shown here by a narrow distribution around a central value of that momentum's corresponding Doppler shift. Qualitatively, this is what a low bandwidth Raman pulse's efficiency might look like when attempting to drive a transition for that momentum class.

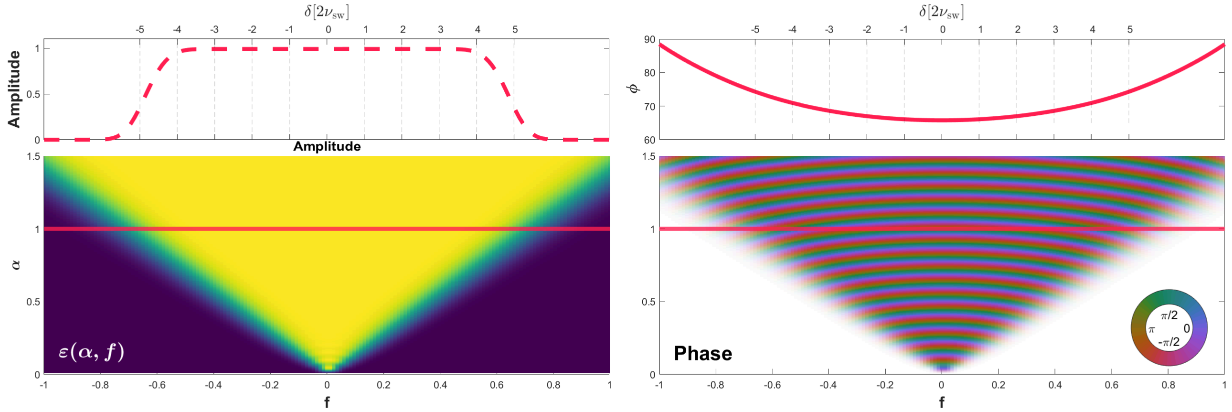

Figure 7.15: Detuning effects on adiabatic passage. Lower left: Amplitude to undergo the transition $\varepsilon(\alpha, f)$, as in Fig. 7.5 (just rotated and zoomed in, same $\epsilon_0 = 0.025 \to Q = 40$). Lower right: Same for the dynamic phase (opacity again set to $\varepsilon(\alpha, f)$). The upper sidebars show the corresponding quantity at fixed $\alpha = 1$. Vertical dashed lines indicate the detuning offsets for nth-order SDK pulses, for $n = 1, , .., 5$ at the appropriate values of f. The horizontal axes match those of the corresponding plots below them. The amplitude top sidebar is dashed to indicate that it's not *quite* the values plotted along the red line below: instead, we've raised those values to the fourth power, since four is the minimum number of pulses at each order required for a complete SDK interferometer.

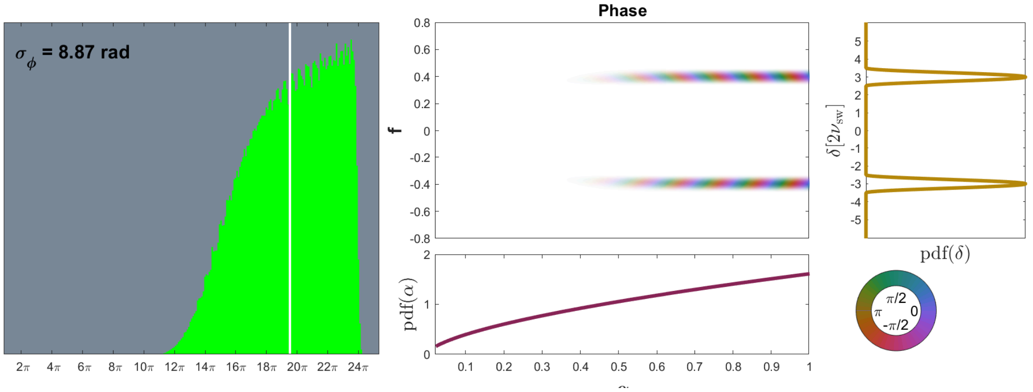

Figure 7.16: Dynamic phase distribution. See main text for description. White vertical line indicates the average of the distribution.

in Doppler shifts, and therefore a spread in dynamic phase ϕ. Since $\phi(\delta)$ is quadratic, we would expect this effect to worsen as the SDK order increases, and the Doppler separation grows between the two arms.

It turns out that the spread in ϕ from the momentum spread of the atoms is (by far) sub-dominant to another effect: the spread in intensities seen by the cloud due to the finite size of both the atom cloud and the laser waist, as discussed in Sec. 4.3.1. The intensity spread effect on ϕ is so much larger that the momentum spread can safely be ignored. In this section, we will calculate the spread in dynamic phase due to the intensity spread.

We begin with the parameterization of the intensity from Sec. 4.3.1 with a unitless variable α:

$$I(\alpha) = \alpha I_0$$

where I_0 is the peak intensity of a gaussian beam (eq. 4.2), and $\alpha \in [0, 1]$. Taking the atom cloud as a spherical gaussian distribution, we obtain the probability distribution function for α:

$$f_A(\alpha) = \frac{w_0^2}{2\sigma^2}\alpha^{\frac{w_0^2}{2\sigma^2}-1}$$

The above is performed in more detail in Sec. 4.3.1.

We start with a uniform momentum distribution over a $2\hbar k$ interval (the lowest Bloch band of cavity-launch optical lattice). The detuning as a function of momentum is just a constant factor, $\delta(p) = \frac{k}{m_{\text{Cs}}}p$, and $f = \delta/\Omega_0$ relates the detuning δ to the detuning parameter f from the numerical simulations and eq. 7.14. The pdf for δ in this case is then flat within a $2\hbar k^2/m_{\text{Cs}}$-wide region.

With these distributions, we are now in a position to consider the *distribution in dynamic phase* that arises from the atomic position and momentum distributions (via the pdfs $f_A(\alpha)$ and $f_D(\delta)$). This is done in Fig. 7.16.

Fig. 7.16 conceptually begins with the “Phase” color plot. Again, this is the same phase plot as in Figs. 7.5 and 7.15, just zoomed in and with a different transparency mask (cosine-squared envelope, robust detuning profile, and $\epsilon_0 = 0.025 \to Q = 40$). Here the opacity is proportional to the joint pdf times the pulse efficiency

$$f_A(\alpha) f_D(\delta) \varepsilon(\alpha, \delta)$$

where f_A and f_D are the pdfs of α and δ, respectively. We include the pulse efficiency $\varepsilon(\alpha, \delta)$ because the phase mattering is conditioned upon the atom participating in the interferometer.

The pdfs for α and δ are shown in the lower and right sidebars, respectively. The pdf for α assumes experimental values $w_0 = 718$ μm, $T = 300$ nK, and $\sigma_0 = 400$ μm, and $t = 0$ ms, resembling a curve in Fig. 4.3.

The figure simulates a 3rd-order SDK pulse, (i.e., before the pulse in question, the atom is in a superposition with the two arms having $8\hbar k$ relative momentum between them). The pdf for δ reflects this, having peaks around $n = \pm 3$. $f_D(\delta)$ is here taken to be a cosine-squared distribution with $2\hbar k$ width because it looks cooler than the uniform distribution we discussed earlier. This is probably more realistic anyways, since we use a velocity selection pulse after the atoms have been launched, narrowing the velocity distribution. The f and δ axes are equivalent, and show their respective labels.

In any event, switching to a uniform distribution (or even changing the width of the momentum spread) changes the results only negligibly for cloud sizes > 100 μm, above which the spread in α dominates.

Changing the SDK order affects the result only insofar as the α distribution is affected. Since the Doppler separation between the arms (and thus δ) increases, the range of α over which $\varepsilon(\alpha, \delta)$ is appreciable shrinks, as seen from Fig. 7.5. This lowers the dynamic phase spread, but addresses fewer atoms (i.e., no free lunch).

The phases shown via color in the opacity-masked phase map can then be sampled from following the joint pdf $f_A(\alpha) f_d(\delta) \varepsilon(\alpha, f)$ (strictly speaking, $\varepsilon(\alpha, f)$ is not part of the pdf, but represents the post-selection of atoms that participate in the interferometer.). After sampling, these phases can be histogrammed to reveal the underlying distribution of phases. The histogram at left shows these phases[1]. The white line shows the mean phase $\bar{\phi}$, and the phase standard deviation σ_ϕ is quoted.

The histogram really drives home this dynamic phase problem: there’s not a well-defined phase here! Furthermore, this is only *half* of the interferometer’s dynamic phase, since the arms of the superposition pick up equal phases with the opposite sign (see eq. 7.12). Apparently we’ll need the dynamic phase cancellation to be pretty good for this phase spread to be successfully reversed to un-wash out the interferometer contrast.

The preceding analysis shows that by far the most consequential effect for the spread in dynamic phase is the spread in α. As such, the cloud size (relative to the laser beam waist) is the dominant physical parameter controlling these spreads. A wide laser beam and small atom cloud is better (what else is new). Fig. 7.17 demonstrates this effect.

---

[1] The phase map in Fig. 7.5 was unwrapped from $[0, 2\pi) \to \mathbb{R}$ to extract these distributions using Refs. [156, 157].

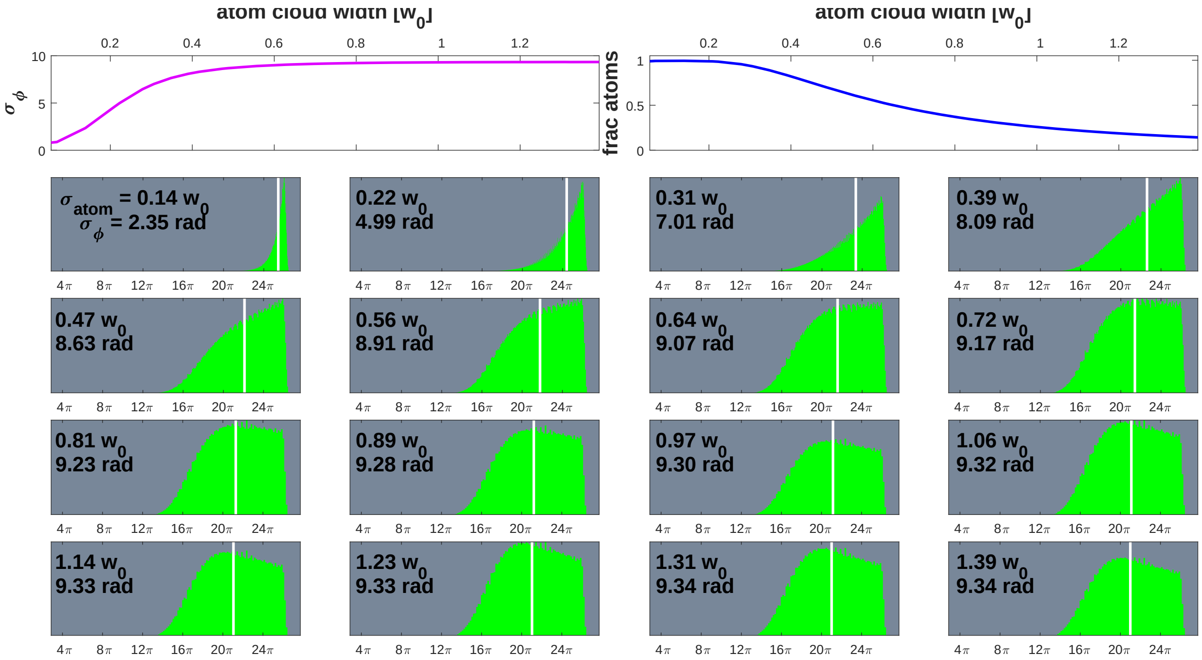

Figure 7.17: Dynamic phase vs cloud size. The same pulse and procedure generating the histogram in Fig. 7.16 is repeated while varying the cloud size in units of the laser waist. Our cavity mode waist is 718 μm, so cloud sizes of 100 μm to 1000 μm are shown. Plots at top of the figure show the standard deviation of the phase σ_ϕ (left) and the fraction of the atom cloud successfully undergoing the pulse (right) as a function of the cloud size σ_{atom}. After a certain cloud size comparable to the beam waist, the distribution stays more or less the same, but fewer and fewer atoms undergo the pulse, as the rest see too low a laser intensity. The steep right slope down from the histogram peak for small cloud sizes (i.e., the first histogram row) is the only effect of finite momentum width; for zero momentum width that slope is vertical, while a higher spread draws out the descent to higher ϕ. Clearly, the intensity spread's effect on the dynamic phase is much larger than that of the momentum spread, especially for the actual cloud sizes used in the experiment ($\gtrsim 0.5 w_0$).

This behavior suggests that catching the atoms in the cavity mode after the interferometer (i.e., performing a radial spatial selection) should decrease the phase spread among atoms participating in the interferometer, increasing contrast (assuming some imperfection in the dynamic phase cancellation). We do see this in the experiment; the catch significantly increases interferometer contrast.

The model presented here so far is a solid start to understanding what's going on with the dynamic phase, and suggests ways one might optimize against SDK interferometer dephasing. However, it's far from complete. A sampling of elements missing from the model is listed below

1. The dynamic phase should in some way depend on the adiabaticity Q. We have not yet investigated at all the dependence of ϕ on this parameter.
2. All of Sec. 4.3.2. Especially the changing Rabi frequency (and thus Q) via the Rabi beatnote.
3. The catch doing a spatial filtering. While we've mentioned the qualitative effect, this has not been carried out quantitatively.
4. Spatial separation of interferometer arms giving different dynamic phases, especially via the Rabi beatnote. This could also lead to some weirdness.

Despite an alarmingly sparse understanding of the dynamic phase (the information in this chapter was worked through almost entirely after the experiments), the interferometers still worked. Apparently, the un-winding of the dynamic phase can be quite efficient. Contrast persisted in the resonant AI after over 100 pulses, and the LMT interferometers worked up to $T = 44$ ms at $16\hbar k$ with the contrast still going strong. In the next section, we will present some steps taken to help the dynamic phase cancellation work well.

7.4.3 Dynamic phase cancellation

The dynamic phase changes sign with the direction of the hyperfine transition $|F=3\rangle \leftrightarrow |F=4\rangle$ and the sign of the detuning profile $\Delta(t)$. Consecutive ARP pulses can thus be set to have their dynamic phases cancel. For the dynamic phase to cancel well between two pulses, the atom should experience the two pulses as similarly as possible. If there is a long time between the pulses, the atom's motion in the radial direction can take it to a region of different intensity (α) for the second pulse than the first pulse. In that case, the total dynamic phase $\phi_{\text{tot}} = \phi_1 - \phi_2$ won't cancel to zero. And since this happens across the ensemble of atoms, there will be a potentially large spread in ϕ_{tot} across the cloud, de-phasing the interferometer.

So we want pulses that are meant to cancel each other's dynamic phase to be close together in time. On the other hand, we want large pulse separation time T to increase sensitivity. It seems we're in a pickle. A way around this is to use the even LMT orders.

Rather than relying on pulses on either side of T to cancel each others' dynamic phases, we can use *pairs* of pulses on either side of T so the dynamic phase cancels irrespective of T.

A small hiccup to doing this involves "pulse-matching", alluded to earlier in the chapter. Since consecutive pulses on either side of T involve opposite transitions k^+ and k^-, they interact differently with the cavity (see Chapter 4). Thus, one transition must be scaled so that the peak Rabi frequency Ω_0 is the same for the two pulses.

It is also necessary to avoid areas of the Rabi beatnote. The low Rabi frequency region lowers the pulse adiabaticity. Additionally, on the slopes of the Rabi beatnote, vertical movement between the pulses degrades the cancellation, even for the ~ 200 μs separations between matched pulses. An atom moving at 50 cm/s at the steepest slope of the beatnote then moves 100 μm between the pulses. For the beatnote wavelength of 1.55 cm, this gives a change in the peak Rabi frequency of about 4%, which is appreciable for large dynamic phases. This behavior is further complicated by finite spatial separation between the interferometer arms.

When calibrating pulse-matching, the atom sample must undergo the same trajectory as in the interferometer. For example, when pulse-matching the 3rd and 4th pulses of an $n = 4$ LMT interferometer, all prior pulses must also be used to ensure the atom is in the same location it will be during the interferometer pulses. Pulse matching is hard and kind of a pain, as we have not yet developed a super solid calibration procedure. In any event, even the odd-order SDK interferometers see contrast survive out to long pulse separation times (Fig. 7.11).

Fig. 7.11 shows some strange contrast dips at intermediate T values for LMT orders $n = 1$ to 3. $n = 4$ seems less affected. The strangeness arises from the Rabi beatnote for the reasons discussed above, where we probably have imperfectly calibrated the pulse-matching as a result. The $n = 4$ interferometer would be less affected, since it is the first order which has 2 each of the $k^\pm$ transitions on either side of T. As a result, pulse matching is less critical because k^+ doesn't need to be well-matched to k^-.

Wavefront aberrations give small-scale variations in the local intensity, which can degrade dynamic phase cancellation even for small movements of an atom. The clean wavefronts of the cavity mode likely help a good deal to suppress this, but it's unclear how much.

We sometimes observe that at the limits of our interferometer performance (especially in the vicinity of Rabi dead-zones), lowering the intensity improves contrast. This seems to go against the pervasive "high Ω_0 is good" sentiment throughout this chapter. This is a signature of imperfect dynamic phase cancellation. By lowering the intensity, we decrease the total dynamic phase, and thus the size of its spread. In some regimes, this dynamic phase cancellation boost seems to outweigh the hit in pulse efficiency, admitting an optimally-scaled intensity (rather than just "infinite").

7.5 Summary

We have demonstrated a new tool for light-pulse atom interferometers by splitting the beam splitter into two operations. This simple change enables the exclusive use of highly efficient adiabatic passage, opening the door to a wide range of new and old geometries. The use of Raman atom optics and a thermal sample greatly relax the complexity required of the atom source to implement these geometries, without precluding their use in existing high-performance devices. This technique combines the advantages of Bragg transitions (LMT compatibility, ac Stark insensitivity) and Raman adiabatic passage (state labeling,high efficiency, wide bandwidth). This tool's flexibility allows specialization for multiple applications. Short pulses forming many loops near a source mass would constitute a lock-in force sensor probing viable mass ranges for light dark matter candidates [155]. High-power, large bandwidth pulses with fast, simple atom preparation could provide LMT for precise inertial sensing. Multi-pulse geometries, e.g., resonant AI or single-source gradiometer, enabled by high fidelities can provide technical benefits to existing and future measurements. A next step may envision a squeezed atom interferometer built using the collective cavity measurement demonstrated in Refs. [158, 159]. The advantages of SDK interferometry are a new item in the atom interferometry toolkit which may be preferable to alternatives for some applications. We hope that SDK interferometry can make demanding experiments tractable, as well as improve sensitivity across a range of measurement types.

Chapter 8

Lattice atom interferometry

In Chapters 5 and 6, we saw that high sensitivity to interactions enables interesting physics measurements. We have seen in several previous interferometer geometries that sensitivity grows with interrogation time (e.g., pulse separation time T in a Mach-Zehnder). To provide long interrogation times, atomic fountains with $\sim$10 m height have been [25] and are being [26] constructed. Pushing this direction even further, plans for a 100 m [160] and a 300 m [161] fountain are in the works.

Very large atomic fountains are technically challenging. The resulting sensitivity to vibrations requires elaborate inertial stabilization (for example, on the VLBAI experiment [26] at Hannover), though certain techniques extract measurements even in the presence of vibrations [16, 67]. Magnetic shielding and atom preparation become more costly and elaborate as well, as does finding /constructing a site that the fountain can fit into.

Additionally, the sensitivity scaling with size is challenging. The atoms' displacement grows quadratically; to double available free-fall time, one would need a fountain 4 times taller. For a Mach-Zehdner, this means that the sensitivity grows linearly with the fountain height. Unfortunately, the experimental cost and complexity likely grows faster than linearly.

The requisite large spatial-scale homogeneity reflects the fact that in a large fountain, the probe atoms' trajectories take them through a large displacement. This large spatial extent hampers spatial-resolution in a measurement. Interactions with a localized source mass of the type in Chapters 5 and 6 are not aided by the nominal increase in sensitivity when the interferometer takes place over such a large region.

One workaround for these difficulties is to go to space [162–164] for microgravity. There, the atoms are in free-fall with the experiment, and interrogation times can be seconds long on small spatial scales. Unfortunately, going to space is a luxury reserved for the few and the powerful.

An alternative avenue is available for those of us who are forced to remain Earth-bound. After separating the atomic wavefunction, one can hold the atoms in a potential, supporting them against free-fall due to Earth's gravity. This has been previously demonstrated in Refs. [117, 118]. However, these two previous demonstrations made clear that requirements on the uniformity of the holding potential are strict.

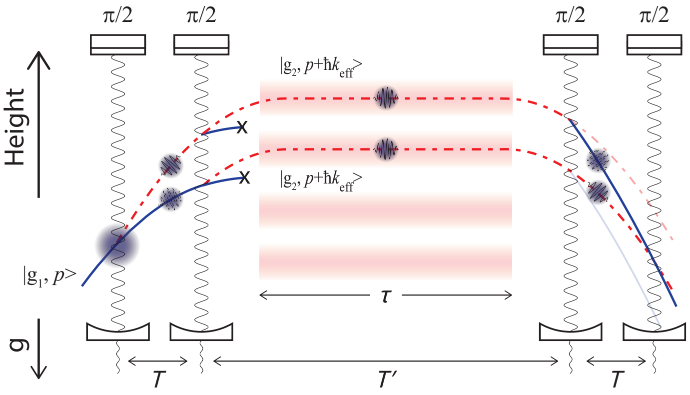

Figure 8.1: Lattice interferometer geometry. Each laser pulse (indicated by squiggly lines) is a beamsplitter pulse. Solid blue and dashed red lines indicate atomic trajectories in opposite hyperfine states. Trajectories marked with an × are blown away. The time between pulses 2 and 3 is $T' = \tau + 2t_{2\mathrm{A}}$, where τ is the time the atoms are held in the optical lattice. Only two of the four output ports interfere at the final pulse.

In our experiment, we have demonstrated an interferometer that coherently holds the atoms in a spatially-separated superposition state for over 10 seconds before reading out interference. This is over a factor of 4 longer than the previous longest atom interferometer we are aware of. We discuss the status of these ongoing efforts in this chapter.

8.1 Trapped atom interferometer in an optical lattice

The trapped interferometer sequence we perform is shown in Fig. 8.1. After launching the atoms upwards, two Raman beamsplitter pulses are performed, separated by a time T. This gives four total output arms. Two arms in one hyperfine state blown away, leaving two spatially separated arms in the same internal state with the same momentum. At the apex of the atomic trajectory, a lattice is adiabatically ramped on, loading the atoms into the lowest Bloch band (see Sec. 8.4 for details on Bloch oscillations). After some hold time, the lattice is adiabatically lowered, releasing the atoms. After falling for a time $t_{2\mathrm{A}}$ ("time to apex"), two more beamsplitters are applied, again separated by a time T. This third beamsplitter again gives four output arms, two of which spatially overlap at the final pulse, and interfere.

This geometry is similar to that of Refs. [117,118]. In both of these previous realizations, performance was limited by beam quality. Wavefront imperfections such as speckle, or parasitic reflections give rise to random momentum kicks of the separated arms relative to each other. When this occurs, the interferometer does not close after the final two beamsplitter pulses.

An optical cavity is then ideally suited to further push this technology. The mode-filtering characteristic of an optical cavity provides clean wavefronts in which the spatially-separated superposition state can Bloch oscillate. The hope is that these clean wavefronts will provide long interrogation times.

A note about terminology. Some of the literature distinguishes between “hybrid” and “trapped” interferometers. In the former, part of the interferometer takes place in free-fall. In the latter, the atoms are trapped for the entire interferometer duration. We may be fairly sloppy with this distinction, but all interferometers discussed here are of the “hybrid” type. We will also call our geometry a “lattice atom interferometer” (“lattice AI”), or lattice interferometer”.

8.1.1 Phase calculation

Laser phase

The phase can be calculated using the machinery from Chapter 2. The laser phase for a lattice AI of the geometry in Fig. 8.1 in a constant gravitational field is given by

$$\begin{aligned}\phi_{\mathrm{L}} &= (\varphi_1 - \varphi_2) - (\varphi_3 - \varphi_4) && (8.1)\\ &= -k_{\mathrm{eff}} g T \left(T + 2t_{2\mathrm{A}}\right) && (8.2)\end{aligned}$$

where g is the acceleration due to gravity, and k_{eff} is the effective wavevector. Eq. 8.2 represents the specialization of eq. 8.1 to the geometry shown in Fig. 8.1.

The appearance of $t_{2\mathrm{A}}$ in eq. 8.2 is a bit jarring on first glance. This simply reflects that for large $t_{2\mathrm{A}}$, the atoms are moving faster between pulses 1&2 (and 3&4), so the distance between points on the atomic trajectory for fixed pulse separation T is larger. Note that in the limit $t_{2\mathrm{A}} \to 0$, the laser phase reduces to the expression for a Mach-Zehnder (which, if $\tau = 0$, the geometry indeed becomes).

Free evolution phase

The free evolution phase (more details in Sec. 2.2) is given by

$$\begin{aligned}\Delta\phi_{\mathrm{FE}} &= \frac{1}{\hbar}\left(\int_{\Gamma_{\mathrm{cl}}} T - U\right)_{\mathrm{upper}} - \frac{1}{\hbar}\left(\int_{\Gamma_{\mathrm{cl}}} T - U\right)_{\mathrm{lower}}\\ &= \phi_K - \phi_U\end{aligned}$$

where ϕ_K is the kinetic phase and ϕ_U is the potential phase. The kinetic phase is given by integrating

$$\phi_K = \frac{1}{2} m \int \left(v_{\mathrm{upper}}(t)^2 - v_{\mathrm{lower}}(t)^2\right) dt \tag{8.3}$$

$$= gk_{\text{eff}}T(T+2t_{2\text{A}}) \tag{8.4}$$

The potential contribution to the free evolution phase is found analogously by integrating the potential seen by the classical paths of the interferometer arms over their trajectories. For the potential $U = mgz$, this is given by

$$\phi_U = mg \int \left(z_{\text{upper}}(t)^2 - z_{\text{lower}}(t)^2\right) dt \tag{8.5}$$

$$= gk_{\text{eff}}T(T+2t_{2\text{A}}+\tau) \tag{8.6}$$

The 8 configurations

There are actually 8 different configurations of the lattice AI. These are determined by

- κ_{12}: Which of the $k^{\pm}$ transitions are used for beamsplitters 1 and 2?
- β_{01}: Do we blowaway the un-kicked of the 4 arms?
- κ_{34}: Which of the $k^{\pm}$ transitions are used for beamsplitters 3 and 4?

We'll take $\kappa_{ij} = \pm 1$ for the $k^{\pm}$ transition. We'll use $\beta_{01} = 1$ when the one un-kicked arm (of the four outputs of the first two beamsplitters) is blown away, and $\beta_{01} = 0$ when it is loaded into the lattice. Typically, we'll prefer to use $\beta_{01} = 1$ since it helps with spatially selecting central atoms.

Since the quantity $gk_{\text{eff}}T(T+2t_{2\text{A}})$ appeared multiple times the previous section, we'll give it a name:

$$gk_{\text{eff}}T(T+2t_{2\text{A}}) \equiv \vartheta \tag{8.7}$$

The 8 configurations, along with their respective phases are shown in Fig. 8.2. To keep a consistent notation, all phases quoted are of the form

$$\phi_X = \phi_X^1 - \phi_X^2$$

where ϕ_X^1 is the phase due to X on arm 1, and arm 1 is defined as the arm that is kicked by the first pulse. The other arm, that interferes with arm 1, is arm 2. This convention also determines the relative sign of phases in this section.

Trajectories for the 8 combinations $\{\kappa_{12}, \beta_{01}, \kappa_{34}\}$ are shown in Fig. 8.2. The common mode motion due to gravity has been subtracted out to help see the differences between the geometries (i.e., the motion of the interferometer arms is shown in a frame freely-falling with the atoms). The set of $\{\ \kappa_{12},\ \beta_{01},\ \kappa_{34}\ \}$ corresponding to each geometry is shown in the upper left of that cell.

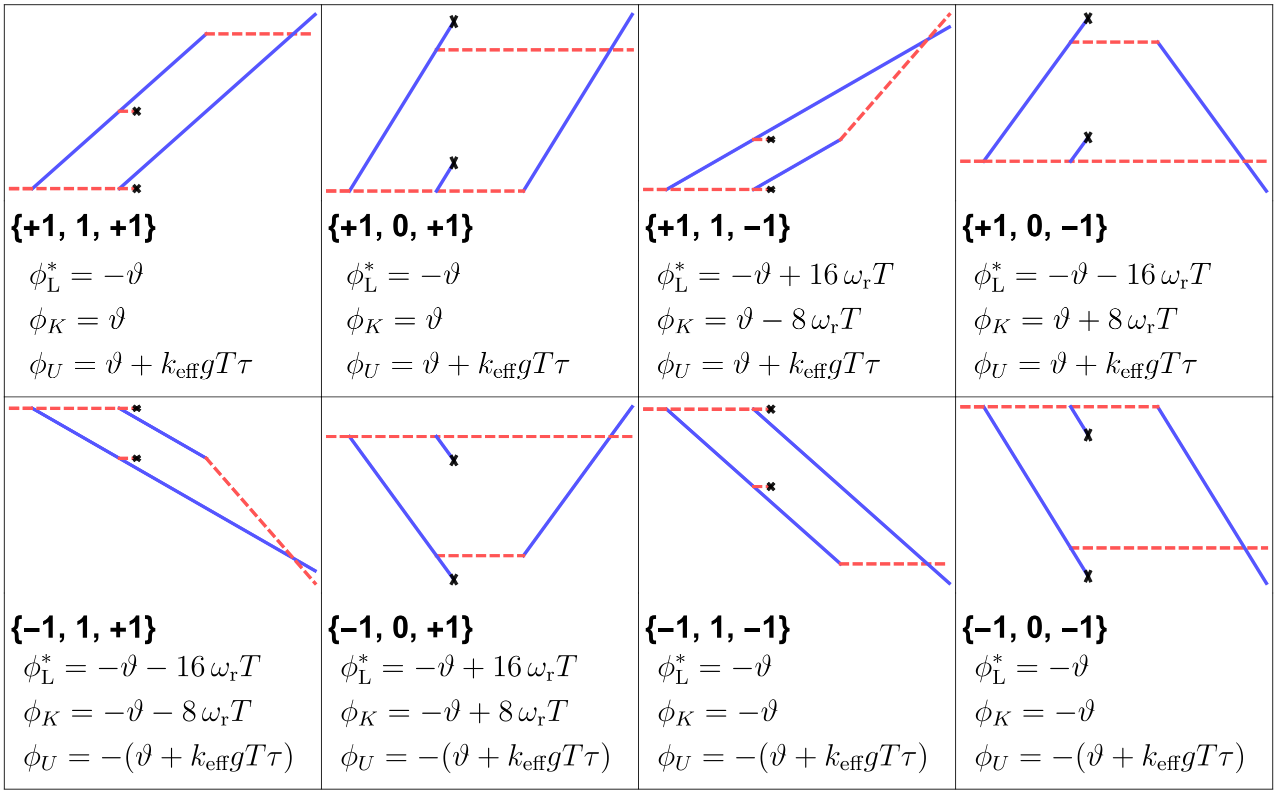

Figure 8.2: Lattice AI configurations. See main text for discussion.

We denote by ϕ_L^* the part of the laser phase independent of the ramp rate, i.e., what the laser phase would be if the Raman frequency were not ramped. That is, the total laser phase will be given by

$$\phi_L = \phi_L^* + \phi_{L,\alpha}$$

where $\phi_{L,\alpha}$ depends on the exact implementation of the gravity ramp (which can no longer be a simple linear ramp, due to a nonzero hold time τ).

While eq. 8.1 applies in all cases (and thus, $\phi_L^* = \sum_{i=1}^{4} k_{\rm eff} z_{1(2)}(t_i)$.), it hides (by vague notation of the ϕ_is) that the correct choice of $z_1(t)$ or $z_2(t)$ must be made to represent the arm that was actually kicked by the pulse.

Several observations are noteworthy. First, we see that the ϑ in the kinetic phase is always canceled by the ϑ in the potential phase since $\phi_{\rm FE} = \phi_K - \phi_U$. This is familiar from the Mach-Zehnder geometry from Section 2.4. Second, we note that the phases do not depend on β_{01}, i.e., which two arms are caught[1].

Half of the geometries are sensitive to the recoil velocity $v_{\rm r}$. These recoil-sensitive geometries look familiar; they're Ramsey-Bordé interferometers. The recoil-sensitive, Ramsey-

---

[1] other than the implied change of $t_{2{\rm A}}$ by ±1 Bloch period $\tau_{\rm B} \approx 708\ \mu$s

Bordé geometries are denoted by black trapezoids. The kinetic phase ϕ_K has the same sensitivity to ω_r for all 4 recoil-sensitive schemes. The laser phase ϕ_L^* gets a contribution as well from the kinematic dependence of the recoil velocity as the wavepackets separate along the laser wavevector.

These effects are all interesting and worth fleshing out, but the real prize is the extra term contained in ϕ_U of the free evolution phase: $k_{\text{eff}} g T \tau$. Our goal will be to make τ very long to make this phase term large. For demonstrated parameters $T = 1.066$ ms, $\tau = 10$ s, this phase term is over 1000 times larger than any of the other phase terms discussed in this section.

8.2 Far-detuned laser system

To introduce a third wavelength into the science cavity, we need a new laser with a widely tunable lockpoint. We use an external cavity diode laser (New Focus TLB7100) at 866 nm. This was chosen for two reasons. The first was so that the new laser wavelength has high reflectivity off the existing coating of the in-vacuum dielectric cavity mirror.

Given this constraint, the second reason was to minimize single-photon scattering. The atomic polarizability from the D2 transition at 852 nm is used to provide the high-field seeking trapping potential. However, the D1 line of cesium is around 894 nm. A beam red-detuned (high-field seeking) by $\lesssim 42$ nm from the D2 line is blue-detuned (low-field seeking) from the D1 line. For intermediate wavelengths between these transitions, these effects compete. At the "tuneout wavelength", the attractive and repulsive effects cancel exactly, and the atom experiences no energy level shift (trapping potential). For the cesium D1 and D2 lines, this tuneout wavelength is $\approx 880.25(4)$ nm [165].

For fixed trap depth then, there exists a wavelength that has a minimum scattering rate. Too close to the D2 line, and the scattering rate $\propto \frac{1}{\Delta^2}$ becomes too high. Too close to the tuneout wavelength, and the required optical power for trapping further increases the scattering rate. This behavior is shown in Fig. 8.3.

The optimal wavelength is around $\lambda = 866.9$ nm, which gives a single-photon scattering rate $\Gamma_{\text{sc}} = 2\pi \times 0.09$ Hz ($\tau_{\text{sc}} = 2\pi\Gamma_{\text{sc}}^{-1} = 10.9$ s). Our laser is at 866.0 nm, which does not change these numbers at the stated precision. Calculations are performed by application of the formulas in Ref. [132]; involving the vector and tensor polarizabilities may somewhat change them (but the simple analysis giving nearly the correct tuneout wavelength indicates that corrections should be small).

8.2.1 Widely-tunable locking scheme

To introduce the 866 nm light into the science cavity, it should be tunable by at least half of the free spectral range (FSR = 399.8 MHz) to guarantee co-locking with the science and

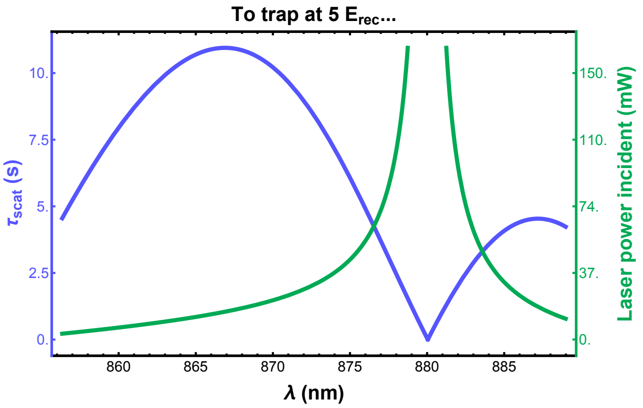

Figure 8.3: Scattering from the D1 and D2 lines. The right axis shows the incident optical power on our cavity at 65% coupling efficiency required to trap cesium atoms at a depth $U_0 = 5E_{\text{rec}}$ at the center of the beam. The left axis shows the resulting single-photon scattering rate. Note that the scattering rate blows up near the tuneout wavelength, where the ac Stark shift becomes so small that very high laser powers are required to form a $5E_{\text{rec}}$-deep lattice. Above this wavelength, the trapping potential is low-field seeking.

tracer lasers. The method used to co-lock the science and tracer lasers is not scalable to an additional laser[2].

To address this problem, we use the first of two methods presented below to provide a widely tunable (> 600 MHz) lockpoint for the 866 nm laser. The first method presented is a bit more expensive (using both a fiber EOM and a free space EOM), but less susceptible to residual amplitude modulation (RAM). The second method uses only the fiber EOM in an interesting scheme, but resulted in RAM that was unfortunately too high.

Both schemes utilize the low V_π of fiber EOMs to provide broadband-edness. Unfortunately, the optical interconnects from optical fiber to EOM crystal back into optical fiber can have poor polarization-maintaining qualities relative to a free space EOM. Fiber EOMs are thus more susceptible to RAM.

Actual method used

The scheme we actually use is fairly simple. A free space EOM is used to put Pound-Drever-Hall modulation at $f_{\text{pdh}} \sim 20$ MHz onto the input beam. The beam then enters a fiber EOM, and is modulated at a much higher, tunable frequency $\Omega_{\text{mod}}/2\pi$ between 675 - 1300 MHz. This creates ±1-order sideband manifolds, separated from the carrier by the tunable Ω_{mod}. Each of these manifolds has the PDH sidebands of the input beam. They each (in addition to the carrier) give a PDH error signal, with opposite signs. Each sideband manifold can be

---

[2] Namely, coarsely finding an appropriate free spectral range to lock the tracer laser to (5 GHz increments), and fine-tuning with a hi-bandwidth AOM would be a pain to implement with yet another laser.

tuned between 675 – 1300 MHz, limited only by an amplifier used, and either can be locked to.

Since this tuning range is greater than the free spectral range of the science cavity, we are guaranteed a co-locking point even with just one of the sideband manifolds. Furthermore, the RAM introduced by the fiber EOM is not at the Pound-Drever-Hall frequency, but at Ω_{mod}, so it doesn't give the error signal an offset.

By locking a sideband manifold to the transfer cavity, the lattice laser itself can be moved by tuning Ω_{mod}. This allows us to co-lock the lattice laser onto the science cavity, alongside the science and tracer lasers. This method works so well that if re-working the experiment, we would set it up for the tracer laser as well.

Alternative, interesting method

A second method was ultimately abandoned due to RAM. However, it's an interesting scheme with possible applications elsewhere, so we'll describe it here.

The basic idea is similar to the previous method: generate sideband manifolds that are separated by a large, tunable frequency, each with their own Pound-Drever Hall structure. However, rather than perform each of these steps separately, they are performed together by phase modulating the phase modulation. This type of lock has previously been proposed [166] and demonstrated [167, 168], and we will refer to it as electronic sideband (ESB) locking.

The work in this section was performed first at the Institut für Quantenoptik at Leibniz Universität Hannover (IQO Hannover) during a 6-week visiting scholar stint I spent there, and later back on the home base with this 866 nm laser.

To generate the PDH sideband manifolds, we send phase-modulated phase modulation into a fiber EOM. This requires a voltage of the form

$$V_{\mathrm{eom}} = V_{\beta_1} \sin\left(\Omega_{\mathrm{mod}} t + \beta_2 \sin(\omega_{\mathrm{pdh}} t)\right), \tag{8.8}$$

where Ω_{mod} is the large, tunable frequency, and $\omega_{\mathrm{pdh}} = 2\pi f_{\mathrm{pdh}}$ is the Pound-Drever-Hall frequency. β_2 is the modulation depth of the phase modulation (i.e., it's the PDH β), and V_{β_1} is the overall scale factor that determines how much of the laser power goes into each sideband manifold. This can be seen more explicitly using the Jacobi-Anger expansion eq. 4.9 to expand the phase modulated laser beam given by

$$\boldsymbol{E}_{\mathrm{out}} = \boldsymbol{E}_0 \exp\left[-i\omega_{\mathrm{L}} t - i\beta_1 \sin\left(\Omega_{\mathrm{mod}} t + \beta_2 \sin(\omega_{\mathrm{pdh}} t)\right)\right], \tag{8.9}$$

for optical input $\boldsymbol{E}_0 e^{-i\omega_{\mathrm{L}} t}$.

To generate this waveform, we use a vector multiplier (Analog Devices ADL5390). This particularly slick implementation of electronic sideband locking is due to Étienne Wodey. The lock scheme using the vector multiplier is shown in Fig. 8.4. The high-frequency signal at Ω_{mod} is first split into its quadrature components before being sent into the vector

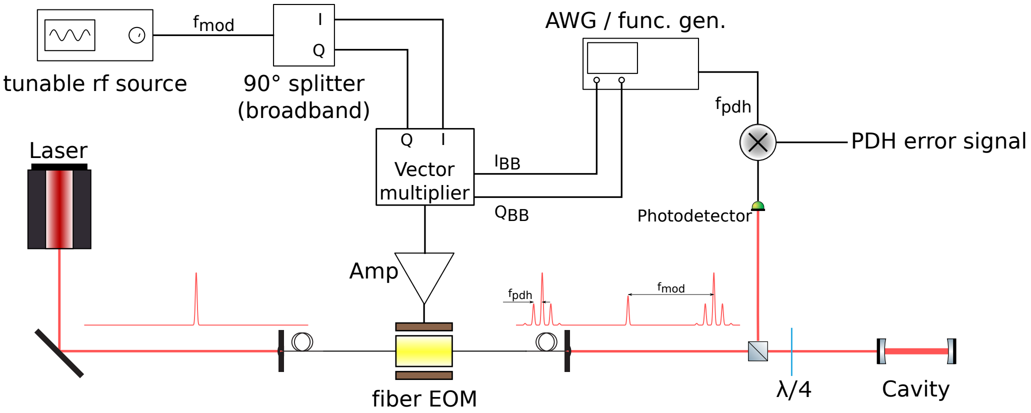

Figure 8.4: Electronic sideband locking with a vector multiplier.

multiplier. An additional input (the "baseband" signal) for each quadrature then multiplies the respective quadrature. These two are summed into the output of the vector multiplier.

For an input $V_{\text{in}} = A \sin(\Omega_{\text{mod}} t)$, the output is given by

$$V_{\text{out}} = G(A \sin(\Omega_{\text{mod}} t + \varphi)) \tag{8.10}$$

where G and φ are given by

$$G = \frac{1}{V_0} \sqrt{V_{\text{IBB}}^2 + V_{\text{QBB}}^2} \tag{8.11}$$

$$\varphi = \arctan\left(V_{\text{QBB}}/V_{\text{IBB}}\right) \tag{8.12}$$

That is, the magnitude of the output is given by the quadrature sum of the baseband signals (scaled to some reference V_0), and the phase is set by the relative size of the baseband signals. This device thus gives arbitrary control of the amplitude and phase of the output, presenting a flexible path to generating the signal required by eq. 8.10. The baseband inputs are simply the waveforms that give $G = 1$, and $\varphi = \beta_2 \sin(\Omega_{\text{pdh}} t)$. The resultant waveforms are

$$V_{\text{QBB}} = \frac{V_{\text{pp}}}{2} \sin\left(\beta_2 \sin(\Omega_{\text{pdh}} t)\right) \tag{8.13a}$$

$$V_{\text{IBB}} = \frac{V_{\text{pp}}}{2} \cos\left(\beta_2 \sin(\Omega_{\text{pdh}} t)\right) \tag{8.13b}$$

These waveforms can be generated with an AWG, and used to drive the baseband inputs of the vector multiplier. Alternatively, they can be approximated by sinusoids to eliminate the use of an AWG. These approximating sinusoids are

$$V'_{\text{QBB}} = \frac{V_{\text{pp}} \sin \beta_2}{2} \sin(\Omega_{\text{pdh}} t) \tag{8.14a}$$

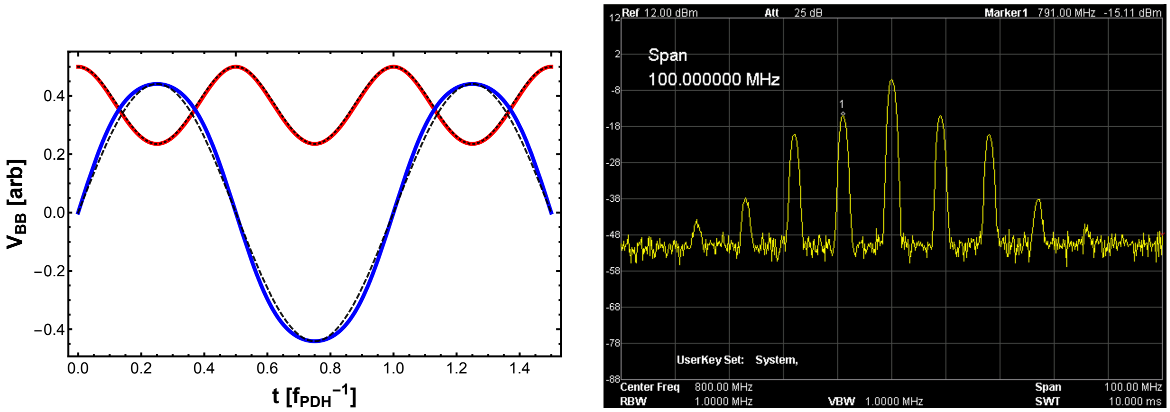

Figure 8.5: Electronic sideband locking baseband inputs. Left: ESB baseband signals for $\beta_2 = 1.08$. Thick red (blue) signals are V_{IBB} (V_{QBB}) from eqs. 8.13. Approximating signals given by the sinusoids eqs. 8.14 are shown in black dotted (dashed) lines. Right: Resulting rf spectrum output from vector multiplier for $\Omega_{\mathrm{mod}} = 2\pi \times 800$ MHz, $\Omega_{\mathrm{pdh}} = 2\pi \times 9$ MHz.

$$V'_{\mathrm{IBB}} = \frac{V_{\mathrm{pp}}(1-\cos\beta_2)}{2}\left(\cos(\Omega_{\mathrm{pdh}}t) + \frac{1}{2}\cot^2\frac{\beta_2}{2}\right) \tag{8.14b}$$

Both the true and approximated waveforms can be seen in Fig. 8.5.

Applying this signal to an EOM, the resulting optical spectrum, as seen in transmission through the Hannover optical cavity, can be seen in Fig. 8.6, alongside the resulting PDH error signals.

V_{pp} is chosen based on the V_π of the EOM. The error signal is maximized when the optical power in the ±1 manifolds are maximized, at $\beta_1 \approx 1.84$.

An interesting side application of this technique is *3f demodulation*. This locking scheme phase modulates hard, at high $\beta \sim 3.83$ such that the first-order sidebands disappear and there are significant 3rd-order sidebands. The PDH photodiode signal is demodulated at $3\Omega_{\mathrm{pdh}}$, rather than the usual $1\Omega_{\mathrm{pdh}}$. This type of locking can be less sensitive to RAM, as well as provide some other benefits[3] [169].

Typically though, one needs to modulate the EOM so hard that this technique is uncommon. When generating the phase modulation via the baseband inputs however, achieving high β is as simple as changing the waveform! The necessary waveforms (eqs. 8.13 with $\beta_2 = 3.83$), the resulting transmission spectra and PDH signals can all be seen in Fig. 8.7.

While the ESB lock worked quite well at Hannover, the fiber EOM used at Berkeley gave more residual amplitude modulation than the previously discussed two-EOM technique. The Hannover fiber EOM (iXBlue Photonics, NIR-MPX800-LN-10) was fabricated with a “proton

---

[3] For example, in cryogenic applications where laser-induced heating of the cavity matters, the 3f-PDH lock gives less power circulating in the cavity at fixed signal-to-noise.

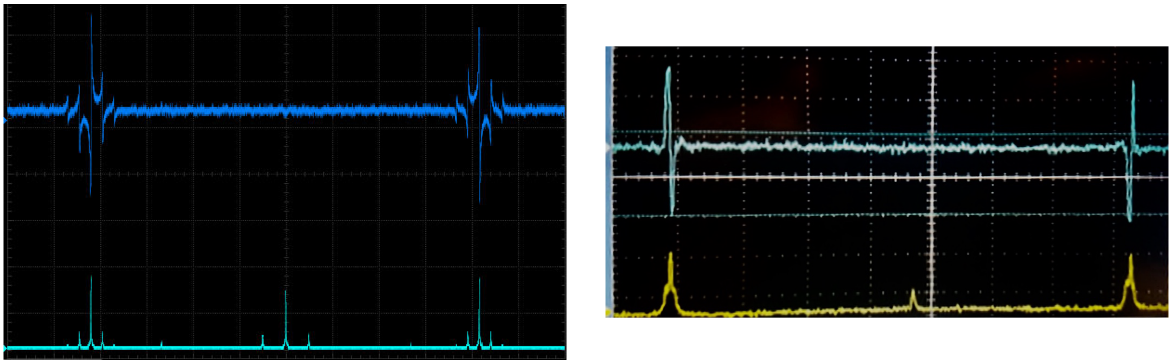

Figure 8.6: ESB error signals with $\beta_2 = 1.25$. Left: ESB lock signals on the Hannover cavity. Lower, cyan trace shows transmission through the cavity, and thus the optical spectrum. PDH error signal is shown in the upper, blue trace. Note the lack of a PDH signal around the non-tunable carrier. The spurious sidebands near the carrier are second order sidebands (giving no error signal) due to incorrect driving of the vector multiplier, and were later corrected (along with the other spurious peaks). Right: Traces of the same quantities on the Berkeley cavity (our transfer cavity; lower finesse than the Hannover cavity).

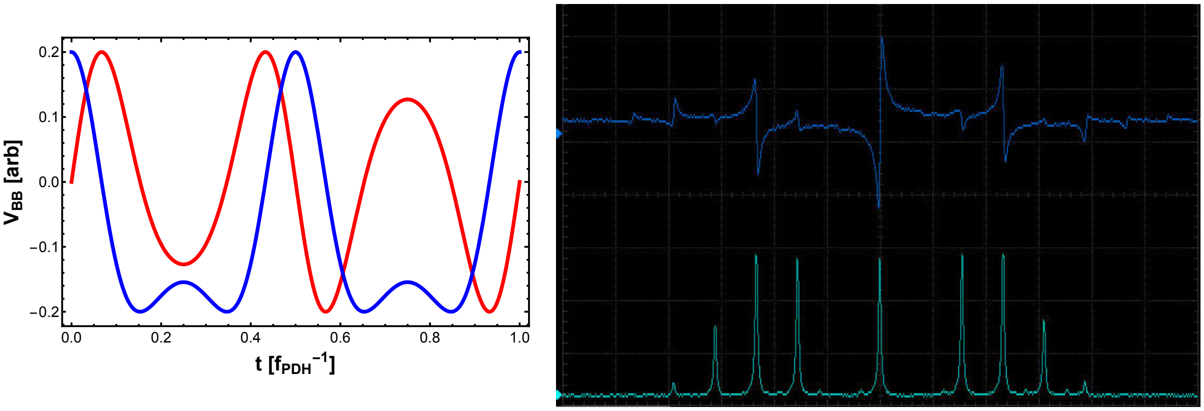

Figure 8.7: Left: Baseband inputs for producing $\beta_2 = 3.83$. Red (blue) signals are V_{IBB} (V_{QBB}). Right: Optical spectrum in transmission and resulting error signal, using the Hannover cavity. Note the absence of the $\omega_{\mathrm{L}} \pm 1\Omega_{\mathrm{pdh}}$ peaks. The offset of the error signal from the dark blue triangle is an artifact of the oscilloscope ground.

exchange based" process, while the Berkeley fiber EOM (EOSpace) manufacturing method is unclear, which could explain the difference. The Berkeley fiber EOM also required fiber-to-fiber mating sleeves to bring the laser light to the experiment, and evidence of etaloning was observed[4]. It's possible that etaloning was still the culprit behind the remaining RAM. This interpretation is also supported by 3f-demodulation not appreciably reducing the RAM. The ESB method was not ultimately used in our cavity interferometer.

8.3 Immunity to vibrations

Vibrations are a difficult and ubiquitous noise source for atom interferometer gravimeters. Significant effort [18, 62, 170–172] is expended to suppress, actively stabilize, and/or post-correct against these vibrations.

It turns out that the lattice interferometer can subvert this noise source. To see how, we take a quantitative look into the vibration response of the lattice AI compared to the traditional AI gravimeter geometry, a Mach-Zehnder.

8.3.1 The framework

We will consider the interferometer pulse durations to be zero, i.e., $\Omega_{2\gamma} \to \infty$. Our analysis could be done without this assumption, as in Refs. [42, 173], but it would unnecessarily complicate the formulas. The basic effect of including a finite Rabi frequency is to introduce a high-frequency cutoff to the interferometer transfer function. This is worth considering, for example if the Raman beams derive from two phase-locked lasers, which can give the laser phase high-frequency noise. For Bragg pulses, or Raman pulses using an EOM (such as ours), this high frequency noise source does not exist, and we concern ourselves with low-frequency noise arising from mechanical vibrations of the retroreflection mirror (which serves as the phase reference to the atoms). We will first look at the vibration sensitivity of the Mach-Zehnder, before extending the formalism to our lattice interferometer. Much of this formalism comes from Ref. [173].

Mach Zehnder geometry

In the Mach-Zehnder, vibrations can enter via the laser phase

$$\Delta\phi^{\mathrm{L}}_{\mathrm{MZ}} = \phi_1 - 2\phi_2 + \phi_3 \tag{8.15}$$

where ϕ_i are the laser phases seen by the atom at pulse i (see Sec. 2.4). The laser phases include the positions ($\phi_i = k_{\mathrm{eff}} x(t_i) + \ldots$), which is how vibration noise enters the interferometer.

---

[4] RAM decreased after application of index-matching gel between the fiber tips

We introduce a quantity $g_{\mathrm{MZ}}(t)$ called the sensitivity function. The sensitivity function is defined so that a jump in the laser phase by $d\phi_L$ at time t shifts the interferometer phase by $d\phi_{\mathrm{MZ}}$. That is,

$$d\phi_{\mathrm{MZ}} = g_{\mathrm{MZ}}(t) d\phi_L$$

Suppose we have noise on the laser phase over the interferometer duration $\phi_{\mathrm{L}}(t)$. This could be, for example, noise on the Raman beatnote, or position noise of the retroreflection mirror. We can calculate the full effect on the interferometer phase by integrating the phase noise against the sensitivity function

$$\phi_{\mathrm{MZ}} = \int dt\, g_{\mathrm{MZ}}(t) \frac{d\phi_{\mathrm{L}}}{dt} \tag{8.16}$$

From the expression for the Mach-Zehnder laser phase in eq. 8.15, we see that the sensitivity function is

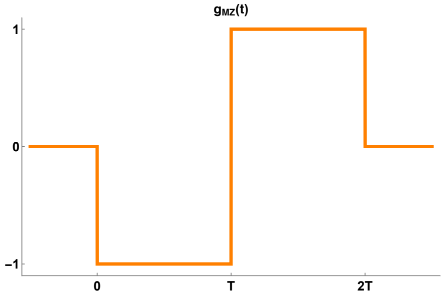

$$g_{\mathrm{MZ}}(t) = \begin{cases} -1 & 0 < t < T \\ +1 & T < t < 2T \\ 0 & \text{else} \end{cases} \tag{8.17}$$

The only problem is that we are interested in the noise contribution to $\phi_{\mathrm{L}}(t)$ which, by definition, we do not have an expression for. Therefore, we'll move to Fourier space to calculate the size of interferometer phase fluctuations for a given distribution of laser phase noise. We will indicate the Fourier transform of a time-domain function with a tilde. That is, $\tilde{f}(\omega)$ is the Fourier transform of $f(t)$. Explicitly, the transform and its inverse are given by

$$\tilde{f}(\omega) = \int_{-\infty}^{\infty} dt\, e^{-i\omega t} f(t) \qquad\qquad f(t) = \int_{-\infty}^{\infty} d\omega\, e^{i\omega t} \tilde{f}(\omega) \tag{8.18}$$

We can expand $\phi_{\mathrm{L}}(t)$ as the inverse Fourier transform of $\tilde{\phi}_{\mathrm{L}}(\omega)$ in eq. 8.16, and use the resulting exponential to convert $g_{\mathrm{MZ}}(t)$ into its Fourier transform. The result is

$$\begin{aligned} \phi_{\mathrm{MZ}} &= \int d\omega\, (-i\omega) \tilde{g}_{\mathrm{MZ}}(\omega) \tilde{\phi}_{\mathrm{L}}(-\omega) \\ &\equiv \int d\omega\, H_{\mathrm{MZ}}^{\phi_{\mathrm{L}}}(\omega) \tilde{\phi}_{\mathrm{L}}(-\omega) \end{aligned} \tag{8.19}$$

where in the second line we have found/defined the transfer function of the interferometer from laser phase noise ϕ_L to interferometer phase noise, $H^{\phi_\mathrm{L}}_\mathrm{MZ}(\omega)$. Explicitly, this is

$$H^{\phi_\mathrm{L}}_\mathrm{MZ}(\omega) = -i\omega\tilde{g}_\mathrm{MZ}(\omega) \tag{8.20}$$

where the Fourier transform of the sensitivity function $g_\mathrm{MZ}(t)$ is

$$\tilde{g}_\mathrm{MZ}(\omega) = \frac{4}{i\omega}e^{-i\omega T}\sin^2\left(\frac{\omega T}{2}\right) \tag{8.21}$$

Again, since we're talking about noise, we are interested in the variance of the interferometer phase noise, $\mathrm{Var}[\Phi_\mathrm{MZ}]$. We'll treat atom interferometer phase noise Φ_AI as a distribution from which a random variable ϕ_AI is drawn (typically, capitalization indicates the distribution of a random variable, while lower case indicates a sample). The distribution Φ_AI is defined by the power spectral density (PSD) of the noisy variable (in this case, the laser phase noise), which we will show next. We can express the variance of an interferometer phase in the form of eq. 8.19 as

$$\begin{aligned}\mathrm{Var}[\Phi_\mathrm{AI}] &= \langle \Phi_\mathrm{AI}^2 - \langle\Phi_\mathrm{AI}\rangle^2\rangle \\ &= \int_{-\infty}^{\infty}d\omega \int_{-\infty}^{\infty}d\omega'\, H_X^*(-\omega)H_X^*(-\omega')\,\langle\ \tilde{X}(\omega)\tilde{X}^*(\omega') - \langle\tilde{X}(\omega)\rangle\langle\tilde{X}^*(\omega')\rangle\ \rangle\end{aligned}$$

where X is the noisy variable, and H_X is the transfer function between the noisy variable and the interferometer output. We have used that $\phi_\mathrm{AI} = \phi_\mathrm{AI}^*$ (because it's real-valued) to arrive at the form above. Note that the expression in the outer expectation brackets is of the form $\langle YZ - \langle Y\rangle\langle Z\rangle\rangle$. If Y and Z are uncorrelated, this expression vanishes. Thus, if we assume that laser phase noise at frequency ω is independent from the noise at frequency $\omega' \neq \omega$, we get

$$\mathrm{Var}[\Phi_\mathrm{AI}] = \int_{-\infty}^{\infty}d\omega|H_X(\omega)|^2\langle|\tilde{X}(-\omega)|^2\rangle$$

where we have also identified that $\langle\tilde{X}(-\omega)\rangle = 0$ because $\tilde{X}(\omega)$ is the Fourier transform of $X(t)$ which, as noise, has expectation value zero; positive and negative fluctuations are equally likely.

If we assume that our noisy variable (in this case, the laser phase noise $\phi_\mathrm{L}(t)$) distribution is a "wide-sense stationary" distribution (basically, parameters of the distribution aren't changing in time), the Wiener–Khinchin theorem identifies the expectation value of the norm-squared of the Fourier transform $\langle|\tilde{X}(-\omega)|^2\rangle$ as the power spectral density $S_X(-\omega)$. The power spectral distribution of a real-valued variable is even, so we finally arrive at

$$\mathrm{Var}[\Phi_\mathrm{AI}] = \int d\omega|H_X(\omega)|^2S_X(\omega)$$

Now that we have worked through this formalism in some detail for the Mach-Zehnder case, we look at the lattice interferometer.

Lattice interferometer laser phase

The laser phase for our lattice interferometer is given by

$$\Delta\phi^{\mathrm{L}}_{\mathrm{latt}} = (\phi_1 - \phi_2) - (\phi_3 - \phi_4) \tag{8.22}$$

By inspection, we can write down the sensitivity function as

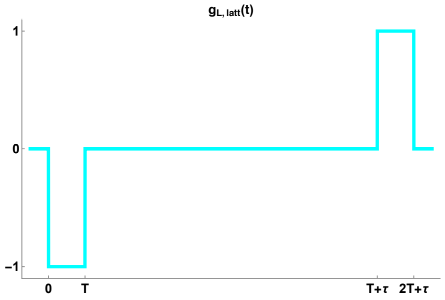

$$g_{\mathrm{L,latt}}(t) = \begin{cases} -1 & , 0 < t < T \\ 0 & , T < t < T+\tau \\ +1 & , T+\tau < t < 2T+\tau \\ 0 & , \text{else} \end{cases} \tag{8.23}$$

The Fourier transform is

$$\tilde{g}_{\mathrm{L,latt}}(\omega) = \frac{4}{i\omega} e^{-\frac{i}{2}\omega(2T+\tau)} \sin\left(\frac{\omega T}{2}\right) \sin\left(\frac{\omega(T+\tau)}{2}\right) \tag{8.24}$$

Since the analog of eq. 8.16 applies to laser phase of the lattice AI as well, the transfer function is

$$H^{\phi_{\mathrm{L}}}_{\mathrm{L,latt}}(\omega) = -i\omega \tilde{g}_{\mathrm{L,latt}}(\omega) \tag{8.25}$$

Lattice interferometer free evolution phase

The fact that the lattice AI laser phase transfer function $g_{\mathrm{L,latt}}(t)$ is zero during τ (which can be much larger than T) hints that the sensitivity to laser phase noise could be suppressed. In the case of accelerations from vibrations of the lattice holding the atoms, does this not violate the equivalence principle? The equivalence principle states that an acceleration is locally indistinguishable from a gravitational field. While the laser phase $\Delta\phi^{\mathrm{L}}_{\mathrm{latt}}$ is not sensitive to transients during the (potentially long) time τ, we are saved from such a violation by the free evolution phase.

We will assume that the atomic wavepacket follows the vibrating lattice. This assumption may be frequency-dependent due to the adiabatic nature of the Bloch oscillations (e.g., do Bloch oscillating atoms average out fast vibrations of the lattice?), but it is the conservative (and reasonable) one to make to assess the vibration sensitivity. In any event, we will be concerned with low frequency vibrations.

Vibrations of the retroreflection mirror are given by an acceleration profile $a(t)$. In our case of a cavity, we can consider the cavity as a rigid body because the length-stabilization feedback bandwidth ($\sim$ 40 kHz) is much faster than the frequencies of vibrations we'll be concerned about ($\sim 1 - 100$ Hz).

The free evolution phase $\Delta\phi_{\mathrm{FE}}$ is given by the integral of the Lagrangian over the classical path (see Sec. 2.2). Since vibration noise does not affect the kinetic part of the free evolution phase, we concern ourselves with the potential part:

$$\begin{aligned}\Delta\phi_{\mathrm{FE}} &= \frac{1}{\hbar}\left(\int_{\Gamma_{\mathrm{cl}}} \cancel{T} - U\right)_{\mathrm{upper}} - \frac{1}{\hbar}\left(\int_{\Gamma_{\mathrm{cl}}} \cancel{T} - U\right)_{\mathrm{lower}} \\ &= -(\phi^U_{\mathrm{upper}} - \phi^U_{\mathrm{lower}}) \\ &\equiv -\phi^U\end{aligned}$$

where $\phi^i_U = \frac{1}{\hbar}\int_{\Gamma_i} U_i$. For acceleration noise due to vibrations, we can use the equivalence principle to think of these accelerations as a noisy gravitational field with potential given by

$$U = ma(t)\Delta z(t)$$

where $a(t)$ is the noisy acceleration, and $\Delta z(t)$ is enforced by the interferometer geometry.

This acceleration due to mirror vibrations only talks to the atoms during the hold, when their trajectory is enforced to follow the mirror position. To fit this into the framework developed for the laser phases, we can write $\Delta z(t) \to \Delta z_{\max}\, g_{\mathrm{U,latt}}(t)$, where $\Delta z_{\max} = v^{\mathrm{eff}}_{\mathrm{rec}}T = \hbar k_{\mathrm{eff}}T/m$. We will also call the unitless $g_{\mathrm{U,latt}}(t)$ a sensitivity function, in analogy with the same quantity for the laser phases of the previous sections. It is given by

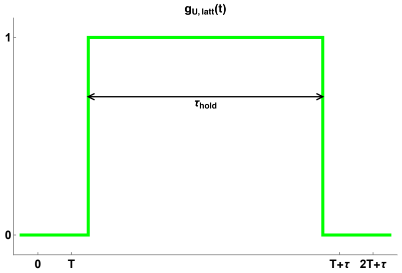

$$g_{\mathrm{U,latt}}(t) = \begin{cases} 1 & , t \in \tau_{\mathrm{hold}} \\ 0 & , \text{else} \end{cases} \tag{8.26}$$

Note that the hold time τ_{hold} is less than the total time τ between laser pulses 2 and 3 because of the times $t_{2\mathrm{A}}$. The noise contribution to the free evolution phase is then

$$\phi_U = k_{\mathrm{eff}}T\int dt\, a(t) g_{\mathrm{U,latt}}(t)$$

From here, we can play the same Fourier tricks from the previous sections to get

$$\phi_U = k_{\mathrm{eff}}T\int d\omega\, \tilde{a}(-\omega)\tilde{g}_{\mathrm{U,latt}}(\omega)$$

$$\equiv \int d\omega \, H^a_{\mathrm{U,latt}}(\omega)\tilde{a}(-\omega) \tag{8.27}$$

again defining a transfer function $H^a_{\mathrm{U,latt}}$ of the interferometer from acceleration noise to free evolution phase noise. Explicitly, these quantities are

$$\tilde{g}_{\mathrm{U,latt}}(\omega) = \frac{2}{\omega} e^{-i\omega(T+\tau)} \sin\left(\frac{\omega\tau_{\mathrm{hold}}}{2}\right) \tag{8.28}$$

and the transfer function is given by

$$H^a_{\mathrm{U,latt}}(\omega) = k_{\mathrm{eff}} T \tilde{g}_{\mathrm{U,latt}}(\omega)$$

Bringing it all together

So far we've looked at laser phase noise and acceleration noise. We are concerned with acceleration noise due to vibrations, so we should express the laser phase noise inputs ϕ_{L} as functions of acceleration noise. The laser phase noise can be expressed in terms of the position phase noise as

$$\phi_{\mathrm{L}}(t) = k_{\mathrm{eff}}\left(x_{\mathrm{retro}}(t) - x_{\mathrm{atom}}(t)\right)$$

The acceleration is the second time-derivative of the position, which we can evaluate by going to Fourier space to take these time derivatives,

$$\tilde{x}(\omega) = \frac{1}{(i\omega)^2}\tilde{a}(\omega) \tag{8.29}$$

It's worth noting that when assuming that the atoms are trapped and localized in lattice sites, the change in $(x_{\mathrm{retro}}(t) - x_{\mathrm{atom}}(t))$ is zero. However, this is incidental since the sensitivity function $g_{\mathrm{L,\ latt}}(t)$ is already zero there; i.e., even if this geometry were used in free fall (no lattice hold during τ), nonzero fluctuations in $(x_{\mathrm{retro}}(t) - x_{\mathrm{atom}}(t))$ during τ do not enter into the laser phase.

We can now use eq. 8.29 to get the laser phase noise in terms of the acceleration noise:

$$\tilde{\phi}_{\mathrm{L}}(\omega) = -\frac{k_{\mathrm{eff}}}{\omega^2} a(t)$$

where we've let $a(t) = (\tilde{a}_{\mathrm{retro}}(\omega) - \tilde{a}_{\mathrm{atom}}(\omega))$, since the previous paragraph argues why we only need to keep track of the acceleration of the retroreflection mirror.

We can now translate all of the transfer functions into the common noisy variable of acceleration noise. That is, we convert the laser phase transfer functions to acceleration transfer functions by

$$H^a_i(\omega) = -\frac{k_{\mathrm{eff}}}{\omega^2} H^{\phi_{\mathrm{L}}}_i(\omega)$$

We can now write the expected fluctuations for each of the three phases ϕ_i ($\phi^{\mathrm{L}}_{\mathrm{MZ}}$, $\phi^{\mathrm{L}}_{\mathrm{latt}}$ and $\phi^{\mathrm{U}}_{\mathrm{latt}}$) in a common language. If we define $(\sigma_i^{\mathrm{rms}})^2 = \mathrm{Var}[\Phi_i]$, we can write the following expressions for the rms fluctuations of the interferometer phase:

$$(\sigma_i^{\mathrm{rms}})^2 = \int d\omega |H_i^a(\omega)|^2 S_a(\omega)$$

Table 8.1 shows the summary of these quantities.

Table 8.1: Vibration-sensitivity expressions for relevant interferometer phases

	Mach-Zehnder laser phase $\boldsymbol{\phi^{\mathrm{L}}_{\mathrm{MZ}}}$	**Lattice AI laser phase $\boldsymbol{\phi^{\mathrm{L}}_{\mathrm{latt}}}$**	**Free evolution phase $\boldsymbol{\phi^{\mathrm{U}}_{\mathrm{latt}}}$**
$\boldsymbol{\phi_{\mathrm{AI}}}$	$\phi_1 - 2\phi_2 + \phi_3$	$(\phi_1 - \phi_2) - (\phi_3 - \phi_4)$	$\frac{m}{\hbar}\int dt\, a(t)\Delta z(t)$
Noisy $\boldsymbol{X(t)}$	$\phi^L(t)$	$\phi^L(t)$	$a(t)$
$\boldsymbol{\Delta\phi_i(X)}$	$\int dt\, g(t)\frac{dX}{dt}$	$\int dt\, g(t)\frac{dX}{dt}$	$k_{\mathrm{eff}}T\int dt\, g(t)X(t)$
$\boldsymbol{g(t)}$			
$\boldsymbol{f : X \mapsto a}$	$-\frac{k_{\mathrm{eff}}}{\omega^2}$	$-\frac{k_{\mathrm{eff}}}{\omega^2}$	1
$\boldsymbol{\lvert H_i^a(\omega)\rvert^2}$	$\frac{16k_{\mathrm{eff}}^2}{\omega^4}\sin^4\left(\frac{\omega T}{2}\right)$	$\frac{16k_{\mathrm{eff}}^2}{\omega^4}\sin^2\left(\frac{\omega T}{2}\right)\sin^2\left(\frac{\omega(T+\tau)}{2}\right)$	$\frac{4k_{\mathrm{eff}}^2T^2}{\omega^2}\sin^2\left(\frac{\omega\tau_{\mathrm{hold}}}{2}\right)$

8.3.2 Comparison of lattice AI and Mach-Zehnder vibration sensitivities

A comparison of the vibration sensitivity of the Mach-Zehnder and lattice AI geometries is shown in Fig. 8.8. In the problematic frequency range of $\approx 1 - 100$ Hz, the lattice AI shows significant suppression compared to the Mach-Zehnder.

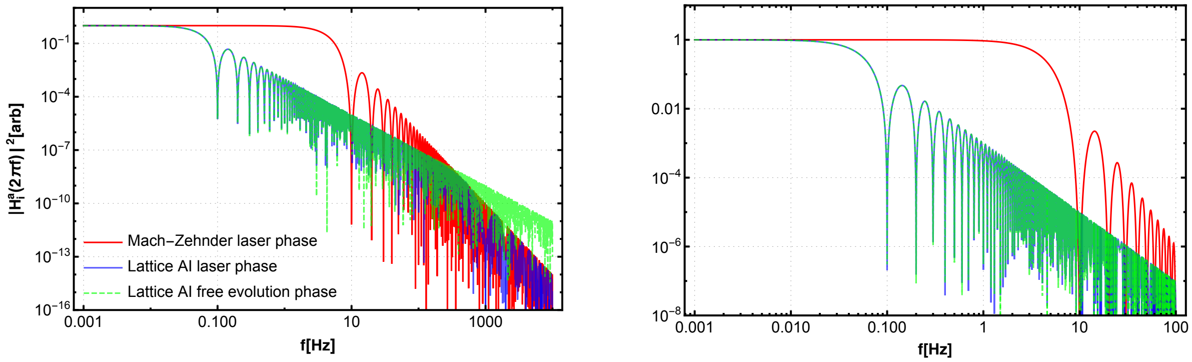

Figure 8.8: Vibration sensitivity of lattice and Mach-Zehnder AIs. Normed transfer functions $|H_i^a(\omega)|^2$ are shown (where $\omega = 2\pi f$) for the Mach-Zehnder (red) and lattice AI (blue) laser phases, and the lattice AI free evolution phase (green). Left plot shows out to high frequency where ω^{-2} and ω^{-4} behavior can be seen. Right plot is a zoomed view of the same plot. Here, $T = 1$ ms, $\tau = \tau_{\text{hold}} = 10$ s, and $T_{\text{MZ}} = \sqrt{T(T+\tau)} = 100$ ms was used in the Mach-Zehnder to give an interferometer with equal sensitivity to the gravitational acceleration.

This suppression is shown as a function of frequency in Fig. 8.9, where the ratio of the norms-squared of the transfer functions $|H_i^a(\omega)|^2$ is plotted. The ratio is seen to go to 0.5 at very low frequencies (near dc), because the lattice interferometer has equal-sized contributions from both the laser phase and the free evolution phase, while the Mach-Zehnder has only the laser phase. In the troublesome frequency range of $1 - 100$ Hz, the lattice interferometer is seen to offer significant suppression. Note that the quantities $|H_i^a(\omega)|^2$ (the ratio of which is plotted) is related to the *variance* of the interferometer phase, so the interferometer phase fluctuations have an rms value related to the square root.

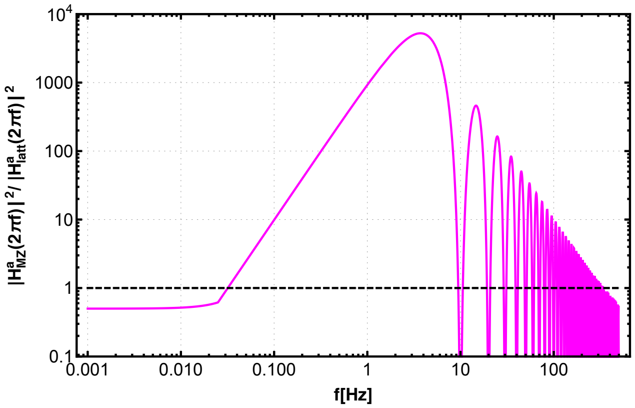

Figure 8.9: Vibration sensitivity suppression factor. The ratio $|H_{\text{MZ}}^a(\omega)|^2/|H_{\text{latt}}^a(\omega)|^2$ is plotted as a function of frequency using the same parameters as described in the Fig. 8.8 caption. Fast oscillations at $\sin^2(\frac{\omega\tau}{2})$ in this plot are averaged smooth for all but the first cycle.

To actually calculate the interferometer phase noise, we need an acceleration power spectral density $S_a(\omega)$ against which to integrate the $|H_i^a|^2$. We can use the isolated-but-unstabilized spectrum from Fig. 3.25 measured on our experiment with a seismometer to calculate $(\sigma_{\text{MZ}}^{\text{rms}})^2$ and $(\sigma_{\text{latt}}^{\text{rms}})^2 = (\sigma_{\text{L,latt}}^{\text{rms}})^2 + (\sigma_{\text{U,latt}}^{\text{rms}})^2$. Comparing these quantities for the same parameters as in Fig. 8.8, we find

$$\sigma_{\text{latt}}^{\text{rms}} = 0.016\,\sigma_{\text{MZ}}^{\text{rms}}$$

That is, the rms phase fluctuation due to vibration noise for the lattice AI is only 1.6% that of a Mach-Zehnder with the same sensitivity to gravity (for this representative vibration spectrum).

8.4 Bloch oscillations

Holding the atoms in a shallow optical lattice is a more dynamical process than first meets the eye. Specifically, the behavior of a matter wave in a periodic potential is known as Bloch oscillation. Consider the potential formed by an optical lattice:

$$\hat{V} = \hbar\, U_0\, \frac{1+\cos(2k\hat{z})}{2} \tag{8.30}$$

where the laser propagates in the z-direction, $k = \frac{2\pi}{\lambda}$ and λ is the laser wavelength. U_0 is the lattice depth. As with the Raman transitions from Sec. 2.3, the potential contains the exponential terms $e^{\pm i2k\hat{z}}$. We therefore expect a state with momentum p to be coupled to states of momentum $p \pm 2\hbar k$. Thus, we will work in a basis of states

$$|p, n\rangle := |p + 2n\hbar k\rangle$$

Putting this potential into the Schrödinger equation using this $|p, n\rangle$ basis yields the Hamiltonian

$$\hat{H}_{\text{Bloch}} = \begin{pmatrix} \ddots & \kappa & 0 & \cdots & 0 & \cdots & 0 \\ \kappa & \beta_{-l}^2 & \kappa & \ddots & \vdots & & \vdots \\ 0 & \kappa & \ddots & \kappa & 0 & \cdots & 0 \\ \vdots & \ddots & \kappa & \beta_0 & \kappa & \ddots & \vdots \\ 0 & \cdots & 0 & \kappa & \ddots & \kappa & 0 \\ \vdots & & \vdots & \ddots & \kappa & \beta_l^2 & \kappa \\ 0 & \cdots & 0 & \cdots & 0 & \kappa & \ddots \end{pmatrix} \tag{8.31}$$

where $\beta_l = \frac{(p+2l\hbar k)^2}{2m} + 2\kappa$ and $\kappa = U_0/4$, and we've set $\hbar = 1$. The matrix being tridiagonal reflects the potential coupling a state $|p, l\rangle$ to itself and $|p, l \pm 1\rangle$.

The periodic nature of the potential means that the Hamiltonian commutes with a translation operator

$$\hat{T}_d = \exp(i\,\hat{p}\,d/\hbar)$$

where $d = \lambda/2$ is the periodicity of the lattice. There therefore exist simultaneous eigenstates of both the Hamiltonian $\hat{H}_{\text{Bloch}}$ and the translation operator $\hat{T}_d$. These eigenstates form the *Bloch basis* that we will use to describe the atoms in the lattice. These states are denoted by $|q, n\rangle$.

The parameter q is called the *quasimomentum*, which is a conserved quantity under $\hat{H}_{\text{Bloch}}$. As the name suggests, the quasimomentum is the periodic potential's analog of the free space momentum. Eigenvalues of $\hat{T}_d$ must be complex numbers with unity norm, so we can write them as e^{iqd}, where $q \in \left[-\frac{\pi}{d}, \frac{\pi}{d}\right]$.[5] This relationship to the eigenvalues of $\hat{T}_d$ is the definition of the quasimomentum q.

The integer n simply enumerates the eigenstates of the Hamiltonian $\hat{H}_{\text{Bloch}}$ at a given quasimomentum q in energy-order; $n = 1$ is the lowest energy state, $n = 2$ is the next lowest, etc. We will also refer to the eigenstates $|q, n\rangle$ with fixed n as "bands" (ground band has $n = 1$, second band has $n = 2$, etc.)

The energies associated with the free-space states $|p, n\rangle$ are given by $E_{p,n} = (p+2n\hbar k)^2/2m$. In the lattice the energies $E_{q,n}$ are given by the eigenvalues of the Hamiltonian $\hat{H}_{\text{Bloch}}$ corresponding to the eigenvectors $|q, n\rangle$. The energies $E_{q,n}$ and $E_{p,n}$ can be seen compared to each other in Fig. 8.10. The salient feature of the comparison is the opening of gap near the edges of the Brillouin zone.

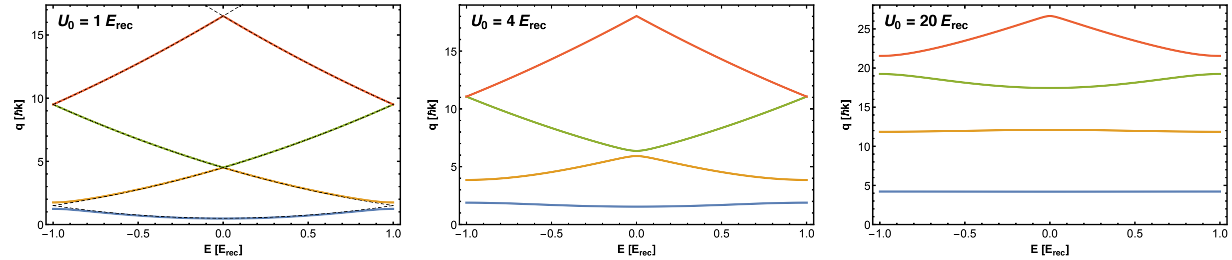

Figure 8.10: Energies of the first four Bloch bands are shown for various lattice depths. For the weakest lattice $U_0 = 1E_{\text{rec}}$, dashed black lines show the free space momentum dispersion relations, and a opening of the gap at the edges of the first Brillouin zone can be seen.

With these states in mind, we now consider the application of a constant force $\boldsymbol{F} = F\hat{\boldsymbol{z}}$ (for example, due to gravity), where $\hat{\boldsymbol{z}}$ is the unit vector along the direction of the Hamiltonian's periodicity. The Hamiltonian $\hat{H}_{\text{Bloch}}$ is then replaced by $\hat{H}_F = \hat{H}_{\text{Bloch}} - F\hat{z}$ (where $\hat{z}$ is the position operator, not the unit vector $\hat{\boldsymbol{z}}$). $\hat{H}_F$ is no longer periodic, so its resulting eigenstates are no longer simultaneous eigenstates of the translation operator

---

[5] This range is called the first Brillouin zone.

$\hat{T}_d$. However, the evolution of $\hat{T}_d$ can be calculated to give the time-dependence of the quasimomentum:

$$\begin{aligned} -i\hbar\frac{d}{dt}\hat{T}_d &= [\hat{H}_F, \hat{T}_d] \\ &= [-F\hat{z}, \hat{T}_d] \\ &= Fd\hat{T}_d \end{aligned}$$

A state that starts as an eigenstate of the translation operator $\hat{T}_d$ therefore *remains* an eigenstate of the translation operator. The eigenvalue (quasimomentum), however, becomes time-dependent, given by

$$q(t) = q(0) + Ft/\hbar \tag{8.32}$$

where $q(0)$ is the initial quasimomentum. This can be seen by identifying $\hat{T}_d \to \exp(iq(t)d)$ when acting on eigenstates $|q, n\rangle$.

Consider a particle trapped with initial quasimomentum $q(0) = 0$ and in the lowest band $n = 1$ in a periodic potential plus a constant force, i.e., subject to the Hamiltonian $\hat{H}_F$. As the quasimomentum evolves according to eq. 8.32, it approaches the edge of the Brillouin zone. We know from eq. 8.32 that the quasimomentum will continue increasing linearly / wrap back into the first Brillouin zone at $q = -\frac{\pi}{d}$. However, in doing so, what will happen to n? In free-space, where we can arrive by simply taking $U_0 \to 0$, we know that n must increase to 2, where we've just massively complicated a particle accelerating due to a constant force.

In the lattice however, the Schrödinger equation with Hamiltonian $\hat{H}_F$ needs to be numerically time-evolved to see how much of the population results in each band n. Consider the Hamiltonian $\hat{H}_{\text{Bloch}}$ without a force. For the quasimomentum at the edge of the first Brillouin zone, an energy gap between the first and second bands (see Fig. 8.10) of height $\approx 2\kappa$ is present. This can be seen by considering only the lowest two bands, turning eq. 8.31 into the two level system

$$\hat{H}_{\text{Bloch,2lvl}} = \begin{pmatrix} \beta_{-1} & \kappa \\ \kappa & \beta_0 \end{pmatrix} \tag{8.33}$$

and diagonalizing with $p = k$.

The two-level Hamiltonian in eq. 8.33 is of the same form as eq. 7.1 describing adiabatic passage! Thus, if the quasimomentum is swept slowly through the edge of the Brillouin zone at $p = k$, the atom will undergo adiabatic passage through the transition $|q = k, n\rangle \to |q = -k, n\rangle$. For an atom held against gravity in a vertical optical lattice, a Bloch oscillation can thus be seen as a first-order Bragg transition undergone via adiabatic passage. As the atom accelerates downwards, the increasing Doppler shift brings its detuning closer to two-photon resonance. The atom then adiabatically passes through the transition, and receives a $2\hbar k$ momentum transfer, bringing it to the other side of the first Brillouin zone in the same Bloch band.

This gives a simple and counterintuitive picture: a quantum particle subject to a constant force in a periodic potential will *oscillate*. This is quite different than the free space expectation of a constant force providing a constant acceleration. This Bloch oscillation phenomenon was first predicted by Bloch [174] in 1929 and Zener [175] in 1934 while describing electron conductivity in a crystal lattice. However, scattering of electrons due to lattice defects is usually much faster than the Bloch period, making the effect unobservable in those systems. Direct experimental realization had to wait until 1993, when Bloch oscillations were observed in a semiconductor superlattice [176] (where the larger spatial period makes the Bloch period short enough (~ 600 fs) to be observed via THz radiation). Later, cold atoms in an optical lattice were first used [177] to demonstrate Bloch oscillations, and have since been an excellent platform for their demonstration and use.

The Bloch period T_B at which these oscillations occur can then be seen as the time required to accelerate an atom until its velocity $v_{\text{atom}} = 2v_{\text{rec}}$ (i.e., when the Doppler shift of the counter-propagating beams forming the lattice are seen in the atom's frame as resonant with a first-order Bragg transition), where the recoil velocity is $v_{\text{rec}} = \hbar k/m$. For a constant acceleration a, $v_{\text{atom}} = at$, and

$$T_B = \frac{\hbar k}{ma}$$

For a cesium atom supported against gravity in an 866 nm lattice, this gives a Bloch period of 707.5 μs.

Since a Bloch oscillation is an adiabatic process, the Landau-Zener formula [178] can be used to calculate the probability that the atom does not undergo the adiabatic process. It can be shown [179] that this loss probability is given by

$$P_{\text{loss}} = e^{-a_c/a} \quad \text{where} \quad a_c = a_0 \frac{\pi}{64}\left(\frac{U_0}{E_{\text{rec}}}\right)^2$$

and $a_0 = \hbar^2 k^3/m^2$ is the *natural acceleration*. For cesium atoms in an 866 nm lattice, $a_0 = 87$ m/s^2. This can therefore be an extremely efficient process. For our cesium atoms supported against gravity in a $6E_{\text{rec}}$-deep 866 nm lattice, $P_{\text{loss}} \approx 1.5 \times 10^{-7}$. Many Bloch oscillations can therefore be done while avoiding atom loss (up to thousands have been previously demonstrated in a non-interferometric setup [180]). This quality is what we hope to capitalize on in our setup, and is shown in Fig. 8.11.

When implementing Bloch oscillations for a lattice hold in our experiment, it is important to ramp the lattice on adiabatically, at the appropriate time, to smoothly map a sub-$2\hbar k$ momentum spread atom sample into the ground band of the lattice. Additionally, this is the same phenomenon underlying the atom launch and catch from Sec. 3.4; these two procedures are simply Bloch oscillations in an accelerated lattice. More in-depth explanations of and calculations for Bloch oscillations can be found in Refs. [22, 179, 181, 182].

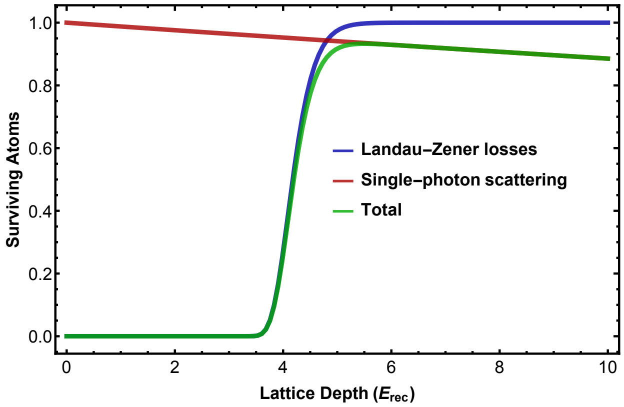

Figure 8.11: Atom loss for Bloch oscillations as a function of lattice depth. Parameters used are cesium atoms in an 866 nm lattice supported vertically against gravity for 1 s (1413 Bloch oscillations). Note the fairly sharp edge where the Bloch oscillation survival probability goes from 0 to 1. In the actual experiment, this edge is smeared out due to the finite size of the atom cloud and beam, and the transverse motion of the atoms.

8.5 Experimental implementation and results

8.5.1 Lifetime limitations for long holds

A long lattice lifetime is a prerequisite to holding a coherent superposition in the lattice for long times. Several effects limit the lattice lifetime, which will be discussed here.

Lattice depth stability

Trap depth noise at the trap frequency parametrically heats the atoms, leading to atom loss [132, 183, 184]. In our case, trap depth noise comes in two forms: intensity noise of the input beam, and frequency noise on the lattice laser relative to cavity resonance, which gets converted into amplitude noise by the cavity lineshape.

The frequency to amplitude noise can come from a number of sources: noise on the lattice laser lock, the science cavity lock, or any lock upon which these two are based (tracer laser, transfer cavity, spectroscopy). When the lattice laser is locked to science cavity resonance, the constituent locks are sufficiently tight to give low frequency-to-amplitude noise. However, if these locks drift relative to each other, the lattice laser moves from the zero-derivative peak of the Lorentzian science cavity lineshape, to its slope off-resonance. Even a few tens of kHz off cavity resonance, this frequency-to-amplitude noise reduces cavity lifetimes. Reducing drifts of the lockpoints was therefore important. This necessitated the switch to the lower-RAM lock discussed in Sec. 8.2.

Intensity noise on the input beam is reduced via amplitude stabilization using an AOM, similar to the system in Ref. [184].

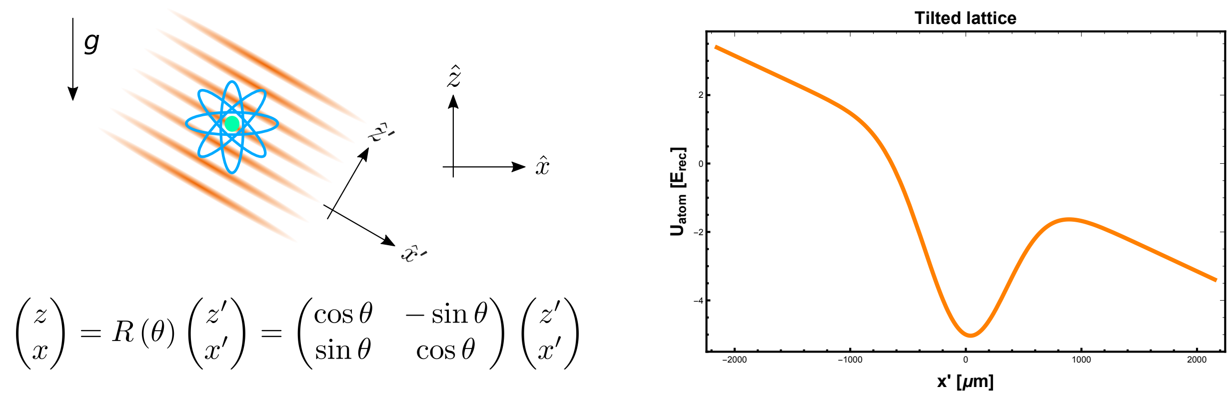

$$\begin{pmatrix} z \\ x \end{pmatrix} = R(\theta) \begin{pmatrix} z' \\ x' \end{pmatrix} = \begin{pmatrix} \cos\theta & -\sin\theta \\ \sin\theta & \cos\theta \end{pmatrix} \begin{pmatrix} z' \\ x' \end{pmatrix}$$

Figure 8.12: Lattice tilted from vertical. Left: Misalignment (greatly exaggerated) by an angle θ of the lattice axes $\{\hat{x}', \hat{z}'\}$ from the axes defined by gravity $\{\hat{x}, \hat{z}\}$. Right: Tilted lattice potential for $\theta = 1$ mrad showing reduced trapping in the transverse direction.

Quantitative evaluation of the remaining trap depth noise on lattice lifetime and contrast decay remains to be performed. Both residual on-resonance frequency-to-amplitude noise, and noise in the intensity stabilization loop should be considered.

Tilt

Radial confinement in the 718 μm waist cavity mode is weak, with a trap frequency of only ~ 2.5 Hz at 5 E_{rec} depth. If the lattice axis is not aligned to the vertical defined by gravity, a component of the gravitational pull to Earth will be along the radial direction of the lattice. This is shown in Fig. 8.12.

The 1 mrad tilt plotted in Fig. 8.12 reduces the trap depth in the transverse dimension from 5 E_{rec} to about 3.4 E_{rec}. This can lead to atom loss either through increased Landau-Zener tunneling, or simply becoming to shallow to confine the transverse velocity distribution of the atoms.

Luckily, we already have the tilt-stabilization system from Sec. 3.5.3.3. We can simply find the tilt setpoint that aligns the cavity mode to the vertical (either by measuring gravity with an interferometer, or looking at atom loss in a long lattice hold), and stabilize the optical table to that point.

Vacuum pressure

Collisions between the cesium atoms and background gas molecules eject atoms from the trap. We have found that this is a non-negligible contribution in our setup.

Firing the titanium sublimation pump gave us an opportunity to temporarily increase our pressures, and the titanium acting as a getter eventually pumped to a lower pressure than we started with. Lattice lifetimes measured during this pump-down can be seen in Fig. 8.13.

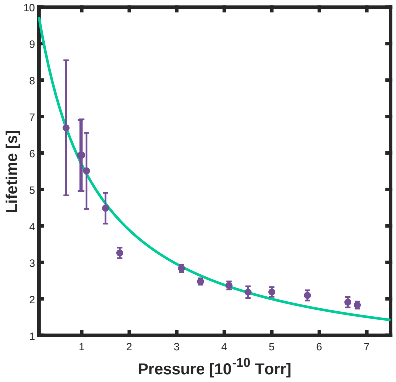

Figure 8.13: Vacuum pressure-limited lifetime. Lattice lifetimes were measured as the pressure P was decreased by sputtered titanium from a sublimation pump acting as a getter. Fit includes the expected lifetime dependence on pressure, $\tau_P \propto \frac{1}{P}$, and single-photon scattering at rate $\Gamma_{\text{sc}} = \tau_{\text{sc}}^{-1}$. Total lifetime τ is given by $\tau = \left(\tau_P^{-1} + \tau_{\text{sc}}^{-1}\right)^{-1}$.

After the titanium pumping equilibrated, an ion gauge ∼10 cm away from the main chamber measured the pressure to be 4×10^{-11} Torr. This is comparable to the x-ray limit of the ion gauge, and so may not be perfectly representative. It's also probably not exactly the relevant pressure, since the ion gauge is located down a tube from the main chamber.

Collisions with the background molecules at room temperature, however, should eject cesium atoms from the trap. Thus, while limiting the lattice lifetime, this process shouldn't have an impact on interferometer contrast, since atoms that do remain in the trap haven't collided.

Single-photon scattering

While 866 nm is reasonably far from both the cesium D1 and D2 lines, there is nonzero single photon scattering. The scattering rate at 866 nm is

$$\Gamma_{\text{sc}}^0 = \frac{1}{54.4\ \text{s}} \left(\frac{U_0}{E_{\text{rec}}}\right)$$

where U_0 is the potential at the center of the trap. Typical trap depths use $U_0 \sim 8E_{\text{rec}}$ (compare with Fig. 8.11). This is necessary due to the finite size of the beam and the cloud: the trap must be deep enough at the edge of the atomic cloud that Landau-Zener losses are low. A larger beam could use a shallower trap.

To get a representative single value for the scattering rate, we can time-average the intensity seen by an atom over one oscillation period at the radial trap frequency (≈ 3 Hz), and average this quantity across the atomic cloud. This gives some numerical factor ξ between about 0 (no atoms see any intensity) and 1 (all atoms spend the entire hold sitting at the deepest point), such that $\Gamma_{\text{sc}} = \xi \Gamma_{\text{sc}}^0$ for a given lattice depth U_0. For a lattice depth of $8E_{\text{rec}}$, and using $\xi = 0.7$ as a reasonable estimate, this gives a single-photon scattering lifetime around $\tau_{\text{sc}} \approx 10$ s, which is consistent with what we see in experiments.

Single-photon scattering effectively randomizes the vertical component of the atom's velocity such that there is a 50% chance the atom remains trapped in the first Bloch band. As a result, half of the atoms that scatter a lattice photon stick around, but do not contribute to the interferometer signal. Thus, we can expect single-photon scattering to contribute to contrast decay with a time constant equal to $2\tau_{\text{sc}}$.

8.5.2 Contrast oscillations

We have observed two effects that modulate the interferometer contrast as a function of pulse separation time T. In this section, we describe each of them.

The first effect is an oscillation of the contrast with a period of about 61.2 μs. We see best contrast when the pulse separation time T is a value such that the wavepacket separation is an integer multiple of the lattice spacing. That is,

$$\begin{aligned} 2v_{\text{rec}}T &= n\frac{\lambda_{\text{latt}}}{2} \\ T &= n\frac{m_{\text{Cs}}}{8\pi\hbar}\lambda_{\text{latt}}\lambda_{\text{Raman}} = n \times (61.2\,\mu\text{s}) \end{aligned} \tag{8.34}$$

where n is an integer, $\lambda_{\text{latt}} = 866$ nm is the lattice laser wavelength, and $\lambda_{\text{Raman}} = 852$ nm is the wavelength of the laser used for the Raman transitions. We will refer to times T satisfying eq. 8.34 as *Talbot times*, in loose analogy with Talbot-Lau matter wave interferometers [185, 186], and the condition eq. 8.34 as the *Talbot condition*.

We interpret this observation as the separated wavepackets wanting to be loaded into the lattice at the same phase of the lattice potential. If this were not the case, maybe this causes the interferometer to improperly close, as each arm sloshes around in its respective lattice pancake with a different phase. We note that this has not been observed in the previous lattice interferometers [117, 118], but the cause of the discrepancy is unclear. We postulate that this is due to our velocity spread: $\approx 2v_{\text{rec}}$, as compared to $0.15v_{\text{rec}}$ in Ref. [118]. But this does not explain the different behavior from the similar $\approx 2v_{\text{rec}}$ velocity spread in Ref. [117]. That experiment uses the same beam for the Raman $\frac{\pi}{2}$ pulses and Bloch oscillations, while we use two different wavelengths (852 nm and 866 nm, respectively). Ref. [117] also used Rb, a different species, and a correspondingly shallower $2E_{\text{rec}}$-deep lattice. While the exact mechanism of this contrast oscillation is yet to be pinned down, its effect is clearly seen in Fig. 8.14.

The second source of contrast modulation comes from the ac Stark phase shift of the tracer laser at 780 nm used to lock the cavity length. For 10 μW of incident optical power, the ac Stark phase shift in the cavity is approximately $\delta_{\text{ac,tracer}} \approx 2\pi \times 20$ Hz. Two arms held in the lattice formed by the 866 nm laser, will in general see different phases of the tracer laser standing wave, and thus different values of $\delta_{\text{ac,tracer}}$. Variations across the cloud of this nonzero ac Stark shift dephase the interferometer. This is also shown in Fig. 8.14.

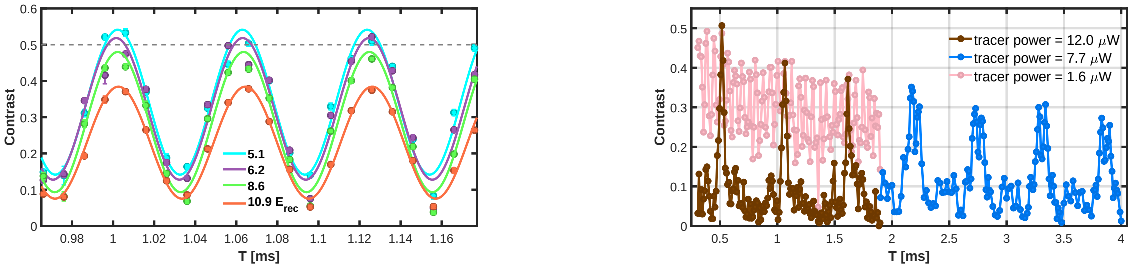

Figure 8.14: Lattice interferometer contrast oscillations. Left: Contrast oscillations with varying T of the lattice AI with period $\approx 61.5\ \mu$s, set by the Talbot condition $v_{\text{rec}}T = n\lambda_{\text{latt}}/2$. Interferometer contrast oscillating with T is shown for several lattice depths (which refer to the depth at the center of the beam). These interferometers had 300 Bloch oscillations, so $\tau \approx 211$ ms. Right: Contrast modulation from ac Stark phase shifts induced by the 780 nm tracer laser. Decoherence is minimized near the super-Talbot condition, when $v_{\text{rec}}T = n\lambda_{\text{latt}}/2 \approx m\lambda_{\text{tracer}}/2$, giving blips of contrast separated by $\approx 560\ \mu$s, as discussed in the main text. Data here uses $\tau = 1.05$ s, $U_0 = 5.9E_{\text{rec}}$. Several tracer powers are shown. Note that the peaks are wider with 7.7 μW tracer power than with 12.0 μW, indicating less severe super-Talbot constraint. At low enough tracer powers, super-talbot-ing is suppressed, as seen from the 1.6 μW trace. The fast Talbot contrast modulation can still be seen in these traces. Contrasts > 0.5 are a result of nearly maximal contrast (which equals 0.5) plus an artifact of image background subtraction at low atom number.

We therefore add a requirement to eq. 8.34 for best contrast, namely

$$2v_{\text{rec}}T = n\frac{\lambda_{\text{latt}}}{2} \approx m\frac{\lambda_{\text{tracer}}}{2} \tag{8.35}$$

Unfortunately, this condition can not be met exactly. But there will be a Talbot time satisfying eq. 8.34 that best satisfies eq. 8.35 every $\approx 561\ \mu$s. We will call these times *super-Talbot times*, and the condition eq 8.35 the *super-Talbot condition.* The super-Talbot period is the time taken to traverse at velocity $2v_{\text{rec}}$ one spatial beatnote of the standing waves formed by the lattice laser (with wavelength $\frac{866\text{ nm}}{2}$) and the tracer laser (with wavelength $\frac{780\text{ nm}}{2}$). This spatial beatnote has wavelength $\lambda_{\text{beat}} = 7.85\ \mu$m, so $\lambda_{\text{beat}}/(2v_{\text{rec}}) = 561\ \mu$s.

We have confirmed this interpretation by varying the tracer laser power used to lock the science cavity, and observing that contrasts at non-super-Talbot times improves with decreasing tracer laser power, while the super-Talbot time contrasts remained roughly fixed. Second, we varied the momentum splitting by implementing a basic SDK lattice interferometer (with $4\hbar k$ momentum splitting), and observed that the super-Talbot period decreased by a factor of 2 to 280 μs, indicating that the effect is really a spatial structure, and not some artifact of loading into/out of the lattice.

Not all super-Talbot times are created equally, unfortunately, as the super-Talbot condition eq. 8.35 can not be exactly met. There is a "carrier-envelope offset phase" analog between (i) the 61 μs - period Talbot condition, and (ii) the requirement to be an integer multiple of the tracer/lattice laser beatnote. Conditions (i) and (ii) are not guaranteed to be able to be met simultaneously. There are some super-Talbot times, for example, where the optimal T for (ii) is centered between two Talbot times of nearly equal contrast. Both conditions cannot be perfectly met.

In practice, once aware of this effect, we were able to reduce the incident tracer laser power used to lock the cavity from 50 μW to $\sim$3 μW. This has improved the situation, but a full assessment of residual limitation from imperfectly satisfying the super-Talbot condition has yet to be performed. If it were possible to use the same wavelength for the tracer and lattice-hold lasers, this effect would disappear.

8.5.3 Preliminary results

With all these considerations, performance of the interferometer is shown in Fig. 8.15. At $\tau = 1$ s, the fringe has peak-to-peak contrast of 44%, out of a maximum possible 50% (see the extra output ports in Fig. 8.1).

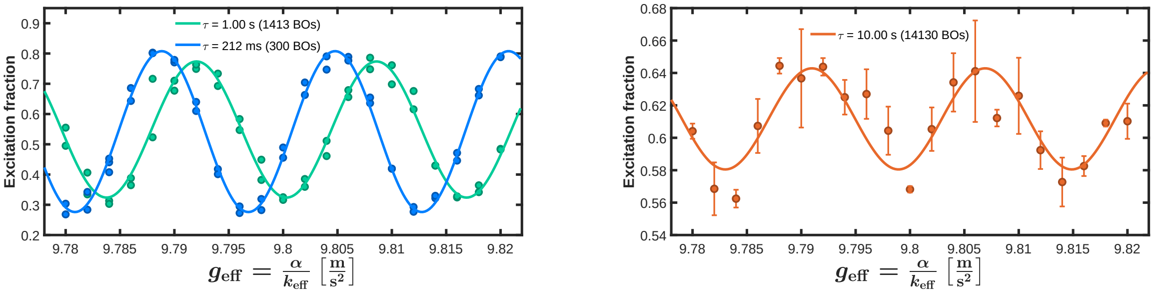

Figure 8.15: Preliminary lattice AI performance at $\tau = 1$ s (left) and $\tau = 10$ s (right). A shorter hold of 300 Bloch oscillations is also shown alongside the 1 s fringe. All fringes here use $T = 1.066$ ms.

Contrast decay as a function of τ and as a function of T can be seen in Fig. 8.16. Single photon scattering should contribute to contrast decay with τ with a time constant of about 20 s. We observe a time constant on this contrast decay of about 5 s. Contributions to the unaccounted-for contrast decay could include

Stray light: Each time we have identified and eliminated a faint source of stray light, the contrast has jumped up.

Residual wavefront imperfections: Though the cavity helps this problem by a factor of something like the finesse (naïvely, at least)[6], it does not completely eliminate it. A higher-finesse cavity may further reduce this contrast decay channel. Quantitative assessment of this effect remains to be performed.

---

[6] One step further, we'd posit a reduction for Hermite-Gaussian mode H_{mn} of $\mathcal{G}(\omega_q + 2\pi\delta f_{mn})/\mathcal{G}(\omega_q)$, where $\mathcal{G}$ is the optical gain, ω_q is the resonance frequency of the H_{00} mode, and δf_{mn} is the cavity's transverse mode shift given by eq. 2.90.

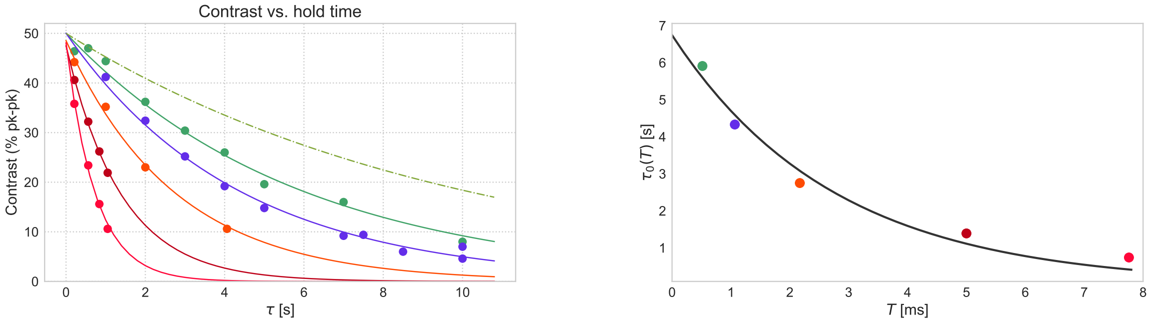

Figure 8.16: Preliminary lattice AI performance. Left: Contrast decay with hold time τ for several pulse separation times $T = \{0.516, 1.066, 2.170, 5.000, 7.760\}$ ms. Measured contrast points are fitted to an exponential $c_0 \exp(-\tau/\tau_0(T))$. The dot-dashed line indicates the expected contrast decay for single-photon scattering alone, for a scattering rate of $\Gamma_{\mathrm{sc}} = (10\text{ s})^{-1}$. Right: The decay time constant $\tau_0(T)$ depends on T, and is shown. It is fitted to its own exponential decay to guide the eye.

The lattice laser is actually not particularly well mode-matched to the cavity ($\approx 50\%$ coupling efficiency). Small dips in reflection can be seen for the modes H_{mn} with $m + n = 15$. For $m + n = 16$, $\delta f_{mn} - \mathrm{FSR} \approx 1.8$ MHz $\approx 0.6\gamma_{\mathrm{FWHM}}$. That is, these modes with $m + n = 16k$ for the first few integers k are nearly resonant with the cavity, and therefore unsuppressed. Adding an appropriate lens setup would improve the mode-matching, and should be done.

Tracer laser ac Stark shift: The super-Talbot condition sets a pulse separation time T that minimizes the ac Stark shift of the tracer laser. Unfortunately, the minimized value is not zero. The size of this effect could be assessed by measuring contrast decay as a function of tracer laser power.

Amplitude modulation of the lattice: The remaining heating rate after amplitude and frequency stabilization remains to be quantitatively assessed.

Other, yet-unknown sources

8.6 Summary

We have presented a geometry allowing for spatially-separated matter wave interferometry with over 10 seconds of interrogation time. The geometry capitalizes on the mode filtering of an optical cavity inside which the atoms are manipulated.

Optimizations of the current setup remain to be had. Furthermore, the method presented (i.e., using a cavity) presents a route to even further extend the capabilities of such an interferometer by appropriate design choices.

This type of interferometer could have applications as a compact gravimeter with suppressed sensitivity to vibrations, or a probe of source-mass interactions (e.g., Chapters 5 and 6) with high spatial resolution. Additionally, the dominant free-evolution phase term $k_{\text{eff}} g T \tau$, being up over 1000 times larger than any other phase term, may help shed light on the matter wave redshift debate (e.g., [187–192], see Sec. 9.3.1.1 for more detail).

Chapter 9

Future prospects

A number of future routes are open for polishing and improving the performance of the apparatus. Additionally, the development of tools in this thesis point towards future experiments and new areas of research. In this chapter, an attempt is made to discuss some of these prospects. We categorize them below into short-, medium-, and long-term projects. Within each of these sections, subsections indicate if the improvements relate to the work from a previous chapter in this thesis.

9.1 Short term

Atom interferometer in an optical cavity (Chapter 4)

Rabi pulses in a cavity were described Ch. 4. However, we did not yet have a full understanding of these effects when performing the experiments in this thesis. As such, there are several general optimizations that can be made to improve interferometer performance. A forthcoming publication will explore some of these optimizations.

Single-sideband EOM. Much of this complication could be avoided if we just had a single-sideband optical modulator. Such a modulator has been used for a rubidium interferometer [193]. Unfortunately, while these modulators exist in the telecom band around 1550 nm (which is then frequency doubled to get the 780 nm light used with Rb atoms), they do not yet exist at 852 nm. There is no fundamental reason why not; once they do, this would dramatically simplify Raman pulses in a cavity.

Time-dependent cavity offset $\delta_{\mathbf{cav}}(t)$. Over their trajectory, the atoms' position in the spatial beatnote of the Rabi frequency changes. So does the Raman frequency, which is chirped to compensate for gravity. Rather than sitting at a fixed (and usually 0) cavity offset, the offset could follow a curve that maximizes the Rabi frequency at each point. This curve is straightforward to calculate from the model presented in Chapter 4.

ac Stark matching. For Mach-Zehnder geometries, cavity offsets can be chosen that match the ac Stark shifts of the first and third $\frac{\pi}{2}$ pulses. Rather than the tedious calibration from Sec. 5.6, this can be inferred from the model, increasing contrast on all interferometers (not just ones that are manually calibrated).

Spin-dependent kicks (Chapter 7)

The quantitative understanding of adiabatic passage in our SDK interferometers was similarly delayed from the experiments. Optimizations for SDK interferometers include

Robust detuning profile. Implementation of the detuning profile given by eq. 7.10 should decrease noise in the adiabatic passage of the SDK interferometers.

Tailor pulses for applications For example, the resonant AI doesn't need the bandwidth of the LMT interferometer. Trade-offs could be made to optimize the pulses for each application. Larger momentum transfer and/or more loops could be demonstrated.

Adiabatic beamsplitters. Ref. [142] describes adiabatic beamsplitter and recombiner pulses. The adiabatic recombiner pulses are not robust against experimental imperfections, but the beamsplitters should impart only a global phase to both interferometer arms, which is therefore of no consequence. Using this adiabatic beamsplitter to open the interferometer (with either a microwave or optical pulse) would be interesting, and a potential improvement.

Dependence on adiabaticity Q. Increasing Q increases both the adiabaticity (good) and the dynamic phase (bad). This parameter was totally unexplored in our setup, so is unlikely to be optimal.

9.2 Medium term

Chameleons (Chapter 5)

The SDK and lattice interferometers both provide routes to increased sensitivity over a Mach-Zehnder, especially within a compact volume. Interactions with a source mass can now be measured with higher precision. One order-of-magnitude improvement would fully cover the parameter space for a dark energy chameleon ($\Lambda_{\text{chameleon}} = \Lambda_{\text{DE}} = 2.4$ meV) with $n = 1$. This would be a significant result: such chameleons would either be discovered or ruled out entirely.

9.3 Longer term

Lattice interferometer (Chapter 8)

If we allow the possibility of changing cavity mirrors, many possibilities for the lattice interferometer open up. First, access to the cavity transmission could be provided by drilling a hole in the lead mount. This would also allow input beams from both sides of the cavity. In that case, the cavity could be locked using the 866 nm laser as the tracer laser. This would remove the 780 nm laser from the setup, and its contrast-limiting ac Stark shift (Sec. 8.5.2) along with it. Care would need to be taken to ensure that the higher power of the lattice-hold beam does not cause shifts in the cavity lock point. However, an appropriate arrangement of polarizations and isolators should be possible.

If the 866 nm laser were replaced with a laser red-detuned from both the cesium D1 and D2 lines, single-photon scattering could be eliminated as a concern. Excellent laser technology exists at, e.g., 1064 nm. The current cavity mirrors do not support this wavelength, hence the 866 nm choice. If we were to upgrade the mirror coatings, fixed reflectivity / linewidth could be maintained at 852 nm (leaving the interferometry pulses unchanged), while providing much higher reflectivity and finesse at 1064 nm for the lattice hold. This increased finesse would allow for even smoother wavefronts (and higher intracavity power) and reduced scattering, potentially even further extending available interrogation times.

Additionally, the lattice interferometer in a cavity presents a novel gravimeter geometry. Using the lattice interferometer as a gravimeter has two major advantages. The first is suppressed vibration sensitivity (Sec. 8.3) by up to 1-2 orders of magnitude. The other is the substantially reduced physical volume over which the interferometer must run. Typically, AI gravimeters increase sensitivity by extending the pulse separation time T in a Mach-Zehnder geometry. For example, a state-of-the-art mobile AI gravimeter uses something like $T = 200$ ms in ≈ 1 m of vertical space. To achieve similar sensitivity per shot to gravity, a lattice interferometer with $T = 4$ ms, $\tau = 10$ s could be used, instead requiring < 400 μm of vertical space. This is not a perfectly fair comparison (for example, the integration rate of a 10 second shot is slower), but illustrates the utility of the lattice hold for gravimeter sensitivity, especially in a compact volume.

9.3.1 New directions

9.3.1.1 Gravitational Aharonov-Bohm effect and the gravitational redshift of the Compton frequency

A longstanding motivation for the cavity interferometer experiment has been a measurement of the gravitational analog of the Aharonov-Bohm effect [140]. The original (electromagnetic) Aharonov-Bohm effect was important in the early days of quantum mechanics for several reasons. First, it was a counterintuitive prediction [194, 195] that was later experimentally confirmed [196–198]. Second, it demonstrated that the fundamental object of electromagnetism was not the $\boldsymbol{E}$ and $\boldsymbol{B}$ fields, but the potential $A^\mu = \{\phi, \boldsymbol{A}\}$.

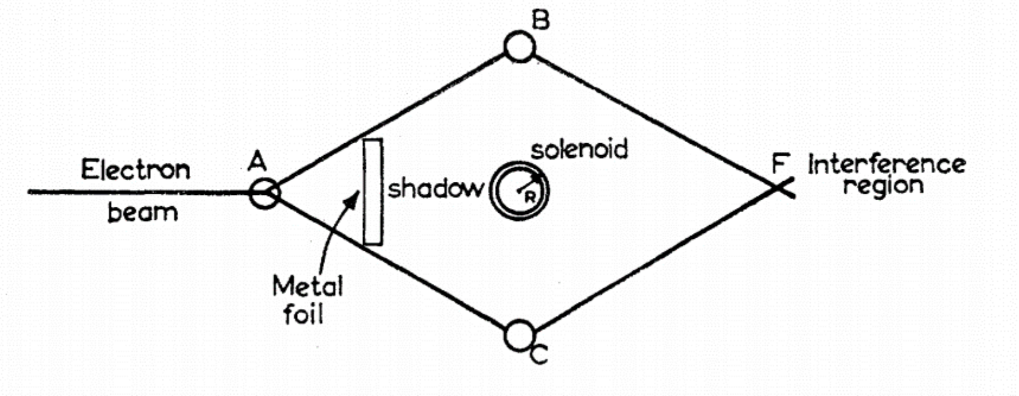

Figure 9.1: Electromagnetic Aharonov-Bohm effect, as seen in a setup described in the text. Figure reused with permission from the original Ref. [195].

A classic depiction of the effect is shown in Fig. 9.1. An electron wavefunction is split, and redirected around an infinite solenoid. The solenoid can have either current or no current running through it. Either way, the magnetic field $\boldsymbol{B}$ is zero everywhere outside the solenoid. Upon recombination of the electron wavefunction, there is a phase shift given by

$$\begin{aligned}\varphi_{\mathrm{AB}} &= \frac{e}{\hbar}\oint \boldsymbol{A}\cdot d\boldsymbol{\ell} \\ &= \frac{e}{\hbar}\Phi_{\mathrm{B}}\end{aligned}$$

where e is the charge of the electron, $\boldsymbol{A}$ is the vector potential, and the integral is around the closed loop formed by the electron interferometer. In the second line, Stokes' theorem plus the relation $\boldsymbol{\nabla}\times\boldsymbol{A}=\boldsymbol{B}$ are used to involve the magnetic flux Φ_{B} passing through the closed contour being integrated around. If there is a current running through the solenoid, there is a magnetic flux through the loop formed by the electron interferometer arms and thus a non-zero phase shift. This effect is topological, in that no number of local measurements could be performed along the electron path to predict the outcome.

The gravitational version of this effect uses the gravitational potential to produce an analogous phase shift. We will call this the *gravitational AB effect*. Consider the mass distribution shown in Fig 9.2. The resulting gravitational potential has 3 extrema (when plotted as a 1D cross-section; in 3D they're saddle points). The maximum between the two minima has a different gravitational potential than the minima. If two arms of an atom interferometer were parked at these points (one minimum and the maximum), they would accumulate a differential phase that could be read out upon recombination. As per the original proposal [140], the phase shift induced on a cesium atom interferometer is

$$\delta\phi_{\mathrm{gravAB}} = 160\ \mathrm{mrad}\times\left(\frac{s}{1\ \mathrm{cm}}\right)\left(\frac{\rho}{10\mathrm{g}\ /\ \mathrm{cm}^3}\right)\left(\frac{\tau}{1\ \mathrm{s}}\right) \tag{9.1}$$

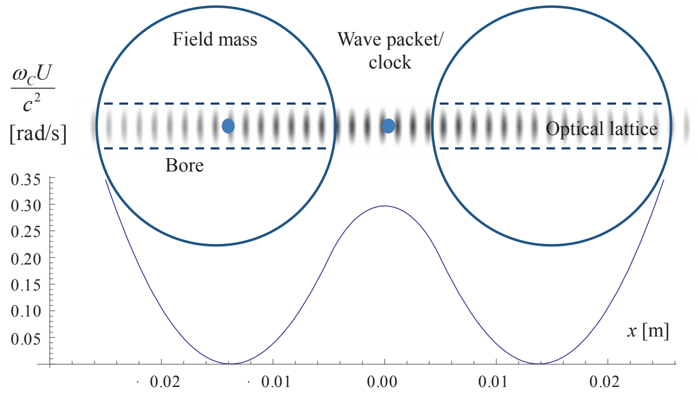

Figure 9.2: Gravitational Aharonov-Bohm effect setup (from Ref. [140]).

where s is the wavepacket separation, ρ is the source mass density, and τ is the time for which the wavepacket is held at the saddle points of the potential. Eq. 9.1 assumes spherical masses of radius $R = 0.72s$, and separation $L = 3R$ between the source mass centers so that the wavepackets are indeed located at the potential extrema.

For a terrestrial experiment, however, Earth's gravity would pull the atoms away from the gravitational potential extrema of the two source masses. We could use the lattice interferometer of Chapter 8 to hold the wavepackets at that separation. The experiments in this thesis have already demonstrated a $\tau = 10$ s hold at $s \sim 10$ μm separation, without even having yet optimized the lattice interferometer. We have used a tungsten source mass (~ 20 g/cm^3), and resolved a phase shifts of ~ 4 mrad (Chapters 5 and 6).

These numbers put us pretty much exactly at the required sensitivity to resolve a phase shift due to the gravitational AB effect. Granted, the implied 7 μm spherical source masses are not practical (they should at least be large enough for the cavity mode to pass through). But put another way, while increasing the wavepacket separation from 10 μm up to 1 cm, we have 3 orders of magnitude available to sacrifice on other parameters while still remaining sensitive enough to see the gravitational AB effect. This consideration neglects any future improvements to the lattice interferometer, which we actually expect to be made.

The gravitational AB effect is interesting for a number reasons. The first is that it inherits all of the interest of electromagnetic AB effects: topological, non-local, non-dispersive, and occurring despite the absence of a classical force. Second, a gravitational AB measurement presents the opportunity for an interesting measurement of Newton's gravitational constant G. Since the wavepackets are located at saddle points of the potential, the interferometer phase is first-order insensitive to positioning uncertainty/fluctuations, which was the leading uncertainty in the most recent atom interferometric measurement of G [7]. Due to the interferometer's small size, single-crystal source masses are feasible. This eliminates a second leading systematic effect of the measurement in Ref. [7]; namely characterization of the source mass distribution at the 10^{-4} level.

A measurement of the gravitational AB effect could also potentially help clarify the "redshift controversy" started when Ref. [187] argued that the Compton frequency $\omega_c = mc^2/\hbar$ is a physical frequency that can be exploited for metrological purposes (in this case, a measurement of the gravitational redshift). This line of reasoning was vociferously argued against in Ref. [188], and subsequently in references such as [189, 191]. Meanwhile, references such as [190, 192] made pro-Compton frequency arguments. A measurement was then performed purporting to lock a crystal oscillator to a subharmonic of the cesium Compton frequency, asserting the physical nature of the Compton frequency as an oscillator [199]. A measurement of the gravitational Aharonov-Bohm effect could help shed experimental light on this controversy.

In fact, demonstration of the long-hold lattice interferometer itself may already be able to bring some clarity to the discussion. After all, the wavepackets sit at force-free points (lattice sites) at different gravitational potentials. The exact formulation of what this all means is somewhat unclear (at least to me). Another future direction of work would be to investigate the impact of the long-hold lattice interferometer on the redshift debate. If physical, the Compton frequency and/or the gravitational AB setup could be leveraged to perform measurements of the type(s) outlined in Ref. [200] that aim to explore the interface of general relativity and quantum mechanics.

9.3.1.2 Dark matter detector using resonant AI

The resonant AI from Sec. 7.3.5 could be used to search for oscillating forces due to dark matter [155]. A measurement campaign over which the loop duration is swept covers a corresponding mass range of dark matter candidates being searched for.

9.3.1.3 Squeezing, and even more cavity benefits

The experiments in this thesis have so far taken advantage of only two qualities of the optical cavity: smooth wavefronts, and resonant enhancement of the optical intensity. More cavity benefits remain to be taken advantage of.

One example is to utilize the higher-order modes of the optical cavity (using, e.g., a spatial light modulator). For example, donut modes could provide radial confinement. Use of higher-order Hermite-Gauss modes has been proposed as a self-aligned rotation sensor [74, 201]. These possibilities have not yet been experimentally explored, and could open interesting possibilities to extend the capability of a cavity atom interferometer.

Probe beams in a cavity can provide an excellent measure of the population ratio between two hyperfine states [202]. Atomic resonances provide dispersion, and thus a phase shift to an incident light beam. Consider an atom such as cesium with two hyperfine ground states, $|g_1\rangle$ and $|g_2\rangle$, and an optically excited state $|e\rangle$. If an incident beam is between the $|g_1\rangle \rightarrow |e\rangle$ and $|g_2\rangle \rightarrow |e\rangle$ transitions, the total phase shift of an intracavity beam (and thus the cavity resonance condition) depends on the atomic population in the two hyperfine states.

Even better than just measuring the population ratio of atoms in the cavity, this technique can turn the cavity into an entangling device. Obtaining collective information about the atomic sample by measuring this phase shift has been used to produce spin-squeezed states up to 20 dB below the standard quantum limit [158,159]. This capability requires a significantly higher cavity finesse than in our setup.

Atom interferometry and spin-squeezing (plus the requisite readout) have now both been demonstrated in an optical cavity. An extremely exciting future direction would be to merge these two paths.

Bibliography

[1] A. A. Michelson and E. W. Morley, “On the relative motion of the Earth and the luminiferous ether,” *American Journal of Science*, vol. s3-34, no. 203, pp. 333–345, Nov 1887. online link

[2] B. P. Abbott *et al.*, “Observation of Gravitational Waves from a Binary Black Hole Merger,” *Physical Review Letters*, vol. 116, no. 6, p. 061102, Feb 2016. online link

[3] B. P. Abbott *et al.*, “Multi-messenger Observations of a Binary Neutron Star Merger,” *The Astrophysical Journal Letters*, vol. 848, no. 2, p. L12, Oct 2017. online link

[4] M. Kasevich and S. Chu, “Atomic interferometry using stimulated Raman transitions,” *Physical Review Letters*, vol. 67, no. 2, pp. 181–184, Jul 1991. online link

[5] R. H. Parker, C. Yu, W. Zhong, B. Estey, and H. Müller, “Measurement of the fine-structure constant as a test of the Standard Model,” *Science*, vol. 360, no. 6385, pp. 191–195, Apr 2018. online link

[6] R. Bouchendira, P. Cladé, S. Guellati-Khélifa, F. Nez, and F. Biraben, “New Determination of the Fine Structure Constant and Test of the Quantum Electrodynamics,” *Physical Review Letters*, vol. 106, no. 8, p. 080801, Feb 2011. online link

[7] G. Rosi, F. Sorrentino, L. Cacciapuoti, M. Prevedelli, and G. M. Tino, “Precision measurement of the Newtonian gravitational constant using cold atoms,” *Nature*, vol. 510, no. 7506, pp. 518–521, Jun 2014. online link

[8] J. B. Fixler, G. T. Foster, J. M. McGuirk, and M. A. Kasevich, “Atom interferometer measurement of the Newtonian constant of gravity,” *Science*, vol. 315, no. 5808, pp. 74–77, Jan 2007. online link

[9] D. Schlippert, J. Hartwig, H. Albers, L. L. Richardson, C. Schubert, A. Roura, W. P. Schleich, W. Ertmer, and E. M. Rasel, “Quantum test of the universality of free fall,” *Physical Review Letters*, vol. 112, no. 20, p. 203002, May 2014. online link

[10] L. Zhou *et al.*, “Test of equivalence principle at 10^{-8} level by a dual-species double-diffraction Raman atom interferometer,” *Physical Review Letters*, vol. 115, no. 1, p. 013004, Jul 2015. online link

[11] A. Peters, K. Y. Chung, and S. Chu, “Measurement of gravitational acceleration by dropping atoms,” *Nature*, vol. 400, no. 6747, pp. 849–852, Aug 1999. online link

[12] Z.-K. Hu, B.-L. Sun, X.-C. Duan, M.-K. Zhou, L.-L. Chen, S. Zhan, Q.-Z. Zhang, and J. Luo, “Demonstration of an ultrahigh-sensitivity atom-interferometry absolute gravimeter,” *Physical Review A*, vol. 88, no. 4, p. 043610, Oct 2013. online link

[13] T. Farah, C. Guerlin, A. Landragin, P. Bouyer, S. Gaffet, F. Pereira Dos Santos, and S. Merlet, “Underground operation at best sensitivity of the mobile LNE-SYRTE cold atom gravimeter,” *Gyroscopy and Navigation*, vol. 5, no. 4, pp. 266–274, Oct 2014. online link

[14] J. M. Mc Guirk, G. T. Foster, J. B. Fixler, M. J. Snadden, and M. A. Kasevich, “Sensitive absolute-gravity gradiometry using atom interferometry,” *Physical Review A - Atomic, Molecular, and Optical Physics*, vol. 65, no. 3, pp. 1–14, Feb 2002. online link

[15] X. Wu, “Gravity Gradient Survey with a Mobile Atom Interferometer,” Thesis, Stanford University, 2009.

[16] P. Asenbaum, C. Overstreet, T. Kovachy, D. D. Brown, J. M. Hogan, and M. A. Kasevich, “Phase Shift in an Atom Interferometer due to Spacetime Curvature across its Wave Function,” *Physical Review Letters*, vol. 118, no. 18, p. 183602, May 2017. online link

[17] I. Dutta, D. Savoie, B. Fang, B. Venon, C. L. Garrido Alzar, R. Geiger, and A. Landragin, “Continuous Cold-Atom Inertial Sensor with 1 nrad/sec Rotation Stability,” *Physical Review Letters*, vol. 116, no. 18, p. 183003, May 2016. online link

[18] R. Geiger *et al.*, “Detecting inertial effects with airborne matter-wave interferometry,” *Nature Communications*, vol. 2, no. 1, p. 474, Sep 2011. online link

[19] X. Wu, F. Zi, J. Dudley, R. J. Bilotta, P. Canoza, and H. Müller, “Multiaxis atom interferometry with a single diode laser and a pyramidal magneto-optical trap,” *Optica*, vol. 4, no. 12, p. 1545, Dec 2017. online link

[20] H. Müller, S.-W. Chiow, Q. Long, S. Herrmann, and S. Chu, “Atom interferometry with up to 24-photon-momentum-transfer beam splitters,” *Physical Review Letters*, vol. 100, no. 18, p. 180405, May 2008. online link

[21] H. Müller, S.-W. Chiow, S. Herrmann, and S. Chu, “Atom interferometers with scalable enclosed area,” *Physical Review Letters*, vol. 102, no. 24, p. 240403, Jun 2009. online link

[22] P. Cladé, S. Guellati-Khélifa, F. Nez, and F. Biraben, “Large momentum beam splitter using bloch oscillations,” *Physical Review Letters*, vol. 102, no. 24, p. 240402, Jun 2009. online link

[23] T. Mazzoni, X. Zhang, R. Del Aguila, L. Salvi, N. Poli, and G. M. Tino, “Large-momentum-transfer Bragg interferometer with strontium atoms,” *Physical Review A - Atomic, Molecular, and Optical Physics*, vol. 92, no. 5, p. 053619, Nov 2015. online link

[24] B. Plotkin-Swing, D. Gochnauer, K. E. McAlpine, E. S. Cooper, A. O. Jamison, and S. Gupta, “Three-Path Atom Interferometry with Large Momentum Separation,” *Physical Review Letters*, vol. 121, no. 13, p. 133201, Sep 2018. online link

[25] T. Kovachy, P. Asenbaum, C. Overstreet, C. A. Donnelly, S. M. Dickerson, A. Sugarbaker, J. M. Hogan, and M. A. Kasevich, “Quantum superposition at the half-metre scale,” *Nature*, vol. 528, no. 7583, pp. 530–533, Dec 2015. online link

[26] J. Hartwig, S. Abend, C. Schubert, D. Schlippert, H. Ahlers, K. Posso-Trujillo, N. Gaaloul, W. Ertmer, and E. M. Rasel, “Testing the universality of free fall with rubidium and ytterbium in a very large baseline atom interferometer,” *New Journal of Physics*, vol. 17, no. 3, pp. 1–12, Mar 2015. online link

[27] B. V. Estey, “Precision Measurement in Atom Interferometry Using Bragg Diffraction,” Ph.D. dissertation, University of California, Berkeley, 2016. online link

[28] A. Zee, *Quantum Field Theory in a Nutshell*, 2003.

[29] P. Storey and C. Cohen-Tannoudji, “The Feynman path integral approach to atomic interferometry. A tutorial,” *Journal de Physique II*, vol. 4, no. 11, pp. 1999–2027, Nov 1994. online link

[30] A. Peters, “High precision gravity measurements using atom interferometery,” Ph.D. dissertation, Stanford University, 1998.

[31] J. M. Hogan, D. M. S. Johnson, and M. A. Kasevich, “Light-pulse atom interferometry,” in *Proceedings of the International Summer School of Physics ”Enrico Fermi” on Atom Optics and Space Physics*, Jun 2008. online link

[32] W. F. Holmgren, M. C. Revelle, V. P. A. Lonij, and A. D. Cronin, “Absolute and ratio measurements of the polarizability of Na, K, and Rb with an atom interferometer,” *Physical Review A - Atomic, Molecular, and Optical Physics*, vol. 81, no. 5, p. 053607, May 2010. online link

[33] S. Machluf, Y. Japha, and R. Folman, “Coherent Stern-Gerlach momentum splitting on an atom chip,” *Nature Communications*, vol. 4, p. 2424, Sep 2013. online link

[34] M. Kasevich and S. Chu, “Measurement of the gravitational acceleration of an atom with a light-pulse atom interferometer,” *Applied Physics B Photophysics and Laser Chemistry*, vol. 54, no. 5, pp. 321–332, May 1992. online link

[35] A. J. Dunning, “Coherent atomic manipulation and cooling using composite optical pulse sequences,” Ph.D. dissertation, University of Southampton, 2014. online link

[36] D. A. Steck, “Cesium D Line Data,” 2010. online link

[37] N. F. Ramsey, “A molecular beam resonance method with separated oscillating fields,” *Physical Review*, vol. 78, no. 6, pp. 695–699, Jun 1950. online link

[38] D. S. Weiss, B. C. Young, and S. Chu, “Precision measurement of $\hbar/m_{\mathrm{Cs}}$ based on photon recoil using laser-cooled atoms and atomic interferometry,” *Applied Physics B Lasers and Optics*, vol. 59, no. 3, pp. 217–256, Sep 1994. online link

[39] K. Moler, D. S. Weiss, M. Kasevich, and S. Chu, “Theoretical analysis of velocity-selective Raman transitions,” *Physical Review A*, vol. 45, no. 1, pp. 342–348, Jan 1992. online link

[40] H. Müller, S.-W. Chiow, and S. Chu, “Atom-wave diffraction between the Raman-Nath and the Bragg regime: Effective Rabi frequency, losses, and phase shifts,” *Physical Review A - Atomic, Molecular, and Optical Physics*, vol. 77, no. 2, p. 023609, Feb 2008. online link

[41] R. H. Parker, C. Yu, B. Estey, W. Zhong, E. Huang, and H. Müller, “Controlling the multiport nature of Bragg diffraction in atom interferometry,” *Physical Review A*, vol. 94, no. 5, p. 053618, Nov 2016. online link

[42] B. Fang, N. Mielec, D. Savoie, M. Altorio, A. Landragin, and R. Geiger, “Improving the phase response of an atom interferometer by means of temporal pulse shaping,” *New Journal of Physics*, vol. 20, no. 2, p. 023020, Feb 2018. online link

[43] A. Siegman, *Lasers*. University Science Books, 1986.

[44] N. Ismail, C. C. Kores, D. Geskus, and M. Pollnau, “Fabry-Pérot resonator: spectral line shapes, generic and related Airy distributions, linewidths, finesses, and performance at low or frequency-dependent reflectivity,” *Optics Express*, vol. 24, no. 15, p. 16366, Jul 2016. online link

[45] T. C. Briles, D. C. Yost, A. Cingöz, J. Ye, and T. R. Schibli, “Simple piezoelectric-actuated mirror with 180 kHz servo bandwidth,” *Optics Express*, vol. 18, no. 10, p. 9739, May 2010. online link

[46] Alexander Franzen, “ComponentLibrary: a free vector graphics library for optics,” 2009. online link

[47] R. H. Pantell, “The Laser Oscillator with an External Signal,” *Proceedings of the IEEE*, vol. 53, no. 5, pp. 474–477, 1965. online link

[48] C. Buczek, R. Freiberg, and M. Skolnick, “Laser injection locking,” *Proceedings of the IEEE*, vol. 61, no. 10, pp. 1411–1431, 1973. online link

[49] R. W. P. Drever, J. L. Hall, F. V. Kowalski, J. Hough, G. M. Ford, A. J. Munley, and H. Ward, “Laser phase and frequency stabilization using an optical resonator,” *Applied Physics B Photophysics and Laser Chemistry*, vol. 31, no. 2, pp. 97–105, Jun 1983. online link

[50] H. J. Metcalf and P. van der Straten, *Laser Cooling and Trapping.* Springer, 1999.

[51] T. W. Hänsch and A. L. Schawlow, “Cooling of gases by laser radiation,” *Optics Communications*, vol. 13, no. 1, pp. 68–69, Jan 1975. online link

[52] S. Chu, L. Hollberg, J. E. Bjorkholm, A. Cable, and A. Ashkin, “Three-dimensional viscous confinement and cooling of atoms by resonance radiation pressure,” *Physical Review Letters*, vol. 55, no. 1, pp. 48–51, Jul 1985. online link

[53] E. L. Raab, M. Prentiss, A. Cable, S. Chu, and D. E. Pritchard, “Trapping of Neutral Sodium Atoms with Radiation Pressure,” *Physical Review Letters*, vol. 59, no. 23, pp. 2631–2634, Dec 1987. online link

[54] P. D. Lett, W. D. Phillips, S. L. Rolston, C. E. Tanner, R. N. Watts, and C. I. Westbrook, “Optical molasses,” *Journal of the Optical Society of America B*, vol. 6, no. 11, p. 2084, Nov 1989. online link

[55] C. G. Townsend, N. H. Edwards, C. J. Cooper, K. P. Zetie, C. J. Foot, A. M. Steane, P. Szriftgiser, H. Perrin, and J. Dalibard, “Phase-space density in the magneto-optical trap,” *Physical Review A*, vol. 52, no. 2, pp. 1423–1440, Aug 1995. online link

[56] J. Dalibard and C. Cohen-Tannoudji, “Laser cooling below the Doppler limit by polarization gradients: simple theoretical models,” *Journal of the Optical Society of America B*, vol. 6, no. 11, p. 2023, Nov 1989. online link

[57] D. S. Weiss, E. Riis, Y. Shevy, P. J. Ungar, and S. Chu, “Optical molasses and multilevel atoms: experiment,” *Journal of the Optical Society of America B*, vol. 6, no. 11, p. 2072, Nov 1989. online link

[58] V. Vuletic, C. Chin, A. J. Kerman, and S. Chu, “Degenerate raman sideband cooling of trapped cesium atoms at very high atomic densities,” *Physical Review Letters*, vol. 81, no. 26, pp. 5768–5771, Dec 1998. online link

[59] A. J. Kerman, V. Vuletić, C. Chin, and S. Chu, "Beyond optical molasses: 3D raman sideband cooling of atomic cesium to high phase-space density," *Physical Review Letters*, vol. 84, no. 3, pp. 439–442, Jan 2000. online link

[60] A. J. Kerman, "Raman sideband cooling and cold atomic collisions in optical lattices," Ph.D. dissertation, Stanford University, 2002.

[61] A. Keshet and W. Ketterle, "A distributed, graphical user interface based, computer control system for atomic physics experiments," *Review of Scientific Instruments*, vol. 84, no. 1, p. 015105, Jan 2013. online link

[62] J. M. Hensley, A. Peters, and S. Chu, "Active low frequency vertical vibration isolation," *Review of Scientific Instruments*, vol. 70, no. 6, pp. 2735–2741, May 1999. online link

[63] A. Stochino *et al.*, "The Seismic Attenuation System (SAS) for the Advanced LIGO gravitational wave interferometric detectors," *Nuclear Instruments and Methods in Physics Research, Section A: Accelerators, Spectrometers, Detectors and Associated Equipment*, vol. 598, no. 3, pp. 737–753, Jan 2009. online link

[64] S. Braccini *et al.*, "The maraging-steel blades of the Virgo super attenuator," *Measurement Science and Technology*, vol. 11, no. 5, pp. 467–476, May 2000. online link

[65] C. Freier, "Measurement of Local Gravity using Atom Interferometry," Diploma thesis, Technische Universitat Berlin, 2010. online link

[66] I. Riou, N. Mielec, G. Lefevre, M. Prevedelli, A. Landragin, P. Bouyer, A. Bertoldi, R. Geiger, and B. Canuel, "A marginally stable optical resonator for enhanced atom interferometry," *Journal of Physics B: Atomic, Molecular and Optical Physics*, vol. 50, no. 15, p. 155002, Aug 2017. online link

[67] S.-W. Chiow, S. Herrmann, H. Mueller, and S. Chu, "6 W, 1 kHz linewidth, tunable continuous-wave near-infrared laser," *Optics Express*, vol. 17, no. 7, p. 5246, Mar 2009. online link

[68] S.-W. Chiow, T. Kovachy, J. M. Hogan, and M. A. Kasevich, "Generation of 43 W of quasi-continuous 780 nm laser light via high-efficiency, single-pass frequency doubling in periodically poled lithium niobate crystals." *Optics Letters*, vol. 37, no. 18, pp. 3861–3863, Sep 2012. online link

[69] G. Tackmann, P. Berg, C. Schubert, S. Abend, M. Gilowski, W. Ertmer, and E. M. Rasel, "Self-alignment of a compact large-area atomic Sagnac interferometer," *New Journal of Physics*, vol. 14, no. 1, p. 015002, Jan 2012. online link

[70] T. M. Brzozowski, M. Maczyńska, M. Zawada, J. Zachorowski, and W. Gawlik, "Time-of-flight measurement of the temperature of cold atoms for short trap-probe beam distances," *Journal of Optics B: Quantum and Semiclassical Optics*, vol. 4, no. 1, pp. 62–66, Feb 2002. online link

[71] "*NIST Digital Library of Mathematical Functions*," http://dlmf.nist.gov/, Release 1.0.20 of 2018-09-15, f. W. J. Olver, A. B. Olde Daalhuis, D. W. Lozier, B. I. Schneider, R. F. Boisvert, C. W. Clark, B. R. Miller and B. V. Saunders, eds. online link

[72] I. Dotsenko, "Raman spectroscopy of single atoms," Masters, Universität Bonn, 2002. online link

[73] I. Dotsenko, W. Alt, S. Kuhr, D. Schrader, M. Müller, Y. Miroshnychenko, V. Gomer, A. Rauschenbeutel, and D. Meschede, "Application of electro-optically generated light fields for Raman spectroscopy of trapped cesium atoms," *Applied Physics B: Lasers and Optics*, vol. 78, no. 6, pp. 711–717, Apr 2004. online link

[74] P. Hamilton, M. Jaffe, J. M. Brown, L. Maisenbacher, B. Estey, and H. Müller, "Atom interferometry in an optical cavity," *Physical Review Letters*, vol. 114, no. 10, p. 100405, Mar 2015. online link

[75] R. M. Wald, *General relativity*, 1984.

[76] C. W. Misner, K. S. Thorne, J. A. Wheeler, and D. Kaiser, *Gravitation*, 1973. online link

[77] E. Hubble, "A relation between distance and radial velocity among extra-galactic nebulae," *Proceedings of the National Academy of Sciences*, vol. 15, no. 3, pp. 168–173, Mar 1929. online link

[78] S. Perlmutter *et al.*, "Measurements of Omega and Lambda from 42 High-Redshift Supernovae," *The Astrophysical Journal*, vol. 517, no. 2, pp. 565–586, Jun 1998. online link

[79] A. G. Riess *et al.*, "Observational Evidence from Supernovae for an Accelerating Universe and a Cosmological Constant," *The Astronomical Journal, Volume 116, Issue 3, pp. 1009-1038.*, vol. 116, pp. 1009–1038, May 1998. online link

[80] S. Weinberg, "The cosmological constant problem," *Reviews of Modern Physics*, vol. 61, no. 1, pp. 1–23, Jan 1989. online link

[81] L. L. Bergström and A. Goobar, *Cosmology and particle astrophysics.* Springer, 2004. online link

[82] M. Kowalski *et al.*, “Improved Cosmological Constraints from New, Old and Combined Supernova Datasets,” *The Astrophysical Journal*, vol. 686, no. 2, pp. 749–778, Oct 2008. online link

[83] M. Betoule *et al.*, “Improved cosmological constraints from a joint analysis of the SDSS-II and SNLS supernova samples,” *Astronomy & Astrophysics*, vol. 568, p. A22, Aug 2014. online link

[84] B. D. Sherwin *et al.*, “Evidence for dark energy from the cosmic microwave background alone using the atacama cosmology telescope lensing measurements,” *Physical Review Letters*, vol. 107, no. 2, p. 021302, Jul 2011. online link

[85] Planck Collaboration *et al.*, “Planck 2015 results. I. Overview of products and scientific results,” *Astronomy & Astrophysics*, vol. 594, p. A1, Oct 2016. online link

[86] Planck Collaboration *et al.*, “Planck 2018 results. VI. Cosmological parameters,” Jul 2018. online link

[87] D. J. Eisenstein *et al.*, “Detection of the Baryon Acoustic Peak in the Large-Scale Correlation Function of SDSS Luminous Red Galaxies,” *The Astrophysical Journal*, vol. 633, no. 2, pp. 560–574, Nov 2005. online link

[88] M. Ata *et al.*, “The clustering of the SDSS-IV extended Baryon Oscillation Spectroscopic Survey DR14 quasar sample: First measurement of baryon acoustic oscillations between redshift 0.8 and 2.2,” *Monthly Notices of the Royal Astronomical Society*, vol. 473, no. 4, pp. 4773–4794, Feb 2018. online link

[89] S. Perlmutter, “Supernovae, dark energy, and the accelerating universe,” pp. 53–60, Apr 2003. online link

[90] R. R. Caldwell, R. Dave, and P. J. Steinhardt, “Cosmological imprint of an energy component with general equation of state,” *Physical Review Letters*, vol. 80, no. 8, pp. 1582–1585, Feb 1998. online link

[91] B. Ratra and P. J. Peebles, “Cosmological consequences of a rolling homogeneous scalar field,” *Physical Review D*, vol. 37, no. 12, pp. 3406–3427, Jun 1988. online link

[92] A. Joyce, B. Jain, J. Khoury, and M. Trodden, “Beyond the cosmological standard model,” pp. 1–98, Mar 2015. online link

[93] S. Schlamminger, K. Y. Choi, T. A. Wagner, J. H. Gundlach, and E. G. Adelberger, “Test of the equivalence principle using a rotating torsion balance,” *Physical Review Letters*, vol. 100, no. 4, p. 041101, Jan 2008. online link

[94] T. A. Wagner, S. Schlamminger, J. H. Gundlach, and E. G. Adelberger, “Torsion-balance tests of the weak equivalence principle,” *Classical and Quantum Gravity*, vol. 29, no. 18, p. 184002, Sep 2012. online link

[95] J. G. Williams, S. G. Turyshev, and D. H. Boggs, "Progress in lunar laser ranging tests of relativistic gravity," *Physical Review Letters*, vol. 93, no. 26 I, p. 261101, Dec 2004. online link

[96] P. Touboul *et al.*, "MICROSCOPE Mission: First Results of a Space Test of the Equivalence Principle," *Physical Review Letters*, vol. 119, no. 23, p. 231101, Dec 2017. online link

[97] E. G. Adelberger, B. R. Heckel, and A. E. Nelson, "Tests of the Gravitational Inverse-Square Law," *Annual Review of Nuclear and Particle Science*, vol. 53, no. 1, pp. 77–121, Dec 2003. online link

[98] E. G. Adelberger, B. R. Heckel, S. Hoedl, C. D. Hoyle, D. J. Kapner, and A. Upadhye, "Particle-physics implications of a recent test of the gravitational inverse-square law," *Physical Review Letters*, vol. 98, no. 13, p. 131104, Mar 2007. online link

[99] D. J. Kapner, T. S. Cook, E. G. Adelberger, J. H. Gundlach, B. R. Heckel, C. D. Hoyle, and H. E. Swanson, "Tests of the gravitational inverse-square law below the dark-energy length scale," *Physical Review Letters*, vol. 98, no. 2, p. 021101, Jan 2007. online link

[100] J. Khoury and A. Weltman, "Chameleon fields: Awaiting surprises for tests of gravity in space," *Physical Review Letters*, vol. 93, no. 17, p. 171104, Oct 2004. online link

[101] J. Khoury and A. Weltman, "Chameleon cosmology," *Physical Review D*, vol. 69, no. 4, p. 044026, Feb 2004. online link

[102] P. J. Steinhardt, L. Wang, and Z. Ivaylo, "Cosmological tracking solutions," *Physical Review D - Particles, Fields, Gravitation and Cosmology*, vol. 59, no. 12, p. 123504, May 1999. online link

[103] I. Zlatev, L. Wang, and P. J. Steinhardt, "Quintessence, cosmic coincidence, and the cosmological constant," *Physical Review Letters*, vol. 82, no. 5, pp. 896–899, Feb 1999. online link

[104] C. Burrage, E. J. Copeland, and E. A. Hinds, "Probing dark energy with atom interferometry," *Journal of Cosmology and Astroparticle Physics*, vol. 2015, no. 3, pp. 042–042, Mar 2015. online link

[105] P. Brax and C. Burrage, "Atomic precision tests and light scalar couplings," *Physical Review D*, vol. 83, no. 3, p. 035020, Feb 2011. online link

[106] B. Elder, J. Khoury, P. Haslinger, M. Jaffe, H. Müller, and P. Hamilton, "Chameleon dark energy and atom interferometry," *Physical Review D*, vol. 94, no. 4, p. 044051, Aug 2016. online link

[107] K. Jones-Smith and F. Ferrer, "Detecting chameleon dark energy via an electrostatic analogy," *Physical Review Letters*, vol. 108, no. 22, p. 221101, May 2012. online link

[108] P. Hamilton, M. Jaffe, P. Haslinger, Q. Simmons, H. Müller, and J. Khoury, "Atom-interferometry constraints on dark energy," *Science*, vol. 349, no. 6250, pp. 849–851, 2015.

[109] M. Jaffe, P. Haslinger, V. Xu, P. Hamilton, A. Upadhye, B. Elder, J. Khoury, and H. Müller, "Testing sub-gravitational forces on atoms from a miniature in-vacuum source mass," *Nature Physics*, vol. 13, no. 10, pp. 938–942, Jul 2017. online link

[110] C. Burrage, E. J. Copeland, and P. Millington, "Radiative screening of fifth forces," *Physical Review Letters*, vol. 117, no. 21, p. 211102, Nov 2016. online link

[111] A. Upadhye, "Symmetron dark energy in laboratory experiments," *Physical Review Letters*, vol. 110, no. 3, p. 031301, Jan 2013. online link

[112] C. Burrage, A. Kuribayashi-Coleman, J. Stevenson, B. Thrussell, and C. Burrage, "Constraining Symmetron Fields with Atom Interferometry," *Journal of Cosmology and Astroparticle Physics*, vol. 2016, no. 12, pp. 041–041, Sep 2016. online link

[113] P. Brax and A. C. Davis, "Atomic interferometry test of dark energy," *Physical Review D*, vol. 94, no. 10, p. 104069, Nov 2016. online link

[114] K. Li *et al.*, "Neutron limit on the strongly-coupled chameleon field," *Physical Review D*, vol. 93, no. 6, p. 062001, Mar 2016. online link

[115] T. Jenke *et al.*, "Gravity resonance spectroscopy constrains dark energy and dark matter scenarios," *Physical Review Letters*, vol. 112, no. 15, p. 151105, Apr 2014. online link

[116] A. D. Rider, D. C. Moore, C. P. Blakemore, M. Louis, M. Lu, and G. Gratta, "Search for Screened Interactions Associated with Dark Energy below the 100 μm Length Scale," *Physical Review Letters*, vol. 117, no. 10, p. 101101, Aug 2016. online link

[117] R. Charrière, M. Cadoret, N. Zahzam, Y. Bidel, and A. Bresson, "Local gravity measurement with the combination of atom interferometry and Bloch oscillations," *Physical Review A - Atomic, Molecular, and Optical Physics*, vol. 85, no. 1, p. 013639, Jan 2012. online link

[118] X. Zhang, R. P. Del Aguila, T. Mazzoni, N. Poli, and G. M. Tino, "Trapped-atom interferometer with ultracold Sr atoms," *Physical Review A*, vol. 94, no. 4, p. 043608, Oct 2016. online link

[119] B. Barrett, L. Antoni-Micollier, L. Chichet, B. Battelier, T. Lévèque, A. Landragin, and P. Bouyer, "Dual matter-wave inertial sensors in weightlessness," *Nature Communications*, vol. 7, p. 13786, Dec 2016. online link

[120] W. Herschel, "Experiments on the Refrangibility of the Invisible Rays of the Sun. By William Herschel, LL. D. F. R. S." *Philosophical Transactions of the Royal Society of London*, vol. 90, no. 0, pp. 284–292, Jan 1800. online link

[121] M. Planck, "Zur theorie des gesetzes der energieverteilung im normalspectrum," in *Verhandlungen der Deutschen Physikalischen Gesellschaft 2*, 1900, pp. 237–245.

[122] L. Rayleigh, "LIII. Remarks upon the law of complete radiation," *Philosophical Magazine Series 5*, vol. 49, no. 301, pp. 539–540, Jun 1900. online link

[123] J. Jeans, "XI. On the partition of energy between matter and Æther," *The London, Edinburgh, and Dublin Philosophical Magazine and Journal of Science*, vol. 10, no. 55, pp. 91–98, Jul 1905. online link

[124] A. A. Penzias and R. W. Wilson, "A Measurement of Excess Antenna Temperature at 4080 Mc/s." *The Astrophysical Journal*, vol. 142, p. 419, Jul 1965. online link

[125] R. H. Dicke, P. J. E. Peebles, P. G. Roll, and D. T. Wilkinson, "Cosmic Black-Body Radiation." *The Astrophysical Journal*, vol. 142, p. 414, Jul 1965. online link

[126] C. L. Bennett, A. Banday, K. M. Gorski, G. Hinshaw, P. Jackson, P. Keegstra, A. Kogut, G. F. Smoot, D. T. Wilkinson, and E. L. Wright, "4-Year COBE DMR Cosmic Microwave Background Observations: Maps and Basic Results," *The Astrophysical Journal*, vol. 464, no. 1, pp. L1–L4, Jun 1996. online link

[127] G. Hinshaw *et al.*, "Three-Year Wilkinson Microwave Anisotropy Probe (WMAP) Observations: Temperature Analysis," *The Astrophysical Journal Supplement Series*, vol. 170, no. 2, pp. 288–334, Jun 2006. online link

[128] M. S. Safronova, D. Jiang, B. Arora, C. W. Clark, M. G. Kozlov, U. I. Safronova, and W. R. Johnson, "Black-body radiation shifts and theoretical contributions to atomic clock research," in *IEEE Transactions on Ultrasonics, Ferroelectrics, and Frequency Control*, vol. 57, no. 1, Jan 2010, pp. 94–105. online link

[129] T. Nicholson *et al.*, "Systematic evaluation of an atomic clock at 2×10^{-18} total uncertainty," *Nature Communications*, vol. 6, no. 1, p. 6896, Dec 2015. online link

[130] NASA, "How Does Our Sun Compare With Other Stars? :: NASA Space Place." online link

[131] M. Sonnleitner, M. Ritsch-Marte, and H. Ritsch, "Attractive optical forces from blackbody radiation," *Physical Review Letters*, vol. 111, no. 2, p. 023601, Jul 2013. online link

[132] R. Grimm, M. Weidemüller, and Y. B. Ovchinnikov, "Optical Dipole Traps for Neutral Atoms," *Advances in Atomic, Molecular and Optical Physics*, vol. 42, no. C, pp. 95–170, Jan 2000. online link

[133] A. Ashkin and J. M. Dziedzic, “Optical trapping and manipulation of viruses and bacteria,” *Science*, vol. 235, no. 4795, pp. 1517–1520, Mar 1987. online link

[134] S. Micalizio, A. Godone, D. Calonico, F. Levi, and L. Lorini, “Blackbody radiation shift of the ^{133}Cs hyperfine transition frequency,” *Physical Review A - Atomic, Molecular, and Optical Physics*, vol. 69, no. 5 B, p. 053401, May 2004. online link

[135] U. D. Jentschura and M. Haas, “Reexamining blackbody shifts for hydrogenlike ions,” *Physical Review A - Atomic, Molecular, and Optical Physics*, vol. 78, no. 4, p. 042504, Oct 2008. online link

[136] J. R. Howell, R. Siegel, and M. P. Menguc, *Thermal Radiation Heat Transfer*, 2011.

[137] M. Sonnleitner, “Thermal radiation and atoms in an open cylinder,” unpublished internal memo, p. 14, 2018.

[138] P. Haslinger, M. Jaffe, V. Xu, O. Schwartz, M. Sonnleitner, M. Ritsch-Marte, H. Ritsch, and H. Müller, “Attractive force on atoms due to blackbody radiation,” *Nature Physics*, vol. 14, no. 3, pp. 257–260, Mar 2018. online link

[139] S. Scheel and S. Y. Buhmann, “Casimir-Polder forces on moving atoms,” *Physical Review A - Atomic, Molecular, and Optical Physics*, vol. 80, no. 4, p. 042902, Oct 2009. online link

[140] M. A. Hohensee, B. Estey, P. Hamilton, A. Zeilinger, and H. Müller, “Force-free gravitational redshift: Proposed gravitational Aharonov-Bohm experiment,” *Physical Review Letters*, vol. 108, no. 23, p. 230404, Jun 2012. online link

[141] R. P. Feynman, F. L. Vernon, and R. W. Hellwarth, “Geometrical Representation of the Schrödinger Equation for Solving Maser Problems,” *Journal of Applied Physics*, vol. 28, no. 1, pp. 49–52, Jan 1957. online link

[142] J. Bateman and T. Freegarde, “Fractional adiabatic passage in two-level systems: Mirrors and beam splitters for atomic interferometry,” *Physical Review A - Atomic, Molecular, and Optical Physics*, vol. 76, no. 1, p. 013416, Jul 2007. online link

[143] D. Rosenfeld, S. L. Panfil, and Y. Zur, “Optimization of Adiabatic Selective Pulses,” *Journal of Magnetic Resonance*, vol. 126, no. 2, pp. 221–228, Jun 1997. online link

[144] S. McDonald and W. S. Warren, “Uses of shaped pulses in NMR: A primer,” *Concepts in Magnetic Resonance*, vol. 3, no. 2, pp. 55–81, Apr 1991. online link

[145] M. Garwood and L. DelaBarre, “The return of the frequency sweep: Designing adiabatic pulses for contemporary NMR,” *Journal of Magnetic Resonance*, vol. 153, no. 2, pp. 155–177, Dec 2001. online link

[146] J. Mizrahi, C. Senko, B. Neyenhuis, K. G. Johnson, W. C. Campbell, C. W. Conover, and C. Monroe, "Ultrafast spin-motion entanglement and interferometry with a single atom," *Physical Review Letters*, vol. 110, no. 20, p. 203001, May 2013. online link

[147] W. C. Campbell and P. Hamilton, "Rotation sensing with trapped ions," *Journal of Physics B: Atomic, Molecular and Optical Physics*, vol. 50, no. 6, p. 064002, Mar 2017. online link

[148] K. Kotru, "Timekeeping and accelerometry with robust light pulse atom interferometers," Thesis, Massachusetts Institute of Technology, 2015.

[149] P. D. Featonby, G. S. Summy, C. L. Webb, R. M. Godun, M. K. Oberthaler, A. C. Wilson, C. J. Foot, and K. Burnett, "Separated-path ramsey atom interferometer," *Physical Review Letters*, vol. 81, no. 3, pp. 495–499, Jul 1998. online link

[150] T. Kovachy, S.-W. Chiow, and M. A. Kasevich, "Adiabatic-rapid-passage multiphoton Bragg atom optics," *Physical Review A - Atomic, Molecular, and Optical Physics*, vol. 86, no. 1, p. 011606, Jul 2012. online link

[151] K. Kotru, D. L. Butts, J. M. Kinast, and R. E. Stoner, "Large-Area Atom Interferometry with Frequency-Swept Raman Adiabatic Passage," *Physical Review Letters*, vol. 115, no. 10, p. 103001, Aug 2015. online link

[152] D. H. Wolpert and W. G. Macready, "No free lunch theorems for optimization," *IEEE Transactions on Evolutionary Computation*, vol. 1, no. 1, pp. 67–82, Apr 1997. online link

[153] M. Dovale-Álvarez, D. D. Brown, A. W. Jones, C. M. Mow-Lowry, H. Miao, and A. Freise, "Fundamental limitations of cavity-assisted atom interferometry," *Physical Review A*, vol. 96, no. 5, p. 053820, Nov 2017. online link

[154] P. W. Graham, J. M. Hogan, M. A. Kasevich, and S. Rajendran, "Resonant mode for gravitational wave detectors based on atom interferometry," *Physical Review D*, vol. 94, no. 10, p. 104022, Nov 2016. online link

[155] P. W. Graham, D. E. Kaplan, J. Mardon, S. Rajendran, and W. A. Terrano, "Dark matter direct detection with accelerometers," *Physical Review D*, vol. 93, no. 7, p. 075029, Apr 2016. online link

[156] M. F. Kasim, "Fast 2D phase unwrapping implementation in MATLAB," 2017. online link

[157] M. A. Herráez, D. R. Burton, M. J. Lalor, and M. A. Gdeisat, "Fast two-dimensional phase-unwrapping algorithm based on sorting by reliability following a noncontinuous path," *Applied Optics*, vol. 41, no. 35, p. 7437, Dec 2002. online link

[158] O. Hosten, N. J. Engelsen, R. Krishnakumar, and M. A. Kasevich, “Measurement noise 100 times lower than the quantum-projection limit using entangled atoms,” *Nature*, vol. 529, no. 7587, pp. 505–508, Jan 2016. online link

[159] K. C. Cox, G. P. Greve, J. M. Weiner, and J. K. Thompson, “Deterministic Squeezed States with Collective Measurements and Feedback,” *Physical Review Letters*, vol. 116, no. 9, p. 093602, Mar 2016. online link

[160] J. Hogan, Mar 2017.

[161] G. Tino, Sep 2018.

[162] D. Becker *et al.*, “Space-borne Bose–Einstein condensation for precision interferometry,” *Nature*, vol. 562, no. 7727, pp. 391–395, Oct 2018. online link

[163] “Cold Atom Laboratory,” 2018. online link

[164] “BECCAL - Bose-Einstein Condensate and Cold Atom Lab — Optical Metrology.” online link

[165] B. Arora, M. S. Safronova, and C. W. Clark, “Tune-out wavelengths of alkali-metal atoms and their applications,” *Physical Review A - Atomic, Molecular, and Optical Physics*, vol. 84, no. 4, p. 043401, Oct 2011. online link

[166] J. I. Thorpe, K. Numata, and J. Livas, “Laser frequency stabilization and control through offset sideband locking to optical cavities,” *Optics Express*, vol. 16, no. 20, p. 15980, Sep 2008. online link

[167] T. Leopold, L. Schmöger, S. Feuchtenbeiner, C. Grebing, P. Micke, N. Scharnhorst, I. D. Leroux, J. R. López-Urrutia, and P. O. Schmidt, “A tunable low-drift laser stabilized to an atomic reference,” *Applied Physics B: Lasers and Optics*, vol. 122, no. 9, p. 236, Sep 2016. online link

[168] G. Milani, B. Rauf, P. Barbieri, F. Bregolin, M. Pizzocaro, P. Thoumany, F. Levi, and D. Calonico, “Multiple wavelength stabilization on a single optical cavity using the offset sideband locking technique,” *Optics Letters*, vol. 42, no. 10, pp. 1970–1973, May 2017. online link

[169] H. Müller, “Modern Optical Tests of Relativity,” Ph.D. dissertation, Humboldt-Universität zu Berlin, 2003.

[170] J. Le Gouët, T. E. Mehlstäubler, J. Kim, S. Merlet, A. Clairon, A. Landragin, and F. P. Dos Santos, “Limits to the sensitivity of a low noise compact atomic gravimeter,” *Applied Physics B: Lasers and Optics*, vol. 92, no. 2, pp. 133–144, Aug 2008. online link

[171] M. K. Zhou, Z. K. Hu, X. C. Duan, B. L. Sun, L. L. Chen, Q. Z. Zhang, and J. Luo, “Performance of a cold-atom gravimeter with an active vibration isolator,” *Physical Review A - Atomic, Molecular, and Optical Physics*, vol. 86, no. 4, p. 043630, Oct 2012. online link

[172] S. Merlet, J. Le Gouët, Q. Bodart, A. Clairon, A. Landragin, F. Pereira Dos Santos, and P. Rouchon, “Operating an atom interferometer beyond its linear range,” *Metrologia*, vol. 46, no. 1, pp. 87–94, Feb 2009. online link

[173] P. Cheinet, B. Canuel, F. P. Dos Santos, A. Gauguet, F. Yver-Leduc, and A. Landragin, “Measurement of the sensitivity function in a time-domain atomic interferometer,” *IEEE Transactions on Instrumentation and Measurement*, vol. 57, no. 6, pp. 1141–1148, Jun 2008. online link

[174] F. Bloch, “Über die Quantenmechanik der Elektronen in Kristallgittern,” *Zeitschrift für Physik*, vol. 52, no. 7-8, pp. 555–600, Jul 1929. online link

[175] C. Zener, “A Theory of the Electrical Breakdown of Solid Dielectrics,” *Proceedings of the Royal Society A: Mathematical, Physical and Engineering Sciences*, vol. 145, no. 855, pp. 523–529, Jul 1934. online link

[176] C. Waschke, H. G. Roskos, R. Schwedler, K. Leo, H. Kurz, and K. Köhler, “Coherent submillimeter-wave emission from Bloch oscillations in a semiconductor superlattice,” *Physical Review Letters*, vol. 70, no. 21, pp. 3319–3322, May 1993. online link

[177] M. Ben Dahan, E. Peik, J. Reichel, Y. Castin, and C. Salomon, “Bloch oscillations of atoms in an optical potential,” *Physical Review Letters*, vol. 76, no. 24, pp. 4508–4511, Jun 1996. online link

[178] C. Zener, “Non-Adiabatic Crossing of Energy Levels,” *Proceedings of the Royal Society A: Mathematical, Physical and Engineering Sciences*, vol. 137, no. 833, pp. 696–702, Sep 1932. online link

[179] P. Cladé, “Bloch oscillations in atom interferometry,” *Rivista del Nuovo Cimento*, vol. 38, no. 4, pp. 173–207, May 2015. online link

[180] G. Ferrari, N. Poli, F. Sorrentino, and G. M. Tino, “Long-lived bloch oscillations with bosonic Sr atoms and application to gravity measurement at the micrometer scale,” *Physical Review Letters*, vol. 97, no. 6, p. 060402, Aug 2006. online link

[181] P. Cladé, E. De Mirandes, M. Cadoret, S. Guellati-Khélifa, C. Schwob, F. Nez, L. Julien, and F. Biraben, “Precise measurement of h/mRb using Bloch oscillations in a vertical optical lattice: Determination of the fine-structure constant,” *Physical Review A - Atomic, Molecular, and Optical Physics*, vol. 74, no. 5, p. 052109, Nov 2006. online link

[182] P. Cladé, T. Plisson, S. Guellati-Khélifa, F. Nez, and F. Biraben, "Theoretical analysis of a large momentum beamsplitter using Bloch oscillations," *European Physical Journal D*, vol. 59, no. 3, pp. 349–360, Sep 2010. online link

[183] T. A. Savard, K. M. O'Hara, and J. E. Thomas, "Laser-noise-induced heating in far-off resonance optical traps," *Physical Review A - Atomic, Molecular, and Optical Physics*, vol. 56, no. 2, pp. R1095–R1098, Aug 1997. online link

[184] N. D. Oppong, "Towards a degenerate Fermi gas of strontium-87 in a 3D optical lattice," Masters, JILA, CU Boulder/NIST and ETH Zurich, 2015. online link

[185] S. Gerlich *et al.*, "A Kapitza-Dirac-Talbot-Lau interferometer for highly polarizable molecules," *Nature Physics*, vol. 3, no. 10, pp. 711–715, Oct 2007. online link

[186] P. Haslinger, N. Dörre, P. Geyer, J. Rodewald, S. Nimmrichter, and M. Arndt, "A universal matter-wave interferometer with optical ionization gratings in the time domain," *Nature Physics*, vol. 9, no. 3, pp. 144–148, Mar 2013. online link

[187] H. Müller, A. Peters, and S. Chu, "A precision measurement of the gravitational redshift by the interference of matter waves," *Nature*, vol. 463, no. 7283, pp. 926–929, Feb 2010. online link

[188] P. Wolf, L. Blanchet, C. J. Borde, S. Reynaud, C. Salomon, and C. Cohen-Tannoudji, "Atom gravimeters and gravitational redshift," *Nature*, vol. 467, no. 7311, pp. E1–E1, Sep 2010. online link

[189] S. Sinha and J. Samuel, "Atom interferometry and the gravitational redshift," *Class. Quantum Grav.*, vol. 28, no. 14, p. 145018, Jul 2011. online link

[190] M. A. Hohensee, S. Chu, A. Peters, and H. Müller, "Equivalence principle and gravitational redshift," *Physical Review Letters*, vol. 106, no. 15, p. 151102, Apr 2011. online link

[191] P. Wolf, L. Blanchet, C. J. Bordé, S. Reynaud, C. Salomon, and C. Cohen-Tannoudji, "Does an atom interferometer test the gravitational redshift at the Compton frequency?" *Classical and Quantum Gravity*, vol. 28, no. 14, p. 145017, Jul 2011. online link

[192] M. A. Hohensee, S. Chu, A. Peters, and H. Müller, "Comment on: 'Does an atom interferometer test the gravitational redshift at the Compton frequency?'," *Classical and Quantum Gravity*, vol. 29, no. 4, p. 048001, Feb 2012. online link

[193] L. Zhu, Y.-H. Lien, A. Hinton, A. Niggebaum, C. Rammeloo, K. Bongs, and M. Holynski, "Application of optical single-sideband laser in Raman atom interferometry," *Optics Express*, vol. 26, no. 6, p. 6542, Mar 2018. online link

[194] W. Ehrenberg and R. E. Siday, "The refractive index in electron optics and the principles of dynamics," *Proceedings of the Physical Society. Section B*, vol. 62, no. 1, pp. 8–21, Jan 1949. online link

[195] Y. Aharonov and D. Bohm, "Significance of electromagnetic potentials in the quantum theory," *Physical Review*, vol. 115, no. 3, pp. 485–491, Aug 1959. online link

[196] R. G. Chambers, "Shift of an electron interference pattern by enclosed magnetic flux," *Physical Review Letters*, vol. 5, no. 1, pp. 3–5, Jul 1960. online link

[197] A. Tonomura, N. Osakabe, T. Matsuda, T. Kawasaki, J. Endo, S. Yano, and H. Yamada, "Evidence for Aharonov-Bohm effect with magnetic field completely shielded from electron wave," *Physical Review Letters*, vol. 56, no. 8, pp. 792–795, Feb 1986. online link

[198] G. Badurek, H. Weinfurter, R. Gähler, A. Kollmar, S. Wehinger, and A. Zeilinger, "Nondispersive phase of the Aharonov-Bohm effect," *Physical Review Letters*, vol. 71, no. 3, pp. 307–311, Jul 1993. online link

[199] S. Y. Lan, P. C. Kuan, B. Estey, D. English, J. M. Brown, M. A. Hohensee, and H. Müller, "A clock directly linking time to a particle's mass," *Science*, vol. 339, no. 6119, pp. 554–557, Feb 2013. online link

[200] A. Roura, "Gravitational redshift in quantum-clock interferometry," Oct 2018. online link

[201] P. Hamilton, M. Jaffe, J. M. Brown, B. Estey, H. Muller, R. Compton, and K. Nelson, "Concept of a miniature atomic sensor," in *2014 International Symposium on Inertial Sensors and Systems (ISISS)*, 2014.

[202] Z. Chen, J. G. Bohnet, J. M. Weiner, K. C. Cox, and J. K. Thompson, "Cavity-aided nondemolition measurements for atom counting and spin squeezing," *Physical Review A - Atomic, Molecular, and Optical Physics*, vol. 89, no. 4, p. 043837, Apr 2014. online link